## REFERENCE ONLY

# UNIVERSITY OF LONDON THESIS

Degree *P h D*     Year *2006*     Name of Author *SARWAR, Misbah*

## COPYRIGHT

This is a thesis accepted for a Higher Degree of the University of London. It is an unpublished typescript and the copyright is held by the author. All persons consulting the thesis must read and abide by the Copyright Declaration below.

## COPYRIGHT DECLARATION

I recognise that the copyright of the above-described thesis rests with the author and that no quotation from it or information derived from it may be published without the prior written consent of the author.

## LOANS

Theses may not be lent to individuals, but the Senate House Library may lend a copy to approved libraries within the United Kingdom, for consultation solely on the premises of those libraries. Application should be made to: Inter-Library Loans, Senate House Library, Senate House, Malet Street, London WC1E 7HU.

## REPRODUCTION

University of London theses may not be reproduced without explicit written permission from the Senate House Library. Enquiries should be addressed to the Theses Section of the Library. Regulations concerning reproduction vary according to the date of acceptance of the thesis and are listed below as guidelines.

A.     Before 1962. Permission granted only upon the prior written consent of the author. (The Senate House Library will provide addresses where possible).

B.     1962 - 1974. In many cases the author has agreed to permit copying upon completion of a Copyright Declaration.

C.     1975 - 1988. Most theses may be copied upon completion of a Copyright Declaration.

D.     1989 onwards. Most theses may be copied.

*This thesis comes within category D.*

☐ This copy has been deposited in the Library of _____ UCC _____

☐ This copy has been deposited in the Senate House Library, Senate House, Malet Street, London WC1E 7HU.

# Computer Simulation of the Adsorption of Chlorinated Organics in Zeolites

Misbah Sarwar

Davy-Faraday Research Laboratory, The Royal Institution of Great Britain
Department of Earth Sciences, University College London

London, March 2006

A thesis submitted for the degree of Doctor of Philosophy

UMI Number: U592391

UMI

Dissertation Publishing

ProQuest

# Abstract

Computer modelling techniques have been used to study the adsorption of three chlorinated hydrocarbons; Dichloromethane, 1,2-Dichloroethane, and Trichloroethene in three different zeolite frameworks; MFI, MOR and FAU. Calculations have been performed using both classical methods based on inter-atomic potentials, quantum mechanical Density Functional Theory (DFT) and combined QM/MM embedded methods.

The first section of this thesis presents results of DFT calculations on purely siliceous and aluminosilicate gas-phase clusters. The results obtained are compared to experimental data and are found to differ significantly from experimental results. The reasons for this are rationalised and alternative methods suggested.

The second section investigates some of these alternative approaches. Results of a Periodic DFT study and cluster calculations using a hybrid functional are presented. The QMPot embedded cluster method is then employed as an alternative to the cluster and periodic DFT approaches. The results of these different approaches are compared and rationalised.

The thesis then moves on to describe atomistic simulations of the adsorption and diffusion of the molecules in the framework structures. The third section of this thesis uses the Grand Canonical Monte Carlo method to simulate adsorption isotherms and isosteric heat plots. The simulated data is found to be in good agreement to that in the literature.

The final chapter describes results of a Molecular Dynamics simulation which models the diffusion of the molecules in the FAU framework at different temperatures.

# Contents

# List of Figures

# List of Tables

# Copyright

# Acknowledgements

# Chapter One: Introduction

Molecular modelling can be used to further our understanding of intra-zeolite chemistry and how zeolites function as adsorbents, catalysts and ion-exchangers. The techniques enable the investigation of relationships between zeolite structure and properties and are a powerful tool when used alongside experimental studies. Simulation allows elucidation of the nature and location of adsorption sites, which cannot be gauged by diffraction techniques or unambiguously determined by spectroscopy. The catalytic behaviour of a zeolite also cannot be fully understood without theoretical information on the Potential Energy Surface (PES), in particular minima and saddle points [1].

With increasing computer power more sophisticated methods have been applied to zeolites, including quantum mechanical based techniques such as DFT and more recently embedded and *ab-initio* Molecular Dynamics methods which permit the examination of many new areas of zeolite science and allow more realistic structures to be modelled [2-4]. Increasingly, theoretical methods are used to predict structural features and to generate hypothetical framework structures [5-7]. Zeolite synthesis can also be simulated to further our understanding of the role of various conditions, as can the diffusion of guest molecules within the micropores [8,9].

This thesis focuses on studying the adsorption of three chlorinated organic molecules within different zeolite structures using a variety of modelling techniques, namely DFT, QM/MM embedded method and Monte Carlo simulations to evaluate the effectiveness of each method. Each technique forms one of the first three results chapters of this thesis. The final chapter will describe a Molecular Dynamics study on the diffusion of the same three molecules within the Faujasite structure.

## 1.1 Structural features of zeolites

By definition, zeolites are a class of crystalline aluminosilicates that possess a three-dimensional framework structure with cavities and pores of molecular dimensions [10]. The zeolite framework is primarily composed of tetrahedral units of silica $(SiO_4)^{4-}$. These tetrahedral units assemble into secondary building units (SBUs) often in the form of simple polyhedra (e.g. cubes, hexagonal prisms), which come together to form either an array of interconnecting channels or a system of cage-like voids as illustrated in figure 1.1.
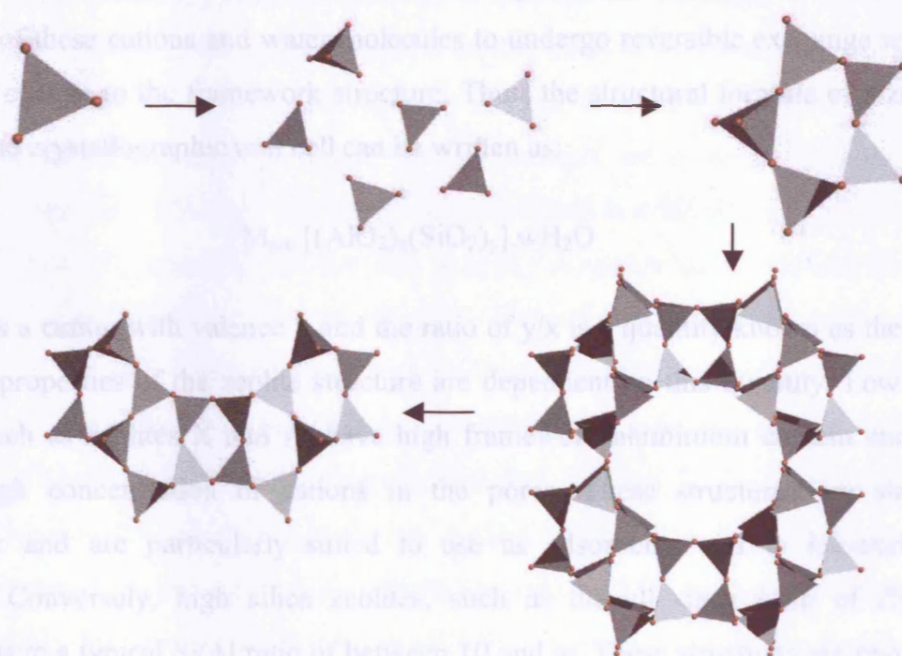
**Figure 1.1** Schematic representation of how zeolites come together: Tetrahedral units come together to form a five-ring unit which assemble to form a larger structure.

Zeolite channels are typically between 3Å and 10Å wide [11] and have a large internal surface, providing a huge area for adsorption. The shape of these unique porous structures coupled with the huge internal surface areas gives rise to a vast number of applications. Due to the shape of the pores and channels, molecules can be excluded on the basis of size and shape (shape selectivity) and catalytic processes can be driven to yield only reaction products that are commensurate with the zeolite pores. The amount of surface area governs the sorption capacity and, thus influences the catalytic activity

of a zeolite. Hence, the chemical properties of a zeolite invariably depend on its structural features.

The zeolite framework can be considered to be dynamic in that it responds to changes in temperature, pressure and to the adsorbate enclosed within it. Isomorphous substitution of $Si^{4+}$ with $Al^{3+}$ can take place resulting in a net negative charge residing on the framework. Charge neutrality is preserved by loosely held cations within the zeolite cavities and/or protonation of the framework oxygens. As well as cations, the zeolite voids and channels can contain water molecules. A particular characteristic of zeolites is the ability of these cations and water molecules to undergo reversible exchange without significant change to the framework structure. Thus, the structural formula of a zeolite, based on the crystallographic unit cell can be written as:

$$M_{x \cdot n} \, [(AlO_2)_x (SiO_2)_y] . wH_2O$$
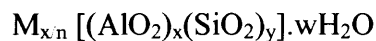
where M is a cation with valence n and the ratio of y/x is a quantity known as the Si/Al ratio. The properties of the zeolite structure are dependent on this quantity. Low silica zeolites, such as zeolites X and A, have high framework aluminium content and thus have a high concentration of cations in the pores. These structures are strongly hydrophilic and are particularly suited to use as adsorbents and in ion-exchange processes. Conversely, high silica zeolites, such as the all silica form of ZSM-5, Silicalite, have a typical Si/Al ratio of between 10 and $\infty$. These structures are known to be hydrophobic and organophilic [12]. These properties allow the high-silica zeolites to remove organic compounds from water. For catalytic applications, highly siliceous structures with highly dispersed cations are desirable. The high silica framework allows the zeolite to withstand the high temperatures associated with catalysis whilst well-separated cations ensure that each site has maximum strength. Additionally, Löwenstein's rule forbids Al-O-Al bridges and therefore the Si/Al ratio cannot be less than one in order to avoid coulombic repulsion between Al atoms.

## 1.2 Zeolites – a brief history and future directions

Natural zeolites are found in rocks of volcanic origin. First discovered by the Swedish minerologist Axel F. Cronstedt in 1756, the term zeolite was coined from the Greek '*zeo*' (to boil) and '*lithos*' (stone) – an allusion to the fact that the mineral appeared to boil when heated [13]. Many of the natural zeolites can be produced synthetically, as can a great number of zeolites with no natural analogue. Zeolites are synthesised by dissolving an alumina source and a silica source in a basic aqueous solution. An alkali cation source is often used to preserve charge neutrality. A structure directing template, in the form of a quaternary ammonium cation is also sometimes added to the synthesis mixture. The structure formed is dependent on the silica to alumina ratio, the cation used and the synthesis temperature. Initially studies focused on synthesising those zeolites that already existed in nature before attempts were made to form novel framework structures. Much of this pioneering work was conducted by R.M. Barrer in the 1940's [14,15]. Inspired by Barrer's results, scientists at the Union Carbide Laboratories synthesised the first zeolites by hydrothermal synthesis – a process requiring less extreme pressures and temperatures than previously. This led to the discovery of the synthetic zeolites X and A, which were subsequently introduced as catalysts in the cracking of hydrocarbons for the fuel industry. In the early 1970's the new MFI type zeolite, a zeolite with key catalytic properties, was synthesised by introducing organic cations into the synthesis procedure. MFI is the framework code that defines the three-letter code for the family. This is explained in more detail on the next page. In the 1980's the ion-exchange properties of zeolite A were first utilised as water softeners in washing powders, now one of the biggest markets for zeolites.

Zeolitic structures have also been made with $AlO_4$ and $PO_4$ tetrahedra, referred to as aluminophosphates or ALPOs [16]. Incorporation of silicon into the ALPO framework results in silico-aluminophospates or SAPOs [17]. Substituting metal atoms other than aluminium into the framework can increase the range of catalytic reactions that can be carried out by zeolites. Titanosilicates are one such example of metal substituted molecular sieves, which can be used to carry out shape selective oxidation reactions [18,19]. There is currently a great deal of research into incorporating other metal atoms into the zeolitic framework [20-22].

Recently mesoporous materials have been synthesised which can have pores in the 2 – 20nm size range [23]. Unlike zeolites these materials are non-crystalline and do not have well defined atomic positions. They do however have a regular structure. These materials have potential zeolite-like properties combined with larger pore sizes, which may extend the range of reactions that can be catalysed.

To date there are more than 160 zeolite structures [24]. The large variety of structures arises from the different ways that the primary building units can assemble to form channels and cavities of different sizes, the various cations that can be used for charge compensation and also the various structures that can be generated by substituting cations for framework atoms. The large numbers of zeolites are classified into structure type codes, which are assigned by the International Zeolite Association. These codes are typically three letters, which in the case of a synthetic zeolite often represent the name of the company or university that carried out the synthesis. It is also common for a number to be denoted after the code. An example is the zeolite ZSM5, which was a Zeolite synthesised by Secony Mobil. In the case of a natural zeolite the three-letter code is often based around the name of the natural mineral. In recent years three letter codes have been assigned to families of zeolite structures – i.e. those that have similar structures. Thus ZSM-5, ZSM-11 and ZSM-12 all belong to the MFI family. In some cases the original name of the zeolite, for example zeolites A, X and Y is still commonly used rather than their family structure codes, LTA, for zeolite A and FAU for zeolites X and Y.

## 1.3 Applications

Zeolites have applications in three main fields: ion-exchange, sorption and catalysis. The properties of a zeolite are strongly related to the framework and each application utilises the features of the particular framework topology used. For example, the ion-exchange properties of zeolites are dependent on the number and nature of the cation sites and their accessibility. Ion-exchange, a property exploited in the detergent industry, accounts for the largest market share of zeolites [25]. The present study will focus only on the adsorption and catalytic properties of zeolites and these are discussed in more detail overleaf.

## 1.3.1 Adsorption

Adsorption can be defined as the preferential separation of substances from the liquid or gaseous phase on the surface of a solid substance. Molecules can adsorb onto the zeolite surface in two ways. The first of these is physisorption whereby the molecule attaches to the surface of the solid by weak intermolecular forces including van der Waals (dispersion-repulsion) and electrostatic interactions. Alternatively a species may chemisorb, whereby electrons are transferred between the adsorbate and the zeolite, and a chemical bond is formed with the surface. When adsorbate molecules are physisorbed they remain intact and can be desorbed relatively easily whilst removal of a chemisorbed species may result in the formation of new products. For the purpose of this study we will only consider physisorption. Polar molecules such as those being investigated have a particularly strong interaction with the zeolite surface due to the strong electrostatic field present within the zeolite crystal.

Zeolites preferentially adsorb molecules that are of smaller size than the pore window and thus adsorption is highly dependent on the size of the pore openings and void volume (i.e. the accessible volume). The adsorption capacity is determined by the availability of internal surfaces. A molecular understanding of the adsorption process is crucial as it is a pre-step to catalysis, since a molecule must adsorb at an active site before it can react. Given that the Si atoms of the zeolite framework are smaller than the oxygen atoms, the adsorbed molecules experience interaction mainly with the large oxygen atoms, whilst interaction with the Si atoms is inhibited since they are shielded by the four surrounding oxygen atoms. The adsorption energy, an indication of how strongly an adsorbate interacts with the zeolite surface, arises from various interactions including the dispersion energy, the repulsion energy and the polarisation energy [26,27]. These are described in more detail in section 1.3.2.

## 1.3.2 Energetics of adsorption in zeolites

Adsorption, in our case physisorption, is a result of weak intermolecular forces including both van der Waals (dispersion-repulsion) and electrostatic interactions. The adsorption energy is equal to the total interaction energy $\varphi_{INT}$ at the equilibrium intermolecular distance. It can include some or all of the following terms:

$$\varphi_{INT} = \varphi_D + \varphi_R + \varphi_P + \varphi_\mu + \Phi_{FQ} + \varphi_{SP}$$

where $\varphi_D$ is the dispersion energy

$\varphi_R$ is the repulsive energy (due to close range repulsion)

$\varphi_P$ is the polarisation energy

$\varphi_\mu$ and $\varphi_{FQ}$ represent the field dipole and field gradient quadrupole interaction respectively

$\varphi_{SP}$ represents the interaction between sorbate molecules.

All these terms are attractive except $\varphi_R$, which works against adsorption at short distances. The dispersion and repulsion components of the interaction energy are always present between any two species. The repulsion part of the interaction energy arises from the interaction of the sorbate with the zeolite wall. Quantum mechanically the dispersive interaction is the hardest to model accurately. For zeolitic adsorption, polarisation energy has to be considered due to the existence of an electric field within the zeolite crystal. The magnitudes of $\varphi_P$ and $\varphi_D$ are proportional to the polarisability of the adsorbate and zeolite. This means that highly polar molecules are more likely to adsorb onto zeolite surfaces. Also the presence of large cations within the zeolite voids makes the zeolite a more potent adsorbent.

## 1.4 Zeolite Acidity and its role in Catalysis

By far the most profitable use of zeolites is in heterogeneous catalysis [25]. A catalyst can be defined as a compound that increases the rate of a chemical reaction, but which is not itself substantially consumed by the reaction. Most catalytic applications of zeolites are based on the introduction of active sites, either in the form of acid or basic sites into the zeolite lattice. Acid sites are far more predominant and are typically utilised in the destruction of chlorinated compounds. Such sites arise from the isomorphous substitution of Si with Al resulting in a net negative charge on the zeolite framework. Electroneutrality is preserved by loosely held cations within the zeolite cavities and/or protons. If the cation is $NH_4^+$, heating the material causes $NH_3$ to desorb, leaving a proton to compensate for the framework charge, forming a Brønsted acid site. The proton is attached to one of the oxygen atoms adjacent to the aluminium atom

therefore producing a bridging hydroxyl group. Alternatively a Brønsted acid site may be formed by calcination of an organic template.

The strength of a Brønsted acid site is dependent on structural factors, such as the flexibility of the lattice and the electrostatic potential created by the structure, and also chemical factors such as changes in the electronic distribution near the acid centre due to covalency of the lattice [28]. Other factors affecting acidity are the number of sites and their distribution. If acid sites are too close in proximity they can dehydrogenate to form Lewis acid sites. If the aluminium concentration is too high the framework may either become unstable and collapse or allow excessive reaction to occur. In the case of hydrocarbons this leads to coke formation, which can block the pores and result in an overall decrease in reactivity.

An isolated acid site is much stronger than several sites close together. Thus, increasing the Si/Al ratio, by treatment with $SiCl_4$ or steam for example, results in acid sites with increased strength [29]. Sites in small cavities tend to be stronger due to the presence of a higher electric field gradient. However, these sites may not always be accessible to the molecules being catalysed. A useful method to gauge the strength of an acid site is to probe it with small molecules such as ammonia or acetonitrile, which are likely to physisorb at an acid site [30]. The physisorption changes some characteristics of the probe molecule such as electron distribution and bond strengths, which can be monitored easily with IR or NMR spectroscopy. Another technique often used to characterise acidity is Temperature Programmed Desorption (TPD) of ammonia. The amount of ammonia desorbed indicates the concentration of acid sites whilst the temperature range at which desorption occurs indicates the strength of the acid site.

## 1.5 Zeolites and catalytic reactions

A catalytic reaction can be considered to be a cyclical process consisting of a number of steps. At the end of each cycle the reactive site is regenerated. Since zeolites are microporous materials the reaction at the active site is coupled with the diffusion of the reactants and products to and from the zeolite exterior. Reactions within the zeolite cavities follow three main steps illustrated in figure 1.2 [31]. These are (i) diffusion of

the reactants from the zeolite exterior to the active site (ii) adsorption at the active site, (iii) the reaction itself and (iv) the desorption of products and diffusion out of the zeolite.
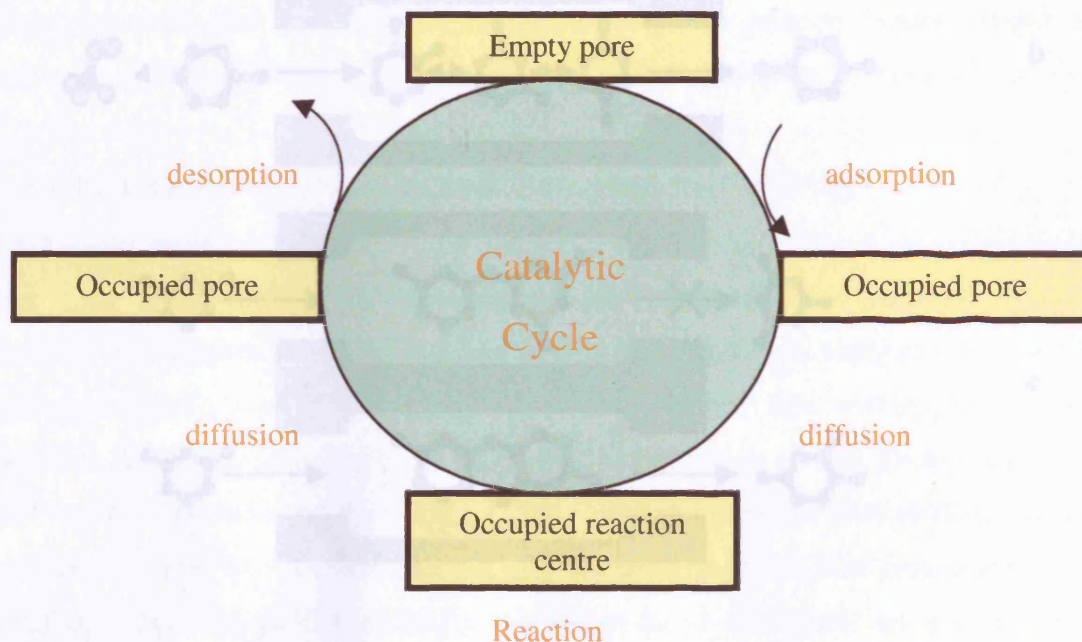


**Figure 1.2:** The catalytic cycle of zeolite catalysis.

As previously described, the pores of a zeolite will only allow reactants/sorbates with a size up to the diameter of the pore. Thus, molecules can be excluded from a pore, and therefore the active site, on the basis of size, resulting in zeolites being classed as a type of molecular sieve. This size selectivity can effectively be used to tailor a reaction to yield selected products (figure 1.3a). In a similar way, a reaction can be forced to yield certain products depending on the size and shape of the pore (figure 1.3b). Once a catalytic reaction has taken place within a zeolite certain products are prevented from leaving the pores as they are too large. The pore volume within the zeolite also plays an important role in the product distribution. The volume available around an active site within the pore may dictate which transition state may be formed, which in turn will determine the products that are formed (figure 1.3c). Product distribution may also be varied on the basis of diffusion. Those that are able to leave the zeolite pores quickly are favoured whilst the slower ones may be interconverted to other compounds. Thus, the highly acidic sites coupled with the shape selective properties of zeolites make this class of materials a powerful industrial catalyst.
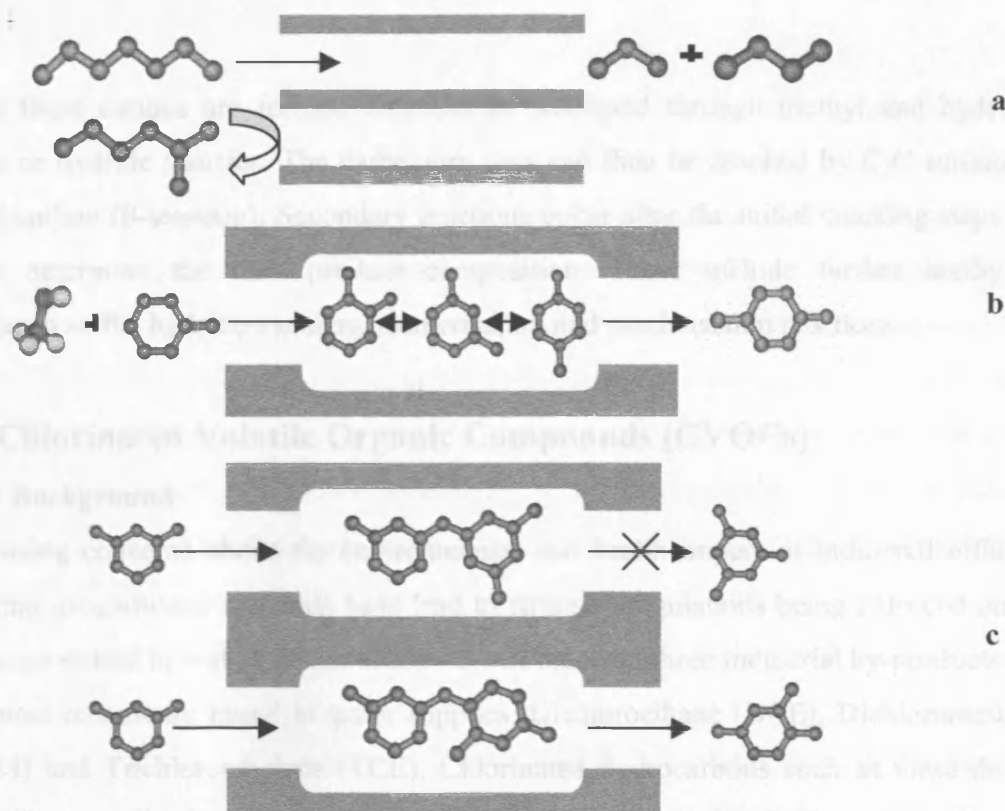
**Figure 1.3:** a) Reactant Selectivity b) Product Selectivity c) Transition-State Selectivity.

Catalytic breakdown of organic compounds is generally accepted to involve the formation of carbocations [32,33]. However, the nature of these cations, whether they occur as a reaction intermediate or transition states, is currently a matter of debate in the literature. The cations formed can be separated into two groups; alkyl carbenium ions and alkyl carbonium ions. Alkyl carbenium cations have a tri-coordinated C atom and are a result of proton transfer from the zeolite to alkenes whilst alkyl carbonium cations result from proton transfer to alkanes and contain a penta-coordinated C atom.
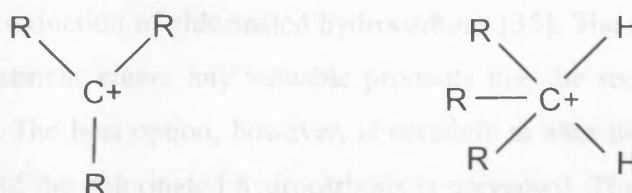


**Figure 1.4:** Alkyl carbenium cation (left) and Alkyl carbonium cation (right)

22

Once these cations are formed they can be stabilised through methyl and hydrogen shifts or hydride transfer. The carbenium ions can then be cracked by C-C scission at the $\beta$ carbon ($\beta$-scission). Secondary reactions occur after the initial cracking steps and these determine the final product composition. These include further methyl or hydrogen shifts, hydride transfers, isomerisation and condensation reactions.

## 1.6 Chlorinated Volatile Organic Compounds (CVOCs)

### 1.6.1 Background

Increasing concerns about the environmental and health impact of industrial effluents entering groundwater and soils have lead to stringent regulations being enforced on the levels permitted in water. In this study we will focus on three industrial by-products that are most commonly found in water supplies: Dichloroethane (DCE), Dichloromethane (DCM) and Trichloroethylene (TCE). Chlorinated hydrocarbons such as these do not naturally occur in the environment; yet they are often found in both groundwater and drinking water supplies. Chlorinated solvents have found widespread use in a variety of industries including the manufacture of plastics, dry cleaning garments and solvent degreasing in the electronic industries and the many by-products include those being studied in this thesis [34]. Further, chlorination of water is a common method of disinfecting water, which can lead to the formation of chlorinated by-products. The presence of these compounds in water is causing concern due to the dangers they may pose to human health as they are suspected carcinogens. Additionally these compounds may be involved in the destruction of the ozone layer in the stratosphere. As such the maximum permitted levels of these compounds in drinking water are 5ppb [35]. In light of this regulation, methods are currently being sought to remove these compounds from drinking water. This can be achieved by either dealing with the polluted water, or by preventing the production of chlorinated hydrocarbons [35]. The first option, thus, is an end of pipe treatment where any valuable products may be recovered and reused in other processes. The best option, however, is certainly to alter the chemical process so that production of the chlorinated hydrocarbons is prevented. This study focuses on the first of these methods and describes the role of zeolites in treating polluted water.

The most widely used method is removal by adsorption on activated carbons [36,37]. These materials are particularly suited to the role as they have a large adsorption capacity and the process is economical. However, the regeneration of the adsorbent can pose a problem due to the flammability of the activated carbon. This problem can be overcome by using inorganic adsorbents such as zeolites, which are stable at high temperatures and thus can be regenerated by heating without affecting the zeolite structure. Zeolites also have a possible advantage over other catalysts in that they may be used to separate a mixture of halocarbons by utilising polarity differences between them [38,39]. Other studies have looked at mesoporous materials as possible adsorbents. Lee et al.. [37] found that MCM-48 was a candidate for CVOC adsorption due to its large internal surface area, uniformity of pore size and high thermal stability.

In this study we will focus on three zeolite framework structures, FAU, MOR and MFI that can be used as possible adsorbents for the removal of CVOCs from water. The fact that zeolite structures readily adsorb water may pose a problem due to competition between CVOCs and water for adsorption sites. The extent to which a zeolite adsorbs water is dependent on the amount of aluminium in the framework, with low Si/Al structures adsorbing more water. It is possible to generate hydrophobic zeolites by modifying the framework using a dealumination process and an example is mentioned on page 20. [40]. The use of hydrophobic zeolites as an adsorbent for the removal of CVOCs was first proposed by Blocki [41]. The all-silica form of the ZSM5 structure, silicalite, was one of the first high-silica zeolites to be synthesised [12].

Chlorinated hydrocarbons interact with the zeolite framework through a van der Waals type attraction between the chlorine and/or hydrogen atoms with the oxygen atoms of the framework. The magnitude of van der Waals interactions is related to the polarisability of the sorbate. Therefore chlorinated hydrocarbons would be expected to have stronger van der Waals interactions than their non-chlorinated analogues and therefore a higher heat of adsorption. Knowledge of the location of adsorption sites and how they are approached by the sorbates is crucial to understand how catalysis proceeds. To this end there have been numerous studies, both experimental and

theoretical, to ascertain the nature of the adsorbed chlorinated species in various frameworks.

### 1.6.2 Adsorption Studies

Gas Chromatography measurements of Anderson [42] show that mordenite (Si/Al=200) and silicalite (Si/Al=1000) display superior adsorption of TCE from water when compared to zeolite Y (Si/Al=75) and activated carbon. The silicalite framework was found to be the most efficient at removing TCE from solution. This was attributed to the fact that TCE fits neatly into the 10-ring pore and can therefore have optimal van der Waals interactions with the framework oxygen atoms. The FAU structure was found to have a low affinity for TCE due to its large pore size relative to the other zeolite frameworks. This result was also observed by Giaya et al.. [36] and Luo et al. [43]. Both FAU and silicalite showed similar adsorption capacities for pure gas phase adsorption of TCE. The low affinity in the presence of water was attributed to the FAU structure adsorbing more water than silicalite and therefore less of the CVOC. It was also found that silicalite adsorbed more TCE than FAU due to the smaller pore diameter of the silicalite structure which optimises sorbate-host interactions [44]. For silicalite the isosteric heat of adsorption was found to increase with loading due to adsorbate-adsorbate interactions. For FAU however the isosteric heat remained more or less constant except at loadings close to the adsorption capacity. This was attributed to the larger pore diameter of the zeolite structure, which resulted in less crowding of the TCE molecules and hence lower adsorbate-adsorbate interactions. Farrell et al. also investigated the competitive adsorption between water and TCE in hydrophobic Y zeolite gravimetrically [45]. They found that for low TCE loadings the presence of water increased TCE adsorption, which was attributed to attractions between TCE and water molecules. However, at higher TCE concentrations water played a negative role and decreased adsorption of the molecule.

Calorimetric measurements and computational Monte Carlo simulations of adsorption of various halogenated hydrocarbons including DCE and TCE in cationic zeolites NaX (Si/Al=1.2), NaY (Si/Al=3.0) and siliceous FAU (Si/Al= $\infty$) were conducted by Mellot et al. [46]. These structures are topologically identical but differ in their Si/Al ratios and

therefore cation content. Mellot and co-workers developed optimal forcefield parameters and they aimed to identify the driving forces of halocarbon adsorption and the influence of various parameters such as Si/Al ratio, cation content and sorbate loading. At low sorbate loadings the heats of adsorption increased with increasing polarity of the zeolite host (i.e. siliceous FAU< NaY < NaX). They found that the polar, cationic zeolites had the highest affinity for chloroform, which was attributed to the stronger electrostatic interactions present. The cation in NaX was found to control the orientation of the molecule in the 12-ring window. At higher loadings the total energy of the system was found to increase due to the dispersive interactions between chloroform molecules, and the molecules were found to distribute in a disordered way over the micropores. A different study by this group [47] found that the chloroform molecules in NaY physically adsorb onto the zeolite walls with their hydrogen atoms pointing into the centre of the supercage. The most favourable binding site was found to be in the 12-ring windows with each chlorine atom interacting with at least two framework oxygen atoms at a distance of between 3.5Å and 3.8Å and the hydrogen atom at 2.75Å from a framework oxygen atom. The Monte Carlo simulations showed that two-thirds of the binding energy arises from the short-range interactions between the sorbate and the zeolite. For TCE in siliceous Y, 90% of the adsorption energy was attributed to short-range interactions at low loadings [48]. As loading is increased, additional interactions between TCE molecules (Cl-Cl and H-Cl) are observed which result in an increase in the heats of adsorption. The Cl-Cl interaction showed a typical distance of 3.6Å whilst the H-Cl interaction was around 2.9Å. Again the intermolecular interactions, which arise due to the polarisability of the chlorine atoms, are of a dispersive nature. Host–guest (O-Cl) interactions were found to be $\approx$ 2.6 Å. In NaX and NaY stronger adsorption is observed due to enhanced electrostatic interactions between the sorbate and the cation in the zeolite pores [48,49].

Chihara *et al.* [50,51] used gravimetric analysis, fixed-bed adsorption experiments and chromatography to obtain isotherms for chloroform and TCE adsorption on USY (Si/Al=6.18) and PQ-USY (Si/Al=70) type zeolites. Their results were in good agreement with Monte Carlo simulations. They also investigated the diffusion of DCM and TCE in the USY type zeolites and NaY (Si/Al=5.6) using gas chromatography [52]

and found that the activated energies of diffusion in the micropores of the zeolites were 40% of the isoteric heats of adsorption. The heat of adsorption on the high-silica USY zeolite was lower than in NaY for both sorbate molecules.

X-ray diffraction studies of the adsorption of DCE in silicalite at 298K [53] found that initially the molecules were located inside the intersections. As loading increased the sinusoidal channels were occupied followed by the straight channels as well. It was observed that there were no molecular clusters formed at higher loadings and that there was no structural change of the zeolite structure upon adsorption. TCE adsorption in silicalite was also investigated using a combination of x-ray diffraction, microcalorimetry and thermogravity by Bouvier *et al.* [54]. They found that the framework structure underwent a monoclinic to orthorhombic structural change upon adsorption of the first few TCE molecules. Upon higher loadings the accommodation of molecules into the zeolite is dependent on the strength of host-guest and guest-guest interactions. The molecules are observed to assemble end to end to form dipole chains in the straight and sinusoidal channels of the zeolite structure. The total length of the chain was found to be 10 molecules, which corresponds to the total length of the channels of one unit cell.

Alvarez-Cohen *et al.* took a slightly different approach and investigated the adsorption of TCE in Silicalite followed by biotransformation of the TCE molecule by methanotrophic bacteria rather than catalytic destruction [55]. The advantage of this kind of system is that the bacteria are likely to be present in the water alongside the CVOC that is to be removed.

Measurements of the heat of adsorptions in dealuminated Y by Clausse *et al.* [56] show that the adsorption energies follow the trend: DCE > TCE > DCM, that is the larger CVOCs adsorb more strongly as they have more favourable interactions with the zeolite framework than the smaller DCM molecule.

## 1.6.3 Catalytic Studies

Traditional methods of destroying halogenated hydrocarbons involved thermal incineration. This method involves heating low concentrations of the CVOC to very high temperatures. However the process offers little control and can lead to the formation of by-products that are more harmful than the starting material [57]. A wide variety of catalysts have been investigated as alternatives to thermal incineration as they offer a greater degree of control. These include perovskites [58], clays, molten salt-based systems, zeolites, alumina [59] and mesoporous materials [37]. Catalytic oxidation using a noble metal based catalyst [60-62] is another popular method for the removal and destruction of chlorinated hydrocarbons. However, a major setback with these types of catalysts is that they are deactivated by halide poisoning and are also susceptible to forming undesirable compounds such as the volatile metal oxychlorides [63]. Much research has been carried out on transition metal based catalysts for the purpose of destroying this class of compounds. These are resistant to halide poisoning, but they have the disadvantage that their destruction activity is significantly lower [64]. In addition they tend to form $Cl_2$ as a product via the Deacon reaction [61].

$$2HCl + \frac{1}{2}O_2 \rightarrow H_2O + Cl_2 \qquad (1.1)$$

Attention is now turning to acid zeolites such as H-Y, H-MFI and H-MOR, which are investigated as potential alternatives to current day catalysts. A particular feature of acid zeolites is their dual functionality whereby they are able to adsorb large amounts of CVOCs and subsequently break these down on their active sites. This coupled with their selective nature, lower temperature of operation and stability during catalytic destruction of CVOCs makes zeolites suited to CVOC abatement [65]. The ideal zeolite catalyst should also display high catalytic activity for oxidative destruction of CVOCs and high selectivity towards the desired deep oxidation products, $H_2O$, $CO_2$ and HCl. $Cl_2$ is a particularly undesirable product and ways of altering product distributions, so that those favoured are produced, have been investigated. Since these CVOCs are found in water the effect of water addition to the solvent mixture has also been probed. The total acidity of the zeolite structure is another important factor to consider as it represents the number of acid sites that are available for CVOC oxidation. However it is found that at ambient temperatures the acid sites also facilitate the adsorption of water

[66]. Thus the best zeolite structure for sorption and catalytic purposes is one that has a modest concentration of high strength acid sites [66,67].

Lopez-Fonseca *et al.* investigated the catalytic oxidation of DCE over H-Y (Si/Al=2.4), H-ZSM-5 (Si/Al=27.5) and H-MOR (Si/Al=5.2) [68]. They found that of these three structures, ZSM-5 was the most effective catalyst for DCE destruction owing to its high density of Brønsted acid sites, which were characterised using TPD, and its hydrophobic nature. H-MOR was also found to have a high density of acid sites but many of these are inaccessible to the DCE molecule. Using a zeolite catalyst was found to lower the oxidation temperature by 200°C compared to thermal incineration. Vinyl chloride was identified as an intermediate by IR spectroscopy, which was subsequently oxidised to CO, $CO_2$ and HCl. This suggests that the removal of HCl (dehydrochlorination) is the first step in the reaction. Acid zeolites have no sites for oxygen adsorption and thus the vinyl chloride is thought to interact with gas-phase oxygen. Other products of partial oxidation were also detected, such as chloroform and TCE but these were decomposed at higher temperatures. Trace amounts of chlorine were also produced via the Deacon reaction (equation 1.1). Addition of water was found to reduce the activity of the zeolites, probably due to competition between the DCE and water molecules for adsorption on the active sites. The aluminium rich zeolite H-Y was found to exhibit the greatest drop in activity in the presence of water. Water addition was also found to inhibit the formation of vinyl chloride and the other partial-oxidation products. Furthermore, the presence of water improved the selectivity to the desired deep oxidation products $CO_2$ and HCl. However the Al-O bond in acidic zeolites can easily be attacked by the HCl formed. This leads to the formation of the volatile $AlCl_3$ which can cause the partial collapse of the framework structure. This process is enhanced in the presence of water. The zeolite catalyst can also be deactivated by coke formation, which blocks access to active sites in the zeolite pores. The amount of coke formed is dependent on the number of carbon and hydrogen atoms in the sorbate molecule. The interconnected channel system of ZSM5 means that there is more than one path to the active site and so coke formation does not deactivate the zeolite as much as it does in MOR, for example, which has unidirectional channels.

A further study by this group compared the use of acidic zeolites for the catalytic oxidation of DCE and TCE [67,69,70]. Once again H-ZSM5 and HY were found to be the most active zeolites for both molecules. The Brønsted acid sites in these structures acted as chemisorption sites and proton transfer initiated breakdown of the adsorbed molecule. TCE was oxidised at higher temperatures than DCE. This was attributed to the presence of the additional chlorine atom in TCE, which causes a redistribution of the electronic charge in the adsorbed molecule. This leads to a change in the orientation relative to the catalyst surface. Further, the large size of the TCE molecule can sterically hinder the adsorption of the molecule. The H-ZSM-5 structure was found to exhibit a higher adsorption capacity than H-Y. When TCE was oxidised, trace amounts of tetrachloroethene were detected in addition to CO, $CO_2$ and HCl. This was also observed by Finocchio $et$ $al.$ [71]. When compared to DCE, higher levels of $Cl_2$ are also formed due to the lack of hydrogen in the TCE molecule. The formation of HCl was promoted by $H^+$ ions present in the zeolite structure. The presence of water was found to enhance catalytic activity at low temperatures and improves selectivity to HCl and $CO_2$ in the case of TCE oxidation. At higher temperatures activity was diminished in the presence of water.

Catalytic oxidation of DCM, DCE and TCE in dealuminated Y zeolites was also investigated under dry and humid conditions to ascertain the effect of dealumination and the presence of water [72,73]. It was found that dealumination increased catalytic activity due to the formation of strong Brønsted acid sites. The DCE molecule was most easily destroyed, followed by DCM and TCE. The main oxidation products were $CO_2$, CO, HCl and $Cl_2$. Water was found to diminish the zeolite activity but changed the product distribution, reducing the formation of by-products and improving the selectivity towards HCl and $CO_2$. A methyl chloride intermediate was detected during the catalytic oxidation of DCM. This intermediate was also observed in another study [74]. Catalysis is believed to proceed via a carbonium ion. $Cl_2$ was formed via the Deacon reaction (equation 1.1).

An investigation of the catalytic oxidation of chlorinated binary mixtures found that the presence of another chlorinated hydrocarbon inhibited destruction of each hydrocarbon

[75]. DCE exhibited the strongest inhibition effect compared to DCM and TCE, possibly because it occupies more of the adsorption sites thereby leaving fewer sites for adsorption and decomposition of other hydrocarbons. TCE on the other hand had the smallest inhibiting effect. H-MOR displayed the highest catalytic activity for a mixture of DCM/TCE. DAY exhibited a better activity for mixtures containing DCE. The product distribution for mixtures also differed from those of single molecule feeds with fewer by-products generated. There was also a notable improvement in HCl selectivity and a reduction in the formation of $Cl_2$, possibly due to an increase in the amount of hydrogen in the mixture.

### 1.6.4 Metal Substituted Zeolites

Several groups have investigated metal substituted zeolites as possible alternatives to acidic zeolites. In this case, a silicon atom is replaced with a metal atom such as chromium      [66, 76-79] or silver [29]. Prakash *et al.* investigated the adsorption of various CVOCs, including TCE on Cr-ZSM5 (Si/Al=16) and CrY (Si/Al=2.8) [77,78]. Chromium was chosen because it has the ability to destroy all unsaturated CVOCs. They found that TCE was adsorbed preferentially in the channels and intersections and that the presence of water lowered the amount of TCE adsorbed. The products of catalytic oxidation were HCl and $CO_2$. Partial dealumination resulted in a lower cation content which resulted in an increase in the amount of CVOC adsorbed due to the increased hydrophobicity of the zeolite but decreased the catalytic activity of the zeolite [79]. Compared to acidic zeolites, chromium exchange of HY increases TCE sorption by 15% whilst on ZSM-5 a drop of 17% is noted [66]. The presence of Cr facilitates the complete oxidation of CO to $CO_2$. However, the use of acidic zeolites has a possible advantage over Cr zeolites since it avoids the incorporation of hazardous transition metal cations such as Cr. Additionally zeolite-supported manganese oxide catalysts were found to be active for CVOC destruction [80]. It was noted that the manganese improved the selectivity of $CO_2$ and reduced CO formation.

## 1.7 The zeolites being modelled

In this study three zeolite frameworks, faujasite (FAU), mordenite (MOR) and ZSM-5 (MFI) will be investigated as possible adsorbents/catalysts for DCM, DCE and TCE. All three framework structures can be made to have a high-silica content and are thus suited to adsorption and catalytic removal of chlorinated organics from waste streams, as they will adsorb the organics in preference to water. The features of each structure will now be described in turn and a pictorial representation is given in figure 1.5.

### 1.7.1 Faujasite

Faujasite has a cubic unit cell comprising 576 atoms [81] . The structure is composed of sodalite cages joined via double 6 rings. These assemble to form a supercage with a 12 ring opening which has a free diameter of 7.4Å [82]. There are 4 such supercages in a unit cell and thus a 3 dimensional channel system is formed. The faujasite structure has 1 crystallographically distinct T site and 4 oxygen sites that may be protonated. The combination of spacious voids, 12-ring pore openings and 3-dimensional channel system makes the zeolite an ideal candidate for both adsorption and catalytic applications.

### 1.7.2 Mordenite

Mordenite has an orthorhombic unit cell with 144 atoms [83]. The structure comprises of units of four 5-rings joined to each other via common edges to form a series of chains. These chains link to form a 12 and 8 ring channel structure. The diameter of the 12 ring is 6.5 x 7.0Å whilst the 8 ring is 5.7 x 2.6Å [82]. The 8 ring and 12 ring channels are connected via 'side-pockets'. However, the chains are displaced with respect to one another and thus there is limited access from one channel to another. Hence, the channel system can be considered effectively one –dimensional. The resulting structure contains 4 T sites in an asymmetric unit.

### 1.7.3 ZSM-5

The ZSM-5 structure consists of pentasil units that are linked to form a series of chains [84]. Mirror images of these chains are connected to form a 3 dimensional channel structure composed of 10- ring straight channels that are intersected by a set of

sinusoidal channels. The sinusoidal channels are nearly circular whilst the straight channels have an elliptical cross-section. The diameter of these 10-rings ranges between 5.1 and 5.5Å [82]. The MFI unit cell adopts an orthorhombic structure comprising 288 atoms. The result is a complex structure containing 12T sites in an asymmetric unit.
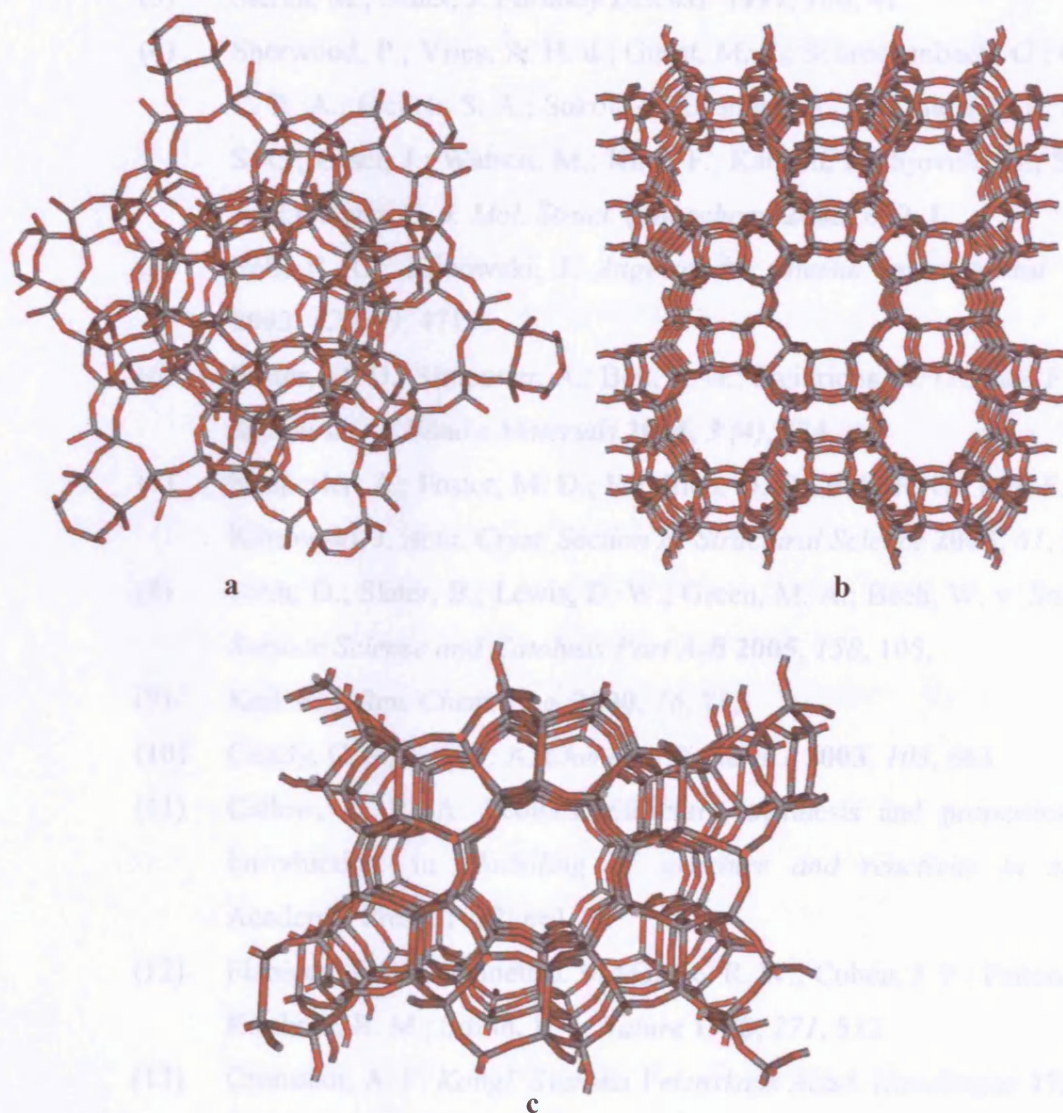


**Figure 1.5:** The zeolite structures being studied a) Faujasite b) Mordenite and c) ZSM-5.

# References

(1)     Sauer, J. Zeolites: Applications of Computational Methods. In *Encyclopedia of Computational Chemistry*.

(2)     Car, R. *Quant. Struct. Acta. Relat.* **2002**, *21*, 97.

(3)     Sierka, M.; Sauer, J. *Faraday Discuss.* **1997**, *106*, 41.

(4)     Sherwood, P.; Vries, A. H. d.; Guest, M. F.; Schreckenbach, G.; Catlow, C. R. A.; French, S. A.; Sokol, A.; Bromley, S. T.; Kendrick, J.; Rogers, S. C.; Casci, J.; Watson, M.; King, F.; Karlsen, E.; Sjovoll, M.; Schafer, A.; Lennartz, C. *J. Mol. Struct. (Theochem)* **2003**, *632*, 1.

(5)     Bell, R. G.; Klinowski, J. *Angewandte Chemie International Edition* **2003**, *42 (39)*, 4719.

(6)     Foster, M. D.; Simperler, A.; Bell, R. G.; Freidrichs, O. D.; Paz, F. A. A.; Klinowski, J. *Nature Materials* **2004**, *3 (4)*, 234.

(7)     Simperler, A.; Foster, M. D.; Freidrich, O. D.; Bell, R. G.; Paz, F. A. A.; Klinowski, J. *Acta. Cryst. Section B: Structural Science* **2005**, *61*, 263.

(8)     Salih, D.; Slater, B.; Lewis, D. W.; Green, M. A.; Beeh, W. v. *Studies in Surface Science and Catalysis Part A-B* **2005**, *158*, 105.

(9)     Keil, F. J. *Rev. Chem. Eng.* **2000**, *16*, 71.

(10)    Cundy, C. S.; Cox, P. A. *Chemical Reviews 1* **2003**, *103*, 663

(11)    Catlow, C. R. A. Zeolites: Structure, synthesis and properties - An introduction. In *Modelling of structure and reactivity in zeolites*; Academic Press, 1992; pp1.

(12)    Flanigen, E. M.; Bennett, J. M.; Grose, R. W.; Cohen, J. P.; Patton, R. L.; Kirchner, R. M.; Smith, J. V. *Nature* **1978**, *271*, 512

(13)    Cronstedt, A. F. *Kongl. Svenska Vetenskaps Acad. Handlingar* **1756**, *17*, 120.

(14)    Barrer, R. M. *J. Am. Chem. Soc* **1948**, *127*.

(15)    Barrer, R. M.; Hinds, L.; White, E. P. *J. Chem. Soc.* **1953**, 1466.

(16)    Wilson, S. T.; Lok, B. M.; Messinan, C. A.; Cannon, T. R.; Flanigen, E. M. *J. Am. Chem. Soc* **1982**, *104*, 1146.

(17)    Flanigen, E. M.; Patton, R. L.; Wilson, S. T. *Studies in Surface Science and Catalysis* **1988**, *37*, 13.

(18)   Perego, G.; Bellusi, G.; Corno, C.; Taramasso, M.; Buonomo, F.; Esposito, A. New developments in zeolite science and technology (Proc. 7th Internat. Zeolite Conf.); Murakami, Y., Iijima, A., Ward, J. W., Eds., 1986.

(19)   Kong, L. Y.; Li, G.; Wang, X. S. *Catal. Today* **2004**, *93-5*, 341.

(20)   Rodriguez-Santiago, L.; Sierka, M.; Branchadell, V.; Sodupe, M.; Sauer, J. *J. Am. Chem. Soc* **1998**, *120*, 1545.

(21)   Pereira, M. S.; Nascimento, M. A. C. *Theoretical Chemistry Accounts* **2003**, *110*, 441

(22)   French, S. A.; Sokol, A. A.; To, J.; Catlow, C. R. A.; Phala, N. S.; Klaff, G.; Steen, E. v. *Catal. Today* **2004**, *93-5*, 535.

(23)   Schuth, F.; Schmidt, W. *Advanced Engineering Materials* **2002**, *4*, 269

(24)   IZC. Database of zeolite structures: http://www.iza-structure.org/**databases/**, 2006.

(25)   Maesen, T.; Marcus, B. The zeolite scene - an overview. In *Introduction to zeolite science and practice*; Bekkum, H. v., Flanigen, E. M., Jacobs, P. A., Jansen, J. C., Eds.; Elsevier, 2001; Vol. 137.

(26)   Thomas, J. M.; Thomas, W. J. *Principles and practice of heterogeneous catalysis*; VCH: New York, 1997.

(27)   Rees, L. V. C.; Shen, D. Adsorption of gases in zeolite molecular sieves. In *Studies in Surface Science and Catalysis*; Bekkum, H. v., Flanigen, E. M., Jacobs, P. A., Jansen, J. C., Eds., 2001; Vol. 137.

(28)   Sastre, G.; Lewis, D. W. *J. Chem. Soc - Faraday Transactions* **1998**, *94*, 3049.

(29)   Swanson, M. E.; Greene, H. L.; Qutubuddin, S. *Appl. Catal. B-Environmental* **2004**, *52*, 91.

(30)   Khaliullin, R. Z.; Bell, A. T.; Kazansky, V. B. *J. Phys. Chem. A* **2001**, *105*, 10454.

(31)   van Santen, R. A.; Rozanska, X. Theory of zeolite catalysis. In *Molecular Modelling and Theory in Chemical Engineering*; Chakraborty, A., Ed.; Academic Press, 2001; pp 399.

(32)     van Santen, R. A.; van der Graaf, B.; Smit, B. *Studies in Surface Science and Catalysis* **2001**, *137*, 419.

(33)     Lercher, J. A.; van Santen, R. A.; Vinek, H. *Catalysis Letters* **1994**, *27*, 91.

(34)     Sidebottom, H.; Franklin, J. *Pure. Appl. Chem* **1996**, *68*, 1757.

(35)     Keller, R. A.; Dyer, J. A. *Chemical Engineering* **1998**, 100.

(36)     Giaya, A.; Thompson, R. W.; Denkewicz, R. *Micropor. Mesopor. Mater* **2000**, *40*, 205.

(37)     Lee, J. W.; Lee, J. W.; Shim, W. G.; Suh, S. H.; Moon, H. *J. Chem. Eng. Data* **2003**, *48*, 381.

(38)     Eckert, J.; Draznieks, C. F. M.; Cheetham, A. K. *J. Am. Chem. Soc* **2002**, *124*, 170.

(39)     Chatterjee, A. *J. Mol. Struct. (Theochem)* **2003**, *630*, 233.

(40)     Pires, J.; Carvalho, A.; Veloso, P.; Varvalho, M. B. d. *J. Mater. Chem.* **2002**, *12*, 3100.

(41)     Blocki, S. W. *Environmental Progress* **1993**, *12*, 226.

(42)     Anderson, M. A. *Environ. Sci. Technol.* **2000**, *34*, 725.

(43)     Luo, J.; Farrell, J. *Environ. Sci. Technol.* **2003**, *37*, 1775

(44)     Giaya, A.; Thompson, R. W. *Micropor. Mesopor. Mater* **2002**, *55*, 265.

(45)     Farrell, J. *Micropor. Mesopor. Mater* **2003**, *59*, 205.

(46)     Mellot, C. F.; Cheetham, A. K.; Harms, S.; Savitz, S.; Gorte, R. J.; Myers, A. L. *J. Am. Chem. Soc* **1998**, *120*, 5788

(47)     Mellot, C. F.; Davidson, A. M.; Eckert, J.; Cheetham, A. K. *J. Phys. Chem B* **1998**, *102*, 2530

(48)     Mellot, C. F.; Cheetham, A. K.; S.Harms; S.Savitz; R.J.Gorte; A.L.Myers. *Langmuir* **1998**, *14*, 6728.

(49)     Mellot, C. F.; Cheetham, A. K. *J. Phys. Chem B* **1999**, *103*, 3864

(50)     Chihara, K.; Hijikata, K.; Yamaguchi, H.; Suzuki, H.; Saito, T.; Takeuchi, Y. "Adsorption removal of the mixed organic solvent stream by high silica zeolite"; 14th International Zeolite Conference, 2004, Cape Town, South Africa.

(51)     Chihara, K.; Mellot, C. F.; Cheetham, A. K.; Harms, S.; Mangyo, H.; Omote, M.; Kamiyama, R. *Korean J. Chem. Eng.* **2000**, *17*, 649.

(52)     Chihara, K.; Terakado, T.; Ninomiya, T.; Mizuochi, H. "Chromatographic adsorption measurement of chlorinated organics on high silica zeolite"; 14th International Zeolite Conference, 2004, Cape Town, South Africa.

(53)     Helene, M.; Grange, S.; Garrot, B. *Langmuir* **2001**, *17*, 8188.

(54)     Bouvier, F.; Weber, G. *J. Thermal Anal* **1998**, *54*, 881.

(55)     Alvarez-Cohen, L.; McCarty, P. L.; Roberts, P. V. *Environ. Sci. Technol.* **1993**, *27*, 2141

(56)     Clausse, B.; Garrot, B.; Cornier, C.; Paulin, C.; Simonot-Grange, M. H.; Boutros, F. *Micropor. Mesopor. Mater.* **1998**, *25*, 169.

(57)     Yashura, A.; Morita, M. *Chemosphere* **1990**, *21*, 479.

(58)     Sinquin, G.; Petit, C.; Libs, S.; Hindermann, J. P.; Kiennemann, A. *Appl. Catal. B: Environmental* **2000**, *27*, 105

(59)     Finocchio, E.; Sapienza, G.; Baldi, M.; Busca, G. *Appl. Catal. B-Environmental* **2004**, *51*, 143.

(60)     Feijen-Jeurissen, M. M. R.; Jorna, J. J.; Nieuwenhuys, B. E.; Sinquin, G.; Petit, C.; Hindermann, J. P. *Catal. Today* **1999**, *54*, 65.

(61)     González-Velasco, J. R.; Aranzabal, A.; Gutiérrez-Ortiz, J. I.; López-Fonseca, R.; Gutiérrez-Ortiz, M. A. *Appl. Catal. B: Environmental* **1998**, *19*, 189

(62)     González-Velasco, J. R.; Aranzabal, A.; López-Fonseca, R.; Ferret, R.; González-Marcos, J. A. *Appl. Catal. B: Environmental* **2000**, *24*, 33

(63)     Mendyka, B.; Musialik-Piotrowska, A.; Syczewska, K. *Catal. Today* **1992**, *11*, 136.

(64)     Spivey, J. J.; Butt, J. B. *Catal. Today* **1992**, *11*, 465.

(65)     Freidel, I. M.; Frost, A. C.; Herbert, K. J.; Meyer, F. J.; Summers, J. C. *Catal. Today* **1993**, *17*, 367.

(66)     Greene, H. L.; Prakash, D. S.; Athota, K. V. *Applied Catalysis B-Environmental* **1996**, *7*, 213.

(67)     González-Velasco, J. R.; López-Fonseca, R.; Aranzabal, A.; Gutiérrez-Ortiz, J. I.; Steltenpohl, P. *Appl. Catal. B-Environmental* **2000**, *24*, 233.

(68)     López-Fonseca, R.; Aranzabal, A.; Stelenpohl, P.; Gutiérrez-Ortiz, J. I.; González-Velasco, J. R. *Catal. Today* **2000**, *62*, 367

(69)     López-Fonseca, R.; Aranzabal, A.; Gutiérrez-Ortiz, J. I.; Álvarez-Uriarte, J. I.; González-Velasco, J. R. *Appl. Catal. B: Environmental* **2001**, *30*, 303

(70)     López-Fonseca, R.; Gutiérrez-Ortiz, J. I.; Gutiérrez-Ortiz, M. A.; González-Velasco, J. R. *Journal of Chemical Technology and Biotechnology* **2003**, *78*, 15

(71)     Finocchio, E.; Pistarino, C.; Dellepiane, S.; Serra, B.; Braggio, S.; Baldi, M.; Busca, G. *Catal. Today* **2002**, *75*, 263.

(72)     López-Fonseca, R.; Gutiérrez-Ortiz, J. I.; Gutiérrez-Ortiz, M. A.; González-Velasco, J. R. *J. Catal* **2002**, *209*, 145

(73)     López-Fonseca, R.; Rivas, B. d.; Gutiérrez-Ortiz, J. I.; Aranzabal, A.; González-Velasco, J. R. *Appl. Catal. B: Environmental* **2003**, *41*, 31

(74)     López-Fonseca, R.; Cibrián, S.; Gutiérrez-Ortiz, J. I.; Gutiérrez-Ortiz, M. A.; González-Velasco, J. R. *AIChE Journal* **2003**, *49*, 496

(75)     López-Fonseca, R.; Gutiérrez-Ortiz, J. I.; Ayastui, J. L.; Gutiérrez-Ortiz, M. A.; González-Velasco, J. R. *Appl. Catal. B: Environmental* **2003**, *45*, 13

(76)     Lester, G. R. *Catal. Today* **1999**, *53*, 407

(77)     Prakash, D. S.; Athota, K. V.; Greene H.L. ;.Vogel. C.A *AIChE* **1995**, *91*, 1.

(78)     Greene, H. L.; Prakash, D.; Athota, K.; Atwood, G.; Vogel, C. *Catal. Today* **1996**, *27*, 289.

(79)     Chintawar, P. S.; Greene, H. L. *Applied Catalysis B-Environmental* **1997**, *14*, 37.

(80)     Gutiérrez-Ortiz, J. I.; López-Fonseca, R.; Aurrekoetxea, U.; González-Velasco, J. R. *J. Catal* **2003**, *218*, 148

(81)     McCusker, L.; Baerlocher, C. Zeolite Structures. In *Introduction to zeolite science and practice*; Bekkum, H. v., Flanigen, E. M., Jacobs, P. A., Jansen, J. C., Eds.; Elsevier, 2001.

(82)     Baerlocher, C.; Meier, W. M.; Olson, D. H. *Atlas of Zeolite Framework Types*; Elsevier: Amsterdam, 2001.

(83)     Martucci, A.; Cruciani, G.; Alberti, A.; Ritter, C.; P.Ciambelli; Rapacciuolo, M. *Micropor. Mesopor. Mater* **2000**, *35-36*, 405.

(84)     Olson, D. H.; Kokotallo, G. T.; Lawton, S. L.; Meier, W. M. *J. Phys. Chem* **1981**, *85*, 2238.

# Chapter Two: Theory and Simulation Methods

Computer simulation methods are often employed to solve chemically related problems using mathematical methods and the laws of Physics. Computer modelling has been fundamental in understanding catalysis at the molecular level and is often used to complement experimental data. Indeed the synergy between theory and experiment has enhanced knowledge of the catalytic process in a number of systems [1,2].

Computer simulations can also be used as a screening process to ascertain whether an experiment is viable, thus avoiding costly experiments. Increasingly computer simulations are being used to predict the likely behaviour of a chemical system. The calculations conducted in this field can be broadly divided into two main areas: Forcefield based calculations and quantum mechanical (QM) calculations. This chapter describes the theory behind the forcefield methods used in this thesis namely, GULP [3], the Solids Docking Module in Insight II [4] and the Sorption Module in Cerius$^2$ [5], as well as the QM codes DMol$^3$[6] and Gaussian03 [7] and the embedded code QMPot [8].

QM methods are used to predict the electronic and molecular structure and the energetics of a system. They are also an essential tool for obtaining insight into reaction mechanisms, in particular to identify reactive intermediates and transition states. Whilst QM methods provide more accurate approximations than those obtained using classical methods, they are restricted to relatively small systems as they are computationally intensive.

Forcefield methods (also referred to as molecular mechanics methods) are based on inter-atomic potentials. These describe the variation in the energy of a system as a function of the nuclear coordinates. In contrast to QM methods, electronic motion is ignored. These methods are thus particularly suited to large systems that are difficult to consider by quantum mechanical methods, but cannot be used to model any property that depends on electronic distribution. These methods are therefore unsuitable for modelling reactions. Forcefield methods are based on several assumptions. The first of these is the Born-Oppenheimer approximation, which enables the electronic and nuclear

motions to be decoupled, thus allowing the energy to be written as a function of nuclear coordinates [9]. Another assumption is that the energy of the system can be written as a sum of contributions from various processes such as bond stretching and bond rotation. Examples of calculations in which forcefield methods are employed are in docking and diffusion [10]. The following sections describe the various methods employed in this work in depth.

## 2.1 Forcefield methods

### 2.1.1 The Forcefield

A forcefield is a set of equations and parameters used to describe the energy of the potential energy surface of a system as a function of its nuclear co-ordinates [11]. The particles in the system are treated using the classical 'ball and spring' model whereby the atoms are represented as deformable spheres and the bonds as springs of varying stiffness.

A forcefield contains all the information required to perform calculations of energy and force including a list of atom types, atomic charges and atom typing rules that describe the atoms the forcefield represents and the hybridisation state. In addition the forcefield contains functional forms for each component of the energy expression and parameters for the functional forms. The forcefield energy is written as a sum of the functional forms, each describing the energy required to distort the molecule in a specific fashion:

$$E_{FF} = E_{str} + E_{bend} + E_{tors} + E_{vdw} + E_{el} + E_{cross} \qquad 2.1$$

The components of the forcefield energy can be separated into two parts. The first four terms of equation 2.1 describe the part of the potential energy surface due to interactions between bonded atoms whilst the rest describe the non-bonded terms. Using such an expression the nuclear co-ordinates, geometries and relative energies can be computed. The advantage of using a forcefield to calculate energies is that it allows the study of fairly large systems comprising thousands of atoms. Each component of the forcefield will now briefly be discussed.

## 2.1.2 The Stretching Energy

A vibrating bond shows harmonic behaviour close to its equilibrium value but shows dissociation at longer bond lengths. This can be most accurately represented using a Morse function:

$$E = D_e [1 - \exp\{\alpha(l - l_0)\}]^2 \qquad 2.2$$

where $D_e$ is the dissociation energy, $\alpha$ the force constant, and $l_0$ the equilibrium bond length. A problem with the Morse description is that computing the exponential term is computationally expensive. Thus most forcefields adopt an alternative description of the stretching energy, using instead a harmonic expression derived from Hooke's law, in which the energy varies as the square of the displacement from equilibrium bond length $l_0$:

$$E = \frac{k}{2}(l - l_0)^2 \qquad 2.3$$

where k is the force constant describing the deformation of the bond upon stretching. Whilst easier to compute, the Hooke's law description is not as accurate as the Morse potential at larger distances away from the equilibrium. According to the harmonic description, the energy increases whether the bond is contracted or lengthened, and continues to increase however much the bond is stretched. However, this is not chemically accurate as a bond can only be stretched to a certain point after which it breaks. In order for the harmonic form to model the bond stretching potential at longer distances to a greater degree of accuracy, cubic and higher terms are added to equation 2.3:

$$E = \frac{k}{2}(l - l_0)^2 [1 - k'(l - l_0) - k''(l - l_0)^2 - k'''(l - l_0)^3 \dots] \qquad 2.4$$

It is more computationally efficient to model a polynomial expression as in equation 2.4 than the exponential expression as in equation 2.2. Hence, most forcefields use the harmonic polynomial expression rather than the Morse potential.

## 2.1.3 Bending Energy

The bending energy describes the energy required to bend an angle formed by three connecting atoms. As with the stretching energy, the bending energy is often written as a harmonic:

$$E_\theta = \frac{k}{2}(\theta - \theta_0)^2$$

<div align="right">2.5</div>

$k_\theta$ is a force constant associated with bending the angle and $\theta_0$ is the equilibrium value for the bond angle. As with the stretching energy, additional cubic and higher terms improve the accuracy of equation 2.5:

$$E_\theta = \frac{k}{2}(\theta - \theta_0)^2 \left[1 - k'(\theta - \theta_0) - k''(\theta - \theta_0)^2 - k'''(\theta - \theta_0)^3 \ldots\right]$$

<div align="right">2.6</div>

## 2.1.4 Torsional Energy

The torsional energy describes the change in energy associated with rotation of atom A around a B-C bond in a four-atom sequence A-B-C-D with respect to D. The functional form of the torsional energy is given by the following function in the form of a Fourier series:

$$E = \sum_{n=0}^{N} \frac{V_n}{2}[1 + \cos(n\omega - \gamma)]$$

<div align="right">2.7</div>

The constant $V_n$ determines the size of the barrier to rotation around the B-C bond. n is the multiplicity value and gives the number of minimum points as the function is rotated through 360°. $\omega$ is the torsional angle and $\gamma$ is the plane factor and determines where the torsion passes through its minimum value. Another type of torsional angle can also exist in a system, in which 4 atoms are not bonded in the sequence A-B-C-D. Such an angle is called an improper torsion and is given by the expression:

$$E(w) = k(1 - \cos 2\omega)$$

<div align="right">2.8</div>

## 2.1.5 Cross Terms

The stretching energy, angle bending and torsional energy cannot be considered as separate entities. For example, as a bond angle is decreased, the bond length of the adjacent bonds increases to reduce the interaction between the connected atoms. The terms therefore couple with each other and cross terms are added to the forcefield to take this into account. Cross terms often represent the coupling of two internal

coordinates, for example stretch-stretch, stretch-bend and stretch-torsion. However in some cases terms are added to reflect the coupling of three internal coordinates such as a bend-bend-torsion term.

### 2.1.6 The 12-6 Short-Range Interaction Energy

The van der Waals energy describes the repulsion or attraction experienced between two atoms that are not directly bonded. The interaction varies as a function of the distance between atoms. When the atoms are very close the interaction energy is strongly repulsive. As the atoms separate the energy becomes first mildly attractive and then negligable at longer distances. The attractive contribution arises as a result of dispersive (London) forces. These dispersive forces are a result of the instantaneous dipoles due to fluctuations in electron clouds. An instantaneous dipole in one molecule can induce one in another molecule, resulting in an attractive inductive effect.

The van der Waals interaction energy between two atoms may be represented in various ways. The most common is as part of the Lennard-Jones 6-12 potential:

$$E_{LJ} = 4\varepsilon \left[ \left( \frac{\sigma}{r} \right)^{12} - \left( \frac{\sigma}{r} \right)^{6} \right]$$

2.9

The potential contains two adjustable parameters, $\sigma$, the collision diameter and $\varepsilon$, the well-depth. The $\left( \frac{\sigma}{r} \right)^{6}$ term represents the dispersion or attractive energy whilst the $\left( \frac{\sigma}{r} \right)^{12}$ term describes the repulsion. Exponentials of 9 or 10 may also be used for the repulsive part of the potential. The Buckingham potential may be used as an alternative to model this behaviour. The Buckingham potential uses an exponential form that can be written as follows:

$$E_{vdw} = A \exp(-Br) - Cr^{-6}$$

2.10

The choice of function used depends on computing requirements. As the Buckingham potential contains an exponential term it takes longer to compute. It is therefore suited to model small molecules where the number of interactions is small. The Lennard-Jones potential on the other hand is easier to compute as it avoids the calculation of a large

number of squares and exponentials and also has the advantage of fewer parameters. However, the exponential term in the Buckingham potential is more accurate than $r^{-12}$.

For polyatomic systems a larger number of interactions, often between different types of atoms need to be considered. A system containing N different atoms would require N(N-1)/2 sets of parameters to be obtained, which can be a complicated and time-consuming process. The process can be simplified somewhat by using the so-called Lorentz-Berthelot mixing rules, with which the parameters between two different types of atoms can be obtained from the parameters of the pure atoms by averaging.

### 2.1.7 Electrostatic Interaction Energy

The electrostatic energy originates from the internal redistribution of electrons that creates positive and negative regions within a molecule. This charge redistribution can be represented in a number of ways. Partial atomic charges, for example, are restricted to the nuclear centres. Other models include the Central Multipole Expansion model which is based on the electric moments present in a molecule, such as the dipole, quadrupole and higher moments. The interaction between two point charges is most commonly given by the coulomb potential which takes the following form:

$$E = \sum_{i=1}^{N_A} \sum_{j=1}^{N_B} \frac{q_i q_j}{4\pi\varepsilon_0 r_{ij}}$$

2.11

Here $\varepsilon_0$ represents the permitivity of free space, $N_A$ and $N_B$ the number of point charges in the two molecules and $q_i$ and $q_j$ represent the charge on atoms A and B, respectively. A common method of calculating electrostatic interactions in periodic systems, such as zeolites, is the Ewald summation method, which has been used in this study and will be discussed next.

## 2.2 Ewald Summation Method

The Ewald summation method [12] is routinely used to calculate long-range electrostatic interactions and is used by the GULP[3] code as well as the Monte Carlo simulations employed in this study. The electrostatic interaction decays as $r^{-1}$ and thus is time consuming to compute. This problem can be overcome by using the Ewald method. The method employs periodic boundary conditions, whereby the unit cell is

replicated in 3 dimensions allowing simulation of the bulk system and minimising surface effects. Thus a particle in the system interacts with all others in the simulation box and with all of their images in an infinite array of periodic cells. Each charge is considered to be surrounded by a neutralising charge distribution of equal magnitude but opposite in sign. A dual summation of the interactions between the charges plus the neutralising charge distribution is then carried out. The electrostatic interactions are divided into near and far-field contributions to improve efficiency. The near field is calculated directly whilst the far-field contributions are carried out in reciprocal space.

## 2.3 Shell Model

The shell model, proposed by Dick and Overhauser [13], describes the coupling between polarisation and short-range interactions in solids. In the model the ions are replaced by a massive positively charged core and a massless shell linked by a harmonic spring. In an electric field the outer shell retains its charge but moves with respect to the core thus introducing a polarisation around the core. The polarisability of an isolated ion, $\alpha$, is proportional to $\dfrac{Y^2}{k}$, where $k$ is the spring constant of the harmonic spring and $Y$ is the charge on the shell. The electrostatic interaction energy is given as a sum over all ions and shells, not taking into account the interaction of an ion with its own shell. The interactions between cores and shells are represented by empirical potentials whose parameters are fitted to reproduce experimental data.

## 2.4 Monte Carlo Methods

Computing the locations and orientations of molecules within zeolite cavities is crucial as it gives an insight into preferential adsorption sites and their relative binding energies [14]. This information can then be used to deduce how the molecules may react within the zeolite pores. Several techniques exist to do this, the Monte Carlo technique being one of them. A Monte Carlo simulation generates a configuration of a system by making random changes to the location and orientations of species and computing the interaction energy. A forcefield is used to represent the atoms involved, in this case the *cff91_czeo* forcefield [15] which is particularly suited to modelling zeolites, and organic guest molecules such as alkenes and alkanes. It is a particularly useful technique since it

generates states with low energies. In this study two different Monte Carlo approaches, both using different algorithms, were used to study adsorption. The first, using the InsightII Solids Docking module [4] was used to obtain energetically favourable adsorption sites which were subsequently refined using Density Functional Theory. The second approach used the Sorption Module [5] of the Cerius$^2$ suite of programs and was used to obtain isosteric heat plots and adsorption isotherms. Each of these approaches will now be described.

### 2.4.1 Solids Docking Approach

In the Solids Docking approach trial interaction energies are computed by randomly placing the sorbate molecule in the host lattice and summing the energy contributions between all atoms of the zeolite host and the sorbate [16]. Interactions of atoms within the same molecule are ignored. If this interaction energy is greater than a predefined threshold value, which is chosen to minimise steric contact, the conformation is discarded and another structure generated. If the interaction energy is lower than this threshold value then the conformation is kept and minimised to optimise the interaction of the sorbate with the zeolite host. The process described above is completely random unlike the Metropolis Monte Carlo technique as described for the Sorption module next, where the new structure is compared to the preceding one.

### 2.4.2 Sorption Approach

The Sorption approach allows two main types of simulations; fixed loading (canonical ensemble), in which the number of sorbates in the framework and temperature is kept fixed and fixed pressure (grand canonical ensemble), in which the number of particles is not fixed but varies as a function of pressure. Each of these simulation types will now be described.

### 2.4.3 Fixed Loading Simulation

The initial configuration for a fixed loading simulation is generated by placing the sorbate at an arbitary position in the zeolite framework. The sorbate molecule is then randomly rotated or translated to generate subsequent configurations. The choice of move is governed by the pre-defined move probabilities and limited by the maximum translation and rotation step-size. Each configuration generated is accepted or rejected

according to a probability, P, obtained using the Metropolis algorithm [17] which takes into account the previous conformation:

$$P = \min\left[1; \exp\left(\frac{-\Delta E}{kT}\right)\right]$$

2.12

where $\Delta E$ represents the energy change between the new configuration and previous configuration, T, the temperature of the simulation and $k$ the Boltzmann constant. If once a move has been made $\Delta E$ is negative the new configuration is accepted. However if it is positive the Boltzmann factor, $\exp\left(\frac{-\Delta E}{kT}\right)$, is calculated and compared to a randomly generated number between zero and one. If the random number is less than the Boltzmann factor the move is accepted, else it is rejected.

## 2.4.4 Fixed Pressure Simulation

In a fixed pressure (grand canonical) simulation the number of particles in the system is varied whilst the chemical potential of each species is kept constant. This chemical potential is converted by Sorption into a partial pressure (fugacity) for each species. The starting configuration is generated by one of four random moves, each of which has a different acceptance criterion.

The first move is the creation of the molecule inside the framework. A random molecule is selected from a list of sorbates and placed in a random position and orientation in the framework. The probability, P, that this configuration is accepted is given by:

$$P = \min\left[1; \exp\left(-\frac{\Delta E}{kT} - \ln\frac{(N_i + 1)kT}{f_i V}\right)\right]$$

2.13

where $N_i$ represents the current number of molecules of component $i$ in the framework, $f_i$ the fugacity of component $i$ in the gas phase, and $V$ the cell volume.

The second move is the destruction of a molecule whereby a molecule is removed from the framework. A random sorbate is removed and the new configuration is accepted according to the probability P:

$$P = \min\left[1; \exp\left(-\frac{\Delta E}{kT} + \ln\frac{N_i kT}{f_i V}\right)\right]$$

2.14

The third type of move is a translation of a molecule in which a randomly chosen sorbate molecule is translated by a random amount within a cube of size $2\delta$ (where $\delta$ corresponds to the maximum step size). The probability, P, that the new configuration is accepted is given by equation 2.12.

The final move type involves the rotation of a random molecule in the framework. The molecule is rotated a random amount about a random rotation axis within the range $-\delta$ and $+\delta$. Once again, the probability that this new configuration is accepted is given by equation 2.12.

## 2.5 Quantum Mechanics

At the turn of the $20^{th}$ century scientists had little reason to doubt that Newtonian mechanics could explain the behaviour of both macroscopic and microscopic systems. In 1900 however, a key experiment by Max Planck indicated that black-body radiation was emitted by microscopic particles in discrete amounts. i.e. it was quantised. These discrete amounts were given by $h\nu$, where $\nu$ is the frequency of the radiation and $h$ is a proportionality constant, referred to as Planck's constant. UV spectroscopy can be used to measure the intensity of absorption in a sample in the UV- vis region of the spectrum. In the following years it became clear that this quantisation argument could be extended to electrons bound in atoms, as they are also limited to discrete energy levels, as indicated by their UV-vis spectra. In order to move between energy levels an electron requires a quantised amount of energy. Classical mechanics failed in describing correctly the behaviour of electrons due to the Heisenberg uncertainty principle:

$$\Delta x \Delta p = \frac{\hbar}{2}$$

2.24

which states that the position of the electron and its momentum cannot be simultaneously determined.

In 1923, Louis de Broglie proposed that microscopic particles have wave-like character. The joint wave and particle-like character of matter is known as wave-particle duality

and contradicts classical mechanics where waves and particles are treated as separate entities. These observations made it clear that Newtonian mechanics was not sufficient to describe microscopic matter and that a new set of concepts was required to describe their behaviour, marking the beginnings of Quantum Mechanics.

### 2.5.1 The Wavefunction

The basis of quantum mechanics was established by introducing so-called wavefunctions that represent each particle contained within a chemical system. The wavefunction is analogous to the concept of a trajectory in classical physics and contains all the dynamical information about the system it describes. Appropriate operators act on this wavefunction to predict the value or range of values for observable properties of the system. Mathematically, this can be written as:

$$v\psi = E\psi \qquad\qquad 2.25$$

Equation 2.25 is an example of an eigenvalue equation, where $v$ is an operator, $E$ is the scalar value for some property, and $\psi$ is an eigenfunction, more commonly referred to as the wavefunction. The wavefunction $\psi$, multiplied by its complex conjugate, $\psi^*$ at a given point, returns the probability of finding a particle at that point. If $\psi^*\psi$ is integrated over all space, the result is one, since the particle must be somewhere, and to satisfy this condition wavefunctions have to be normalised.

There are certain conditions that a wavefunction must meet in order for it to be acceptable for use in calculations. One of these conditions is that the wavefunction must be single-valued and continuous. A further condition is that the overall wavefunction must obey the Pauli Principle, which states that the wavefunction of a system must be anti-symmetric upon the simultaneous interchange of the space and spin coordinates of any two identical fermions, in this case electrons.

### 2.5.2 The Schrödinger Equation

The Schrödinger equation lies at the heart of quantum mechanics and is equivalent to Newton's Second Law in classical physics. It can be used to compute the probability of events or outcome. The time dependent Schrödinger equation is an eigenvalue equation and follows the format of equation 2.25 above:

$$H\psi = E\psi \qquad\qquad 2.26$$

H is the Hamiltonian operator which is associated with the energy of the system. It is composed of two parts representing the kinetic and potential energies of the nuclei and electrons. The kinetic part of the Hamiltonian is given by:

$$\frac{-\hbar^2}{2m}\nabla^2 \qquad\qquad 2.27$$

where m is the mass and $\nabla^2$ is the Laplacian operator, which accounts for the kinetic energy of the electrons and is given by:

$$\nabla^2 = \frac{\partial^2}{\partial x^2} + \frac{\partial^2}{\partial y^2} + \frac{\partial^2}{\partial z^2} \qquad\qquad 2.28$$

The potential part considers the attraction of the nuclei and electrons as well as the inter-nuclear and inter-electron repulsions. The particles are considered as point charges, q, separated by a distance r and the potential energy V given as:

$$V_{ij} = \frac{-\sum Z_A}{r_i A} + \sum \frac{q_i q_j}{r_{ij}} \qquad\qquad 2.29$$

The expression for the potential energy implies that the motion of the nuclei and electrons are correlated which can complicate matters. Obtaining solutions to the Schrödinger equation is simplified somewhat by applying two approximations. The first, the Born Oppenheimer approximation [9] enables the nuclear and electronic motions to be decoupled, since the mass of the nuclei is so much greater than that of the electrons they can effectively be considered to be stationary. This reduces the problem to one that involves solving the electronic Schrödinger equation at fixed nuclear positions:

$$H_e = T_e + V_{ne} + V_{ee} + V_{nn} \qquad\qquad 2.30$$

where $T_e$ is the kinetic energy of the electrons and $V_{ne}$, $V_{ee}$ and $V_{nn}$ represent the potential energy between the nuclei and electrons, electrons and electrons and nuclei and nuclei respectively. The equation is now simpler as the electron-nuclear correlation is removed. The remaining correlation between electrons still complicates matters somewhat but will be discussed later. The second approximation is the adiabatic approximation, which restricts the solution of the total wavefunction to one electronic surface.

Once $\psi$ is known for a particular state of a system then any physical observable may, in principle, be determined using the following relationship:

$$\text{Observable} = \frac{\int \psi * \upsilon \psi \partial \tau}{\int \psi * \psi \partial \tau}$$

2.31

where $\upsilon$ represents an operator for the property being determined. Exact solutions to the Schrödinger equation are only possible in a few cases such as the particle in a box, the harmonic oscillator and the hydrogen atom and other one-electron systems. Even in these cases it is necessary to impose certain requirements, referred to as *boundary conditions* on possible solutions to the solutions of the Schrödinger equation. For example, in the case of the particle in a box the wavefunction is required to go to zero at the boundaries.

### 2.5.3 Constructing a wavefunction

A number of factors complicate solving the Schrödinger equation. As explained earlier, the Schrödinger equation cannot be solved exactly, even for a helium atom as this involves three or more interacting particles. Thus, any solution for a polyelectronic system can only be an approximation to the true Schrödinger equation. A further complication is that until this point electron spin has been unaccounted for. Each electron has a spin quantum number of ½. In the presence of a magnetic field the spins can align in two ways, either along the field or opposite the field. These spins are denoted as $\alpha$ and $\beta$ spins respectively and obey the following orthonormality conditions:

$$<\alpha|\alpha> = <\beta|\beta> = 1$$
$$<\alpha|\beta> = <\beta|\alpha> = 0$$

Electron spin is incorporated into the Schrödinger equation by introducing the concept of spin-orbitals. Each one-electron wavefunction can be written as the product of a spatial function and a spin function. The resulting solutions are called spin orbitals, $\chi$. The spatial part depends on the coordinates of the electron in space and describes the distribution of the electron density. The spin part depends on the electron spin and each spatial orbital can accommodate 2 electrons of opposite spins.

The problem that remains now is to find the functional form of the wavefunction for a polyelectronic system that satisfies the Pauli principle. The overall wavefunction for an atom can be written as a product of one-electron eigenfunctions:

$$\Psi_{atom} = \chi_1(1)\chi_2(2)\chi_3(3)...\chi_n(N) \qquad 2.32$$

where $\chi_k$ are atomic orbitals. This description of the wavefunction is called the Hartree Product description. According to this the probability of finding an electron at a given point is independent of finding another electron at the same point. However, the motion of the electrons are correlated. This approach treats the interelectronic repulsions in an average way, with each electron considered to be moving in the electrostatic field of the other n-1 electrons. Further, the Hartree Product wavefunction is symmetric with respect to the interchange of two electrons, therefore ignoring the requirements of the Pauli Principle.

An antisymmetric wavefunction can be generated using the concept of a Slater determinant, first proposed by Slater in 1930 [20]. For the general case of N electrons and N spin orbitals, a Slater determinant can be written as:

$$\phi_{SD} = \frac{1}{\sqrt{N!}} \begin{vmatrix} \chi_1(1) & \chi_2(1) & \chi_3(1) & .... & \chi_N(1) \\ \chi_1(2) & \chi_2(2) & \chi_3(2) & .... & \chi_N(2) \\ \vdots & \vdots & \vdots & \vdots & \vdots \\ \chi_1(N) & \chi_2(N) & X_3(N) & .... & \chi_N(N) \end{vmatrix} , \quad <\chi_i | \chi_j> = \delta_{ij}$$

The $\frac{1}{\sqrt{N!}}$ factor ensures that the wavefunction is normalized and the $\chi_N(N)$ indicates a spin orbital of the nth electron. Exchanging any two rows of the determinant, a process equivalent to exchanging two electrons, results in a change in sign of the determinant thereby retaining the antisymmetry property. Any identical rows would correspond to two electrons being placed in the same spin orbital, a violation of the Pauli Principle, and so the determinant vanishes.

The variational principle is employed to generate trial wavefunctions. This states that any approximate wavefunction has an energy greater than or equal to the exact energy. The better the wavefunction, the lower the energy obtained. Thus, once a basis set is

selected, the coefficients $c_{ik}$ should be chosen so as to minimise the energy for all linear combinations of the basis functions. The energy of an approximate wavefunction can be calculated using the following relationship:

$$E = \frac{\int \psi^* H \psi \partial \tau}{\int \psi^* \psi \partial \tau}$$

2.33

The quality of the wavefunction can be judged by analysis of the energy obtained. The wavefunction that returns the lowest value for the energy will be the most accurate and likely to compute accurate properties using other operators.

The next step is to evaluate the energy of the trial wavefunction, which results in the following expression:

$$E = \frac{\sum_{ik} c_i c_k H_{ik}}{\sum_{ik} c_i c_k S_{ik}}$$

2.34

where $H_{ik}$ is the resonance integral and $S_{ik}$ is the overlap integral and represents the extent to which two basis sets overlap in space.

In order to minimise the energy of the basis functions the coefficients of the basis functions must have derivatives that are equal to zero i.e. $\dfrac{\delta E}{\delta c_{ik}} = 0$

This leads to N set of secular equations with N unknowns (the individual coefficients);

$$\sum_{i=1}^{N} c_{ik} (H_{ik} - ES_{ik}) = 0$$

2.35

There is always one trivial solution when all coefficients equal zero. Non-trivial solutions for certain values of E are obtained by forming a secular determinant:

$$\begin{vmatrix} H_{11}\text{-}ES_{11} & H_{12}\text{-}ES_{12} & \cdots\cdots & H_{1N}\text{-}ES_{1N} \\ H_{21}\text{-}ES_{21} & H_{22}\text{-}ES_{22} & \cdots\cdots & H_{2N}\text{-}ES_{2N} \\ \vdots & \vdots & \vdots & \vdots \\ \vdots & \vdots & \vdots & \vdots \\ H_{N1}\text{-}ES_{N1} & H_{N2}\text{-}ES_{N2} & \cdots\cdots & H_{NN}\text{-}ES_{NN} \end{vmatrix} = 0$$

In general, there will be N roots E1, E2, E3...$E_N$, which satisfy the secular equations, some of which may be degenerate. Once the values of E are known, they can be used to obtain the basis set coefficients $c_{ik}$ for that molecular orbital, which can in turn be used to determine the value of $\varphi_k$. The molecular orbitals obtained in this way are all mutually orthogonal.

### 2.5.4 The Hartree-Fock approach

When considering polyelectronic systems the interaction between electrons needs to be taken into account. The aim now is to find a method which simultaneously allows for all electronic motion. This is crucial as the correlated motions of the electrons mean that a change in the spin of an electron in one spin orbital will affect the behaviour of an electron in another spin orbital. For the moment, to simplify matters, we will concentrate on a single electron in a spin orbital $\chi_i$ in the field of the nuclei with the other electrons in their fixed spin orbitals $\chi_j$.

Returning briefly to the electronic Hamiltonian operator, we consider the three types of interaction that contribute to the total energy of a polyelectronic system. The first contribution arises from the kinetic and potential energy of each electron moving in the field of the nuclei. If inter-electronic interactions were ignored then this would be the only operator that would need to be considered and would represent the motion of a single electron moving in the field of the single nuclei. This can be given by the core Hamiltonian operator, written as:

$$H^{core} = \int \partial \tau_i \chi_i(1) \left( \frac{-\hbar^2}{2m} - \sum_{A=1}^{M} \frac{Z_A}{r_i A} \right) \chi_i(1)$$

2.36

Secondly, there is the contribution from the electrostatic repulsion between pairs of electrons. This interaction is unfavourable and is a function of the distance between electrons. This is given by the coulomb operator $J_{ij}$:

$$J_{ij} = \iint \partial \tau_i \partial \tau_2 \chi_i(1) \chi_j(2) \left( \frac{1}{r_{12}} \right) \chi_i(1) \chi_j(2)$$

2.37

Finally, there is a contribution from the exchange interaction, which is a manifestation of the fact that the motions of electrons with parallel spins are correlated. This is due to the Pauli Principle and is written as:

$$K_{ij} = \int\int \delta\tau_1 \partial\tau_2 \chi_i(1)\chi_j(2)\left(\frac{1}{r_{12}}\right)\chi_i(2)\chi_j(1)$$

2.38

Thus, the total energy can be written as a sum of these individual contributions:

$$H^{core}(1)\chi_i(1) + \sum_{j\neq 1}^{N} J_j(1)\chi_i(1) - \sum_{j\neq 1}^{N} K_j(1)\chi_i(1) = \sum_j \varepsilon_{ij}\chi_j(1)$$

2.39

This can be simplified further by replacing the constants with the Fock operator, F, which is effectively a one-electron Hamiltonian for the electron in a polyelectronic system:

$$F = H^{core} + \sum_j^{N} (J_j - K_j)$$

2.40

## 2.5.5 The SCF approach

The Hartree-Fock equations take the standard eigenvalue form:

$$F_i\chi_i = \varepsilon_i\chi_i$$

2.41

As explained earlier, when setting up the equations it was assumed that each electron moves in a fixed field of the nuclei and the other electrons. This has important consequences, as any solutions that are obtained will affect solutions for other electrons in the system. The SCF approach to find solutions to the Hartree Product wavefunction was first proposed by Hartree in 1928 [21]. The process is iterative in nature and begins with an initial guess for the wavefunction, $\psi$, for all the occupied molecular orbitals. The necessary one-electron Fock operators are then constructed. The solution of the Hartree equation gives rise to a new set of wavefunctions. This process is repeated with the new wavefunction to generate a revised set of wavefunctions, which are better than the last. This process is continued, gradually refining the solutions, until the difference between the new set and the one immediately preceding it meets some predefined convergence criterion. At this point the solutions are said to be self-consistent. Fock, in 1930 [22], proposed the extension of this SCF procedure to determinental wavefunctions, thereby obeying the Pauli Principle.

## 2.6 Basis Sets

For molecules it is not practical to solve the Hartree-Fock equations directly and so the Linear Combination of Atomic Orbitals (LCAO) method is adopted. In this approach each spin orbital is written as a linear combination of electron orbitals:

$$\varphi i = \sum_k C_{ik} \chi_k \qquad 2.42$$

The one-electron orbitals, $\chi_k$, are usually referred to as basis sets and correspond to the atomic orbitals.

A basis set is a group of mathematical functions that are an approximate representation of the atomic orbitals. In essence a basis set describes the space in which the wavefunction can exist. There are two main forms that these functions may take. The first, proposed by Slater in 1930 [20] are known as Slater Type Orbitals (STOs). STOs take the following form:

$$\aleph_{\zeta,n,l,m}(r,\theta,\varphi) = NY_{lm}(\theta,\varphi)r^{n-1}e^{-\zeta r} \qquad 2.43$$

where n, l, and m are the quantum numbers, $\zeta$ is the orbital exponent, $\varphi$ is the spherical harmonic and N is a normalisation constant. $\zeta$ is a variational parameter which controls the width of the orbital – large values give a tight function whilst small values give diffuse functions. The values of $\zeta$ are determined using variational Hartree Fock calculations and the exponents which give the lowest energies are used.

STOs have a number of features that facilitates their use in electronic structure calculations. They decay exponentially with increasing distance from the nucleus, representing exactly a hydrogen atom. The orbital also correctly displays a cusp at the nucleus for the 1s orbital. STOs do not however have any radial nodes which can be introduced by making linear combinations of STOs. The exponential dependence means that STOs converge rapidly with increasing number of functions. Whilst it is simple enough to evaluate integrals for atomic and diatomic systems, STOs cannot be evaluated analytically for larger systems and therefore the use of these types of orbitals is restricted to small systems.

Gaussian Type Orbitals (GTOs) were proposed as an alternative to Slater Type Orbitals by Boys in 1950 [23] on practical grounds since the integrals in this type of function

could be solved analytically and would thus be easier to compute. Gaussian type orbitals have the following form:

$$\aleph_{\zeta,n,l,m}(r,\theta,\varphi) = NY_{lm}(\theta,\varphi)r^{2n-1}e^{-\zeta r^2} \qquad 2.44$$

STOs decay exponentially whilst convergence of Gaussian type orbitals is dependent on the $r^2$ term in the exponential. For this reason GTOs are inferior to STOs. In particular, GTOs do not exhibit the correct behaviour at the nucleus, since unlike STOs there is no cusp. In addition GTOs tend to fall away too rapidly far away from the nucleus. This means that behaviour further away from the nucleus is not appropriately represented; in particular Gaussian functions underestimate the long-range overlap between atoms. However, the computational efficiency of these functions outweighs any of these limitations. Nevertheless, simply replacing a STO with a single Gaussian function leads to significant errors. These errors can be overcome by replacing each atomic orbital with a linear combination of Gaussian functions:

$$\phi_\mu = \sum_{i=1}^{L} d_i\mu\phi_i(\zeta_{i\mu}) \qquad 2.45$$

where d are the contraction coefficients and $\zeta$ is the orbital exponent. Both are variational parameters.

The limitations described above suggest that an STO needs to be replaced with at least 3 GTOs, in order to approach the accuracy achieved in a full Slater type orbital calculation. The individual Gaussians from which the linear combination is formed are called primitive Gaussians. Calculations with primitive Gaussians are rarely performed since much of the computational effort would go towards calculating the energies and coefficients of core orbitals, which are chemically unimportant as it is the valence electrons involved in processes such as chemical bonding. The concept of using a fixed linear combination of contracted basis functions was first introduced by Clementi and co-workers [24]. In this method the coefficients of the core orbitals are kept constant, using pre-determined values and only those of the valence orbitals varied. This reduces the number of variables to be calculated thus significantly reducing computational time. In order to increase computational efficiency, the same Gaussian exponents are often used for the s and p orbitals.

## 2.7 Classification of basis sets

Basis sets can be grouped according to the type of functions (Slater type or Gaussian) and the number of functions used.

### 2.7.1 Minimal, multiple-zeta and split valence basis sets

A *minimal basis* set contains only the number of functions required to represent all the electrons in a neutral atom. In practice, a minimal basis set often includes all the atomic orbitals in the shell. The STO-nG series derived by Pople and co-workers are all minimal basis sets [25] and are routinely used in electronic structure calculations. These functions are all based on STOs with n primitive Gaussian types. Here the exponents are determined by fitting to an STO rather than optimising them using a variational procedure. Basis sets with n =2-6 exist but as described above at least 3 GTOs are needed to accurately represent an STO. Thus the STO-3G basis set is a commonly used basis set. Increasing n beyond three gives little improvement in accuracy whilst increasing computational effort significantly. However, the minimal basis set approach has several disadvantages. A minimal basis set cannot represent the non-spherical aspects of the electron distribution. Since a minimal basis set contains only one contraction per atomic orbital and the exponents for these are not allowed to vary the basis functions cannot expand and contract in response to the molecular environment. The limitations of the minimal basis can be overcome if more than one function is used for each atomic orbital giving rise to a group of multiple-zeta basis sets. A *double zeta* (DZ) basis set is one in which there are two functions for each atomic orbital, for example, for hydrogen 1s and 1s' are used. This offers a significant advantage over the use of minimal basis sets, now allowing for the fact that the electron distribution is different in different directions. A variation of the double zeta basis sets is the split valence basis set where only the valence orbitals are doubled, keeping a single function for the core orbitals. This is a reasonable approximation since the chemical properties are largely unaffected by the core orbitals. The *triple zeta* and *quadruple zeta* basis sets have three and four functions for each atomic orbital respectively. The split valence rationale can also be applied to these orbitals.

Another class of basis set is the k-nlmG series. These are all split valence basis sets. The value of k indicates the number of contracted core orbitals, n,l and m denote the number of functions that the valence orbitals are split into. If only two values, n and l are present then the orbital is a split valence, whilst three values, n,l and m give a triple split valence. An example of a split valence basis set is the 6-31G basis. Here the core orbitals are a contraction of six GTOs, the inner part of the valence orbital is given by three GTOs and the outer part by one GTO. Larger basis sets are also often employed in electronic structure calculations.

### 2.7.2 Polarisation and diffuse functions

Further functions are added to the basis set to give it more flexibility. Polarisation functions are added to basis sets to describe the bonding in molecules more accurately. For example, p orbitals can be added to polarise s orbitals and d orbitals added to polarise p orbitals and so on. These additional functions are used to describe the distortion of the atomic orbitals when molecules are formed.

The addition of polarisation functions is denoted by an asterisk at the end of a basis function. For example, the addition of polarisation functions to all atoms except hydrogen in the 6-31G basis set would give a 6-31G* basis whilst including polarisation on the hydrogen atom as well would give a 6-31G** basis set.

The basis sets described so far are unable to describe species such as anions and molecules containing lone pairs whose electron density is more spatially diffuse than normal molecular orbitals. This can be addressed by adding a set of diffuse functions to the basis set, which are denoted with a +. Using the 6-31G basis set again as an example, the addition of diffuse functions to all the atoms except hydrogen is given as 6-31G+ whilst including hydrogen gives a 6-31G++ basis.

### 2.7.3 Choice of basis set

The choice of a basis set is critical and needs to be chosen to represent the system under study in the best possible way. It should be able to approximate the actual wavefunction sufficiently to produce chemically meaningful results. The number of GTOs used for each class of basis set increases in the following way:

Minimal < Split Valence < double zeta < polarised < diffuse
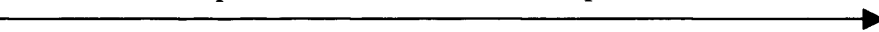
Get an increasingly good approximation to the actual wavefunction

Whilst accuracy is increased from moving across from a minimal to a diffuse basis set the integrals take significantly longer to compute. Usually the choice of basis set involves a balance between accuracy of results obtained and the computational effort required to evaluate the integrals.

## 2.7.4 The Basis Set Superposition Error

The basis set superposition error (BSSE) is present in all molecular orbital calculations that employ incomplete basis sets. The BSSE is particularly prevalent in the calculations of interaction energies. This can be explained further by considering a chemical system AB composed of two interacting fragments A and B. The interaction energy of the system is most commonly determined using the supermolecular approximation, where the energy is taken as the difference in energy of the complex AB and the energy of its fragments A and B:

$$E_{interaction(A-B)} = E_{AB} - E_A - E_B \qquad 2.56$$

The problem with this approach is that the description of fragment A in the complex is improved by the basis functions of fragment B and vice versa. This improvement is not possible for the individual fragments. The result is that the overall description of the complex AB is better than that of the fragments from which it is composed. This leads to an error referred to as the basis set superposition error (BSSE) and was first noted by Jansen and co-workers [26]. The calculated interaction is artificially lowered by this error. An obvious way of overcoming this error is to perform each calculation using a complete basis set to describe the complex and the individual fragments. However, this is not feasible in a computational sense. A number of approaches have been suggested for overcoming this error. The most widely used is the Counterpoise correction method suggested by Boys and Bernardi [27]. In this method equation 2.56 is modified to give the interaction energy as:

$$E_{\text{interaction(A-B)}} = E_{AB} - E_{AG} - E_{BG} \qquad\qquad 2.57$$

The energy of the fragment A is calculated in the presence of ghost orbitals of B (denoted G in equation 2.57) i.e. without the nuclei or electrons of B. A similar calculation is also performed on B, using the ghost orbitals of A. However many believe that the Counterpoise approach overestimates the basis set superposition error and as a result the interactions are too repulsive [28,29].

## 2.8 The Roothaan –Hall Approach

An alternative method for solving the Hartree-Fock equations was proposed independently by Roothaan and Hall in 1951[30,31]. In this approach, the Hartree-Fock equations were reformulated in matrix form. The Roothaan-Hall equations can be written as a matrix equation:

$$FC=SCE \qquad\qquad 2.58$$

The Fock matrix, F, approximates the single-electron energy operator. S is the overlap matrix, representing the overlap between basis functions. The C matrix contains the coefficients of the molecular orbitals and E is a diagonal matrix whose elements are the orbital energies. The first step in finding solutions to the Roothaan-Hall equations is to diagonalise the matrices. This results in the basis functions being transformed so that they are orthomormal. Equation 2.58 is then solved in an iterative manner, analogous to the SCF approach described previously, where an initial guess of the Fock matrix is used to construct a new Fock matrix. This approach can only be used for a closed-shell system, i.e. a system with no unpaired electrons.

## 2.9 Moller Plesset Perturbation Theory

As discussed above, a severe limitation of the Hartree-Fock approach is that it neglects the effect of electron correlation. Several methods have been proposed to overcome this including Moller Plesset Perturbation, Configuration Interaction and Coupled Cluster theories [9,11,32]. Of the three methods Moller Plesset Perturbation theory is the most computationally feasible and is the method used in this study.

The Moller Plesset Perturbation theory provides a means for adding excitations to the Hartree-Fock wavefunction, $\psi_0$, and therefore includes the effects of electron correlation. This can be done by adding a small perturbation $V$ to the unperturbed Hamiltonian operator $H_0$:

$$H = H_0 + \lambda V \qquad\qquad 2.59$$

The aim then is to relate the unknown eigenvalues and eigenfunctions of the perturbed system to the known values of the unperturbed system. This is done by adding a parameter $\lambda$ to the equation which determines the strength of the perturbation. $\lambda$ can take values between 0 and 1. When $\lambda$ is 0, the system is unperturbed. As $\lambda$ increases the perturbation grows larger and when it equals 1 the system is fully perturbed.

If the perturbation is small then the resulting wavefunction and energy can be described as a power series:

$$\psi = \lim_{n\to\infty} \sum_i^n \lambda^i \psi^i \qquad\qquad 2.60$$

$$E = \lim_{n\to\infty} \sum_i^n \lambda^i E^i \qquad\qquad 2.61$$

These equations can be substituted into the time-independent Schrödinger equation. The solutions to first and second order correspond to the Hartree-Fock energy. Thus to improve on the Hartree-Fock energy it is necessary to use Moller Plesset Perturbation theory to at least second order. This is referred to as MP2 level theory. The scaling behaviour of MP2 is roughly $N^5$, where N is the number of basis functions [9]. The solutions can also be taken to third and fourth order, termed MP3 and MP4 respectively.

A limitation of MP2 theory is that it is not variational. Hence it is possible for the correlation energy to be overestimated. However, in practice this rarely happens as basis set limitations always introduces an error that lowers the correlation energy [32]. MP2 calculations are computationally intensive and their use therefore is usually restricted to single point calculations on systems that have been optimised using a lower level of theory.

## 2.10 Density Functional Theory

Hartree-Fock theory is based on a complicated many electron wavefunction which is dependent on 3N variables, that is the 3 spatial variables for each electron. However DFT simplifies the problem by instead considering the density which is a function of 3 variables. The basis of DFT lies in the theorem proposed by Hohenberg and Kohn in 1964 [33] that all properties of the ground state of a system are functions of the electron charge density $\rho$. Kohn and Sham [34] went further and proposed that the total energy of the system as a function of the electron density, in the presence of an external field, (known as the density functional) may be written as:

$$E_T(\rho) = T(\rho) + U(\rho) + E_{xc}(\rho) \qquad 2.62$$

Here $T(\rho)$ represents the kinetic energy of the *non-interacting* electrons, $U(\rho)$ the electrostatic energy due to coulombic interactions between the electrons and $E_{xc}(\rho)$ the exchange-correlation function which represents the many-body interactions.

The exchange-correlation term can be split into two parts; the exchange interaction and the correlation energy. The exchange interaction is due to the Pauli Principle which states that two electrons having parallel spin cannot be in the same state at the same time. The correlation energy arises from electrons with parallel spins aligning next to each other due to electron-electron repulsion.

The wavefunction of the electron is taken as an antisymmetrised product or Slater determinant of the molecular orbitals:

$$\Psi = A\ (n)\ |\varphi_1\ (1)\varphi_2(2)...\varphi_n(n)| \qquad 2.63$$

The molecular orbitals must also be orthonormal, i.e. perpendicular to each other, in which case the charge density is given by the following expression:

$$\rho\ (r) = \Sigma|\ \varphi_i\ (r)|^2 \qquad 2.64$$

The MOs are occupied by either spin –up ($\alpha$) electrons or spin-down electrons ($\beta$). If the same value of $\varphi_i$ is used for both $\alpha$ and $\beta$ electrons then the calculation is spin-restricted whereas if both $\alpha$ and $\beta$ electrons have different values of $\varphi_i$ the calculation is spin – unrestricted. For the purposes of this study, spin-restricted calculations have been performed as the system being modelled has no unpaired electrons.

To account for the exchange correlation term an approximation must be made. Two such methods are the Local Density Approximation (LDA) and the Gradient Generalised Approximation (GGA). The LDA is a method based on the known correlation energy of a uniform electron gas. This method assumes that the charge density varies very slowly on the atomic scale: that is, each region of the molecule resembles that of a cloud of uniform electron gas. The total exchange correlation energy can be obtained by integrating over all space using the following expression:

$$\varepsilon_{xc}(\rho) \approx \int \rho \, (r) \; \varepsilon_{xc} \, [\rho \, (r)] \; dr \qquad\qquad 2.65$$

where $\varepsilon_{xc}(\rho)$ is the exchange correlation energy per electron in a uniform electron gas. However the LDA approach is unrealistic since the electron density is typically non-uniform.

A significant improvement to the LDA is the GGA [35,36], which takes into account the extent to which the electron density varies locally. The GGA method obtains a value for $E_{xc}$ from both the electron density and the gradient of the density at a point r, thus accounting for the non-local regions of the electron gas. An example of such an approximation is in the PW91 [37] which has been employed in this study. This method performs extremely well when compared to LDA. For atomisation energies for example, the error per bond is 0.1 eV compared to 0.7eV for LDA methods. However, GGA functionals are known to overestimate bond lengths.

To solve the Kohn-Sham equations, a self-consistent approach is utilised. An initial guess of the electron density is made using equation 2.64 from which a new set of orbitals can be derived with an improved electron density. These new sets of orbitals are then used in the second iteration to derive a third set of orbitals with an improved electron density. This process is repeated until convergence is reached.

So-called hybrid Hartree-Fock/Density Functional methods are an attractive way to include the effects of exchange in Hartree-Fock calculations. In simple terms this involves deriving the correlation energy using DFT and then adding it to the Hartree-Fock energy. A popular hybrid functional is the B3LYP functional which comprises of a

Lee-Yang-Parr(LYP) [38] correlation functional and a standard local correlation functional of Vosko, Wilk and Nusair [39].

In DFT the description of the energy of a system is based entirely on the electron density and/or the density gradient. This leads to one of the main limitations of DFT in that it is unable to describe van der Waals (dispersive) interactions since they derive from electron correlation at long range. Clearly this is a severe drawback in describing intermolecular interactions. This problem cannot be rectified by adding HF exchange to the DFT functional since HF theory neglects the effects of electron correlation. There is currently a great deal of research into ways of including dispersive interactions [40-43].

## 2.11 Numerical basis sets

The DMol$^3$ suite of programs used to carry out the electronic structure calculations use basis functions that are numerical values on an atomic-centred spherical polar mesh, rather than use analytical functions such as GTOs [44]. The angular part of each basis function is given by the appropriate spherical harmonic, $Y_{lm}(\theta,\phi)$, whilst the radial part is obtained by solving the atomic DFT equations numerically. Using numerical orbitals of this type minimises the effects of basis superposition [6] and can describe weak bonds with accuracy. In a similar way to Gaussian basis sets, the number of functions describing each orbital can be doubled to produce a double numerical (DN) basis set, which is analogous to the double zeta (DZ) basis. Polarisation and diffuse functions may also be added to give a DNP and DND basis set respectively. The DNP basis set is comparable to the Gaussian 6-31G** basis whilst the DND is comparable to the 6-31G$^{++}$ basis set.

## 2.12 Energy Minimisation

The potential energy surface describes the way in which the energy of a system varies with atomic co-ordinates [18]. For a system with N atoms, each with three degrees of freedom, this means that there are 3N-6 variables to be minimised. The minimum points of the energy surface are of particular interest since they represent stable states of the system. For any given energy surface there may be several stationary states. The one

with the lowest energy is the most stable and is referred to as the global minimum. At each stationary point the first derivative of the function with respect to each variable is zero. The second derivatives are all positive. A minimisation algorithm is used to search for stationary points on the potential energy surface. An energy minimisation calculation is often used as a starting point for subsequent calculations to ensure that a stable structure with a reasonable geometry is used. The minimum is reached when a pre-defined criterion is met. Such a criterion may be that the difference between energies of consecutive iterations falls below a specified threshold. The steepest descents, conjugate gradients and Newton-Raphson minimisation algorithms are the most widely used [19].

The steepest descents algorithm is driven purely by force gradients along the potential energy surface. The method is good for lowering the energy of a system, since it works well when large forces are present. It is the method of choice when the starting configuration is far from the minimum. However, since the direction of the search is always perpendicular to the previous one it is not the most reliable method of obtaining the true minimum. The steepest descent algorithm is usually used to generate a reasonable structure, which can then be refined using another method such as conjugate gradients or Newton-Raphson, described next.

The conjugate gradients method uses information from the previous derivatives to determine the optimum direction in the search for minima. In the first step, the gradient vector is denoted $g1$ and the first move, $s1$, is given by:

$$s1 = -g1 \qquad\qquad 2.15$$

The second step takes this gradient into consideration and the new direction is given by:

$$s_k = -g_k + b_k s_{k-1} \qquad\qquad 2.16$$

where $s_{k-1}$ is the previous search direction and $b_k$ is a scaling factor given by:

$$b_k = \frac{g_{i+1} \bullet g_{i+1}}{g_i \bullet g_i} \qquad\qquad 2.17$$

This procedure is repeated in an iterative fashion until a minima is reached.

The Newton-Raphson algorithm differs from the Steepest descents and Conjugate gradient methods in that it uses both the first and second derivatives in the search for a minimum. As stated above at the minima, $x*$ the first derivative of the energy is zero:

$$f'(x*) = 0 \qquad\qquad 2.18$$

For a starting point, $x$, the minima can be written as:

$$x* = x + dx \qquad\qquad 2.19$$

where $dx$ is the increment that $x$ must change by in order to reach the minimum. Thus the condition for the minimum can be given by:

$$f'(x + dx) = 0 \qquad\qquad 2.20$$

This can be expanded about point $x$ using a Taylor series expansion, which is also set to equal zero:

$$f'(x + dx) = f'(x) + f''(x)dx + f'''(x)dx^2 + .... \qquad\qquad 2.21$$

If the Taylor expansion is truncated at the second order term it is assumed that the minimum is exactly quadratic in behaviour. This assumption may not be valid for a complex surface that is far from the minimum, but will hold true as the energy moves closer to the minimum. The expression can then be arranged to give the change that $x$ must undergo in order to reach the minimum:

$$dx = \frac{-f'(x)}{f''(x)} \qquad\qquad 2.22$$

Substituting back into equation 2.15 gives:

$$x* = x - \frac{f(x)}{f''(x)} \qquad\qquad 2.23$$

The case above is for a one-dimensional system. For a multi-dimensional system, such as in the case of molecules, where each atom has 3 degrees of freedom, the term $f'(x)$ is replaced by a matrix (F), which contains the derivatives of the potential energy with respect to a change in coordinates. The second derivatives are also contained in a matrix (the Hessian, H). The Newton-Raphson algorithm is efficient for systems with a small number of atoms; however for a larger system the number of matrix elements in the Hessian increases significantly and the algorithm becomes slower. The increased number of terms in the Hessian may also pose a problem in terms of computer storage requirements. Variations on the Newton-Raphson method have been proposed to overcome problems with the Hessian, including block diagonal Newton-Raphson,

which neglects off-diagonal interactions between atoms and diagonal Newton-Raphson which only calculates second derivatives and neglects the correlation between the 3 degrees of freedom for an atom.

The choice of algorithm depends on various factors, including the size of the system being modelled, the storage and memory requirements and the speed at which the calculation is performed. It also depends on the type of calculation being performed. Quantum mechanical calculations require a lot of computational effort and thus an algorithm that reaches the minimum in a few steps is best suited. Also as systems modelled using quantum mechanical methods have fewer atoms than those using molecular mechanics, certain algorithms that may require more computer storage are more suited. As stated above, there may be a large number of minima on the energy surface. Care must be taken when analysing results as a local minimum or saddle point rather than a global minimum may have been reached. Confirmation of a global minimum can be obtained by analysing the second derivatives as they must be positive at a minimum and negative at a maximum or saddle point.

## References

(1)     Catlow, C. R. A.; Bell, R. G.; Gale, J. D. *J. Mater. Chem.* **1994**, *4*, 781.

(2)     Catlow, C. R. A.; Ackermann, L.; Bell, R. G.; Gay, D. H.; Holt, S.; Lewis, D. W.; Nygren, M. A.; Sastre, G.; Sinclair, P. E. *J. Mol. Catal. A: Chemical* **1997**, *115*, 431.

(3)     Gale, J. D. *J. Chem. Soc - Faraday Transactions* **1997**, *93*, 629.

(4)     Biosym/MSI *Solids Docking Manual*San Diego, October 1995.

(5)     Accelrys;Inc *Sorption Manual, Release 4.5*San Diego, June 2000.

(6)     Delley, B. *Journal of Chemical Physics* **1990**, *92*, 508

(7)     Gaussian 03, R. C., M. J. Frisch, G. W. Trucks, H. B. Schlegel, G. E. Scuseria, M. A. Robb, J. R. Cheeseman, J. A. Montgomery, Jr., T. Vreven, K. N. Kudin, J. C. Burant, J. M. Millam, S. S. Iyengar, J. Tomasi, V. Barone, B. Mennucci, M. Cossi, G. Scalmani, N. Rega, G. A. Petersson, H. Nakatsuji, M. Hada, M. Ehara, K. Toyota, R. Fukuda, J. Hasegawa, M. Ishida, T. Nakajima, Y. Honda, O. Kitao, H. Nakai, M.

Klene, X. Li, J. E. Knox, H. P. Hratchian, J. B. Cross, V. Bakken, C. Adamo, J. Jaramillo, R. Gomperts, R. E. Stratmann, O. Yazyev, A. J. Austin, R. Cammi, C. Pomelli, J. W. Ochterski, P. Y. Ayala, K. Morokuma, G. A. Voth, P. Salvador, J. J. Dannenberg, V. G. Zakrzewski, S. Dapprich, A. D. Daniels, M. C. Strain, O. Farkas, D. K. Malick, A. D. Rabuck, K. Raghavachari, J. B. Foresman, J. V. Ortiz, Q. Cui, A. G. Baboul, S. Clifford, J. Cioslowski, B. B. Stefanov, G. Liu, A. Liashenko, P. Piskorz, I. Komaromi, R. L. Martin, D. J. Fox, T. Keith, M. A. Al-Laham, C. Y. Peng, A. Nanayakkara, M. Challacombe, P. M. W. Gill, B. Johnson, W. Chen, M. W. Wong, C. Gonzalez, and J. A. Pople, Gaussian, Inc., Wallingford CT, 2004. Gaussian03.

(8)     Sierka, M.; Sauer, J. *Faraday Discuss.* **1997**, *106*, 41.

(9)     Leach, A. R. *Molecular Modelling Principles and Applications*; Prentice Hall: Essex, 2001.

(10)    Allinger, N. L. Force Fields: A brief introduction. In *Encyclopedia of Computational Chemistry*; pp 1013

(11)    Jensen, F. *Introduction to Computational Chemistry*; Wiley: Chichester, 1999.

(12)    Ewald, P. P. *Ann. d. Physik* **1921**, *64*, 253.

(13)    Dick, B. G.; Overhauser, A. W. *Phys. Rev.* **1958**, *112*, 90.

(14)    Smit, B.; Krishna, R. *Curr. Opin. Solid State and Mat. Sci.* **2001**, *5*, 455.

(15)    Hill, J. R.; Sauer, J. *J. Phys. Chem* **1994**, *98*, 1238.

(16)    Freeman, C. M.; Catlow, C. R. A.; Thomas, J. M. *Chem. Phys. Letters* **1991**, *186*, 137.

(17)    Metropolis, N.; Metropolis, A. W.; Rosenbluth, M. N.; Teller, A. H.; Teller, E. *J. Chem. Phys* **1953**, *21*, 1087.

(18)    Schlegel, H. B. Geometry Optimisation 1. In *Encyclopedia of Computational Chemistry*; pp 1136.

(19)    Schlick, T. Geometry Optimisation 2. In *Encyclopedia of Computational Chemistry*; pp 1142.

(20)    Slater, J. C. *Phys. Rev* **1930**, *36*, 57

(21)    Hartree, D. R. *Proc. Cambridge Phil. Soc.* **1928**, *24*, 111.

(22)    Fock, J. *Z. Phys* **1930**, *61*, 126.

(23)    Boys, S. F. *Proc. Royal Soc. Chem* **1950**, *A200*, 542

(24)    Clementi, E.; Davis, D. R. *IBM J. Res. Dev.* **1965**, *9*, 2.

(25)    Hehre, W. J.; Stewart, R. F.; Pople, J. A. *J. Chem. Phys* **1969**, *51*, 2657

(26)    Jansen, H. B.; etal. *Chem. Phys. Lett* **1969**, *3*, 140.

(27)    Boys, S. F.; Bernardi, F. *Mol. Phys* **1970**, *19*, 553

(28)    Senent, M. L.; Wilson, S. *Int. J. Quant Chem.* **2001**, *00*, 1

(29)    Wells, B. H.; Wilson, S. *Chem. Phys. Lett* **1983**, *101*, 429

(30)    Roothaan, C. C. J. *Rev. Mod. Phys.* **1951**, *23*, 69.

(31)    Hall, G. G. *Proc. R. Soc. (London)* **1951**, *A205*, 541.

(32)    Cramer, C. J. *Essentials of Computational Chemistry : Theories and Models,* Wiley, **2002**

(33)    Hohenberg, P.; Kohn, W. *Physical Review* **1964**, *136*, B864

(34)    Kohn, W.; Sham, L. J. *Physical Review* **1965**, *140*, A1133

(35)    Perdew, J. P.; Burke, K.; Ernzerhof, M. *Phys. Rev. Letts* **1996**, *77*, 3865.

(36)    Dal Corso, A.; Pasquarello, A.; Baldereschi, A.; Car, R. *Physical Review B* **1996**, *53*, 1180.

(37)    Perdew, J. P.; Chevary, J. A.; Vosko, S. H.; Jackson, K. A.; Pederson, M. R.; Singh, D. J.; Fiolhais, C. *Physical Review B* **1992**, *46*, 6671

(38)    Lee, C.; Yang, W.; Parr, R. G. *Phys. Rev. B* **1988**, *37*.

(39)    Vosko, S. J.; Wilk, L.; Nusair, M. *Can. J. Phys.* **1980**, 1200.

(40)    Dobson, J. F.; Dinte, B. P. *Phys. Rev. Letts* **1996**, *76*, 1780.

(41)    Dobson, J. F. *Int. J. Quantum. Chem.* **1998**, *69*, 615.

(42)    Dobson, J. F.; Wang, J. *Phys. Rev. Letts* **1999**, *82*, 2123.

(43)    Dobson, J. F.; McLennan, K.; Rubio, A.; Wang, J.; Gould, T.; Le, H. M.; Dinte, B. P. *Aus. J. Chem.* **2001**, *54*, 513.

(44)    Molecular Simulations *DMol 96.0/4.0.0 Quantum Chemistry User Guide* San Diego, 1996.

# Chapter Three: An atomistic and quantum mechanical study of the adsorption of chlorinated hydrocarbons in zeolites

## 3.1 Introduction

A detailed understanding of how reactions proceed within zeolites requires knowledge of the nature of the adsorbed species within the zeolite cavity. Whilst techniques based on inter-atomic potentials are able to provide useful information such as heats of adsorption, and enable the simulation of adsorption isotherms, they do not provide any information about the electron distribution within the zeolite and adsorbate and how it changes upon adsorption. Electronic structure methods such as Density Functional Theory and Hartree- Fock theory must therefore be employed to obtain information on the electronic distribution. These methods are crucial in improving our understanding of the adsorption process and to investigate reaction mechanisms; in particular providing useful information on the nature of reaction intermediates and transition states leading to the final products. The transfer of a proton from a Brønsted acid site to an adsorbed hydrocarbon is one of the most important steps in acid catalysis. However, there is some debate in the literature as to the nature of the protonated complex generated and whether it exists in the form of a stable carbonium ion species or as a short-lived transition state [1,2]. Quantum mechanical calculations are a useful tool to ascertain the true nature of the intermediate species.

## 3.1.1 The cluster technique

Industrially important zeolites have unit cells containing many hundreds of atoms. As such, electronic structure calculations, whilst rigorous, can prove computationally prohibitive. The most important interaction affecting the reaction is the interaction of the adsorbate with the zeolite wall or acid site. Since this interaction is localised to a specific finite area (i.e. the active site can be clearly identified) the cluster model approach can be employed. In this approach a limited number of atoms surrounding the active site are extracted and dangling bonds are terminated using hydrogen atoms.

These clusters are then modelled using an electronic structure method. This cluster technique has been employed by a number of groups and has produced promising results [3-6]. Sauer *et al.* [3] have used the technique to predict NMR quadrupole coupling constants in ZSM-5 and produced results consistent with experimental studies. The activation barrier for ethane cracking in ZSM-5 has also been investigated using the cluster method [4] and Zygmunt *et al.* [5] illustrate the importance of cluster size and the long-range electrostatic effect of the lattice on the adsorption energy. Studies of acid catalysis of linear alkenes using the cluster method have yielded useful information about the reactants, transition states and products [6].

## 3.1.2 Overview of this work

This chapter describes the methods used and the results obtained in investigating the adsorption of dichloromethane (DCM), 1,2-dichloroethane (DCE) and trichloroethene (TCE) molecules within the MOR, MFI and FAU zeolite frameworks.

The first section of this chapter describes results of a Monte Carlo docking study within the siliceous zeolite framework, which served as a starting point for subsequent electronic structure cluster calculations. These are described in the second section, and were used to refine the geometries and energies for each system. The third section will describe the interaction of the sorbate molecules with clusters representing the acidic forms of the zeolite frameworks, H-MOR, H-MFI and H-FAU.

## 3.2 Monte Carlo Docking methodology

The Monte Carlo calculations were performed using the Solids Docking module in MSI's InsightII package [7,8]. Simulations were conducted in the canonical (NVT) ensemble. The zeolite structures were taken from the crystallographic information in the Solids Builder module of Cerius2. This database of zeolite structures contains crystallographic data for aluminosilicate structures. As we are modelling purely siliceous frameworks all aluminium atoms in the structures were replaced with silicon, but the structure was not relaxed from the experimental values. Models of the sorbate molecules were also built using the sketcher facility within the Insight II program. The *cff91_czeo* forcefield was employed and the calculations were performed for 500

iterations. A real space cut off of 10Å was set. Periodic Boundary Conditions were applied in all simulations and the unit cell was assumed to be rigid.

## 3.3 Monte Carlo Docking Results

The results obtained for each sorbate molecule in each of the frameworks are summarised in table 3.1 below. The adsorption energy, $E_{ads}$, was calculated using the following equation:

$$E_{ads} = E_{(zeo+sorbate)} - E_{zeo} - E_{sorbate} \qquad 3.1$$

where:           $E_{(zeo+sorbate)}$ is the energy of the cluster with the sorbate present

                 $E_{zeo}$ is the energy of the zeolite cluster framework with the sorbate absent

| Framework Structure | $E_{ads}$ for each of the Sorbate molecule (kJ/mol) | | |
|---|---|---|---|
| | DCE | DCM | TCE |
| MFI | -31.0 | -25.1 | -33.8 |
| MOR | -68.7 | -66.9 | -71.5 |
| FAU | -56.1 | -58.6 | -63.1 |

**Table 3.1:** Adsorption energies obtained by Monte Carlo Docking.

## 3.3.1 MFI and MOR frameworks

Our results show that the TCE molecule is the most strongly adsorbed in the MFI and MOR frameworks and DCM is the least strongly adsorbed. This can be rationalised by considering how each of these molecules interacts with the zeolite framework. Since the Si atoms of the zeolite framework are smaller than the oxygen atoms the adsorbed molecules experience interactions mainly with the large O atoms, whilst interactions with the Si atoms are inhibited. The large van der Waals radii of the three chlorine atoms of the TCE molecule interact favourably with the zeolite framework oxygen atoms and thus this molecule is the most strongly adsorbed. Conversely, the DCM molecule is the smallest of the three sorbate molecules and does not match the zeolite cavities of MFI and MOR well. Thus the molecule is unable to have such favourable interactions with the zeolite framework oxygen atoms.

For the MOR framework the DCM molecule and DCE molecule adsorb favourably in both the 12-membered ring channels and in the 8-ring side pockets, illustrated for DCM in figures 3.1a and 3.1b. The TCE molecule also adsorbed favourably in the 12-membered ring However adsorption was found to be unfavourable in the 8-ring side pockets since the molecule would be too large to enter through the 8-membered ring leading to the side pocket.



a                                    b
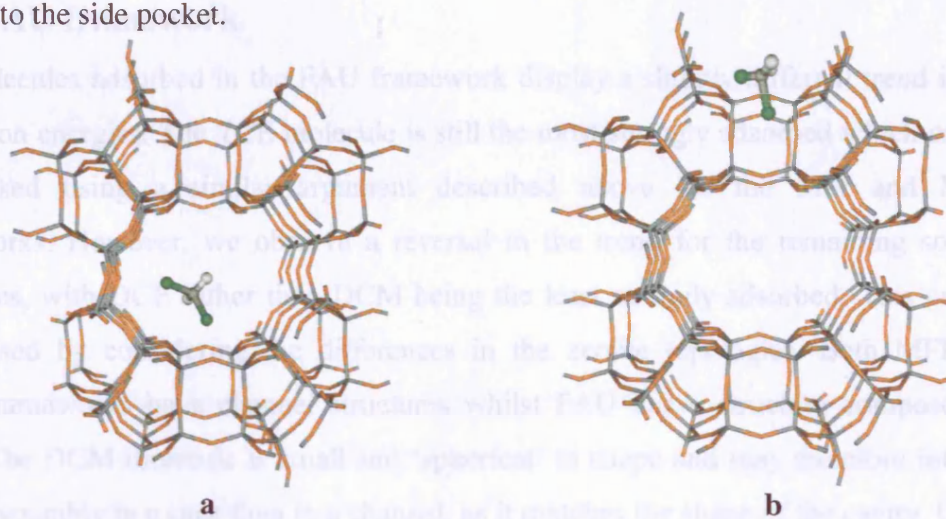
**Figure 3.1:** Adsorption geometry of DCM in the MOR framework a) in the 12-membered ring and b) in the 8-ring side-pocket.

For the MFI framework the three sorbate molecules were found to be adsorbed in both the straight and sinusoidal channels , illustrated for DCM in figures 3.2a and 3.2b.



a                                    b
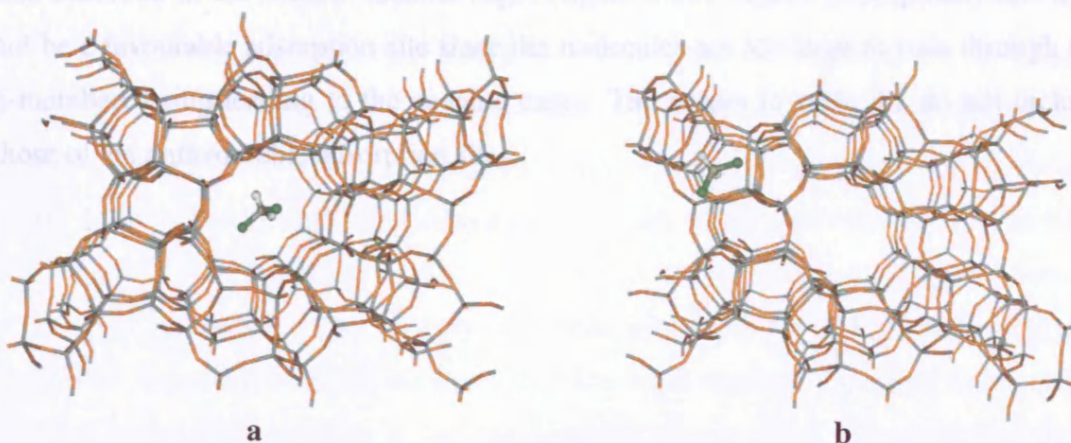
**Figure 3.2:** Adsorption geometries for DCM in the MFI framework a) in the straight channel and b) in the sinusoidal channel.

75

To summarise, the TCE molecule with three chlorine atoms has a higher adsorption energy than DCE and DCM. The energies of the DCM and DCE molecules, each with two chlorine atoms are similar in magnitude, with the shape of the adsorbate being the pre-dominant factor in "fine-tuning" the interaction energy.

## 3.3.2 FAU framework

The molecules adsorbed in the FAU framework display a slightly different trend in the adsorption energies. The TCE molecule is still the most strongly adsorbed which can be rationalised using a similar argument described above for the MFI and MOR frameworks. However, we observe a reversal in the trend for the remaining sorbate molecules, with DCE rather than DCM being the least strongly adsorbed. This can be rationalised by considering the differences in the zeolite topologies. Both MFI and MOR frameworks have channel structures whilst FAU has a structure composed of cages. The DCM molecule is small and 'spherical' in shape and may therefore interact more favourably in a cage than in a channel, as it matches the shape of the cavity. Using a similar argument, the DCE molecule may align along a channel matching the shape of the zeolite region it is interacting with and thus optimise its interaction with the framework atoms.

All three sorbate molecules adsorbed favourably above the 12-membered ring in the supercage as illustrated in figure 3.3a. In addition, the DCM and DCE molecules were also adsorbed in the smaller sodalite cages (figure 3.3b). Again, conceptually this may not be a favourable adsorption site since the molecules are too large to pass through the 6-membered ring leading to the sodalite cages. The values in table 3.1 do not include those of the unfavourable adsorption sites.
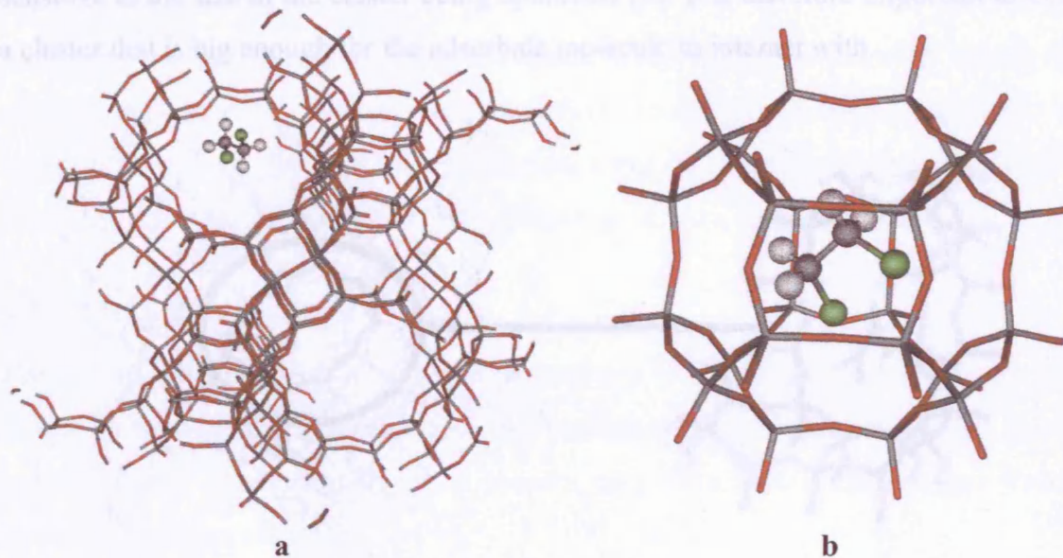
**Figure 3.3:** Adsorption geometries for DCE in the FAU framework a) in the 12ring

supercage  and b) in the sodalite cage (rest of zeolite omitted for clarity).

## 3.4 Siliceous cluster methodology

By using the results of the adsorption studies, the most favourable sites were selected based on both the energetics of the system (i.e. according to their thermodynamic stability) and on the orientation of the sorbate molecule. In order to refine the geometries of the sorbate –zeolite interaction electronic structure methods were employed to study the system in more detail.

A cluster was extracted from the zeolite lattice to retain as much of the framework around the adsorption site as possible. As such the clusters are quite large, composed of between 102 – 132 atoms. The dangling oxygen atoms were capped with hydrogen atoms and the bond lengths of the terminating hydroxyl groups were fixed at an O-H bond length of 0.97Å. Care was taken to ensure that the terminating hydrogen atoms did not interact with each other. The sorbate molecule was relaxed with respect to the framework fragment. Thus, all atoms of the framework fragment remained fixed, as the aim was to model the zeolite to the best possible extent, and a full relaxation of the cluster can lead to unrealistic geometries. The adsorption energy obtained is quite

sensitive to the size of the cluster being optimised [9]. It is therefore important to extract a cluster that is big enough for the adsorbate molecule to interact with.
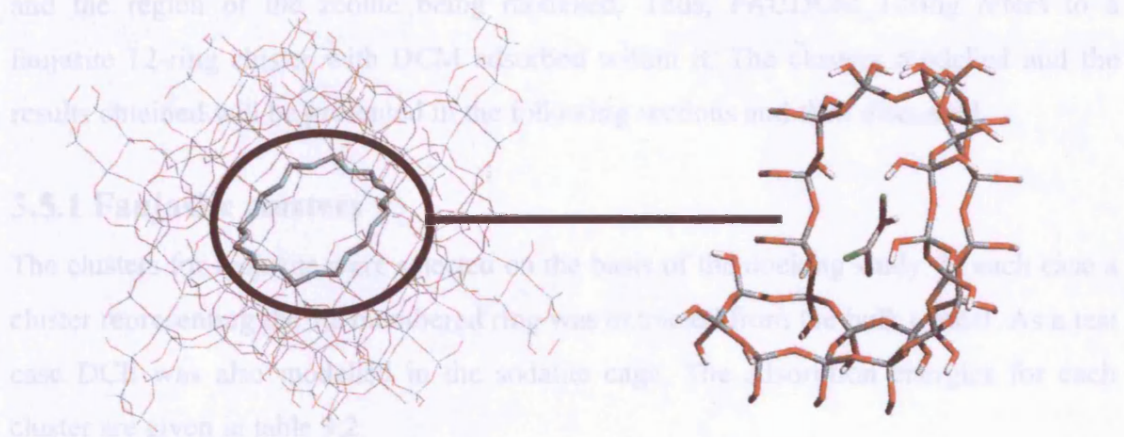


**Figure 3.4:** A pictorial representation of a cluster being extracted from a zeolite lattice.

The aim of this particular study was to validate the results obtained from the docking study. Therefore the adsorption sites, and thus the clusters extracted, differ. We seek to find the most favourable adsorption site for each of the sorbates and the maximum interaction energy they can have in a particular framework. The clusters were modelled using the PW91 functional [10,11] to account for exchange and correlation with a DNP basis set, (comparable to the 6-31G** gaussian basis set) within the DMol code [12]. A medium integration grid was employed providing a good balance between accuracy and computational efficiency. A convergence criterion of $10^{-6}$ was set. Single point energy calculations were performed on the DFT optimised structures using an extra fine integration grid.

## 3.5 Siliceous Cluster Results

The clusters in the following section are named according to the adsorbate within them and the region of the zeolite being modelled. Thus, FAUDCM_12ring refers to a faujasite 12-ring cluster with DCM adsorbed within it. The clusters modelled and the results obtained will be presented in the following sections and then discussed.

## 3.5.1 Faujasite clusters

The clusters for faujasite were selected on the basis of the docking study. In each case a cluster representing the 12-membered ring was extracted from the bulk crystal. As a test case DCE was also modelled in the sodalite cage. The adsorption energies for each cluster are given in table 3.2:

| Cluster | $E_{ads}$ (kJ/mol) |
|---|---|
| FAUDCM_12ring | -12.74 |
| FAUDCE_12ring | -17.12 |
| FAUTCE_12ring | -15.17 |
| FAUDCE_sodalite | 24.88 |

**Table 3.2:** Adsorption energies for FAU clusters.

The adsorption strength is the weakest for DCM and strongest for DCE. The energies obtained for each are of the same order of magnitude with there being only 4.4kJ/mol difference in energies between DCM and DCE. Contrary to the docking study, the cluster calculations indicate that the sodalite cage is not a favourable adsorption site. The clusters being modelled and the optimised sorbate geometries are shown in figures 3.5a-c. In all the remaining figures the saturating H groups have been omitted for clarity.

**Figure 3.5:** Optimised adsorbate geometries in the FAU framework with
a) DCM b) DCE c) TCE.

## 3.5.2 Mordenite clusters

For mordenite the clusters extracted from the bulk crystal represent the 12-ring channel. The adsorption energies for the clusters are presented in table 3.3. As test cases, DCM and DCE were also modelled in clusters representing the 8-ring side pocket for comparison with the docking study.

| Cluster | $E_{ads}$ (kJ/mol) |
|---|---|
| MORDCM_12ring | -19.98 |
| MORDCE_12ring | -20.12 |
| MORTCE_12ring | -23.89 |
| MORDCM_sidepocket | 18.10 |
| MORDCE_sidepocket | 25.82 |

**Table 3.3:** Adsorption energies for MOR clusters.

The trend in adsorption energies obtained by the cluster calculations indicate that DCM is the most weakly adsorbed followed by the DCE molecule. However, the energy difference between these two sorbates is only 0.14kJ/mol. Trichloroethene is the most strongly adsorbed being 3.9kJ/mol more favourable than dichloromethane. Adsorption is not favourable in the sidepockets as predicted by the docking study. The optimised geometries are shown in figure 3.6a-c.
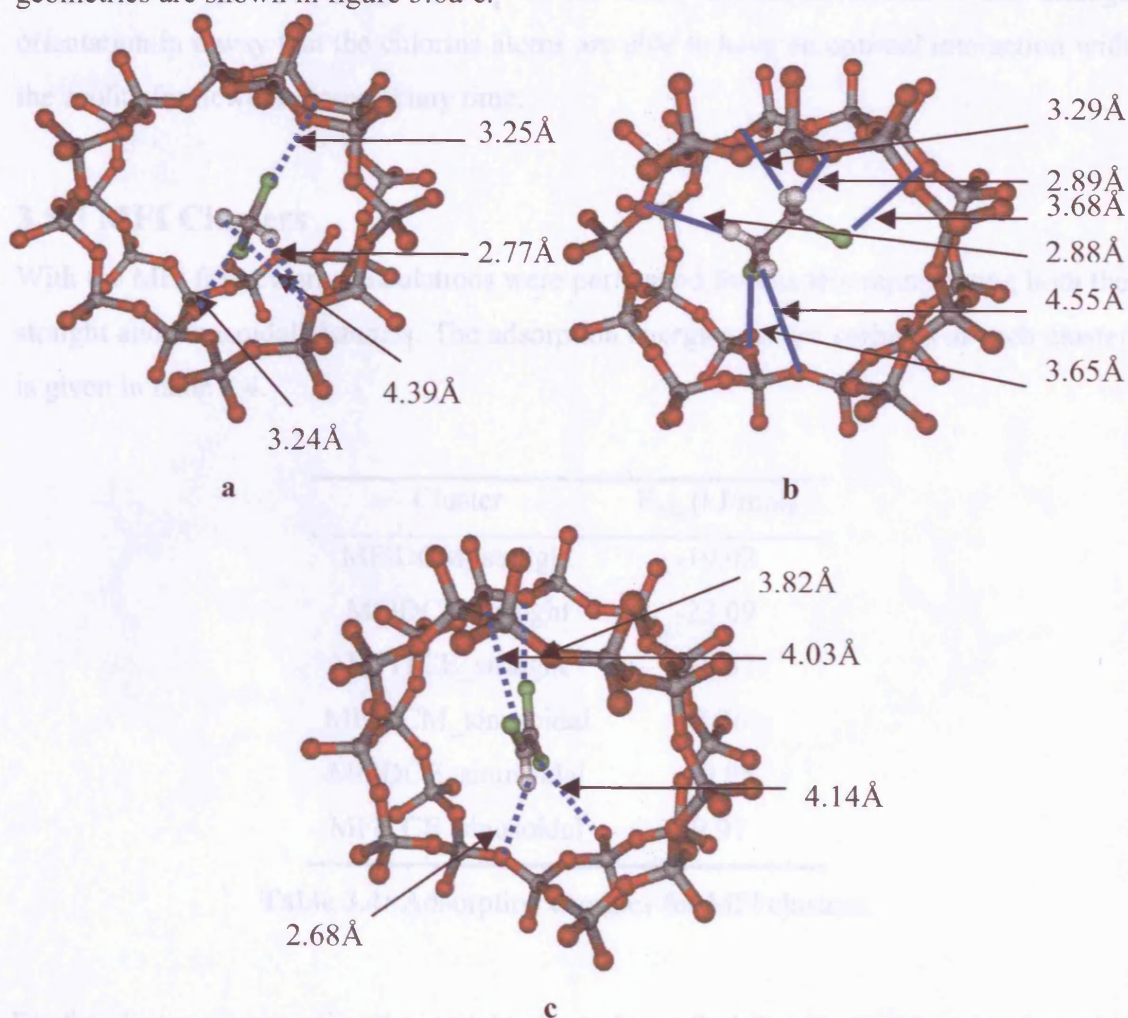


**Figure 3.6:** Optimised adsorbate geometries for MOR clusters with
a) DCM b) DCE and c) TCE.

The DCE molecule undergoes a change in conformation upon adsorption, with the chlorine atoms changing from an anti (chlorine atom opposite to each other) to a syn orientation (chlorine atoms adjacent to each other). This change in orientation costs 9kJ/mol, but by changing to the syn conformation the DCE molecule fits better into the zeolite cavity since the molecule becomes more compact. Thus, since the DCE molecule is the most conformationally flexible of the three sorbate molecules it can change orientation in a way that the chlorine atoms are able to have an optimal interaction with the zeolite framework atoms at any time.

## 3.5.3 MFI Clusters

With the MFI framework, calculations were performed for clusters representing both the straight and sinusoidal channels. The adsorption energies for the sorbates in each cluster is given in table 3.4.

| Cluster | $E_{ads}$ (kJ/mol) |
| --- | --- |
| MFIDCM_straight | -19.02 |
| MFIDCE_straight | -23.09 |
| MFITCE_straight | -28.37 |
| MFIDCM_sinusoidal | -8.36 |
| MFIDCE_sinusoidal | -10.05 |
| MFITCE_sinusoidal | -9.97 |

**Table 3.4:** Adsorption energies for MFI clusters.

For the clusters representing the straight channels we find that the DCM molecule is the least strongly adsorbed and TCE the most strongly. The TCE molecule is 9.35kJ/mol more strongly adsorbed than the DCM. In the case of the clusters representing the sinusoidal channels we find that the DCE molecule is the most strongly adsorbed and the DCM the least strongly adsorbed. The adsorption energies in the sinusoidal clusters are between 10 and 20 kJ/mol lower than the straight. The cluster sizes for both channels are comparable in size (figures 3.7a-c and 3.8a-c below) and so this difference does not appear to be the result of a cluster size effect.
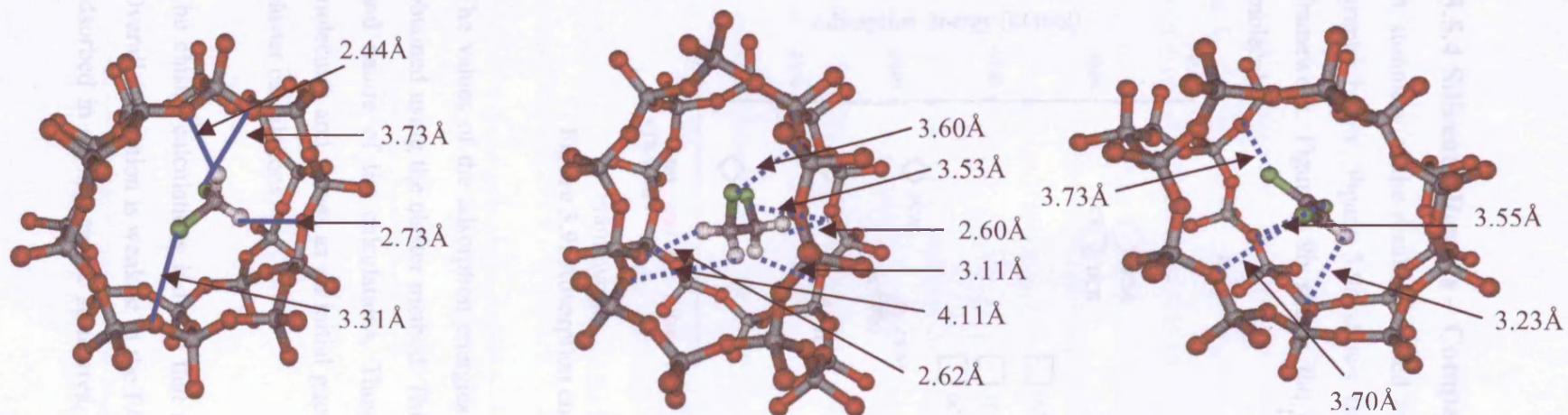
**Figure 3.7:** Optimised adsorbate geometries for MFI straight channel clusters with a) DCM b) DCE and c) TCE.
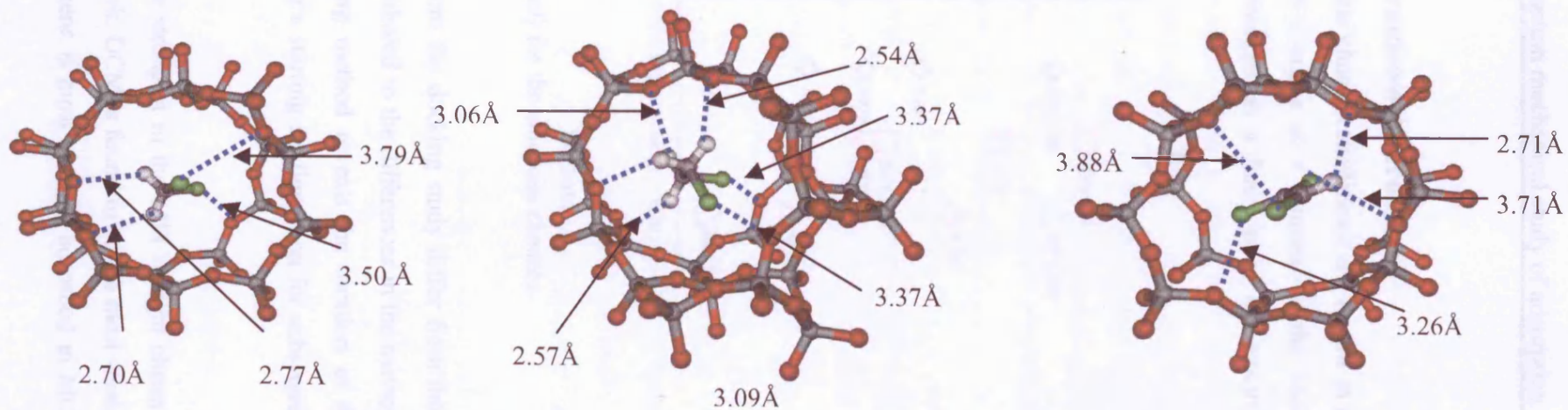


**Figure 3.8:** Optimised adsorbate geometries for MFI sinusoidal channel clusters with a) DCM b) DCE and c) TCE.

### 3.5.4 Siliceous Results – Comparison of framework structures

A summary of the results obtained for the siliceous cluster calculations are shown in the graphs below. Figure 3.9a shows the adsorption energies as a function of the zeolite framework. Figure 3.9b shows the adsorption energies as a function of the adsorbed molecule.
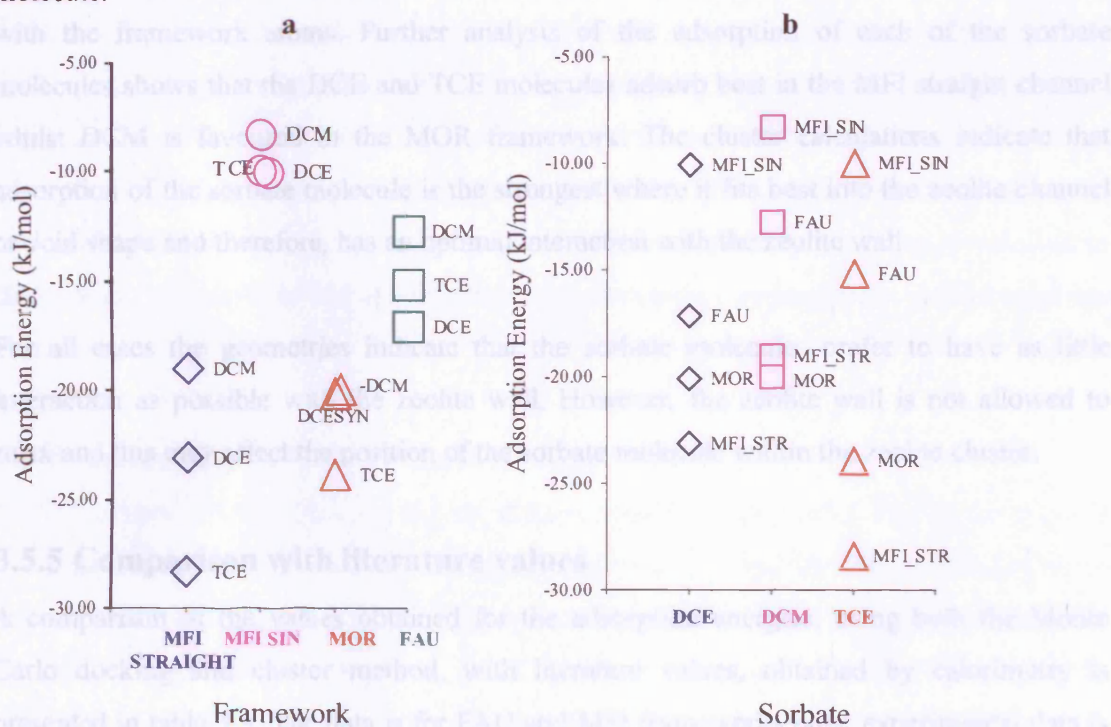


**Figure 3.9:** Adsorption energies (kJ/mol) for the siliceous clusters.

The values of the adsorption energies obtained from the docking study differ from those obtained using the cluster method. This can be attributed to the differences in the methods and nature of the calculations. Thus, the docking method reveals the location of the molecules and serves as an initial guess, providing a starting configuration for subsequent cluster calculations.

The cluster calculations indicate that adsorption is strongest in the MFI straight channel. Overall adsorption is weakest in the FAU framework. DCM is found to be the most weakly adsorbed in all framework structures. Trichloroethene is most strongly adsorbed in MOR

and MFI frameworks. However in FAU, DCE rather than TCE is more strongly adsorbed. This may be attributed to the differences in pore structures. Both MFI and MOR have channel structures and the "flatter" TCE molecule may align along these and optimise its interaction with framework oxygen atoms. However, in the case of FAU, which has a structure consisting of large pores, the TCE molecule is unable to interact as favourably with the framework atoms. Further analysis of the adsorption of each of the sorbate molecules shows that the DCE and TCE molecules adsorb best in the MFI straight channel whilst DCM is favoured in the MOR framework. The cluster calculations indicate that adsorption of the sorbate molecule is the strongest where it fits best into the zeolite channel or void shape and therefore, has an optimal interaction with the zeolite wall.

For all cases the geometries indicate that the sorbate molecules prefer to have as little interaction as possible with the zeolite wall. However, the zeolite wall is not allowed to relax and this may affect the position of the sorbate molecule within the zeolite cluster.

### 3.5.5 Comparison with literature values

A comparison of the values obtained for the adsorption energies, using both the Monte Carlo docking and cluster method, with literature values, obtained by calorimetry is presented in table 3.5. The data is for FAU and MFI frameworks only; experimental data is not available for MOR.

| System | Monte Carlo Docking Results $E_{ads}$ (kJ/mol) | Cluster Results $E_{ads}$ (kJ/mol) | Literature Values (kJ/mol) |
|---|---|---|---|
| FAU_DCM | -58.6 | -12.74 | -41.0 [13] |
| FAU_DCE | -56.1 | -17.12 | -47.0 [13] |
| FAU_TCE | -63.1 | -15.17 | -48.0 [13] |
| MFI_DCM | -25.1 | -19.02 | Not available |
| MFI_DCE | -31.0 | -23.09 | -55.0 [14] |
| MFI_TCE | -25.1 | -28.37 | -51.0 [15] |

**Table 3.5:** Comparison of docking and cluster results with experimental values.

This comparison, as expected, does not show a perfect match between our calculated and experimental data. The values obtained using the cluster method are approximately 30kJ/mol lower than experimental values. This indicates that the neglect of the long-range effects of the zeolite crystal are significant. It also highlights the poor representation of dispersion forces within the DFT method. The docking results for FAU are approximately 15kJ/mol higher than the literature values. This may be due to the fact that during the docking simulation temperature effects are neglected and this may have resulted in sites being sampled that are lower in energy than in reality. For MFI the docking energies are approximately 25kJ/mol lower than experimental values. These are usual shortcomings of QM and docking methods, but nevertheless, both the methods proved highly valuable in determining the position and alignment of the chlorinated hydrocarbons within a zeolite framework.

## 3.6 Aluminosilicate Cluster methodology

For the aluminosilicate clusters a slightly different approach was taken. The introduction of a Brønsted acid site in the framework means that there is a specific site for the sorbate to interact with. As such the Monte Carlo Docking approach was not employed to find favourable binding sites. Thus the initial step for the aluminosilicate clusters was to introduce aluminium into the siliceous framework. In each framework structure the main channel/void sections were selected where the chlorinated hydrocarbon would be expected to adsorb (e.g. in MOR the 12-membered ring). Aluminium atoms were distributed in this selected area in such a way that the subsequently extracted clusters represent the experimental Si/Al ratio shown in table 3.6.

| Framework Structure | Experimental Si/Al ratio | Cluster Si/Al ratio |
|:---:|:---:|:---:|
| MOR | 5.2  [16,17] | 4 |
| MFI | 27.1  [16-18] | 27 |
| FAU | 2.6  [17-19] | 2 |

**Table 3.6:** Experimental Si/Al ratio and the Si/Al ratios used in our cluster calculations.

The calculation of the Al and Brønsted protons was determined by a systematic minimisation protocol as follows [20]: an aluminium atom was placed into a unit cell of each framework at each of the crystallographic positions in turn. A Brønsted proton was then placed on all the surrounding oxygen atoms in turn and the systems minimised to determine the most stable site. The thermodynamically most stable acid site that was orientated towards the open pore, and thus accessible to the sorbate molecules was then selected. In order to maintain charge neutrality, acid protons were then placed on the oxygen atoms adjacent to the remaining aluminium atoms and these were orientated away from the ring to avoid simultaneous interaction of the adsorbate with more than one acid site. In distributing the remaining aluminium atoms Löwenstein's rule was obeyed. The unit cell was then optimised using GULP [21] to obtain the correct geometries. We used the potential developed by Schröder *et al.* [22-23, 29]. Details of the parameters used are shown in appendix 1.

A cluster was then extracted from the lattice and an attempt was made to retain as much of the pore shape around the acid site as possible. The clusters for the aluminosilicate clusters are slightly larger than the siliceous ones, with between 157 and 256 atoms per cluster. The interaction of interest is that of the sorbate molecule with the thermodynamically most stable acid site. Hence each sorbate molecule was placed in the cluster approximately 3Å away from the acid site. The most stable acid site, its neighbouring $SiO_4$ and $AlO_4$ unit and the sorbate molecule, illustrated in figure 3.10, were optimised, using the PW91 functional and DNP basis set as for the siliceous clusters. In contrast to the silecious clusters, the clusters being modelled are identical for all the adsorbates.
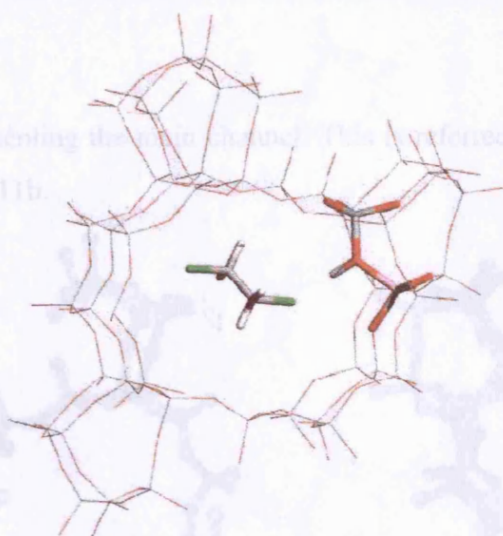
**Figure 3.10:** An example of an aluminosilicate cluster. The cylinders in the cluster represent the regions that are relaxed with respect to the framework.

## 3.7 Aluminosilicate results

The results for the aluminosilicate study will be analysed in terms of the strength of the interaction between the chlorine atoms of the adsorbate and the hydrogen atom of the Brønsted acid site. This will enable us to ascertain whether this is the main contributing factor to adsorption energy. In addition the results will be analysed in terms of the geometry and orientation of the sorbate molecules with respect to the acid site and the zeolite framework.

## 3.7.1 Mordenite Clusters

For the mordenite framework two types of clusters, shown in figure 3.11, were investigated. Firstly a cluster was extracted which contained just the 12-membered ring and the surrounding framework. This is referred to as the ring cluster and is shown in figure 3.11a. The second cluster extracted was larger and contained two 12-membered rings to

form a cluster representing the main channel. This is referred to as the channel cluster and is shown in figure 3.11b.



a          b
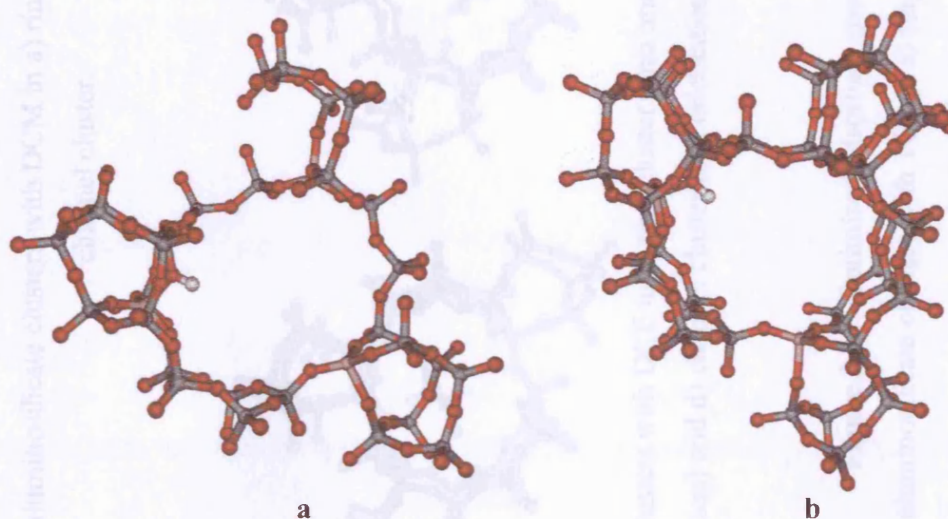
**Figure 3.11:** The MOR Ring (a) and MOR Channel (b) clusters.
The results for each are now presented in tables 3.7 and 3.8.

| | DCE-A | DCE-S | DCM | TCE |
|---|---|---|---|---|
| r(C-Cl) (Å) | 1.827 | 1.819 | 1.797 | 1.721 |
| r(O-H) (Å) | 0.999 | 0.995 | 0.983 | 0.977 |
| r(Cl..H) (Å) | 2.112 | 2.182 | 2.588 | 3.187 |
| $\theta$ (Cl..O-H) (°) | 164.6 | 161.8 | 140.0 | 127.7 |
| $\theta$ (C-Cl..H) (°) | 112.6 | 114.5 | 102.7 | 63.0 |
| $\theta$ (C-Cl..H-O) (°) | 156.9 | 177.5 | 163.6 | -132.9 |
| $E_{ads}$ (kJ/mol) | -39.45 | -39.68 | -29.52 | -34.31 |
| zeo alone r(O-H) (Å) | 0.976 | | | |

**Table 3.7:** Adsorption energies and geometries of the molecules adsorbed in the MOR ring cluster.

| | DCE-A | DCE-S | DCM | TCE |
|---|---|---|---|---|
| r(C-Cl) (Å) | 1.831 | 1.825 | 1.814 | 1.73 |
| r(O-H) (Å) | 0.999 | 1.000 | 0.990 | 0.984 |
| r(Cl..H) (Å) | 2.108 | 2.065 | 2.207 | 2.476 |
| $\theta$ (Cl..O-H) (°) | 172.9 | 168.1 | 163.4 | 153.9 |
| $\theta$ (C-Cl..H) (°) | 107.5 | 103.2 | 123.0 | 116.8 |
| $\theta$ (C-Cl..H-O) (°) | -162.1 | 176.6 | 161.2 | 164.9 |
| $E_{ads}$ (kJ/mol) | -40.66 | -40.99 | -28.45 | -30.3 |
| zeo alone r(O-H) (Å) | 0.976 | | | |

**Table 3.8:** Adsorption energies and geometries of the molecules adsorbed in the MOR channel cluster.
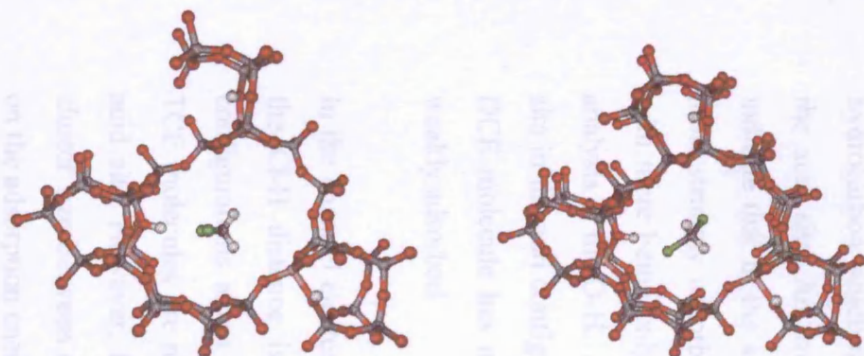
**Figure 3.12:** Optimised adsorbate geometries for MOR aluminosilicate clusters with DCM in a) ring cluster and b) channel cluster.
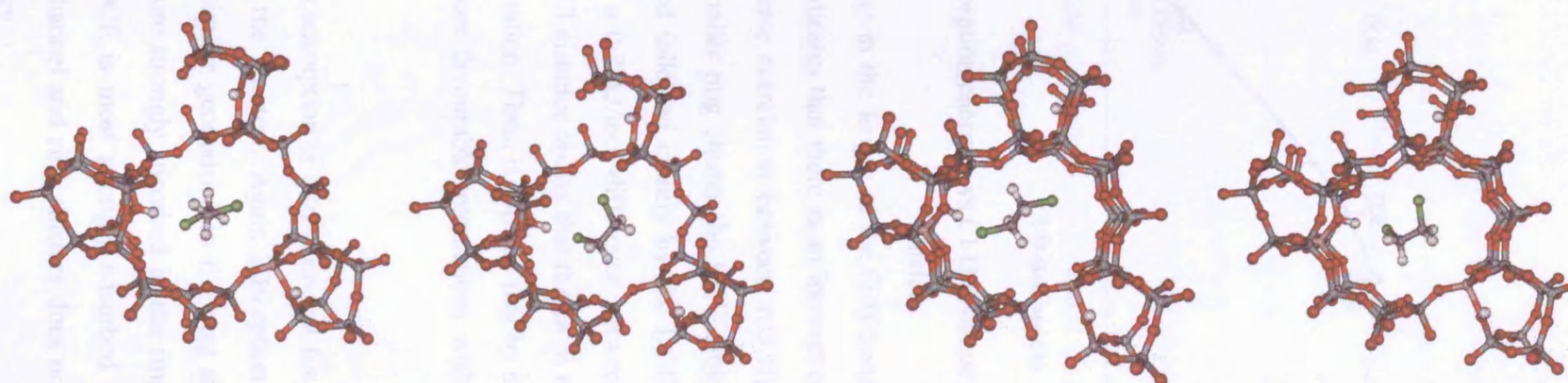
**Figure 3.13:** Optimised adsorbate geometries for MOR aluminosilicate clusters with DCE in a) ring cluster (anti orientation) and b) channel cluster (syn orientation) c) ring cluster (anti orientation) and d) channel cluster (syn orientation).
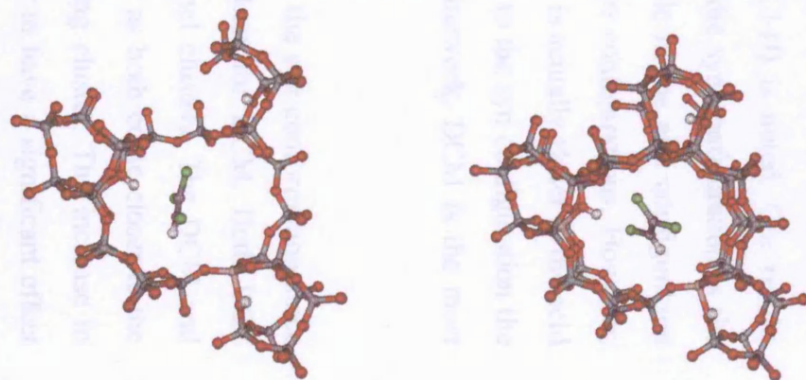
**Figure 3.14:** Optimised adsorbate geometries for MOR aluminosilicate clusters with TCE in a) ring cluster and b) channel cluster.
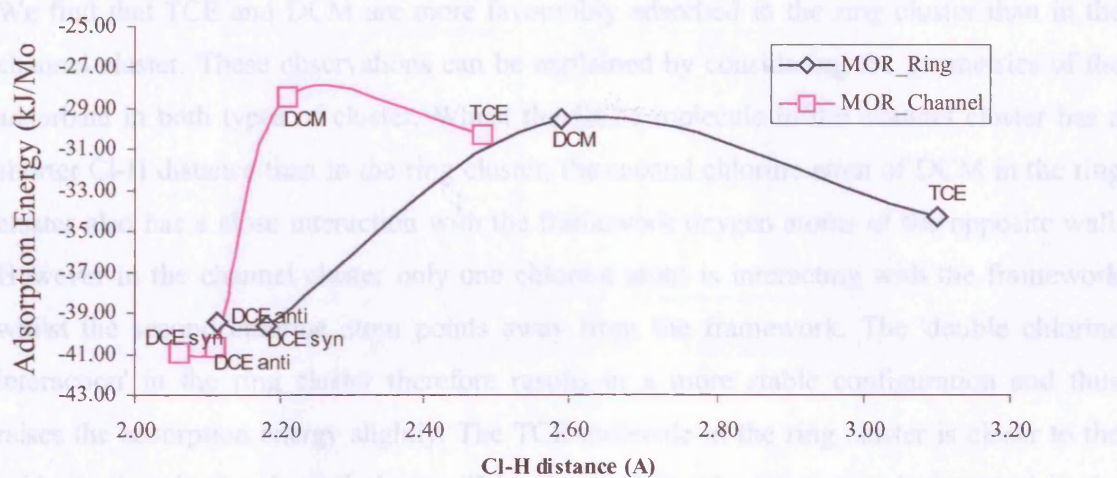
**Figure 3.15:** Adsorption energies vs Cl-H distance for adsorbed molecules in MOR clusters.

We observe an increase in the length of the O-H bond upon adsorption of the chlorinated hydrocarbon which indicates that there is an interaction between the sorbate molecule and the acid site. An inverse correlation between r(O-H) and r(Cl-H) is noted. Our results indicate that in the smaller ring cluster the DCE molecule in the syn configuration is the most strongly adsorbed followed closely by the DCE molecule in the anti configuration with there being only a 0.23kJ/mol difference between the two configurations. However, analysis of the O-H…Cl distance shows that the DCE molecule is actually closer to the acid site in the anti configuration. Thus, it appears that by changing to the syn configuration the DCE molecule has more favourable interactions with the framework. DCM is the most weakly adsorbed.

In the channel clusters adsorption is also strongest for DCE in the syn conformation since the Cl-H distance is the shortest. Again adsorption is weakest for DCM. Both DCE configurations adopt similar geometries in the ring and channel clusters. The DCM and TCE molecules are more strongly adsorbed in the ring cluster as both come closer to the acid site. However, DCE is most strongly adsorbed in the ring cluster. The increase in cluster size between channel and ring clusters does not appear to have a significant effect on the adsorption energy.

91

We find that TCE and DCM are more favourably adsorbed in the ring cluster than in the channel cluster. These observations can be explained by considering the geometries of the adsorbate in both types of cluster. Whilst the DCM molecule in the channel cluster has a shorter Cl-H distance than in the ring cluster, the second chlorine atom of DCM in the ring cluster also has a close interaction with the framework oxygen atoms of the opposite wall. However in the channel cluster only one chlorine atom is interacting with the framework whilst the second chlorine atom points away from the framework. The 'double chlorine interaction' in the ring cluster therefore results in a more stable configuration and thus raises the adsorption energy slightly. The TCE molecule in the ring cluster is closer to the acid site than in the channel cluster. This may explain why adsorption is favoured in the ring cluster over the channel.

## 3.7.2 Faujasite Clusters

For faujasite one type of cluster representing the 12-ring supercage was modelled. This is illustrated in figure 3.16 below. The geometries of the sorbate molecules and the corresponding energies as summarised in table 3.9 and figures 3.17 a-c and 3.18.
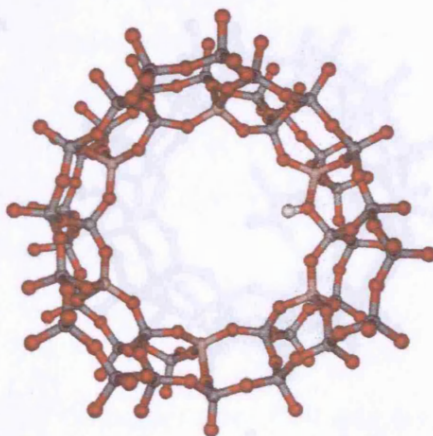


**Figure 3.16:** FAU aluminosilicate cluster.

|  | DCE | DCM | TCE |
|---|---|---|---|
| r(C-Cl) (Å) | 1.830 | 1.807 | 1.756 |
| r(O-H) (Å) | 0.990 | 0.983 | 0.987 |
| r(Cl..H) (Å) | 2.335 | 2.581 | 2.339 |
| θ (Cl..O-H)(°) | 161.7 | 157.8 | 163.8 |
| θ (C-Cl..H) (°) | 119.2 | 125.6 | 98.6 |
| θ (C-Cl..H-O) (°) | -169.6 | -162.1 | -161.7 |
| $E_{ads}$ (kJ/mol) | -33.49 | -24.19 | -32.62 |
| Zeo alone r(O-H) (Å) | 0.976 |  |  |

**Table 3.9:** Adsorption energies and geometries of the molecules adsorbed in the FAU cluster.
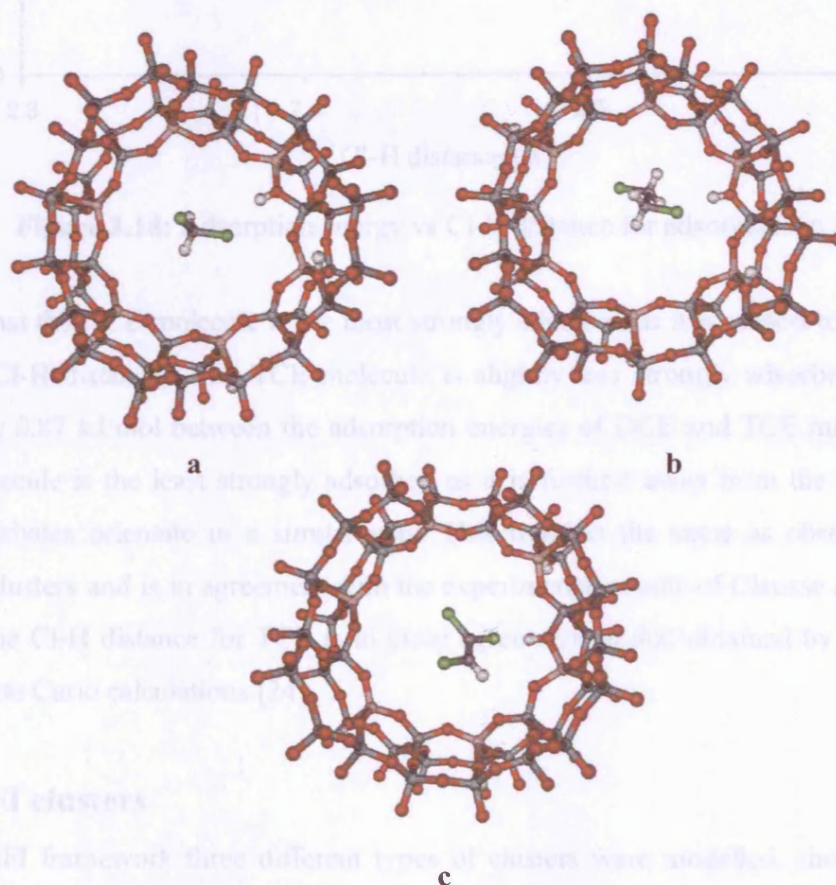


**Figure 3.17:** Optimised adsorbate geometries for FAU aluminosilicate clusters with a) DCM b) DCE and c) TCE adsorbed.
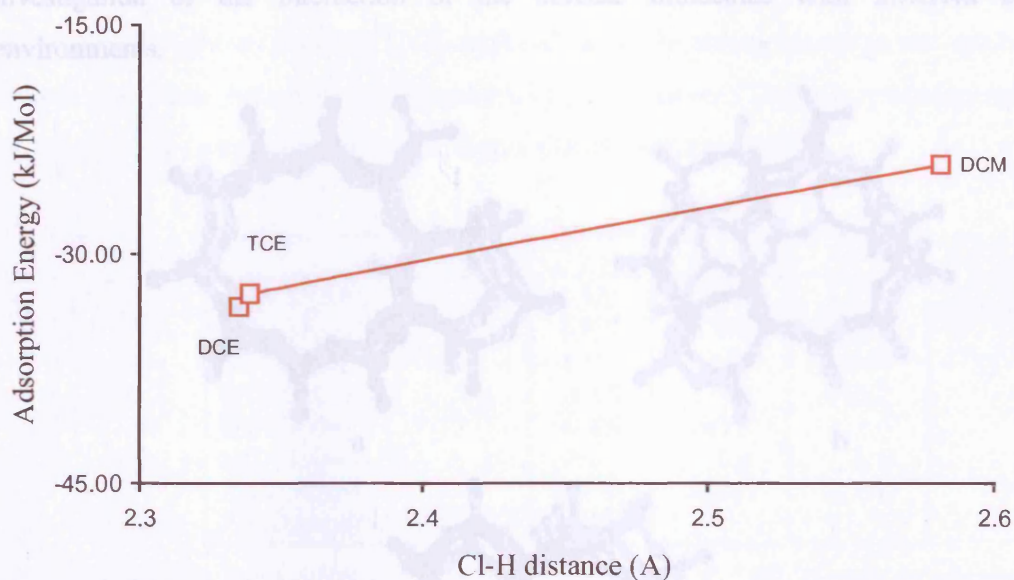
**Figure 3.18:** Adsorption energy vs Cl-H distance for adsorbates in FAU.

We find that the DCE molecule is the most strongly adsorbed as it is closest to the acid site (shortest Cl-H distance). The TCE molecule is slightly less strongly adsorbed with there being only 0.87 kJ/mol between the adsorption energies of DCE and TCE molecules. The DCM molecule is the least strongly adsorbed as it is furthest away from the acid site. All three adsorbates orientate in a similar way. This trend is the same as observed for the siliceous clusters and is in agreement with the experimental results of Clausse *et al.* [13]. In addition the Cl-H distance for TCE is in close agreement to that obtained by Mellot *et al.* using Monte Carlo calculations [24].

### 3.7.3 MFI clusters

For the MFI framework three different types of clusters were modelled, shown in figure 3.19. The first cluster represents the 10-membered ring of the straight channel and is referred to as the straight channel cluster. In addition clusters were also extracted for the intersection between the sinusoidal and straight channels and the sinusoidal channel alone referred to as the intersection and sinusoidal clusters respectively. This allowed an

94

investigation of the interaction of the sorbate molecules with different acid site environments.
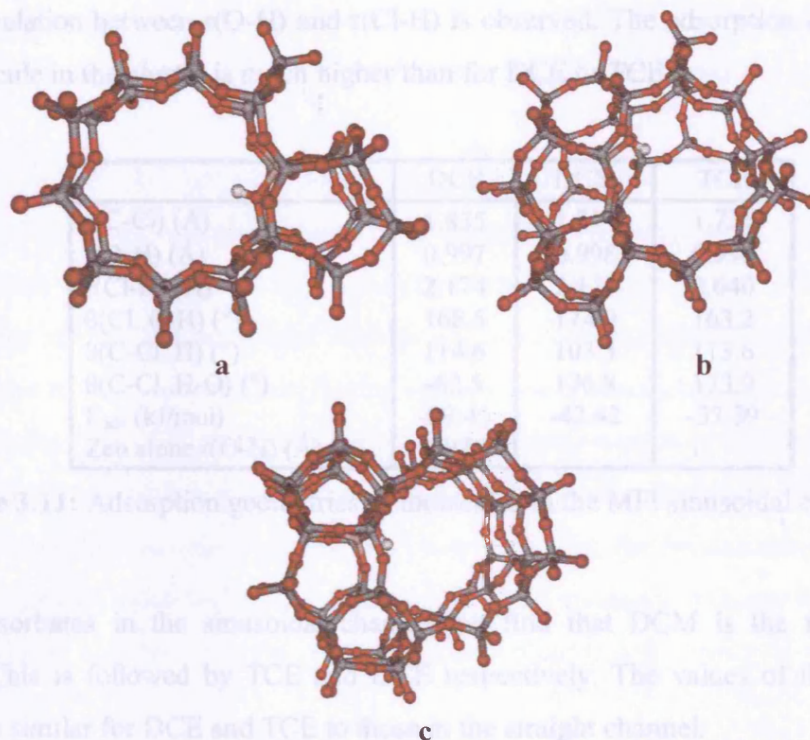


**Figure 3.19:** MFI clusters representing a) straight channel, b) sinusoidal channel and c) intersection clusters.

The adsorption energies and geometries of the sorbate molecules are presented in table 3.10 -3.12.

|  | DCE | DCM | TCE |
|---|---|---|---|
| r(C-Cl)(Å) | 1.859 | 1.852 | 1.739 |
| r(O-H) (Å) | 1.003 | 1.002 | 0.987 |
| r(Cl..H) (Å) | 2.075 | 2.127 | 2.489 |
| θ(Cl..O-H)(°) | 169.8 | 167.8 | 170.6 |
| θ (C-Cl..H) (°) | 102.0 | 101.5 | 119.1 |
| θ (C-Cl..H-O) (°) | 86.2 | 74.1 | 153.9 |
| $E_{ads}$ (kJ/mol) | -36.95 | -63.73 | -37.39 |
| Zeo alone R(O-H) (Å) | 0.977 |  |  |

**Table 3.10:** Adsorption geometries of molecules in the MFI straight channel.

We find that adsorption is strongest for DCM in the straight channel. However, analysis of the geometries shows that the DCE molecule actually comes closer to the acid site. An inverse correlation between r(O-H) and r(Cl-H) is observed. The adsorption energy for the DCM molecule in the cluster is much higher than for DCE or TCE.

| | DCE | DCM | TCE |
|---|---|---|---|
| r(C-Cl) (Å) | 1.835 | 1.814 | 1.726 |
| r(O-H) (Å) | 0.997 | 0.998 | 0.998 |
| r(Cl-H) (Å) | 2.174 | 2.174 | 2.040 |
| θ(Cl..O-H) (°) | 168.5 | 174.0 | 163.2 |
| θ(C-Cl..H) (°) | 114.6 | 103.5 | 113.6 |
| θ(C-Cl..H-O) (°) | -62.5 | 176.8 | 173.9 |
| $E_{ads}$ (kJ/mol) | -29.46 | -42.42 | -37.39 |
| Zeo alone r(O-H) (Å) | 0.976 | | |

**Table 3.11:** Adsorption geometries of molecules in the MFI sinusoidal channel.

For the adsorbates in the sinusoidal channel we find that DCM is the most strongly adsorbed. This is followed by TCE and DCE respectively. The values of the adsorption energies are similar for DCE and TCE to those in the straight channel.

| | DCE | DCM | TCE |
|---|---|---|---|
| r(C-Cl) (Å) | 1.835 | 1.810 | 1.759 |
| r(O-H) (Å) | 0.997 | 0.988 | 0.989 |
| r(Cl-H) (Å) | 2.174 | 2.370 | 2.206 |
| θ (Cl..O-H)(°) | 168.5 | 147.0 | 159.7 |
| θ (C-Cl-H) (°) | 114.6 | 124.2 | 110.5 |
| θ (C-Cl..H-O) (°) | -62.5 | -118.9 | 142.4 |
| $E_{ads}$ (kJ/mol) | -44.04 | -24.59 | -45.89 |
| Zeo alone R(O-H) (Å) | 0.974 | | |

**Table 3.12:** Adsorption geometries of molecules in the MFI intersection.

In the intersection we find that TCE is most strongly adsorbed followed by DCE and DCM. This follows the expected trend. The TCE molecule is the largest of the three adsorbates and would therefore be expected to have optimal interactions with the zeolite framework atoms. The adsorption energies for TCE and DCE are very close, with there being only

1.85 kJ/mol between them. Conversely DCM is the smallest and experiences less interaction with the framework. However, analysis of the geometries shows that DCM comes closest to the acid site followed by TCE and DCE. As for the straight channel clusters, an inverse correlation between r(O-H) and r(Cl-H) is observed.

Overall, the values for the adsorption energy for DCE and TCE are higher in the intersection than in the straight or sinusoidal channels. This may be a reflection of the extent to which the adsorbate is able to interact with the framework. The intersection is larger than the straight and sinusoidal clusters and there are more framework atoms for the chlorine atoms to interact with. The 10-ring of the straight channel has similar dimensions to the molecules. The TCE molecule prefers the intersection as it is the biggest molecule and has to distort to fit into the channels. DCM is the smaller molecule and fits into the channel better. It can therefore optimise its interaction with the framework oxygen atoms and is most strongly adsorbed in the channel. The DCE molecule is larger than the DCM molecule and is able to fit better into the intersection and is therefore most strongly adsorbed there.

## 3.7.4 Testing the model

In order to test whether the distribution of the aluminium atoms around the cluster had a significant effect on the adsorption energies, test calculations were performed on a FAU and MOR_Ring cluster with only one aluminium atom in the framework. In both cases the same starting configuration was used as for the cluster with a higher aluminium content. The results are presented in table 3.13.

| System | Aluminosilicate Results (kJ/mol) | Test Model Results (kJ/mol) |
|---|---|---|
| MOR_DCM | -29.52 | -35.61 |
| FAU_DCM | -24.19 | -30.36 |

Table 3.13 : Comparison of test model results with the original cluster.

It can be seen that increasing the amount of aluminium in the framework has the effect of decreasing the adsorption energy. There is approximately 6kJ/mol difference between the test and original clusters. The geometries of the DCM molecule inside the cluster are shown in table 3.14 along with a comparison with the cluster with a higher aluminium content.

| | MOR Original Cluster Si/Al=5.2 | MOR Test model Si/Al=12 | FAU Original Cluster Si/Al=2.6 | FAU Test model Si/Al=12 |
|---|---|---|---|---|
| r(C-Cl) (Å) | 1.797 | 1.83 | 1.807 | 1.82 |
| r(O-H) (Å) | 0.983 | 0.98 | 0.983 | 0.99 |
| r(Cl-H) (Å) | 2.588 | 2.40 | 2.581 | 2.370 |
| θ(Cl-O-H) (°) | 140.0 | 160.7 | 157.8 | 163.1 |
| θ (C-Cl-H) (°) | 102.7 | 42.0 | 125.6 | 34.3 |
| θ (C-Cl-H-O) (°) | 163.6 | 139.7 | -162.1 | -136.3 |
| $E_{ads}$ (kJ/mol) | -29.52 | -35.61 | -24.19 | -30.36 |

**Table 3.14** : Comparison of adsorption geometries of the test clusters with the original clusters.

The DCM molecule in both the test clusters adopts a slightly different geometry compared to the original clusters. Since the starting configurations were identical the difference can be attributed to the distribution of aluminium atoms in the cluster. There is an approximately 6kJ/mol gain in the adsorption energy between the aluminosilicate clusters and the test models. In the case of the MOR clusters the adsorbate molecule is approximately 0.2Å closer to the acid site in the test model cluster than in the aluminosilicate cluster. Similarly in the case of FAU the adsorbate molecule is 0.6Å closer to the acid site in the test model cluster. This observation may be attributed to the shorter Si-O bond, which may make the acid site more accessible.

### 3.7.5 Aluminosilicate Results – Comparison of framework structures

A summary of the results obtained for the siliceous cluster calculations is shown in figure 3.20 below.



**Figure 3.20:** Adsorption energies for the aluminosilicate clusters.

Our results for the cluster calculations, in general do not follow a simple trend. This indicates that the interaction of the sorbate within the cluster is complex and not simply determined by the interaction of the adsorbate with the acid site, but also by the zeolite topology. The Cl-H interaction energy contributes a large part to the adsorption energy and

therefore how the topology influences approach to the acid site may be more important than the size, shape and number of chlorine atoms in the sorbate molecule.

The cluster calculations indicate that adsorption of DCE and TCE is favoured in the MFI intersection. DCM is the weakest adsorbed in all framework structures except in the case of the cluster representing the MFI straight channel. Adsorption of DCM is favoured in the MOR framework. Overall adsorption is weakest in the FAU framework. As for the siliceous clusters, the calculations on aluminosilicate clusters indicate that adsorption of the sorbate molecule is strongest where it fits best into the zeolite cavity thereby optimising its interaction with the framework oxygen atoms.

## 3.8 Summary

Overall the adsorption energies obtained using the cluster method are significantly lower than the experimental values in the literature. A significant limitation of the cluster approach is the neglect of the long-range electrostatic effects of the zeolite crystal. Mellot and co-workers estimate that the long-range electrostatic effect contributes approximately 38% of the adsorption energy for chloroform adsorption in NaY [25]. The cluster approach, whilst being computationally efficient in comparison to modelling the zeolite unit cell, has several disadvantages. The most significant of these is the absence of the long-range electrostatic forces caused by the Madelung potential of the zeolite. These electrostatic forces are particularly important for the stabilisation of charged species in the zeolite channels or cavities [26]. Inclusion of these forces is therefore important when modelling reaction mechanisms since they may proceed via carbocation intermediates. Another problem may arise due to the dangling bonds at the edges of the clusters, which need to be saturated with hydrogen atoms to preserve charge neutrality. This may lead to boundary effects since the atoms that are in the cluster are in a different chemical environment to those in the zeolite crystal. This can result in the atoms in the cluster behaving differently towards an adsorbate than the corresponding atoms in the zeolite crystal. The size of the cluster also has an effect on the geometry of the adsorbate. Due to their computational expense, cluster calculations have traditionally involved a limited number of atoms. This

usually means that the interaction of the adsorbate with the opposite wall is neglected. However improvements in numerical algorithms and computer hardware have made quantum mechanical calculations on practical systems, such as a periodic unit cell, more feasible. This can be more realistic since the long-range electrostatic forces are accounted for and the boundary effect are also avoided. In many cases periodic DFT calculations have a lower computational cost compared to large clusters which attempt to account for the long-range electrostatics [26-28]. However, due to limitations in current computing technology such calculations are limited to zeolites with highly symmetric unit cells or those that have a small number of atoms per unit cell. A compromise may be reached by employing an embedded method which combines the computational efficiency of the cluster method with the more realistic model of the zeolite crystal by inclusion of long range electrostatics. We have attempted a periodic DFT calculation for the sorbates in mordenite unit cell and the QMPot embedded approach is also utilised. These results are presented in the proceeding chapter and a comparison is made to the cluster calculations presented in this chapter.

A further limitation of this study may be of the DFT method itself. The PW91 functional employed is a pure density functional and as such does not account for dispersive interactions, which in polar adsorbates such as the ones being modelled, would be expected to contribute a sizable amount to the adsorption energy.

The cluster calculations in this chapter have detailed the alignment and positions of the adsorbate molecules within the zeolite framework. The siliceous study clearly demonstrates that the molecules arrange in such a way that they experience optimal interaction with the zeolite wall. Unlike the siliceous clusters, the adsorbate molecules within the aluminosilicate clusters have a specific region (the acid site) to interact with. The results of the aluminosilicate study clearly indicate that the Cl-H interaction contributes a large part to the adsorption energy. However, the rest of the molecule still tries to get in a position where it experiences optimal interaction with the framework. The extent to which these two factors contribute to the adsorption energy cannot be separated.

The next step in this study is therefore to try to account for some of the limitations of the cluster method. The following chapter describes some results of cluster calculations using a hybrid DFT functional which may offer an improvement on pure density functionals. The thesis then moves on to describe two methods used to try and include the long-range effects of the zeolite crystal namely periodic DFT and an embedded QM/MM approach.

# References

(1)    van Santen, R. A.; Rozanska, X. Theory of zeolite catalysis. In *Molecular Modelling and Theory in Chemical Engineering*; Chakraborty, A., Ed.; Academic Press, 2001; pp 399.

(2)    Lercher, J. A.; van Santen, R. A.; Vinek, H. *Catalysis Letters* **1994**, *27*, 91.

(3)    Krossner, M.; Sauer, J. *J. Phys. Chem B* **1996**, *100*, 6199

(4)    Boronat, M.; Zichovich-Wilson, C. M.; Corma, A.; Viruela, P. *Phys. Chem. Chem. Phys.* **1998**, *4*, 537

(5)    Zygmunt, S. A.; Curtiss, L. A.; Iton, L. E.; Erhardt, M. K. *J. Phys. Chem* **1996**, *100*, 6663

(6)    Svelle, S.; Kolboe, S.; Swang, O. *J. Phys. Chem.* **2004**, *108*, 2953.

(7)    Biosym/MSI *Solids Docking Manual* San Diego, October 1995.

(8)    Freeman, C. M.; Catlow, C. R. A.; Thomas, J. M. *Chem. Phys. Letters* **1991**, *186*, 137.

(9)    Perdew, J. P.; Burke, K.; Ernzerhof, M. *Phys. Rev. Letts* **1996**, *77*, 3865.

(10)   Perdew, J. P.; Chevary, J. A.; Vosko, S. H.; Jackson, K. A.; Pederson, M. R.; Singh, D. J.; Fiolhais, C. *Physical Review B* **1992**, *46*, 6671

(11)   Accelrys Inc *DMol³ program*, 1999.

(12)   Brändle, M.; Sauer, J. *J. Mol. Catal. A-Chem.* **1997**, *119*, 19

(13)   Clausse, B.; Garrot, B.; Cornier, C.; Paulin, C.; Simonot-Grange, M. H.; Boutros, F. *Micropor. Mesopor. Mater.* **1998**, *25*, 169.

(14)   Helene, M.; Grange, S.; Garrot, B. *Langmuir* **2001**, *17*, 8188.

(15)   Bouvier, F.; Weber, G. *J. Thermal Anal* **1998**, *54*, 881.

(16)   López-Fonseca, R.; Gutiérrez-Ortiz, J. I.; Ayastui, J. L.; Gutiérrez-Ortiz, M. A.; González-Velasco, J. R. *Appl. Catal. B: Environmental* **2003**, *45*, 13

(17)   López-Fonseca, R.; Aranzabal, A.; Stelenpohl, P.; Gutiérrez-Ortiz, J. I.; González-Velasco, J. R. *Catal. Today* **2000**, *62*, 367

(18)   González-Velasco, J. R.; López-Fonseca, R.; Aranzabal, A.; Gutiérrez-Ortiz, J. I.; Steltenpohl, P. *Appl. Catal. B-Environmental* **2000**, *24*, 233.

(19) López-Fonseca, R.; Gutiérrez-Ortiz, J. I.; Gutiérrez-Ortiz, M. A.; González-Velasco, J. R. *J. Catal* **2002**, *209*, 145

(20) Gray, A. E.; Foster, M. D.; Lewis, D. W. *Unpublished Results*.

(21) Gale, J. D. *J. Chem. Soc - Faraday Transactions* **1997**, *93*, 629.

(22) Sanders, M. J.; Leslie, M.; Catlow, C. R. A. *J. Chem. Soc - Chem. Comm* **1984**, *19*, 1271.

(23) Saul, P.; Catlow, C. R. A.; Kendrick, J. *Philos. Mag B* **1985**, *51*, 107.

(24) Mellot, C. F.; Cheetham, A. K.; S.Harms; S.Savitz; R.J.Gorte; A.L.Myers. *Langmuir* **1998**, *14*, 6728.

(25) Mellot, C. F.; Davidson, A. M.; Eckert, J.; Cheetham, A. K. *J. Phys. Chem B* **1998**, *102*, 2530

(26) van Santen, R. A. *Catal. Today* **1999**, *50*, 511.

(27) Boronat, M.; Zicovich-Wilson, C. M.; Viruela, P.; Corma, A. *Chem. Eur. J.* **2001**, *7*, 1295.

(28) Rozanska, X.; van Santen, R. A.; Hutschka, F. *J. Phys. Chem.* **2002**, *106*, 4652.

(29) Schroder K P, Sauer J, Leslie M, Catlow C R A and Thomas J M **1992** *Chem. Phys. Lett.* 188, 320

# Chapter Four: Extending the cluster study

## 4.1 Introduction

The previous chapter focused on using the cluster approach to model the adsorption of DCM, DCE and TCE in MOR, MFI and FAU frameworks. Our results showed that the energies obtained using this method are significantly lower than the experimental values. This difference in energies was attributed to one or more of the following factors. Firstly, the nature of the cluster method neglects the long-range electrostatic effects of the zeolite crystal. Further, the hydrogen bonds used to saturate the cluster may lead to boundary effects whereby the atoms in the cluster may behave differently towards the adsorbate compared to the bulk crystal. Another possible reason for the large difference between the simulated and experimental values may be due to limitations in the DFT method itself since the method is unable to simulate dispersion. In highly polar systems, such as those being modelled, the dispersive interactions are thought to contribute significantly to the adsorption energy.

## 4.1.1 Overview of this work

The work in this chapter attempts to overcome some of the limitations of the cluster method outlined above and at the end of the previous chapter. The first section describes the results of some cluster calculations using a hybrid functional as opposed to a pure density functional used in chapter 3. The next section describes the results of a periodic DFT study of DCM, DCE and TCE adsorbed in the MOR framework and compares the results with the cluster study in chapter 3. Finally, results of a hybrid QM/MM approach using the QMPot scheme are presented.

## 4.2 Hybrid Functional Cluster Calculations

As described in the previous chapter, one of the problems with the PW91 functional utilised in the cluster calculations is that, as a pure density functional, it makes the energy a

function entirely of the local density and/or density gradient. This means that it is incapable of describing London dispersion forces, which arise entirely from electron correlation at 'long-range'. Thus the energy calculated using the pure density functional is purely repulsive. Adding some Hartree-Fock exchange to the DFT functional may alleviate this problem somewhat, although not entirely, since the Hartree-Fock level of theory does not account for opposite spin electron correlation [1]. Nevertheless hybrid DFT methods have been shown to give some improvement over pure DFT functionals and thus we attempt to repeat some of the cluster calculations using a hybrid functional.

## 4.2.1 Hybrid Functional Calculations - Computational Details

The series of siliceous FAU clusters modelled in the previous chapter were taken and optimised using a hybrid functional. This allows direct comparison with the results obtained using the pure density functional. The calculations were performed using the Gaussian03 code [2], the B3LYP functional and the 6-31G(d,p) basis set.

## 4.2.2 Hybrid Functional Cluster Results

The results of the calculations performed using the hybrid functional and a comparison with pure DFT results detailed in the previous chapter are presented in table 4.1 below:

| System | Pure DFT functional $E_{ads}$ (kJ/mol) | Hybrid functional $E_{ads}$ (kJ/mol) | Experimental results $E_{ads}$ (kJ/mol) |
|---|---|---|---|
| FAU_DCM | -12.74 | -19.07 | -41.0 [3] |
| FAU_DCE | -17.12 | -11.93 | -47.0 [3] |
| FAU_TCE | -15.17 | -3.47 | -48.0 [3] |

**Table 4.1**: Free cluster results using a hybrid functional.

The hybrid functionals do not offer an improvement over the pure density functional. In the case of DCE and DCM the values of the adsorption energies are actually lower than

predicted using the cluster method. However, it is important to note that although the 6-31g(d,p) and DNP basis sets are comparable they are different in nature. The 6-31g(d,p) basis set is an analytical one based on Gaussian type functions. By comparison the DNP basis set within DMol³ contains numerical basis functions. Thus to some extent the difference between the results obtained can be attributed to the differing nature of basis functions employed and it is more useful to compare the individual set of results to the experimental values rather than to each other. The optimised geometries are presented in figures 4.1-4.3 along with a comparison with the DMol³ optimised clusters discussed in chapter 3.
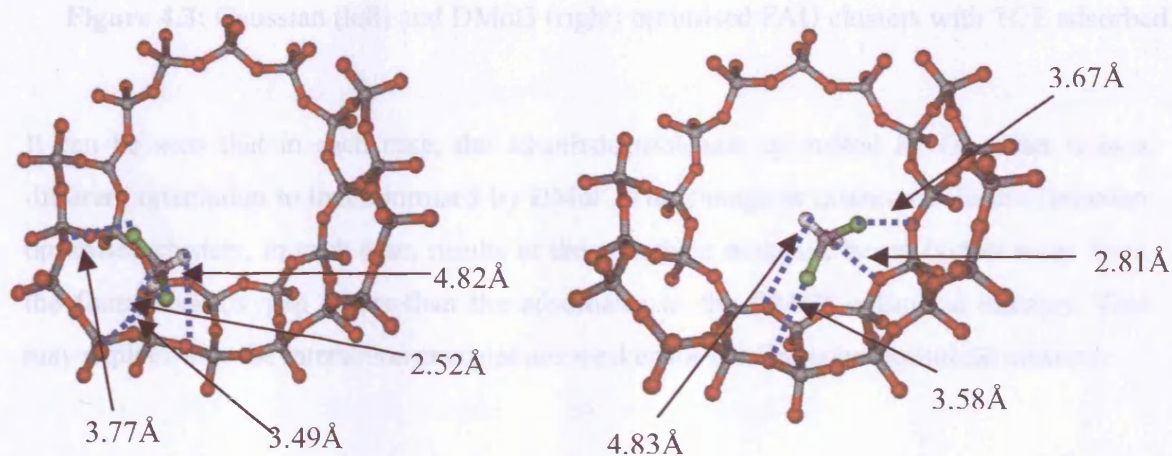


**Figure 4.1:** Gaussian (left) and DMol3³ (right) optimised FAU clusters with DCM adsorbed.
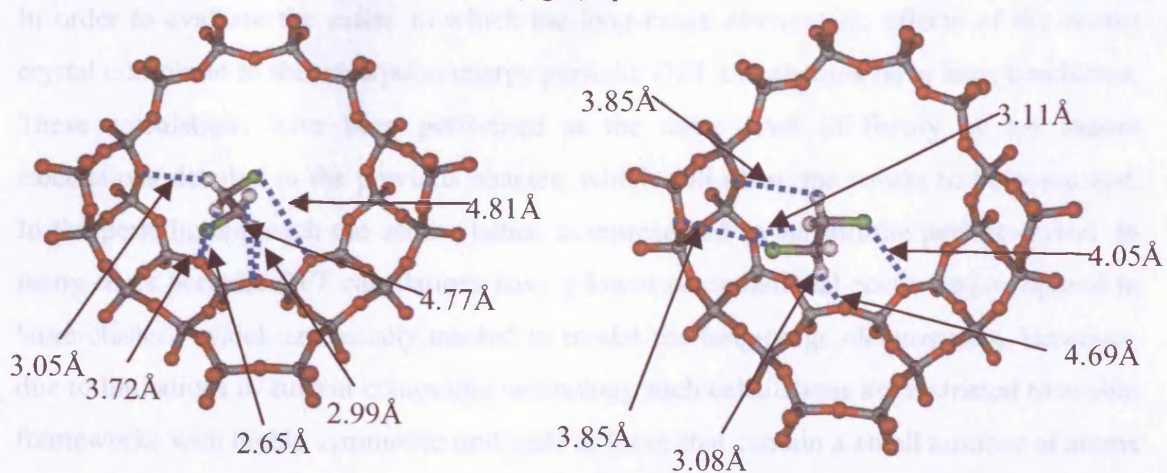


**Figure 4.2:** Gaussian (left) and DMol3³ (right) optimised FAU clusters with DCE adsorbed.

107
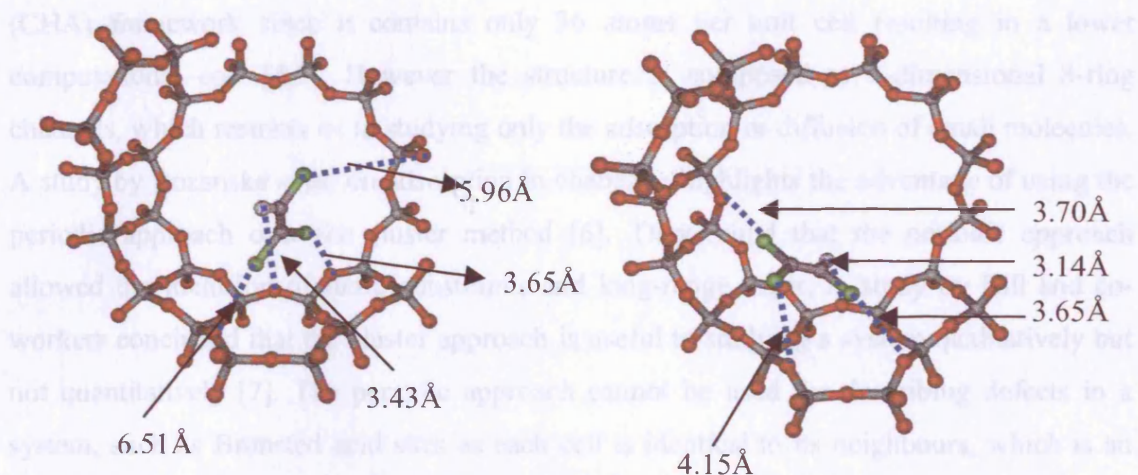
**Figure 4.3:** Gaussian (left) and DMol3 (right) optimised FAU clusters with TCE adsorbed.

It can be seen that in each case, the adsorbate molecule optimised by Gaussian is in a different orientation to that optimised by DMol$^3$. The change in orientation in the Gaussian optimised clusters, in each case, results in the adsorbate molecule being further away from the framework oxygen atoms than the adsorbates in the DMol$^3$ optimised clusters. This may explain why the interaction energies are weaker for the Gaussian optimised clusters.

## 4.3 Periodic DFT Calculations

In order to evaluate the extent to which the long-range electrostatic effects of the zeolite crystal contribute to the adsorption energy periodic DFT calculations have been conducted. These calculations have been performed at the same level of theory as the cluster calculations detailed in the previous chapter, which will allow the results to be compared. In the periodic approach the zeolite lattice is represented by an infinite perfect crystal. In many cases periodic DFT calculations have a lower computational cost when compared to large clusters, which are usually needed to model the long-range electrostatics. However, due to limitations in current computing technology such calculations are restricted to zeolite frameworks with highly symmetric unit cells or those that contain a small number of atoms per unit cell. As such, previous studies have mainly focussed on modelling the chabazite

(CHA) framework since it contains only 36 atoms per unit cell resulting in a lower computational cost [4,5]. However the structure is composed of 3-dimensional 8-ring channels, which restricts us to studying only the adsorption or diffusion of small molecules. A study by Rozanska *et al.* on adsorption in chabazite highlights the advantage of using the periodic approach over the cluster method [6]. They found that the periodic approach allowed the inclusion of steric constraints and long-range order. A study by Hill and co-workers concluded that the cluster approach is useful to studying a system qualitatively but not quantitatively [7]. The periodic approach cannot be used for describing defects in a system, such as Brønsted acid sites as each cell is identical to its neighbours, which is an unrealistic scenario.

In this section of the study we have chosen to model the MOR framework, which contains 144 atoms per unit cell. This system is large enough to accommodate the sorbate molecule and the periodicity of the unit cell does not cause sorbent molecules to be too close to one another. However, to date there have been no experimental studies on the adsorption of DCM, DCE or TCE in MOR to compare with the results obtained. The aim therefore is to ascertain whether the adsorption energies obtained using the periodic approach are closer to the experimental values than those obtained using the cluster method.

## 4.3.1 Periodic DFT - Computational Details

Periodic DFT calculations, using the DMol$^3$ code [8], were performed on a single molecule of DCM, DCE and TCE in the MOR framework. As for the cluster calculations, described in the previous chapter, the starting configurations were taken from the results of the Monte Carlo docking study. Thus the starting configurations for the periodic system and clusters are identical. The unit cells were modelled using the Gradient Generalised Approximation [9], with a PW91 functional to account for exchange and correlation and a DNP basis set. This is an all-electron basis set composed of two numerical functions per valence orbital, enhanced with a polarisation function. The framework and adsorbate molecule atoms were allowed to relax during the simulation.

## 4.3.2 Periodic DFT Results

The results for the Periodic DFT calculations are presented in table 4.2 below:

| System | Periodic Study $E_{ads}$ (kJ/mol) | Cluster Study $E_{ads}$ (kJ/mol) |
|--------|--------|--------|
| MOR_DCM | -16.14 | -19.98 |
| MOR_DCE | -21.37 | -20.12 |
| MOR_TCE | -20.59 | -23.89 |

**Table 4.2:** Periodic DFT approach for adsorbate molecules in the MOR framework.

The results show that DCE is the most strongly adsorbed, followed by TCE and DCM respectively. This trend differs from that obtained using the cluster method which shows that TCE is the most strongly adsorbed followed by DCE and DCM.

The adsorption energies from the periodic calculations for DCM and TCE are even lower in magnitude than those of the cluster study and slightly higher for DCE. The higher values of the adsorption energy for the cluster results compared to the periodic indicate that the clusters are stabilised by the terminating O-H groups. These results seem to indicate that the low values of the adsorption compared to experimental values may not just be attributed to the nature of the cluster method, but may also be a limitation of DFT itself since dispersive interactions are not accounted for in the method.

The optimised geometries at the end of the periodic DFT calculation are presented in figure 4.4.
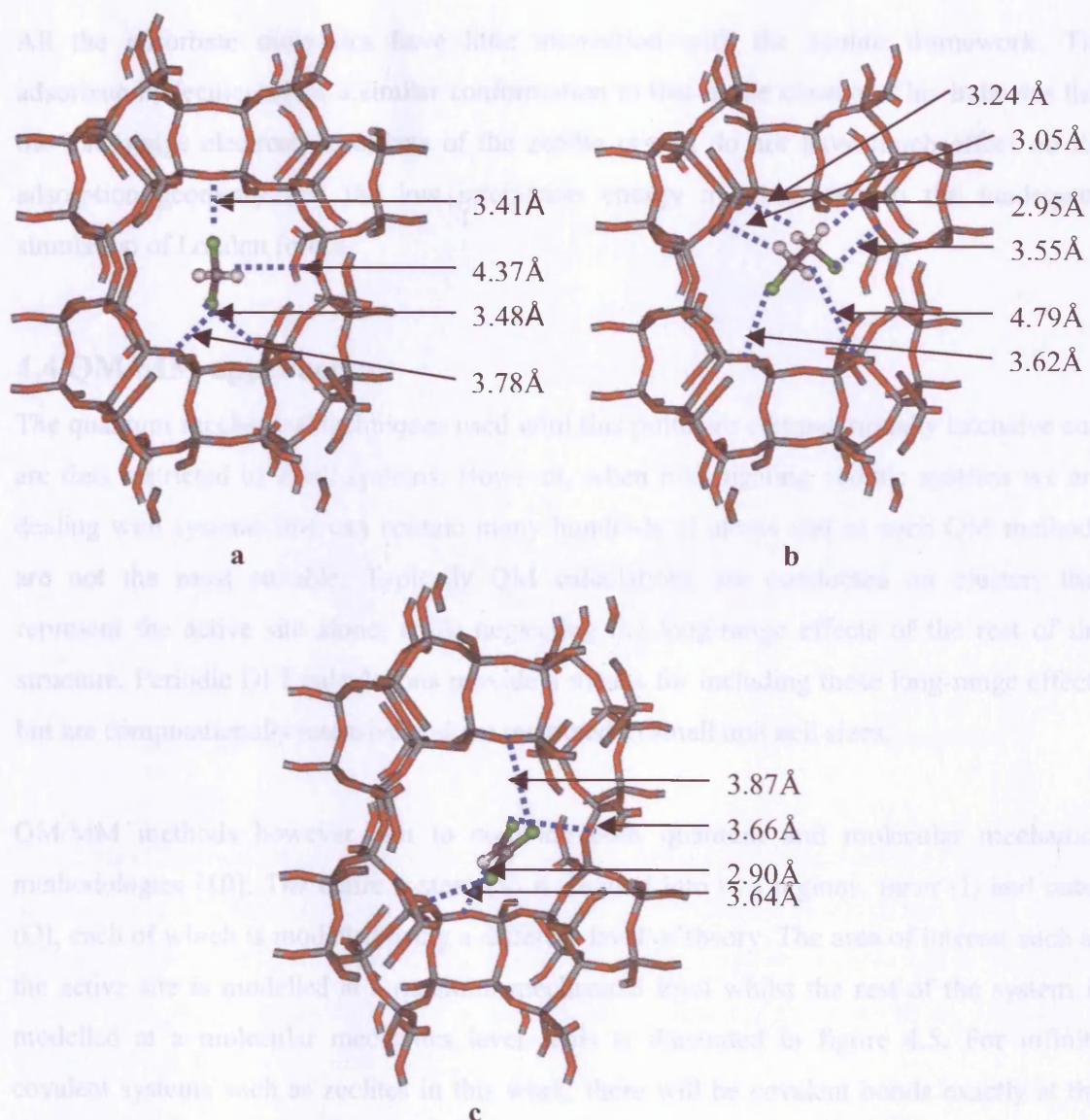
**Figure 4.4:** Positions and orientations of adsorbates in the MOR framework after optimisation a) DCM b) DCE and c) TCE.

All the adsorbate molecules have little interaction with the zeolite framework. The adsorbate molecules adopt a similar conformation to that in the clusters. This indicates that the long-range electrostatic effects of the zeolite crystal do not have much effect on the adsorption geometry and the low interaction energy must be due to the inadequate simulation of London forces.

## 4.4 QM/MM approaches

The quantum mechanical techniques used until this point are computationally intensive and are thus restricted to small systems. However, when investigating zeolitic systems we are dealing with systems that can contain many hundreds of atoms and as such QM methods are not the most suitable. Typically QM calculations are conducted on clusters that represent the active site alone, while neglecting the long-range effects of the rest of the structure. Periodic DFT calculations provide a means for including these long-range effects but are computationally intensive and are restricted to small unit cell sizes.

QM/MM methods however aim to combine both quantum and molecular mechanics methodologies [10]. The entire system (S) is divided into two regions, inner (I) and outer (O), each of which is modelled using a different level of theory. The area of interest such as the active site is modelled at a quantum mechanical level whilst the rest of the system is modelled at a molecular mechanics level. This is illustrated in figure 4.5. For infinite covalent systems such as zeolites in this work, there will be covalent bonds exactly at the boundary between the QM and MM region, which will not fall into either region. Thus, dangling bonds are artificially created, and the atoms in this boundary region must be described in an appropriate way. Many embedding schemes overcome this problem by placing a link atom, usually hydrogen, at a specified distance along the bond between the QM and MM regions. The inner part and the link atoms form the cluster (C) and are treated at QM level. The link atoms are invisible to the MM part of the system. The QMPot approach [11,12] utilized in this study is a mechanical embedding scheme in which the QM calculation is performed as an isolated cluster and the electrostatic interaction between the

QM and MM regions is performed by the MM code. The QMPot code currently has a range of interfaces, including GULP [13] and Discover [14] for the MM region and Gaussian [2], Turbomole [15] and DMol$^3$ [8] for the QM region.
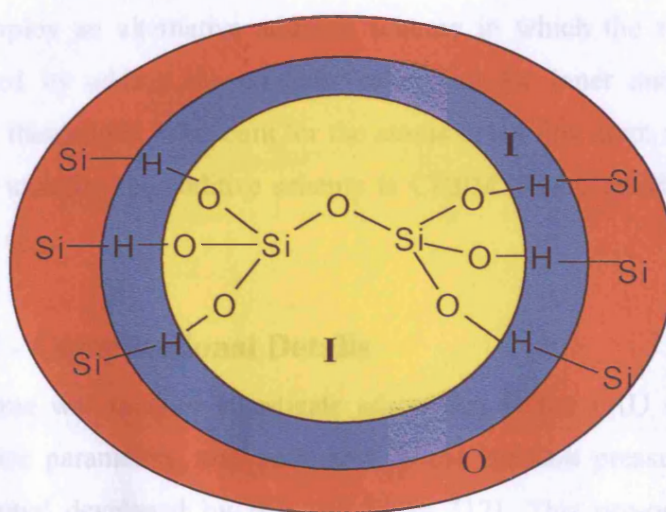


**Figure 4.5:** The definition of inner (I), outer (O) and link atom (L) regions.

The QMPot method employs periodic boundary conditions and polarisation is treated using the shell model. The QMPot approach uses a subtraction scheme in which the entire system is treated at MM level, the inner region at QM level and a separate calculation is conducted for the inner region at the MM level to eliminate the effects of the link atoms. The energy of the entire system is calculated as:

$$E_{QMPot}(S) = E_{QM}(C) + E_{Pot}(S) - E_{Pot}(C) \qquad 4.1$$

where S denotes the entire system and C the cluster. This indicates that the energy of the system is not only dependent on the positions of the real atoms but also on those of the link atoms. The energy contribution of the link atoms is given by the following expression:

$$\Delta = -E_{QM}(L) - E_{QM}(L-I) + E_{Pot}(L) + E_{Pot}(L-I) \qquad 4.2$$

The magnitude of $\Delta$ is linked to the quality of the inter-atomic potential and how well it fits the quantum mechanical potential energy surface. It will also decrease as a function of cluster size as the interactions between the active site and the link atom region will

decrease. The advantage of using a subtractive scheme such as this is that it allows a wide range of forcefields to be used, although they must be well parameterised.

Several codes employ an alternative additive scheme in which the total energy for the system is obtained by adding the energies calculated for inner and outer regions. A correction term is then added to account for the atoms in the link atom region. An example of a method that includes the additive scheme is CHEMSHELL developed by Sherwood and co-workers [16].

## 4.4.1 QM/MM - Computational Details
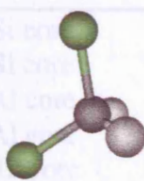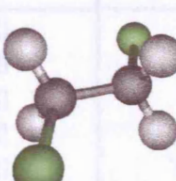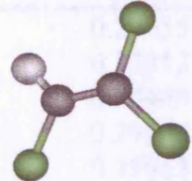
The QMPot scheme was used to investigate adsorption in the FAU series. The system, including the lattice parameters, was optimized in the constant pressure mode using the shell model potential developed by Hill and Sauer [17]. This pre-optimisation has the advantage that the positions of the atoms in the outer region are already relaxed, which saves optimization cycles in the following QMPot calculation. Details of the potential are given in tables 4.3-4.8. The starting configurations of the adsorbate atoms were taken from the Monte Carlo Docking study described in the previous chapter. Thus, the starting configuration for the clusters and the embedded system are the same.

An energy threshold of 0.00001eV was taken as the convergence criterion. The electrostatic energy was evaluated using an Ewald summation technique for all the cores and shells. The QM part of the system was modelled using the DMol$^3$ code with the PW91 functional and DNP basis set. This allows for comparison with the cluster calculations performed in the previous chapter. Calculations were also performed using the Gaussian03 code, with both 3-21g and 6-31g(d,p) basis sets. The rest of the lattice was modelled using GULP. The clusters were selected consisting of the 12-membered ring window of FAU and were terminated with OH groups. The O-H link atom distance was set to 0.97Å. The sorbate molecule was then placed in the 12-membered ring, approximately 3Å away from the framework. Figure 4.6 represents the system modelled, with DCM adsorbed as an example.
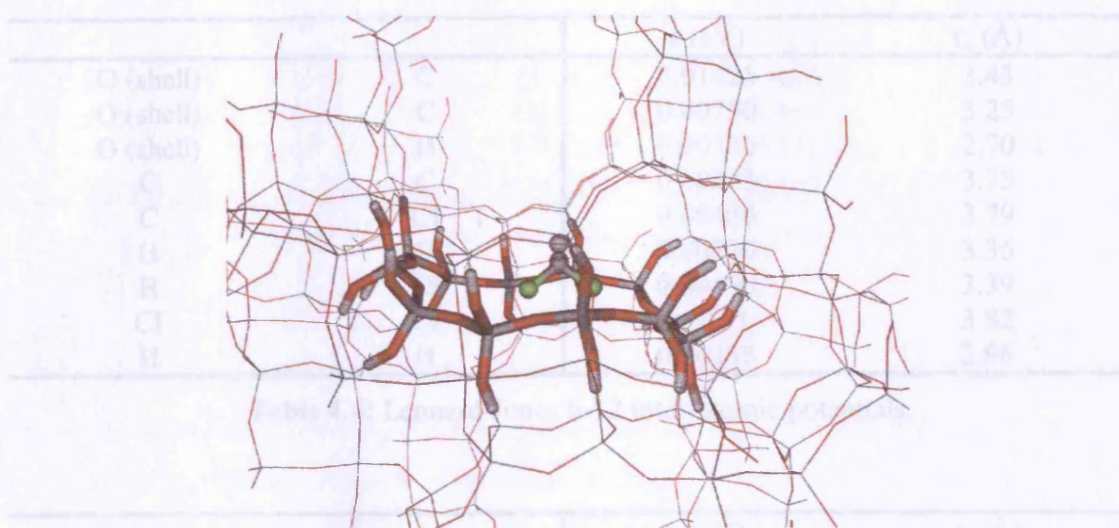
**Figure 4.6:** The system modelled using the QMPot approach. The cylinders represent the atoms in the QM region.

The charges on the adsorbate were derived from Hartree-Fock calculations using Gaussian03 and the TZP basis set. These charges are detailed in table 4.3. The parameters used for the adsorbate were derived by Mellot and co-workers based on results from calorimetry experiments [18]. These parameters are presented in tables 4.4-4.8 below.

| DCM | | DCE | | TCE | |
|---|---|---|---|---|---|
| C | 0.1370 | C | 0.0370 | C1 | 0.1865 |
| Cl | -0.1955 | Cl | -0.2680 | C2 | -0.0236 |
| H | 0.1270 | H | 0.1158 | H | 0.1671 |
| | | | | Cl1 | -0.1217 |
| | | | | Cl2 | -0.1273 |
| | | | | Cl3 | -0.0810 |

**Table 4.3:** The charges on the adsorbate molecules obtained using Hartree-Fock calculations.

115

| | | ε (eV) | $r_0$ (Å) |
|---|---|---|---|
| O (shell) | C | 0.01425 | 3.43 |
| O (shell) | C | 0.00750 | 3.25 |
| O (shell) | H | 0.00780 | 2.70 |
| C | C | 0.00223 | 3.75 |
| C | Cl | 0.00480 | 3.79 |
| H | C | 0.00230 | 3.36 |
| H | Cl | 0.00496 | 3.39 |
| Cl | Cl | 0.0103 | 3.82 |
| H | H | 0.00238 | 2.96 |

**Table 4.4:** Lennard-Jones 6-12 inter-atomic potentials.

| | | k (eV) | $r_0$ (Å) |
|---|---|---|---|
| C | H | 59.08 | 1.105 |
| C | Cl | 54.46 | 1.761 |

**Table 4.5:** Intra-atomic Lennard Jones 6-12 parameters.

| | | | k (eV) | $\theta_0$ (°) |
|---|---|---|---|---|
| C | Cl | H | 5.8108 | 107.10 |
| C | H | H | 3.4258 | 109.47 |
| C | Cl | Cl | 8.6730 | 109.50 |

**Table 4.6:** Adsorbate three-Body potential.

| | | A (eV) | $\rho$(Å) |
|---|---|---|---|
| Si core | O1 shell | 1612.4592 | 0.29955 |
| Si core | O2 shell | 997.88097 | 0.33212 |
| Al core | O1 shell | 1395.7746 | 0.30449 |
| Al core | O2 shell | 1644.88177 | 0.29139 |
| H2 core | O1 shell | 7614.58003 | 0.19913 |
| H2 core | O2 shell | 368.648030 | 0.22511 |
| H1 core | O1 shell | 772.068140 | 0.18524 |

**Table 4.7:** Buckingham zeolite parameters.

|  |  |  | A (eV) | $\theta_0$ (°) |
|---|---|---|---|---|
| Si core | O1 shell | O1 shell | 0.144703 | 109.47 |
| Si core | O1 shell | O2 shell | 0.384711 | 109.47 |
| Al core | O1 shell | O2 shell | 0.893930 | 109.47 |
| Al core | O1 shell | O2 shell | 0.686678 | 109.47 |

**Table 4.8:** Zeolite three -Body potential parameters.

## 4.4.2 Selecting an appropriate cluster

It is important when selecting clusters representing the QM region to choose a cluster that is able to include all relevant short-range interactions between the adsorbate and the surrounding framework. Additionally it is important that the cluster is large enough for the adsorbate molecule to avoid interacting with the link atoms between the QM and MM regions. A compromise must therefore be reached between the cluster size and computational efficiency. Selecting an inappropriate cluster can lead to differences in the energetics of the system and also in the position of the adsorbate within the cluster.

## 4.4.3 QMPot results

The results for the clusters modelled using the QMPot method for DMol$^3$ and Gaussian are presented in tables 4.9-4.12 below. The total adsorption energy obtained using the QMPot scheme has also been separated into long-range and QM contributions.

| System | Adsorption Energy (kJ/mol) | QM contribution (kJ/mol) | Long-range contribution (kJ/mol) | DMol$^3$ cluster (kJ/mol) |
|---|---|---|---|---|
| FAUDCM | -64.10 | -9.71 | -54.39 | -12.74 |
| FAUDCE | -66.41 | -10.20 | -56.26 | -17.12 |
| FAUTCE | -61.36 | -16.52 | -44.84 | -15.17 |

**Table 4.9:** Adsorption energies obtained using the QMPot approach with the QM region modelled with DMol$^3$.

| System | Adsorption Energy (kJ/mol) | QM contribution (kJ/mol) | Long-range contribution (kJ/mol) |
|--------|--------------------------|-------------------------|----------------------------------|
| FAUDCM | -39.32 | -27.57 | -11.75 |
| FAUDCE | -64.29 | -34.95 | -29.34 |
| FAUTCE | -51.94 | -50.14 | -1.79 |

**Table 4.10:** Adsorption energies obtained using the QMPot approach with the QM region modelled with Gaussian03 and the 3-21G basis set.

Our results show that DCE is the most strongly adsorbed followed by TCE and DCM respectively. The values obtained using the 3-21G basis set seems to improve on the values obtained using the cluster method. However, these values do not take into account the Basis Set Superposition Error (BSSE), which will lower the values. Since the 3-21G basis set is small and incomplete a large BSSE is expected. The calculations were repeated using a larger 6-31G basis set, which are presented in table 4.11 below. A comparison with a 12-ring free cluster optimized using Gaussian03 is also presented.

| System | Adsorption Energy | QM contribution | Long-range contribution | Gaussian cluster |
|--------|-------------------|-----------------|-------------------------|------------------|
| FAUDCM | -26.55 | -15.96 | -10.59 | -18.84 |
| FAUDCE | -21.67 | -9.21 | -12.46 | - |
| FAUTCE | -18.87 | -9.13 | -9.74 | - |

**Table 4.11:** Adsorption energies obtained using the QMPot approach with the QM region modelled with Gaussian03 and the 6-31G(d,p) basis set.

The trend in adsorption energies obtained using the 6-31G(d,p) basis set differs from that using the 3-21G basis set. In this case DCM is the most strongly adsorbed followed by DCE and TCE respectively. The overall adsorption energies are lower than those obtained

using the 3-21G basis set. This is a reflection on the improved basis set and these values are likely to be more accurate. The difference between the adsorption energies using the different basis sets can be attributed to the BSSE. In all three cases it can be seen that the long-range electrostatics play a significant role, contributing to approximately 50% of the total adsorption energy. Thus neglecting the long-range electrostatics in the cluster approach is a significant omission.

As a comparison a 12-ring cluster with DCM adsorbed was modelled using the free cluster approach. This result is presented in table 4.12 for direct comparison with the QMPot result. It can be seen that the adsorption energy obtained using the free cluster approach is comparable to the QM contribution obtained using QMPot. However, the energy obtained using the free-cluster approach is slightly lower than the QM contribution energy. This may be attributed to the stabilising effect of the terminating O-H groups, which is removed in the QMPot scheme.

The values obtained using the DMol$^3$ approach are higher than those obtained using Gaussian. This can be attributed to the differences in the codes but also due to the fact that the basis sets used, whilst comparable in size, are different in nature. Gaussian uses analytical functions whilst DMol$^3$ employs numerical functions. As such the results obtained using the two approaches cannot be compared directly and it is more useful to compare the values obtained to experimental results as in table 4.12.

| System | DMol$^3$ free cluster adsorption energy E$_{ads}$ (kJ/mol) | QMPot embedded cluster adsorption energy E$_{ads}$ (kJ/mol) (6-31G(d,p)) | Literature Values E$_{ads}$ (kJ/mol) |
|--------|--------|--------|--------|
| FAUDCM | -12.74 | -15.47 | -41.0 [3] |
| FAUDCE | -17.12 | -21.67 | -47.0 [3] |
| FAUTCE | -15.17 | -18.87 | -48.0 [3] |

**Table 4.12:** Comparison of results obtained using the free cluster and embedded approach.

The adsorption energies obtained using the QMPot method offer some improvement on the DMol$^3$ free cluster approach, however, they are still significantly lower than the experimental literature values.

## 4.4.4 Adsorption Geometries

The adsorption geometries obtained at the end of the QMPot calculation are shown in figures 4.7-4.9 below. It can be seen that the adsorbate adopts a different position when optimized with each basis set.



3.02Å    3.56Å

3.62Å    3.68Å
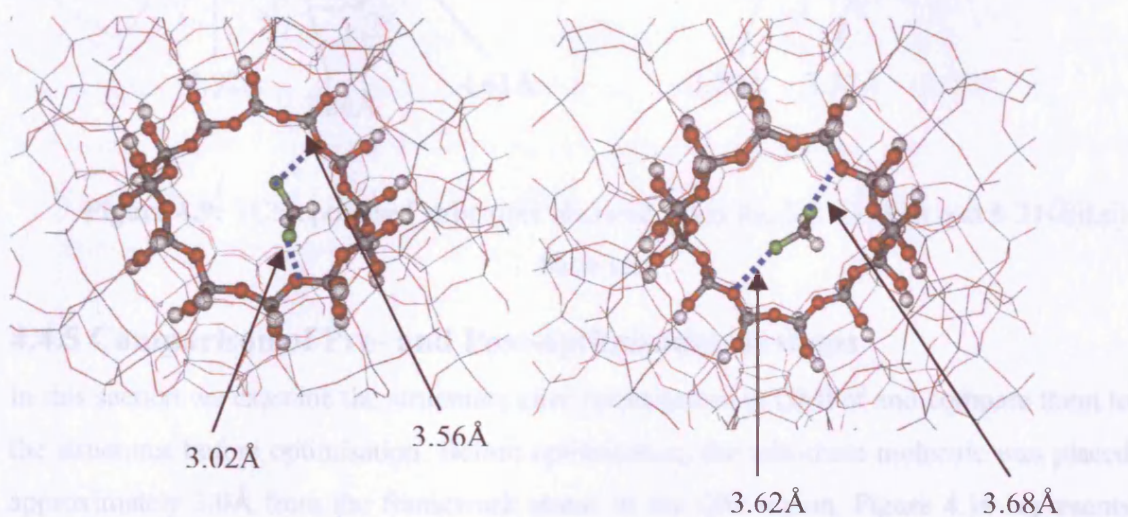
**Figure 4.7:** DCM optimised structures obtained using the 3-21G (left) and 6-31G(d,p) basis sets.
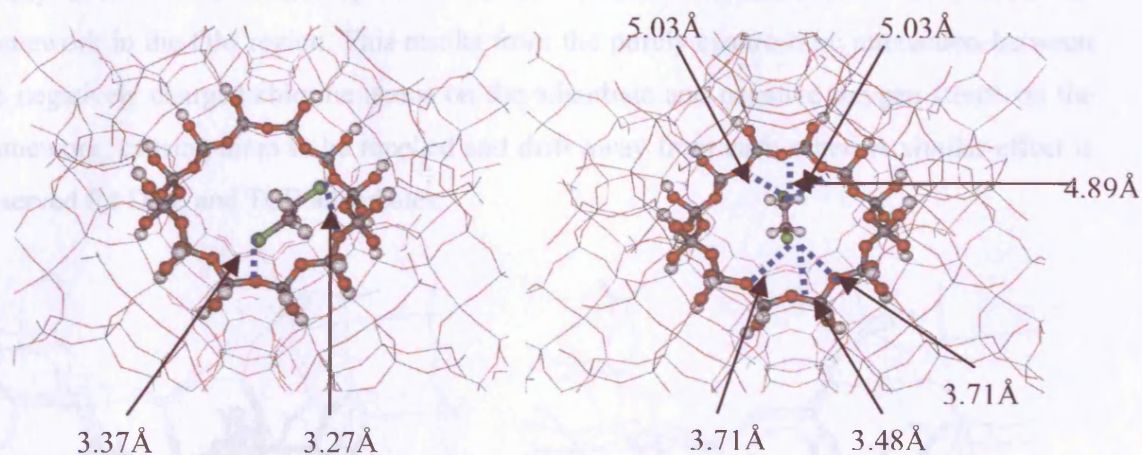
**Figure 4.8:** DCE optimised structures obtained using the 3-21G (left) and 6-31G(d,p) basis sets.
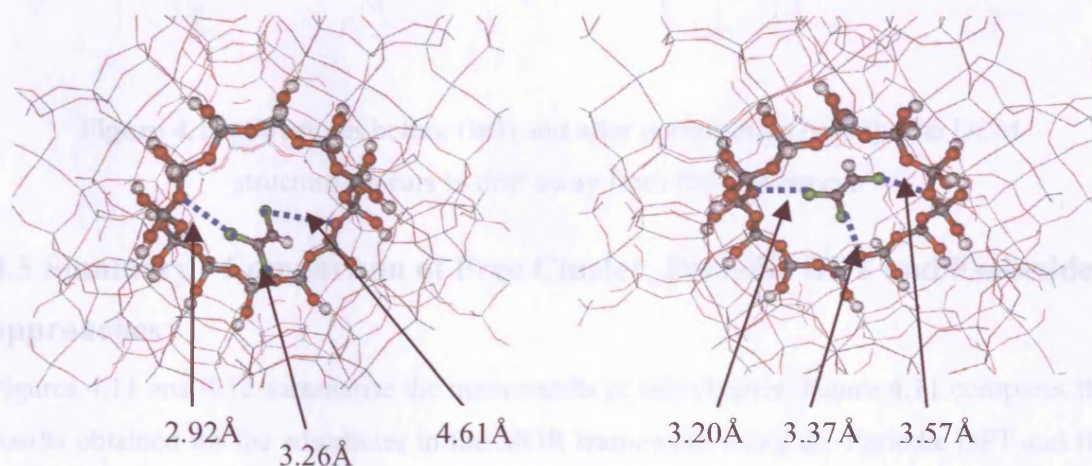


**Figure 4.9:** TCE optimised structures obtained using the 3-21G (left) and 6-31G(d,p) basis sets.

## 4.4.5 Comparison of Pre- and Post-optimisation systems

In this section we examine the structures after optimization in QMPot and compare them to the structures before optimisation. Before optimisation, the adsorbate molecule was placed approximately 3.0Å from the framework atoms in the QM region. Figure 4.10 represents the structures before and after optimization, using the DCM system as an example. It can

clearly been seen that after optimization the adsorbate molecule drifts away from the framework in the QM region. This results from the purely electrostatic interaction between the negatively charged chlorine atoms on the adsorbate and negative oxygen atoms on the framework, causing them to be repelled and drift away from each other. A similar effect is observed for DCE and TCE adsorbates.
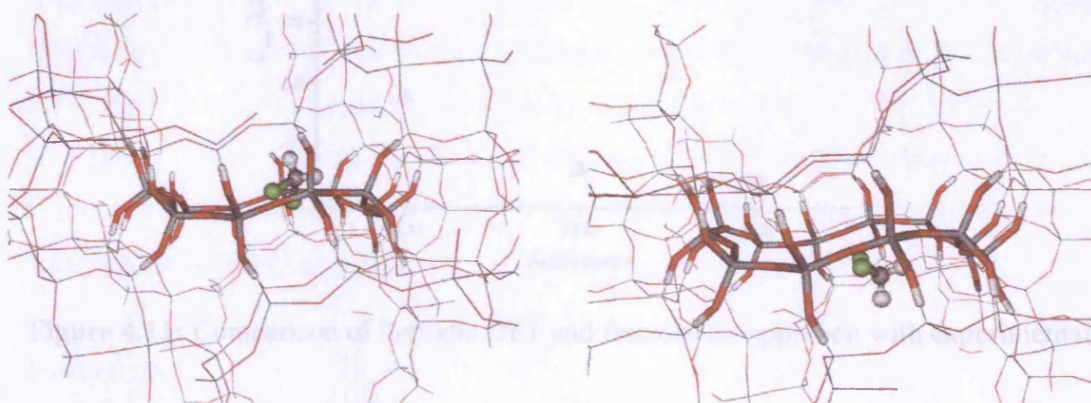


**Figure 4.10:** Structures before (left) and after optimisation (right). The DCM structure appears to drift away from the QM region.

## 4.5 Summary - Comparison of Free Cluster, Periodic DFT and Embedded approaches

Figures 4.11 and 4.12 summarise the main results of this chapter. Figure 4.11 compares the results obtained for the adsorbates in the MOR framework using the Periodic DFT and the free cluster approach with experimental results. Figure 4.12 compares the results obtained for the adsorbates in the FAU framework using the QMPot embedded approach and the free cluster approach with experimental results.

It can be seen from figure 4.11 that in general the periodic DFT underestimates the adsorption energy compared to the free cluster approach. The embedded cluster approach (figure 4.12) however produces results that are consistently higher than the cluster approach and are closer to the experimental heats of adsorption. This improvement over the cluster approach can be attributed to the inclusion of the long-range effects as well as some contribution from the interatomic potentials. The interaction energy obtained using the QMPot approach however is still approximately 30kJ/Mol weaker than the experimental value. This value may be improved upon by using a post Hartree-Fock approach such as MP2 theory, which will allow inclusion of electron correlation effects. Attempts were made to repeat the cluster and QMPot calculations using MP2 theory but these proved to be too computationally expensive to run.



**Figure 4.11:** Comparison of Periodic DFT and free cluster approach with experimental results.



**Figure 4.12:** Comparison of results obtained using the QMPot and free cluster approaches with experimental results.

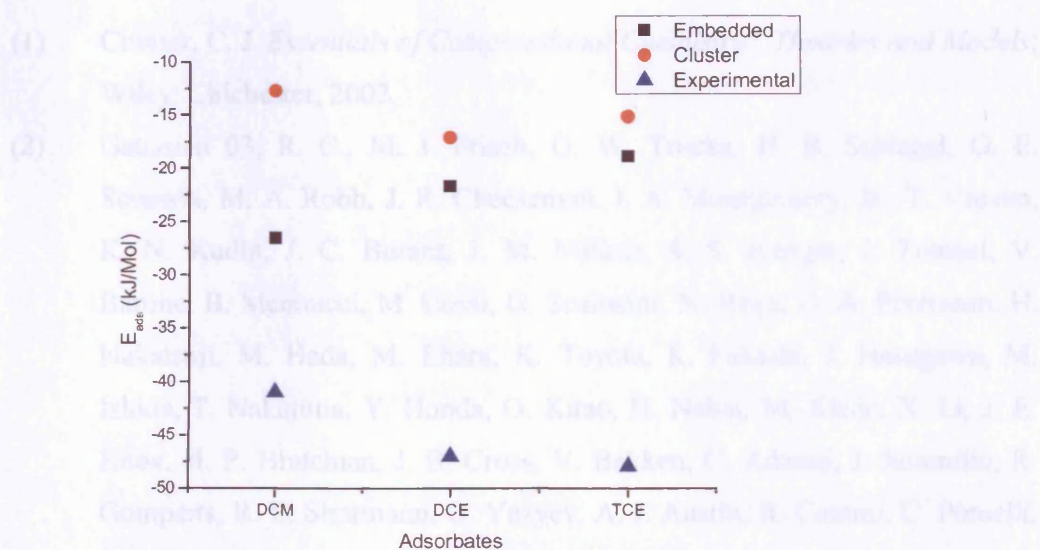It can be seen from figure 4.11 that in general the periodic study underestimates the adsorption energy compared to the free cluster approach. The QMPot embedded approach (figure 4.12) however, produces results that are consistently higher than the cluster approach and are closer to the experimental heats of adsorption. This improvement over the cluster approach can be attributed to the inclusion of the long-range effects as well as some contribution from the interatomic potentials. The interaction energy obtained using the QMPot approach however is still approximately 30kJ/Mol weaker than the experimental value. This value may be improved upon by using a post Hartree-Fock approach such as MP2 theory, which will allow inclusion of electron correlation effects. Attempts were made to repeat the cluster and QMPot calculations using MP2 theory but these proved to be too computationally expensive to run.

# References

# References

(1)    Cramer, C. J. *Essentials of Computational Chemistry: Theories and Models*; Wiley: Chichester, 2002.

(2)    Gaussian 03, R. C., M. J. Frisch, G. W. Trucks, H. B. Schlegel, G. E. Scuseria, M. A. Robb, J. R. Cheeseman, J. A. Montgomery, Jr., T. Vreven, K. N. Kudin, J. C. Burant, J. M. Millam, S. S. Iyengar, J. Tomasi, V. Barone, B. Mennucci, M. Cossi, G. Scalmani, N. Rega, G. A. Petersson, H. Nakatsuji, M. Hada, M. Ehara, K. Toyota, R. Fukuda, J. Hasegawa, M. Ishida, T. Nakajima, Y. Honda, O. Kitao, H. Nakai, M. Klene, X. Li, J. E. Knox, H. P. Hratchian, J. B. Cross, V. Bakken, C. Adamo, J. Jaramillo, R. Gomperts, R. E. Stratmann, O. Yazyev, A. J. Austin, R. Cammi, C. Pomelli, J. W. Ochterski, P. Y. Ayala, K. Morokuma, G. A. Voth, P. Salvador, J. J. Dannenberg, V. G. Zakrzewski, S. Dapprich, A. D. Daniels, M. C. Strain, O. Farkas, D. K. Malick, A. D. Rabuck, K. Raghavachari, J. B. Foresman, J. V. Ortiz, Q. Cui, A. G. Baboul, S. Clifford, J. Cioslowski, B. B. Stefanov, G. Liu, A. Liashenko, P. Piskorz, I. Komaromi, R. L. Martin, D. J. Fox, T.

Keith, M. A. Al-Laham, C. Y. Peng, A. Nanayakkara, M. Challacombe, P. M. W. Gill, B. Johnson, W. Chen, M. W. Wong, C. Gonzalez, and J. A. Pople, Gaussian, Inc., Wallingford CT, 2004. Gaussian03.

(3)     Clausse, B.; Garrot, B.; Cornier, C.; Paulin, C.; Simonot-Grange, M. H.; Boutros, F. *Micropor. Mesopor. Mater.* **1998**, *25*, 169.

(4)     Boronat, M.; Zichovich-Wilson, C. M.; Corma, A.; Viruela, P. *Phys. Chem. Chem. Phys.* **1998**, *4*, 537

(5)     Brändle, M.; Sauer, J.; Dovesi, R.; Harrison, N. M. *J. Chem. Phys* **1998**, *109*, 10383

(6)     Rozanska, X.; van Santen, R. A.; Hutschka, F. *J. Catal* **2001**, *200*, 79.

(7)     Hill, J. R.; Freeman, C. M.; Delley, B. *J. Phys. Chem. A* **1999**, *103*, 3772.

(8)     Accelrys Inc *DMol³ program*, 1999.

(9)     Perdew, J. P.; Burke, K.; Ernzerhof, M. *Phys. Rev. Lett.* **1996**, *77*, 3865.

(10)    Sherwood, P. Hybrid Quantum Mechanics/Molecular Mechanics Approaches. In *Modern methods and algorithms of quantum chemistry*; Grotendorst, J., Ed.; John von Neumann Institute for Computing, 2000; Vol. 3; pp 285.

(11)    Eichler, U.; Brandle, M.; Sauer, J. *J. Phys. Chem. B* **1997**, *101*, 10035.

(12)    Sauer, J.; Sierka, M. *J. Comp. Chem* **2000**, *21*, 1470

(13)    Gale, J. D.; Rohl, A. L. *Molecular Simulation* **2003**, *29*, 291.

(14)    Accelrys Inc. Discover Module San Diego, California.

(15)    Ahlrichs, R.; Bar, M.; Haser, M.; Horn, H.; Kolmel, C. *Chem. Phys. Lett* **1989**, *162*, 165.

(16)    deVries, A. H.; Sherwood, P.; Collins, S. J.; Rigby, A. M.; Rigutto, M.; Kramer, G. J. *J. Phys. Chem. B* **1999**, *103*, 6133.

(17)    Hill, J. R.; Sauer, J. *J. Phys. Chem* **1994**, *98*, 1238.

(18)    Mellot, C. F.; Cheetham, A. K. *J. Phys. Chem B* **1999**, *103*, 3864

# Chapter Five: Simulation of Single Component Adsorption

## 5.1 Introduction

The term adsorption was first introduced by Kayser in 1881 to describe the condensation of gases on surfaces [1]. This is in contrast to the term absorption where the molecules are able to penetrate into the bulk of the solid. The term sorption is often used to encompass both adsorption and absorption phenomena. Unlike open systems, the presence of the opposite walls in microporous systems results in an increase of the attractive energy experienced by the adsorbate. A further complication is that microporous systems contain pores of differing sizes. As a consequence adsorption in certain areas of the solid is inhibited and thus the measured uptake will correspond to only a fraction of the total available surface.

Studying adsorption in zeolites is crucial for many industrial applications both to obtain a mechanistic understanding of catalysis and for separation processes to purify gas streams. Adsorption of small probe molecules can also be used to characterise zeolites, providing information on the total surface area and pore size distribution. In order to build a detailed picture of the adsorption process knowledge of the energetics of adsorption and adsorptive behaviour under various conditions is required. The energetics of alkane sorption in zeolites has been extensively studied experimentally and includes studies of both single and multi-component adsorption [2-5]. In recent years a number of computational studies have been undertaken to obtain both thermodynamic data, such as heats of adsorption and adsorption isotherms [6-10]. In addition simulation enables us to obtain details of the location and orientation of the adsorbate enclosed within the zeolite pores, which can give insight into how a catalytic reaction may proceed. In the previous two chapters quantum mechanical approaches were used to probe the adsorption of the molecules in the various zeolite

frameworks. This chapter presents results of forcefield based Monte Carlo simulations which have been used to obtain adsorption isotherms and heats of adsorption.

## 5.1.1 Isotherm models

Under equilibrium conditions the distribution of the adsorbate molecules on the surface of the adsorbent is dependent on a number of factors. These include the nature and area of the adsorbent, the nature of the adsorbate and experimental conditions such as the temperature and pressure. An adsorption isotherm describes the relationship between the amount adsorbed and the pressure, for a given gas on a given solid at a constant T.

Many models have been developed to describe adsorption processes. Most isotherms are fitted to the Langmuir equation, which relates the loading N at a given pressure (P) to the maximum loading ($N_{max}$):

$$N = \frac{N_{max}P}{1 + N_{max}P_0}$$ 5.1

The Langmuir model makes several assumptions. These include:

- that monolayer adsorption occurs
- that all adsorption sites are equivalent
- the surface is uniform
- that molecular adsorption is independent of occupation of neighbouring sites.

This model was initially developed to describe adsorption on open surfaces but the assumptions hold true to adsorption in zeolites. When the saturation region is approached the interactions between adsorbates become significant. In this case the Langmuir model breaks down and an alternative model, such as that suggested by Lacher [11] and also by Fowler and Guggenheim must be employed [12]. Other adsorption isotherm models have also been developed [13,14]. The Dubinin-Kaganer-Radushkevich isotherm describes physical adsorption up to monolayer coverage. The Freundlich isotherm was developed to describe adsorption at low coverages. The Brunauer-Emmett-Teller isotherm extends the

Langmuir isotherm model to multilayer adsorption. The Dubinin- Radushkevich and Virial isotherms also describe multilayer adsorption in microporous materials. High area solids such as zeolites display one of five types of adsorption isotherm given by the Brunauer classification, illustrated in figure 5.1 [13, 15].
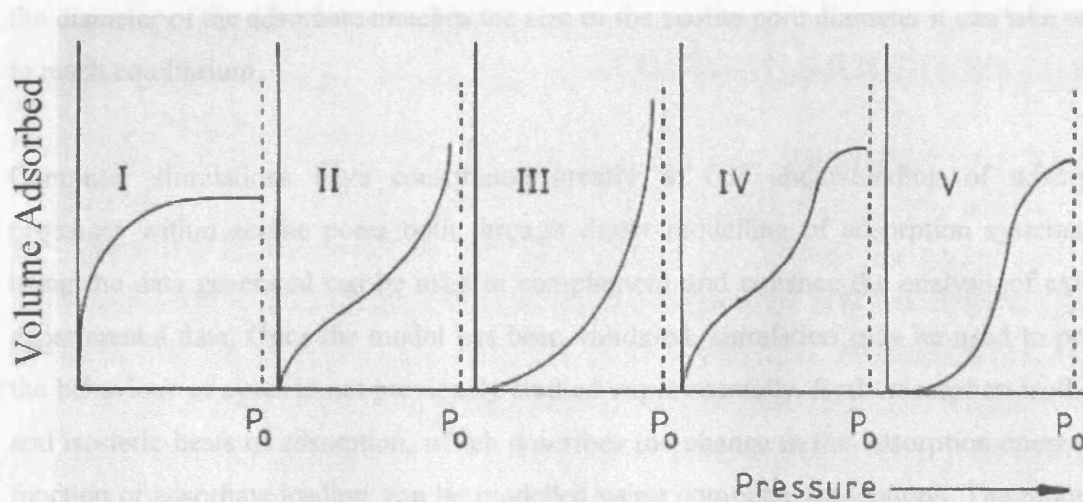


**Figure 5.1:** Brunauer classification of adsorption isotherms commonly observed in zeolite structures [13,15].

As described in section 1.4.2, the adsorption energy is composed of both van der Waals and electrostatic forces. In hydrophobic zeolites such as the high-silica zeolites modelled in this chapter there is no specific region of the framework for the adsorbate to interact with and therefore the molecules interact with the zeolite via dispersive van der Waals and repulsive forces. At high coverages adsorbate-adsorbate interactions also contribute to the adsorption energy.

## 5.1.2 Methods of measuring adsorption

Adsorption isotherms are usually measured using volumetric or gravimetric techniques. The volumetric technique involves introducing a known pressure of adsorbate over a known quantity of adsorbent [14,16]. The amount of gas adsorbed is calculated as the difference between the original amount of adsorbate and the amount left after equilibrium

has been reached. In the gravimetric method the amount of gas adsorbed is determined from the increase in weight of the adsorbent after being exposed to the adsorbate. An isotherm is obtained by introducing the adsorbate at increasing pressures. The adsorption of hydrocarbons in zeolite pores can be a slow process especially for large molecules which have to move through the porous network to reach the adsorption site. In the case where the diameter of the adsorbate matches the size of the zeolite pore diameter it can take weeks to reach equilibrium.

Computer simulations have contributed greatly to our understanding of adsorption processes within zeolite pores both through direct modelling of adsorption systems and using the data generated can be used to complement and enhance the analysis of existing experimental data. Once the model has been validated, simulation may be used to predict the behaviour of systems not previously studied experimentally. Both adsorption isotherms and isosteric heats of adsorption, which describes the change in the adsorption energy as a function of adsorbate loading, can be modelled using computer simulations. The process is faster than using experimental methods, with it taking only a few hours to simulate an isotherm.

It is also possible to simulate the Henry coefficients for a system. The Henry co-efficient represents the affinity for a particular adsorbate for a zeolite. At very low pressure the number of molecules adsorbed, $\theta$, within a zeolite pore is proportional to its Henry coefficient, $k_H$:

$$\theta = k_H P \qquad\qquad 5.2$$

where P is the external pressure. Heats of adsorption and Henry co-efficient data can be combined to give a good indication of how readily a molecule will adsorb in a particular zeolite structure.

## 5.2 Overview of this work

In this chapter the Monte Carlo approach was used to simulate isosteric heat curves and adsorption isotherms for single component adsorption of DCM, DCE and TCE in siliceous MOR, FAU and MFI frameworks. Using a purely siliceous framework is a reasonable approximation since pore geometry has been shown to contribute more to the adsorption energy of alkanes compared to acid site concentration and strength [17]. A comparison with literature studies is then presented and the results analysed in terms of the relative contributions to the adsorption energy.

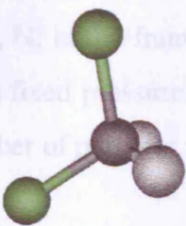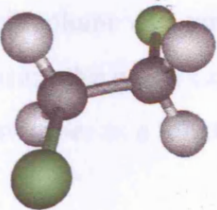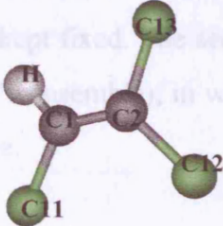## 5.3 The Forcefield used in the simulations

The zeolite–adsorbate and adsorbate–adsorbate interactions were described using a forcefield. The adsorbate-adsorbate and adsorbate-zeolite interactions were described using 12-6 Lennard-Jones parameters, developed by Mellot and co-workers [18]. The short-range parameters between adsorbate C and H atoms and zeolite oxygen atoms were taken from Monte Carlo simulations studies of heats of adsorption of methane in various zeolite framework structures. The short-range parameters between adsorbate Cl and framework oxygen atoms were derived from argon in zeolitic structures. The values were then scaled up to account for the increase in polarisability from Ar to Cl. The intra-sorbate bond lengths were described using a harmonic term and angles were described using a three-body harmonic term. The parameters for these were taken from the *cvff* forcefield [19]. The framework tetrahedral atoms were also described using a three-body potential in conjunction with a Buckingham potential.

The partial charges on the zeolite atoms were the same as in the publication by Mellot and co-workers, which are consistent with those in *ab initio* silicalite potentials [20] and X-ray diffraction measurements [21] and are also adopted by other authors [22]. The partial charges on the adsorbates used in the simulations were derived from Hartree-Fock calculations using the TZP basis set. This is consistent with the charges derived for the chlorofluorocarbons by Mellot *et al.*.

Given that the Si atoms of the zeolite framework are less accessible and generally held to be smaller than the oxygen atoms the adsorbed molecules experience interaction mainly with the large O atoms, whilst interaction with the Si atoms is inhibited. For this reason the parameters only include the interaction of the adsorbate with the framework oxygen atoms. However coulombic interactions between Si atoms and the sorbate molecules are accounted for. This has the added advantage that the number of variables is reduced and thus saves on CPU time. The parameters used in the forcefield and the partial charges of the adsorbates and framework are presented in tables 5.1-5.3.

| Atom | Partial Charge |
|------|----------------|
| Si   | 2.400          |
| O    | -1.200         |

**Table 5.1:** Charges on the zeolite framework atoms.



| DCM | | DCE | | TCE | |
|-----|--------|-----|--------|-----|--------|
| C   | 0.1370  | C   | 0.0370  | C1  | 0.1865  |
| Cl  | -0.1955 | Cl  | -0.2680 | C2  | -0.0236 |
| H   | 0.1270  | H   | 0.1158  | H   | 0.1671  |
|     |         |     |         | Cl1 | -0.1217 |
|     |         |     |         | Cl2 | -0.1273 |
|     |         |     |         | Cl3 | -0.0810 |

**Table 5.2:** Charges on the atoms in the adsorbate molecules.

| | | $\varepsilon$ (eV) | $r_0$ (Å) |
|---|---|---|---|
| C | H | 0.00230 | 3.36 |
| C | O | 0.00750 | 3.25 |
| H | O | 0.00784 | 2.70 |
| Cl | O | 0.01425 | 3.43 |
| Cl | C | 0.00480 | 3.79 |
| Cl | H | 0.00496 | 3.39 |
| C | C | 0.00223 | 3.75 |

**Table 5.3:** Lennard-Jones parameters describing zeolite-adsorbate interactions.

## 5.4 Computational Details

Monte Carlo simulations were performed using Accelrys's Sorption module in Cerius2 [23]. Two types of simulations were conducted for each framework and sorbate. The first of theses is at a fixed loading (using the canonical or NVT ensemble), in which the number of sorbates, N, in the framework, the cell volume and temperature are kept fixed. The second type is a fixed pressure simulation (using the grand canonical or $\mu$VT ensemble), in which the number of particles is not fixed but varies as a function of pressure.

The zeolite structures were taken from the crystallographic information in the Solids Builder module of Cerius2. This database of zeolite structures contains crystallographic data for aluminosilicate structures. As we are modelling purely siliceous frameworks all aluminium atoms in the structures were replaced with silicon. The aluminosilicate structure is unlikely to be identical to the siliceous framework since the Al-O bond is longer than the Si-O bond and thus the size of the pore is likely to be slightly smaller in the siliceous structure. However, it is believed that this difference is very small and in most cases smaller than other inherent approximations such as the rigidity of the framework during the simulation. Models of the sorbate molecules were also built using the 3D sketcher facility in Cerius2.

Canonical Monte Carlo simulations were performed for $10^6$ iterations at a temperature of 300K. For MOR and FAU frameworks blocking "dummy" atoms were placed in the 8-ring side-pockets and sodalite cages respectively. This was to prevent the sorbate molecules being placed there, as in the case of MOR the molecules would have to pass through an 8-ring window and for FAU they would have to traverse a six ring. Both these manoeuvres would be impossible due to the size of the sorbate in relation to the diameter of these rings. For MOR a real space cut-off of 7.0Å was used whilst a cut-off of 9.5Å was used for the FAU and MFI frameworks. A reciprocal space cut-off was estimated using the appropriate option in the sorption module and a different value was obtained for each system under study.

Grand Canonical Monte Carlo simulations were also conducted for a range of pressures between 0.001 and 100 kPa at a temperature of 300K to enable adsorption isotherms to be simulated. Again the simulations were run for $10^6$ iterations and the same cut-offs were used as for the Canonical Monte Carlo simulations. Periodic boundary conditions were applied in both sets of simulations. The framework was assumed to be rigid. Parameters of the zeolite framework being modelled are given in table 5.4:

| Framework | No. of cells | No. of O atoms | Average pore diameter (Å) | a (Å) | b (Å) | c (Å) | Angles (°) |
|---|---|---|---|---|---|---|---|
| MOR | 1x1x2 | 192 | 6.7 | 18.0940 | 20.5160 | 15.0480 | 90° |
| MFI | 1x1x2 | 384 | 5.4 | 20.0220 | 19.8990 | 26.7660 | 90° |
| FAU | 1x1x1 | 384 | 7.4 | 24.2068 | 24.2068 | 24.2068 | 90° |

**Table 5.4:** Properties of the zeolite frameworks being modelled.

## 5.5 Results of Canonical Monte Carlo Simulations

### 5.5.1 Faujasite

Simulations were conducted for DCM, DCE and TCE in the FAU framework. The heats of adsorption for a loading of one molecule per unit cell are presented in table 5.5. The binding energies reveal the degree to which the adsorbate molecules can optimise their interaction with the zeolite framework. Adsorption is favoured where the number of favourable interactions is maximised without imposing internal strain on the adsorbate.

| Sorbate | $E_{ads}$ (kJ/mol) | $E_{ads}$ (kJ/mol) literature value |
|---------|---------|---------|
| DCM | -40.95 | -41.00 [24] |
| DCE | -48.53 | -47.00 [24] |
| TCE | -44.90 | -48.00 [24] |

**Table 5.5:** Heats of adsorption obtained for 1 adsorbate molecule in the FAU framework.

Our simulations show that DCE is the most strongly adsorbed followed by the TCE and DCM molecules. The values are in good agreement with experimental values and the simulated values do not differ more than 4kJ/mol from experimental values. An isosteric heat graph showing how the heats of adsorption vary as a function of loading for each of the adsorbates is presented in figure 5.2.
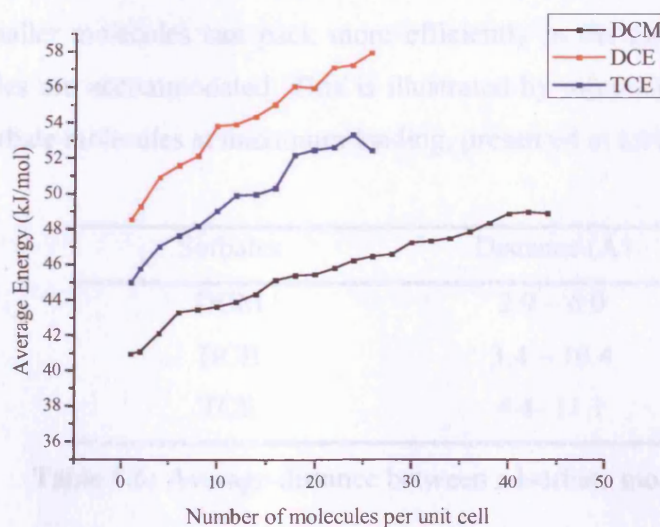


**Figure 5.2:** Heats of adsorption as a function of loading (isosteric heat plot) for adsorbate molecules in FAU, simulated at 300K.

In all cases it can be seen that the heats of adsorption increase linearly with increased sorbate loading. This can be attributed to the adsorbate-adsorbate interactions that arise when more than one molecule is in the zeolite void. For DCE the isosteric heats range from 54kJ/mol to 58kJ/mol as a function of loading which differs from the range of 40kJ/mol to 56kJ/mol obtained by Farrell et al. [25]. This difference at low loadings may be attributed to the fact that we cannot model adsorption at loadings of less than one molecule per unit cell. A maximum of 44 DCM molecules can be accommodated into the faujasite framework. Since there are 8 supercages per unit cell this corresponds to 6.125 molecules per supercage. This value is in good agreement with the calorimetric results obtained by Clausse and co-workers [24], who obtained a value of 6.4 molecules per supercage. The slightly higher value obtained experimentally may be due to adsorption taking place at the surface of the zeolite crystal at the saturation point. Further, there may be imperfections in the zeolite structure, such as defects in the framework arising from the dealumination process and gaps between the zeolite crystals where adsorption may take place. In the simulated isotherm, a perfect crystal is utilised and therefore the situation where adsorption takes place at the surface of the crystal is not included in the model. By comparison 26 DCE and 25 TCE molecules may be adsorbed. This corresponds to 3.250 and 3.125 molecules per supercage respectively. This compares to a value of 4.8 and 4.1 respectively obtained by calorimetric studies. The maximum loading corresponds to the size of the adsorbate molecules; DCM is the smallest of the three adsorbates followed by DCE and TCE. The smaller molecules can pack more efficiently in the zeolite void and therefore more molecules are accommodated. This is illustrated by measuring the average distance between adsorbate molecules at maximum loading, presented in table 5.6.

| Sorbates | Distance (Å) |
|----------|--------------|
| DCM | 2.9 – 6.0 |
| DCE | 3.4 – 10.4 |
| TCE | 4.4- 11.1 |

**Table 5.6:** Average distance between adsorbate molecules.

An estimation of the total adsorbent-adsorbate interactions, $I_{Aa}$, was made in the study by Clausse *et al.* [24], by extrapolating the adsorption enthalpies for each of the systems to zero-filling. This interaction takes into account the effect of the polarity of the adsorbed molecule on the residual cations and also the effect of the universal dispersion forces, $I_u$. However the value of $I_{Aa}$ cannot be simulated for our system since we use a cation-free zeolite structure. The polarity effect $I_P$, may also be estimated from the difference between the adsorption energy at zero-filling, $I_{Aa}$ and that at the minimum of the plot, i.e. the maximum adsorption enthalpy, given by $I_{aa}$. Again, the value of $I_P$ has not been calculated by simulation as it is for a system containing cations, rather than the siliceous system being simulated. The values for $I_u$ and $I_{aa}$ are presented in table 5.7. Values in brackets are experimental values obtained by Clausse *et al.* [24]

|       | $I_u$ (kJ/mol) |        | $I_{aa}$ (kJ/mol) |        |
|-------|------------|--------|------------|--------|
| DCM   | -40.95     | *(-41)* | -48.97     | *(-51)* |
| DCE   | -48.54     | *(-48)* | -57.95     | *(-61)* |
| TCE   | -44.99     | *(-48)* | -53.34     | *(-63)* |

**Table 5.7:** Parameters obtained by analysis of the isosteric heat plot for FAU.

The simulated values of $I_u$ and $I_{aa}$ agree well with experimental values for DCM and DCE but differ slightly for TCE. The values for $I_u$ are similar for the adsorbates with two carbon atoms (C2 compounds) and slightly weaker for DCM (C1 compound). This can be attributed to the fact that the atom-atom interactions are smaller for a C1 compound.

Figures 5.3 and 5.4 show the conformations adopted by the adsorbate molecules in the zeolite pores at the end of the simulation run, at low and high loadings.
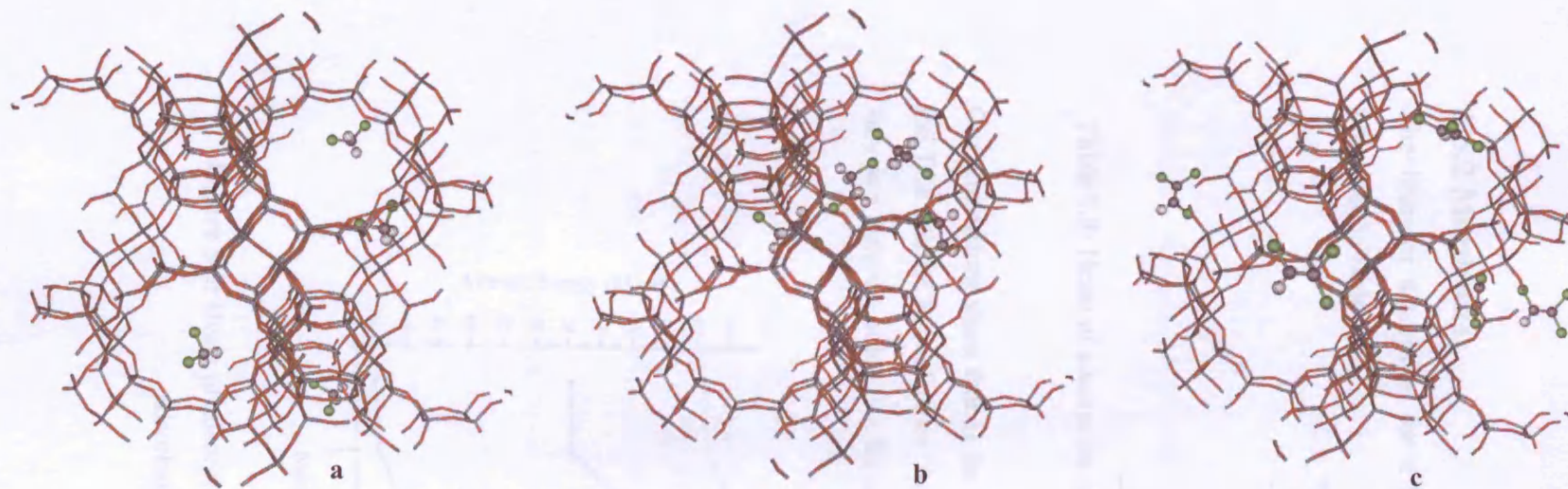
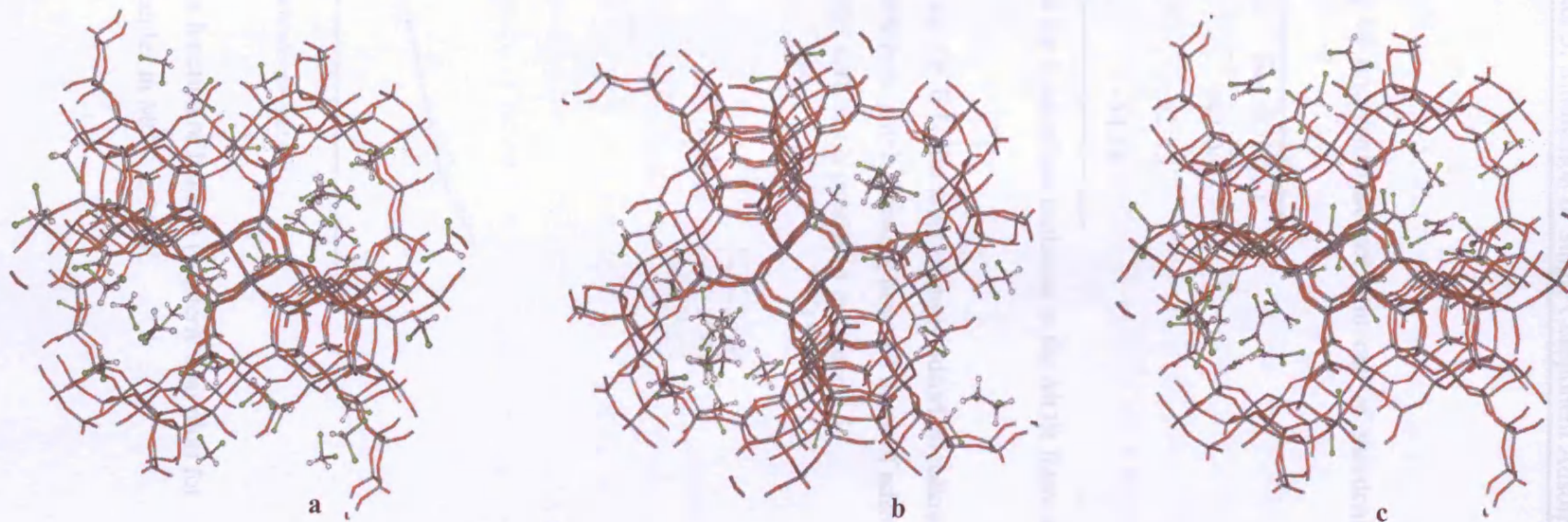**Figure 5.3:** a) FAU DCM b) FAU DCE and c) FAU TCE at low loading.



**Figure 5.4:** a) FAU DCM b) FAU DCE and c) FAU TCE at high loading.

137

## 5.5.2 Mordenite

The heats of adsorption for a loading of one molecule per unit cell of mordenite are presented in table 5.8.

| Sorbate | $E_{ads}$ (kJ/mol) |
|---------|--------------------|
| DCM     | -42.06             |
| DCE     | -62.43             |
| TCE     | -54.18             |

**Table 5.8:** Heats of adsorption obtained for 1 adsorbate molecule in the MOR framework.

Our simulations show that as for Faujasite, DCE is the most strongly adsorbed followed by the TCE and DCM molecules. An isosteric heat graph showing how the heats of adsorption vary as a function of loading for each of the sorbates is presented in figure 5.5.
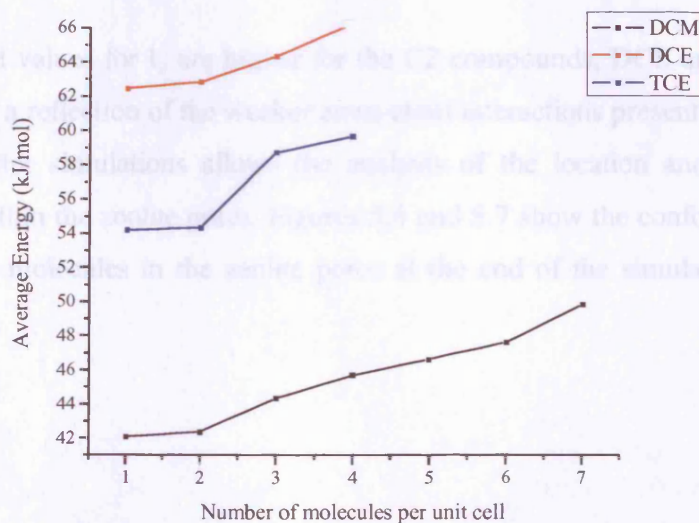


**Figure 5.5:** Heats of adsorption as a function of loading (isosteric heat plot) for adsorbate molecules in MOR at 300K.

As for FAU, the adsorption energies increase linearly with loading, which can be attributed to adsorbate-adsorbate interactions. A maximum of 7 DCM molecules can be accommodated in the mordenite unit cell. By comparison a maximum of only 4 DCE and TCE molecules can be adsorbed. Once again this trend follows the size of the adsorbates with more of the smaller DCM molecules being adsorbed. An estimation of the parameters obtained by analysis of the isosteric heat plots are presented in table 5.9 below. To date there have been no experimental studies on the adsorption of DCM, DCE or TCE in MOR so the accuracy of these values cannot be evaluated.

| | $I_u$ (kJ/mol) | $I_{aa}$ (kJ/mol) |
|---|---|---|
| DCM | -42.06 | -49.83 |
| DCE | -62.43 | -66.24 |
| TCE | -54.18 | -59.66 |

**Table 5.9:** Parameters obtained by analysis of the isosteric heat plots for MOR.

The simulated values for $I_u$ are higher for the C2 compounds, DCE and TCE compared to DCM. This is a reflection of the weaker atom-atom interactions present for a C1 compound. Using computer simulations allows the analysis of the location and orientations of the adsorbates within the zeolite pores. Figures 5.6 and 5.7 show the conformations adopted by the adsorbate molecules in the zeolite pores at the end of the simulation run, at low and high loadings.
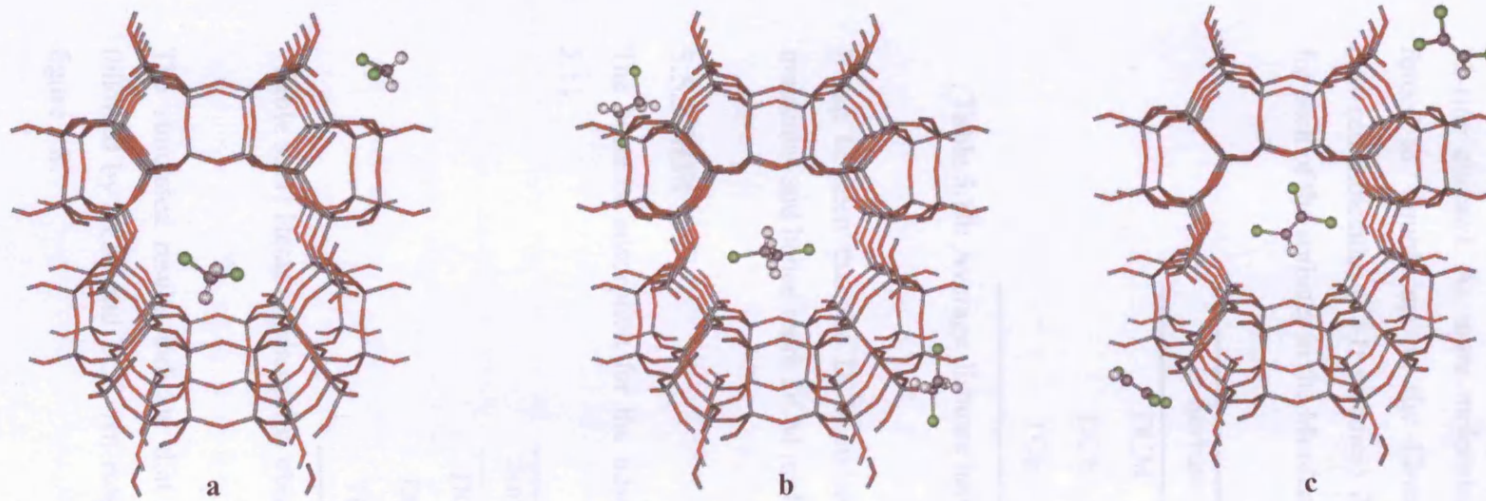
**Figure 5.6:** a) MOR DCM b) MOR DCE and c) MOE TCE at low loading.
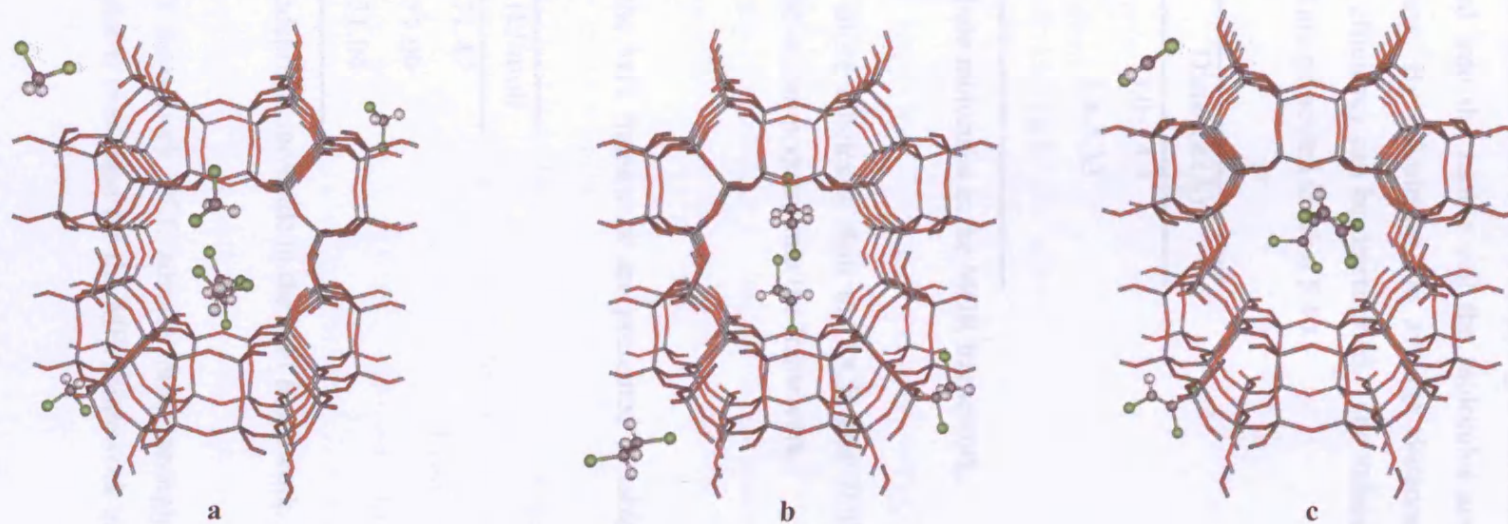


**Figure 5.7:** a) MOR DCM b) MOR DCE and c) MOE TCE at high loading.

At low loadings the molecules appear to be well spaced out, each occupying a different 12-ring channel. As more molecules are loaded into the zeolite cell the molecules are forced to 'double up' in the 12-membered ring. By calculating the average distance between molecules (Cl-H distance) the packing efficiency can be determined. The values for each of the sorbates in the Mordenite unit cell are presented in table 5.10.

| Sorbate | Distance (Å) |
|---------|--------------|
| DCM | 3.0 – 4.1 |
| DCE | 3.4-5.33 |
| TCE | 10.5 |

**Table 5.10:** Average distance between adsorbate molecules in the MOR framework.

It can be seen that the DCM molecule packs more efficiently than the DCE and TCE molecules and hence more DCM molecules can be accommodated into the framework.

## 5.5.3 MFI

The heats of adsorption for the adsorbates in the MFI framework are presented in table 5.11.

| Sorbate | $E_{ads}$ (kJ/mol) |
|---------|---------------------|
| DCM | -71.47 |
| DCE | -77.09 |
| TCE | -71.04 |

**Table 5.11:** Heats of adsorption obtained for 1 adsorbate molecule in the MFI framework.

The simulated results indicate that in the MFI framework DCE adsorbs most strongly followed by DCM and TCE. An isosteric heat plot is presented for the MFI framework in figure 5.8.
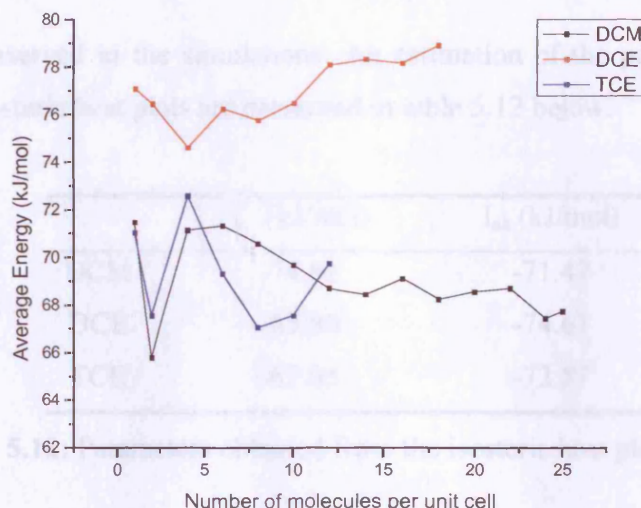
**Figure 5.8:** Isosteric heat plot for adsorbates in MFI at 300K

In contrast to FAU and MOR frameworks the isosteric heat of adsorptions do not increase with sorbate loading. Instead the heats of adsorption are found to fluctuate. This may be due to the fact that in the MFI structure three different types of adsorption sites are being sampled whereas in the MOR and FAU frameworks the presence of blocking atoms means that only one type of site is being sampled.

For DCM a maximum of 25 DCM molecules can be adsorbed. By comparison 17 DCE and 12 TCE molecules may be accommodated in the MFI framework. This trend follows the size of the adsorbate molecules. The simulated value for TCE is slightly higher than the 10 molecules obtained by Bouvier and co-workers [26]. They found that the heats of adsorption increased from -50 to -70kJ/mol during the adsorption of the 10 molecules and attributed this rise in adsorption energy to increased adsorbate-adsorbate interactions. X-ray diffraction spectra also indicated that the zeolite undergoes a structural change upon adsorption of TCE, going from a monoclinic unit cell to an orthorhombic one. Since the simulation assumes a rigid unit cell this is something that cannot be measured. The study also found that the TCE molecules were self-assembled end to end, forming dipole chains in the straight and sinusoidal channels. However, upon visualisation of the structures, this is

not something observed in the simulations. An estimation of the parameters obtained by analysis of the isosteric heat plots are presented in table 5.12 below.

|  | $I_u$ (kJ/mol) | $I_{aa}$ (kJ/mol) |
|---|---|---|
| DCM | -74.61 | -71.47 |
| DCE | -65.80 | -74.61 |
| TCE | -67.05 | -72.57 |

**Table 5.12:** Parameters obtained from the isosteric heat plot for MFI.

Analysis of the siting of the sorbate molecules at the end of the Monte Carlo run indicates that adsorption is favoured in the intersection, followed by the straight and sinusoidal channels respectively. For TCE this is in contrast to results obtained by Bouvier and co-workers [26] who found that adsorption occurred preferentially in the straight and sinusoidal channels. Figure 5.9 shows the siting of adsorbates at maximum loading. In the figures the atoms coloured in grey are located in the intersections, those in orange in the straight channels and those in blue are located in the sinusoidal channels.
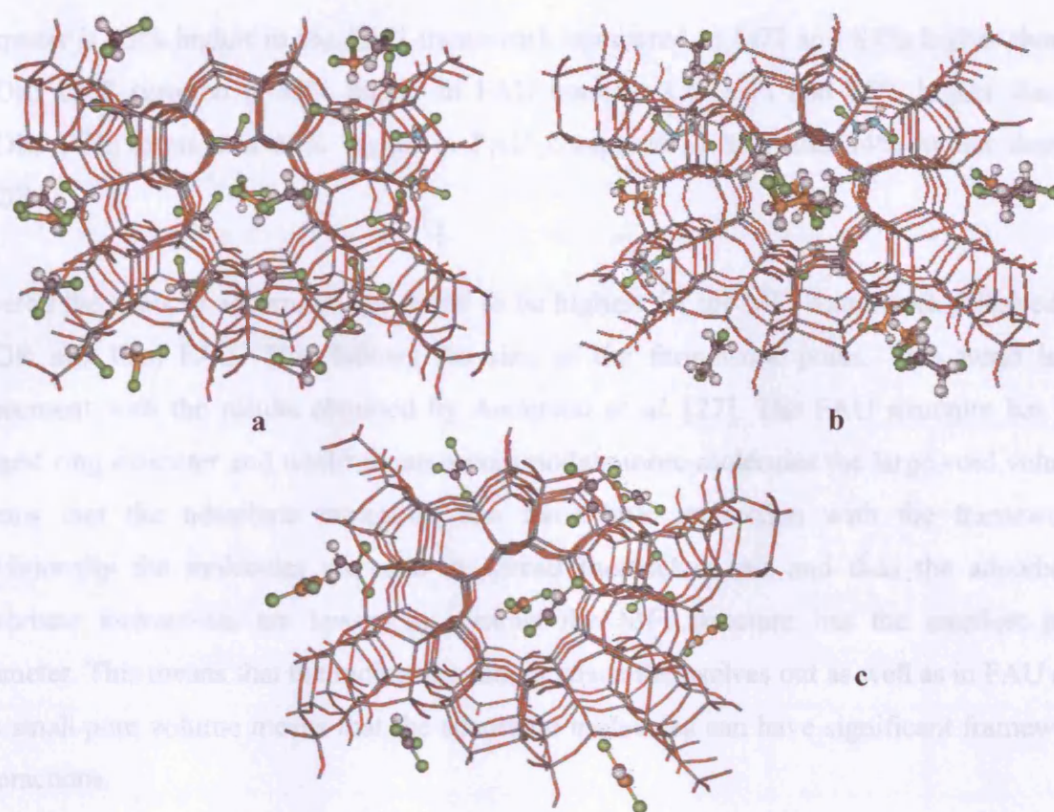
**Figure 5.9:** a)MFI DCM b) MFI DCE c) MFI TCE at high loading.

## 5.5.4 Comparison of zeolite frameworks

Table 5.13 shows the maximum loading for each framework and sorbate molecule.

|      | DCM | DCE | TCE |
|------|-----|-----|-----|
| MOR  | 7   | 4   | 4   |
| MFI  | 25  | 17  | 12  |
| FAU  | 44  | 26  | 25  |

**Table 5.13:** Comparison of maximum adsorbate loading for the three zeolite frameworks.

The FAU structure is able to accommodate the most molecules since it has the largest ring size and void volume. This is followed by MFI and then MOR. It can be seen that DCM

sorption is 43% higher in the FAU framework compared to MFI and 84% higher than in MOR. DCE sorption is 35% higher in FAU compared to MFI and 85% higher than in MOR. TCE sorption is 52% higher in FAU compared to MFI and 84% higher than in MOR.

Overall the heats of adsorption are found to be highest for the MFI framework followed by MOR and then FAU. This follows the size of the framework pores. This trend is in agreement with the results obtained by Anderson *et al.* [27]. The FAU structure has the largest ring diameter and whilst it can accommodate more molecules the large void volume means that the adsorbate molecules can have little interaction with the framework. Additionally the molecules are able to spread themselves out and thus the adsorbate-adsorbate interactions are lower. In contrast the MFI structure has the smallest pore diameter. This means that the molecules cannot space themselves out as well as in FAU and the small pore volume means that the adsorbate molecules can have significant framework interactions.

## 5.5.5 Comparison with results obtained using the Insight Solids Docking Module

Monte Carlo simulations were also conducted for the three adsorbates in the various frameworks using the Insight Solids Docking Module [28]. The structures obtained formed the starting point for subsequent electronic structure calculations. The results obtained for each system are presented in table 5.14.

| Framework Structure | $E_{ads}$ for each of the sorbate molecules (kJ/mol) | | | | | |
|---|---|---|---|---|---|---|
| | DCE Solids Docking | DCE Sorption | DCM Solids Docking | DCM Sorption | TCE Solids Docking | TCE Sorption |
| MFI | -31.0 | -77.09 | -25.1 | -71.47 | -33.8 | -71.04 |
| MOR | -68.7 | -62.43 | -66.9 | -42.06 | -71.5 | -54.18 |
| FAU | -56.1 | -48.33 | -58.6 | -40.95 | -63.1 | -44.90 |

**Table 5.14:** Comparison of results using Sorption and Solids Docking modules.

The values for the adsorption energy obtained using the Solids Docking module are higher in all cases than those obtained using the Sorption module. The most significant difference is observed for the MFI framework with a difference of almost 50kJ/mol between the methods. One of the main differences between the simulations is the different forcefields used. For the Solids Docking method the *cvff* forcefield is used whilst for sorption parameters especially developed for chlorinated compounds were utilised. The *cvff* forcefield in Solids Docker is unrealistically repulsive at short intermolecular distances. The differences may also arise due to the fact that in the solids docking simulation the effect of temperature is not taken into account and so sites that are sampled are lower in energy than in reality. Also blocking cations were not used in the simulation for FAU or

MOR. This would mean that the energy would also take into account those sorbate configurations that were placed in the side pockets and sodalite cage. The interaction energy in the side pocket and sodalite cages would be higher than in the 12-membered rings and so the total energy could be 'skewed' by a few configurations.

## 5.6 Results of Grand Canonical Monte Carlo Simulations

### 5.6.1 Faujasite

The adsorption isotherm for the three adsorbates in Faujasite is presented in figure 5.10.
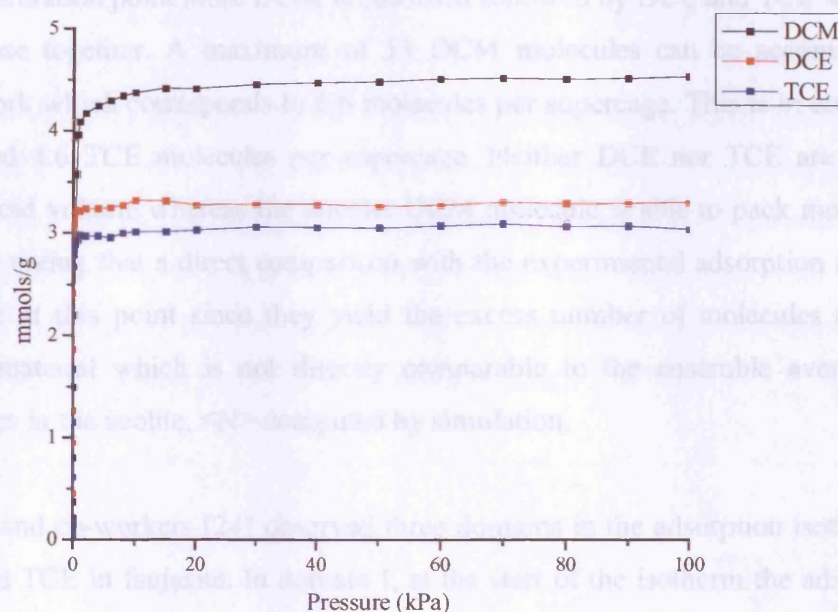


**Figure 5.10:** Adsorption isotherm for the adsorbates in FAU.

All three adsorption isotherms are type V isotherms, which are characterised by slight adsorption at low pressures followed by a sharp increase. The isotherms for all three adsorbates are in good agreement with the results obtained by Clausse and co-workers [24]. The saturation points for each of the adsorbates are given in table 5.15.

| Adsorbate | Saturation point mmols/g | Number of molecules per unit cell at saturation point |
|-----------|--------------------------|--------------------------------------------------------|
| DCM | 4.50 | 53 |
| DCE | 3.21 | 39 |
| TCE | 3.19 | 37 |

**Table 5.15:** Saturation point data for the adsorbates in FAU.

At the saturation point more DCM is adsorbed followed by DCE and TCE whose values are very close together. A maximum of 53 DCM molecules can be accommodated in the framework which corresponds to 6.6 molecules per supercage. This is in comparison to 4.9 DCE and 4.6 TCE molecules per supercage. Neither DCE nor TCE are able to fill the whole void volume whereas the smaller DCM molecule is able to pack more efficiently. It is worth noting that a direct comparison with the experimental adsorption isotherm cannot be made at this point since they yield the excess number of molecules adsorbed in the porous material which is not directly comparable to the ensemble average number of molecules in the zeolite, <N> computed by simulation.

Clausse and co-workers [24] observed three domains in the adsorption isotherms of DCM, DCE and TCE in faujasite. In domain I, at the start of the isotherm the adsorption and the thermal effects are weak. The isotherm at this stage is type III. In domain II, the micropores start to fill up and adsorbate –adsorbate interactions become more significant and the isotherm is characterised by an inflection point. Domain III comes into effect once the micropores are saturated and adsorption on the external surface of the zeolite becomes prevalent. The simulated isotherms also display similar behaviour with domain I and domain II observed at low pressures. This is illustrated in figure 5.11-5.13 for the three adsorbate molecules.
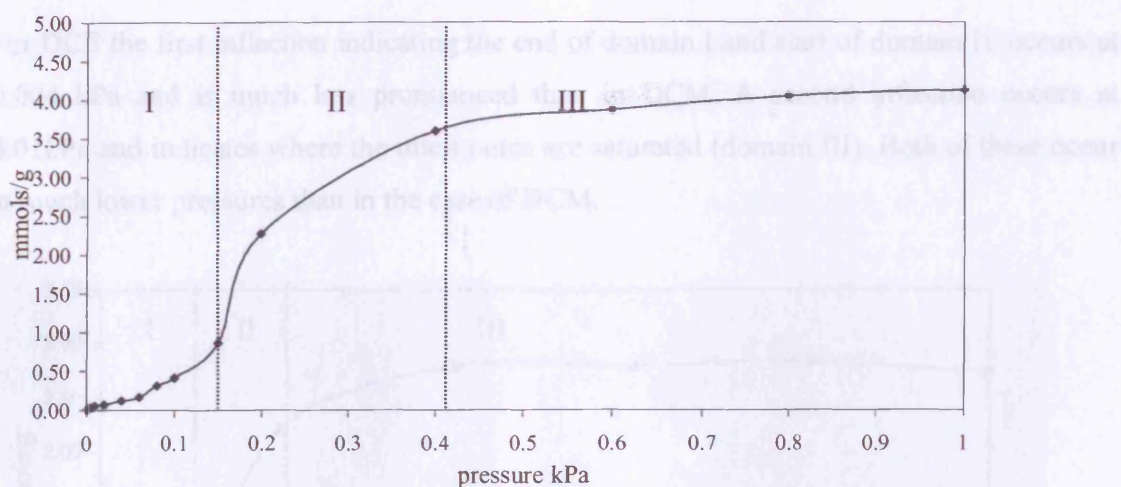
**Figure 5.11**: Domains I, II and III for DCM in FAU.

For DCM domain I occurs in the 0.1 – 0.15kPa pressure range. As the simulated system did not contain any cationic sites this domain may correspond to Henry's region, where Henry's law is obeyed. The domain is much narrower than in the experimental isotherm as there are no cationic sites in the simulated system. At 0.15kPa there is an inflection in the isotherm representing the start of domain II. At 0.4kPa there is another inflection in the isotherm and it is at this point that the saturation limit is reached.
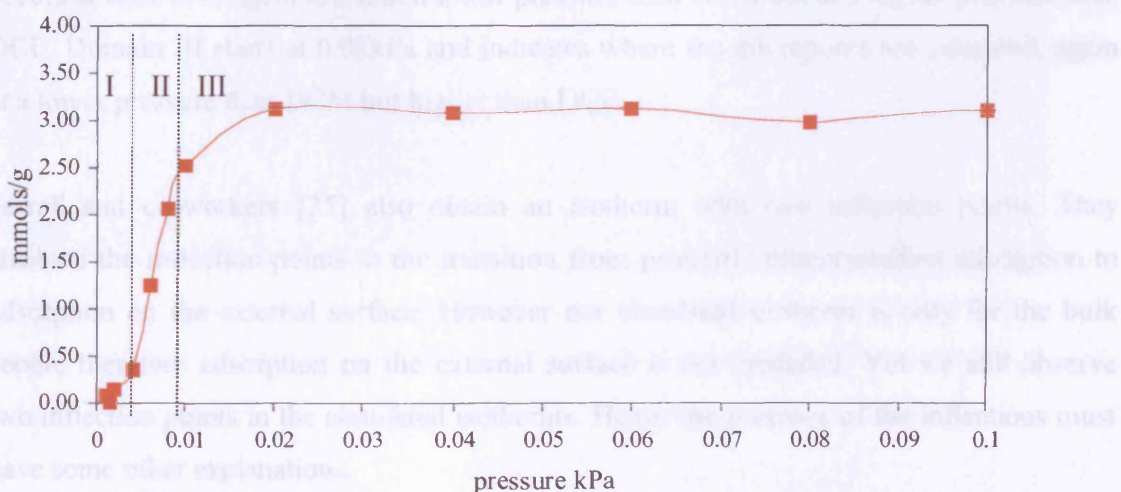


**Figure 5.12:** Domains I, II and III for DCE in FAU.

For DCE the first inflection indicating the end of domain I and start of domain II, occurs at 0.004 kPa and is much less pronounced than in DCM. A second inflection occurs at 0.01kPa and indicates where the micropores are saturated (domain III). Both of these occur at much lower pressures than in the case of DCM.
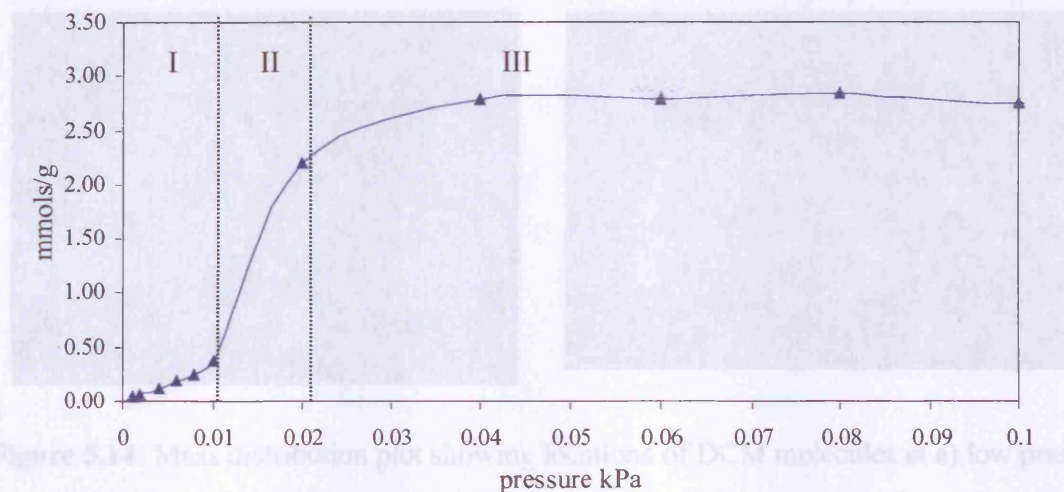


**Figure 5.13:** Domains I, II and III for TCE in FAU.

For TCE the first inflection point, indicating the end of domain I and start of domain II, occurs at 0.01 kPa, again at a much lower pressure than DCM but at a higher pressure than DCE. Domain III starts at 0.02kPa and indicates where the micropores are saturated, again at a lower pressure than DCM but higher than DCE.

Farrell and co-workers [25] also obtain an isotherm with two inflection points. They attribute the inflection points to the transition from primarily intracrystalline adsorption to adsorption on the external surface. However our simulated isotherm is only for the bulk zeolite therefore adsorption on the external surface is not modelled. Yet we still observe two inflection points in the simulated isotherms. Hence the presence of the inflections must have some other explanations.

Figures 5.14 -5.16 show mass distribution plots detailing the distribution of molecules during the simulation at low and high pressures. In all cases it can be seen that at low

150

pressures the molecules the molecules are found to be uniformly distributed throughout the framework structure. At high pressures the molecules are not so evenly spaced out, preferring to occupy certain sites. This may also be a result of steric hindrance due to the larger number of molecules at higher pressures, resulting in a "freezing" effect.
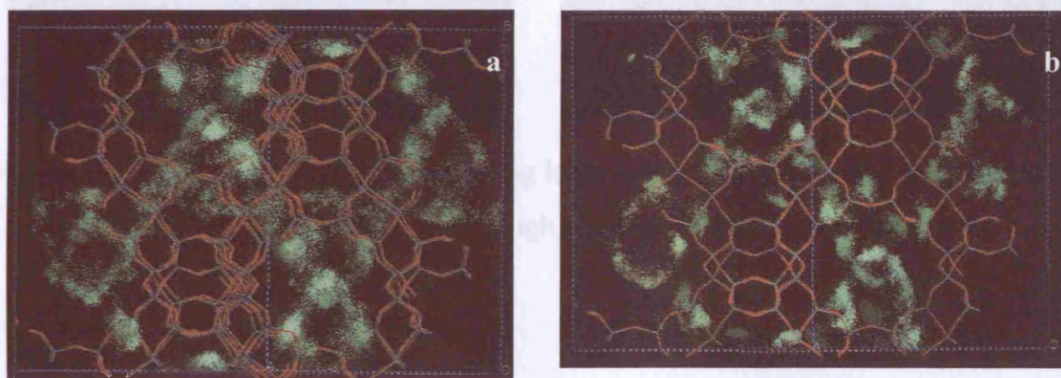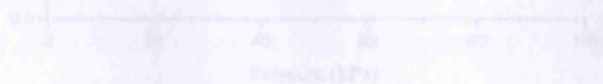


**Figure 5.14:** Mass distribution plot showing locations of DCM molecules at a) low pressure (0.01kPa, 0.62 molecules u/c) and b) high pressure (10.0kPa 50 molecules u/c).
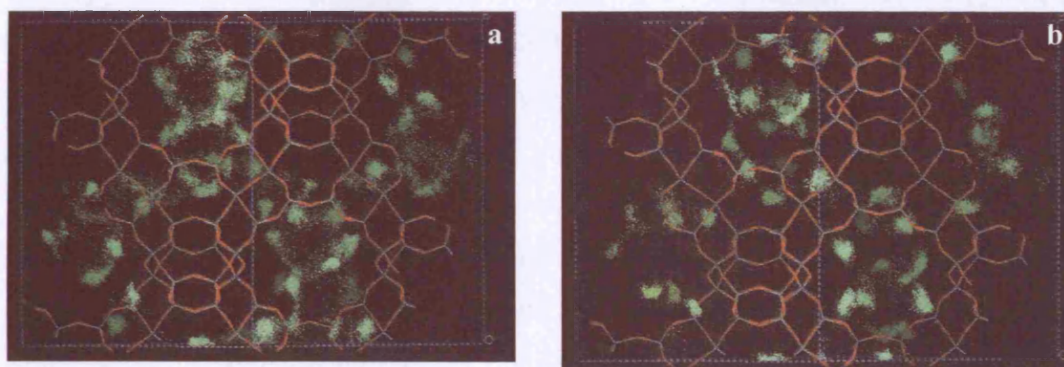


**Figure 5.15:** Mass distribution plot showing locations of DCE molecules at a) low pressure (0.01kPa, 29 molecules/u.c) and b) high pressure (10.0kPa, 37 molecules/u.c).
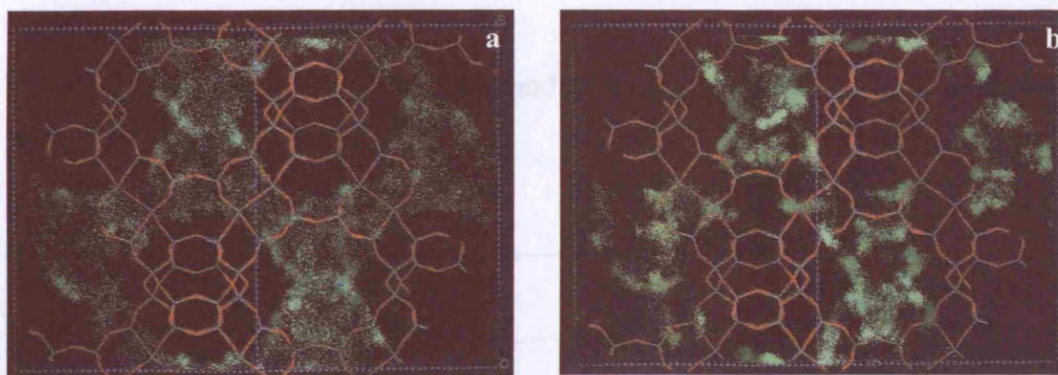
**Figure 5.16:** Mass distribution plot showing locations of TCE molecules at a) low pressure (0.01kPa, 4. molecules/u.c) and b) high pressure (10.0kPa, 35 molecules/u.c).

## 5.6.2 MFI

The adsorption isotherm for DCM, DCE and TCE in the MFI framework is presented in figure 5.17.
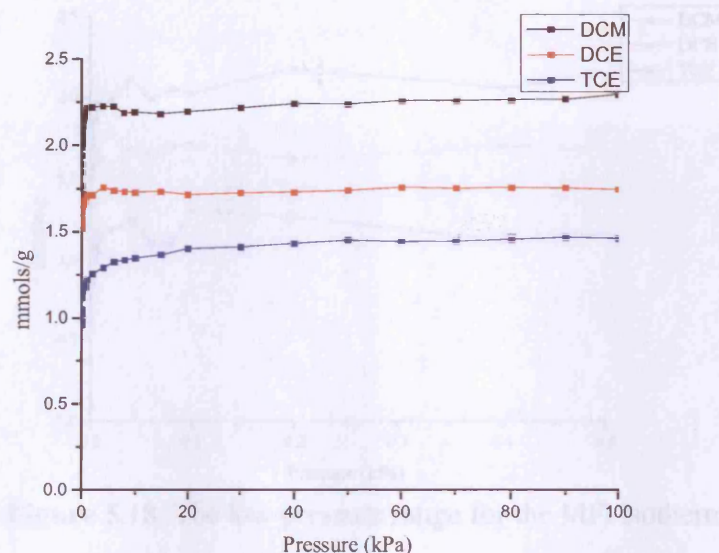


**Figure 5.17:** Adsorption isotherm for adsorbates in MFI.

All three adsorption isotherms appear to be type I isotherms. Type I isotherms are characterised by a rapid increase in the adsorption at low pressures, an inflection point and a long flat branch which is almost horizontal at higher pressures. The assumption is made that in type I isotherms the adsorbed layer is one molecule thick and the plateau corresponds to completion of the monolayer. Smit and Maesen [29] attribute inflections in isotherms to a 'commensurate freezing' effect. According to this, a uniform distribution of the molecules in the zeolite are found at low pressure while at higher pressure almost all the molecules are found to be localised in the sinusoidal channels, leaving the straight channels free for further filling. However, visualisation of the simulated adsorbates in the framework does not confirm this view.

Analysis of the isotherm at low pressures (figure 5.18) does not show a presence of an inflection point as observed for Faujasite. Bouvier and co-workers [26] also observe a type I isotherm for TCE adsorption in Silicalite as do Thompson and co-workers [30]. The

153

isotherm also appears to show much more fluctuation at lower pressures than observed for Faujasite.
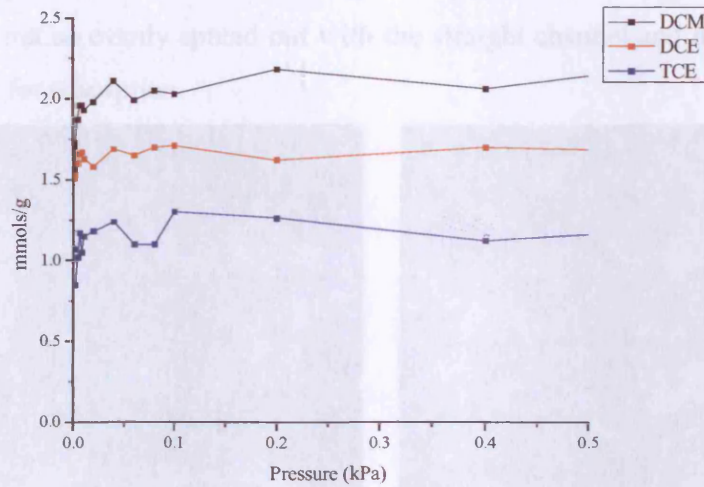


**Figure 5.18**: The low pressure range for the MFI isotherm.

The saturation points for each of the adsorbates in the MFI framework are given in table 5.16.

| Adsorbate | Saturation point mmols/g | Number of molecules per unit cell at saturation point |
|---|---|---|
| DCM | 2.35 | 27 |
| DCE | 1.80 | 21 |
| TCE | 1.52 | 17 |

**Table 5.16:** Saturation point data for adsorbates in MFI.

At the saturation point, as for Faujasite, more DCM is adsorbed followed by DCE and TCE. Once again this can be rationalised by considering how efficiently the molecules are able to pack in the void volume. DCM, being the smallest molecule is able to maximise the use of the space available. On the other hand neither DCE nor TCE are able to fill the whole void volume.

Figures 5.19-5.21 show mass distribution plots for the adsorbates in the MFI frameworks at low (0.01kPa) and higher pressures (10kPa). In all cases the molecules are evenly spaced along the straight and sinusoidal channels at low pressures, whereas at high pressures the molecules are not so evenly spread out with the straight channel and intersection being the preferred sites for adsorption.
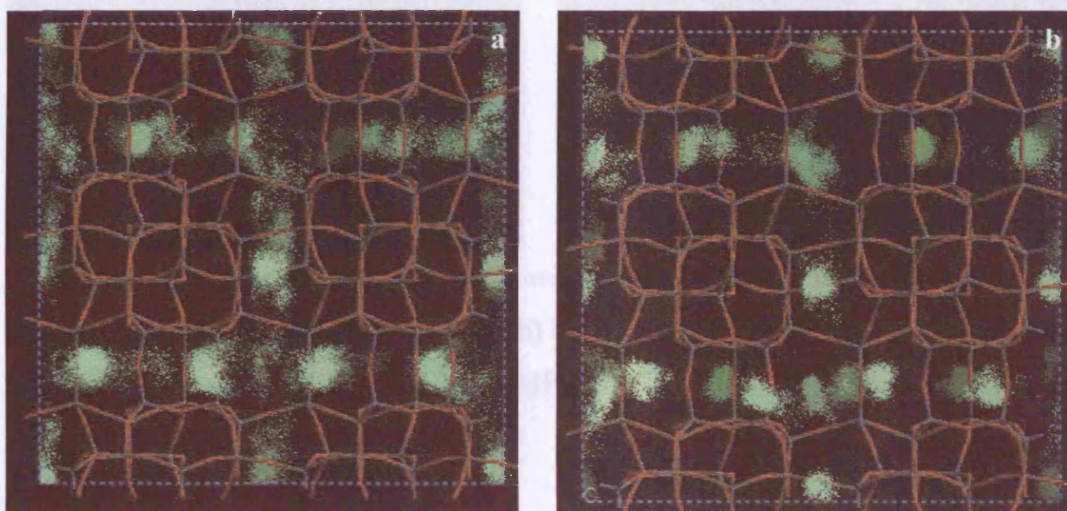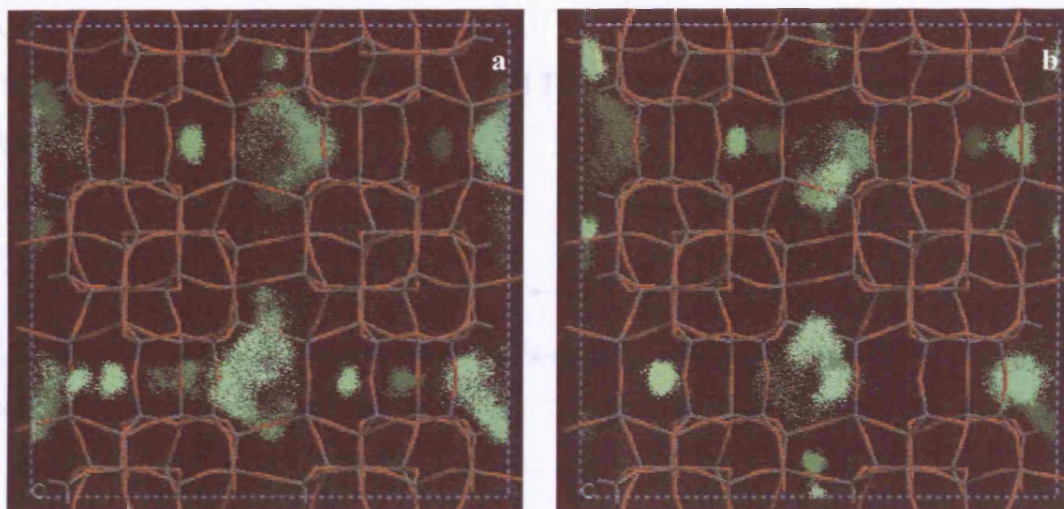


**Figure 5.19:** Mass distribution plot showing locations of DCM molecules at a) low pressure (0.01kPa, 22 molecules/u.c) and b) high pressure (10.0kPa, 26 molecules/u.c) in MFI.
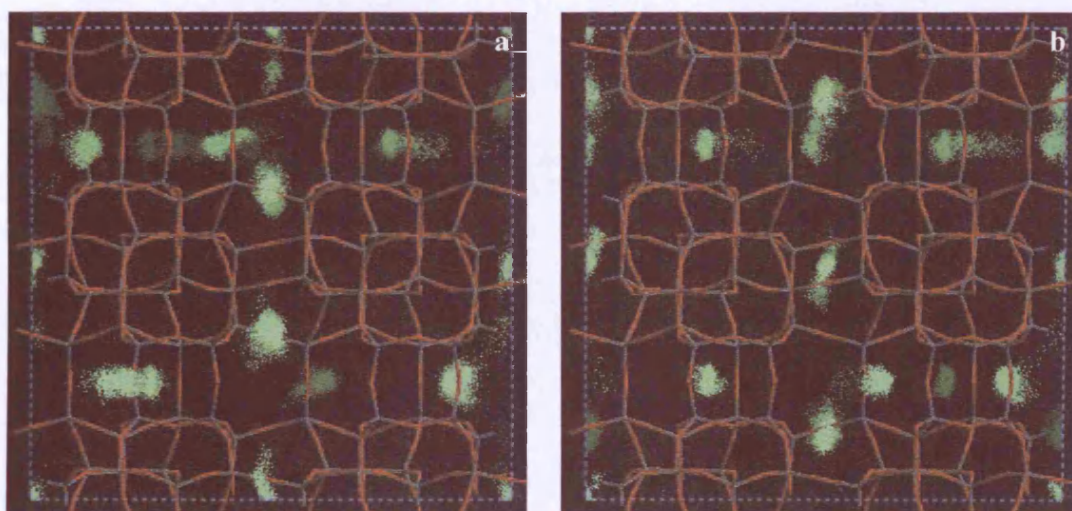


**Figure 5.20:** Mass distribution plot showing locations of DCE molecules at a) low pressure (0.01kPa, 15 molecules/u.c) and b) high pressure (10.0kPa, 21 molecules/u.c) in MFI.

**Figure 5.21:** Mass distribution plot showing locations of TCE molecules at a) low pressure (0.01kPa, 12 molecules/u.c) and b) high pressure (10.0kPa, 16 molecule/u.c) in MFI.

## 5.6.3 Mordenite

The adsorption isotherm for DCM, DCE and TCE in the MOR framework is presented in figure 5.22.
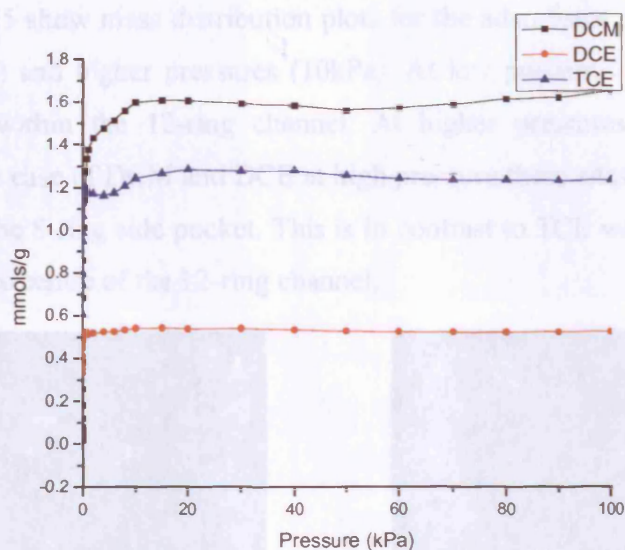


**Figure 5.22:** Adsorption isotherm for adsorbates in MOR.

As for the faujasite and MFI frameworks more DCM is adsorbed. However the trend for TCE and DCE are reversed, with more TCE rather than DCE being adsorbed.

The saturation points for the three adsorbates are presented below:

| Adsorbate | Saturation point mmols/g | Number of molecules per unit cell at saturation point |
|-----------|--------------------------|-------------------------------------------------------|
| DCM | 1.66 | 9 |
| DCE | 0.55 | 6 |
| TCE | 1.32 | 8 |

**Table 5.17:** Saturation point data for MOR.

157

It can be seen that more DCM is adsorbed as for faujasite and MFI frameworks. However, more TCE is adsorbed than DCE, in contrast to results obtained for the other frameworks.

Figures 5.23-5.25 show mass distribution plots for the adsorbates in the MOR frameworks at low (0.01kPa) and higher pressures (10kPa). At low pressures the molecules are fairly evenly spaced within the 12-ring channel. At higher pressures only certain sites are occupied. In the case of DCM and DCE at high pressure these sites are found to be close to the opening of the 8-ring side pocket. This is in contrast to TCE which at high pressures is found to be in the centre of the 12-ring channel.
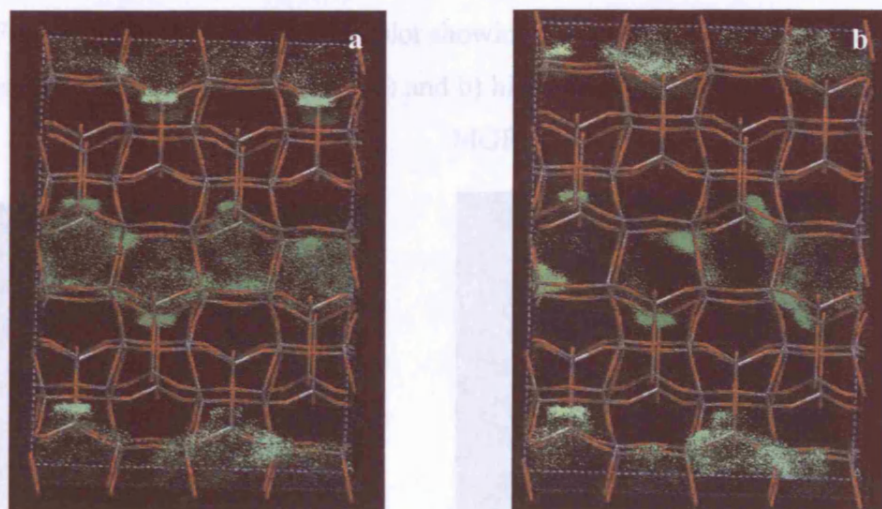


**Figure 5.23:** Mass distribution plot showing locations of DCM molecules at a) low pressure (0.01kPa, 0.7 molecules/u.c) and b) high pressure (10.0kPa, 9 molecules/u.c) in MOR.
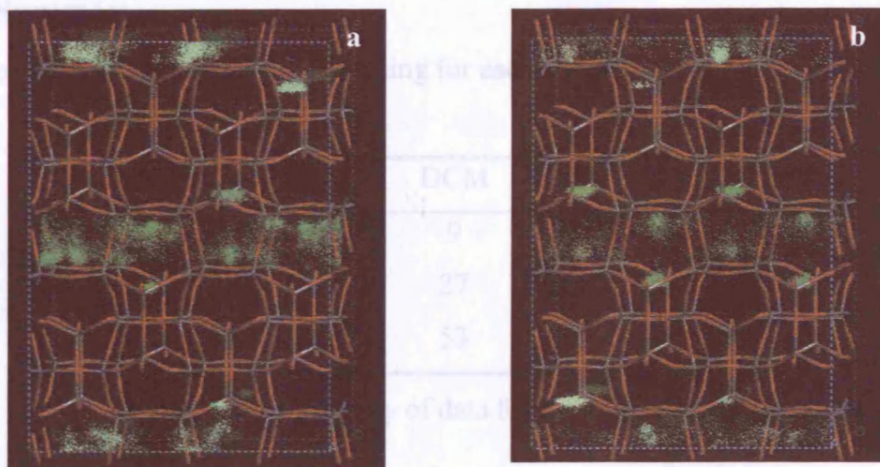
**Figure 5.24:** Mass distribution plot showing locations of DCE molecules at a) low pressure (0.01kPa, 4 molecules/u.c) and b) high pressure (10.0kPa, 6 molecules/u.c) in MOR.
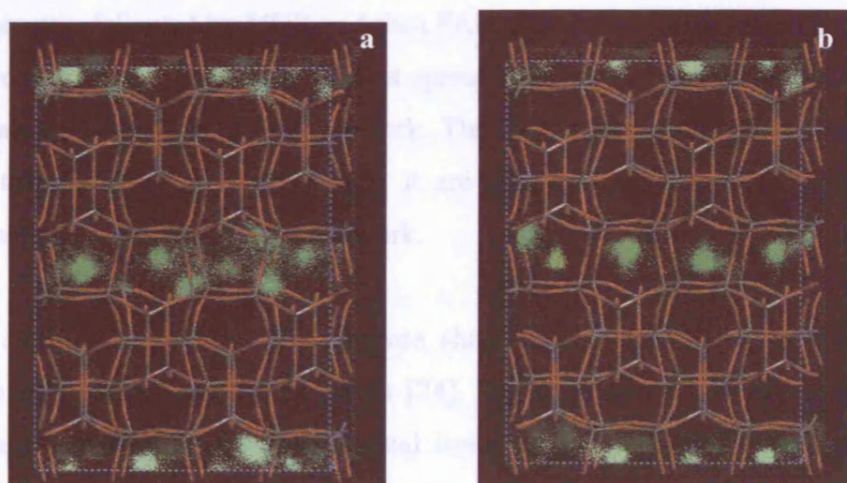


**Figure 5.25:** Mass distribution plot showing locations of TCE molecules at a) low pressure (0.01kPa, 5 molecules/u.c) and b) high pressure (10.0kPa, 7 molecules/u.c) in MOR.

## 5.7 Summary

Table 5.18 shows the maximum loading for each framework and sorbate molecule.

|      | DCM | DCE | TCE |
|------|-----|-----|-----|
| MOR  | 9   | 6   | 8   |
| MFI  | 27  | 21  | 17  |
| FAU  | 53  | 39  | 37  |

**Table 5.18:** Summary of data for three framework structures.

Our results show that increasing the pressure results in more molecules being accommodated into the zeolite framework. The faujasite framework accommodates the most molecules as it has the largest void volume. This is followed by MFI and then MOR framework structures. Our results also show that overall adsorption is strongest in the MFI framework, followed by MOR and then FAU. This trend follows that of the pore sizes. The molecules in the smaller pore cannot spread themselves out and therefore have maximum interaction with the zeolite framework. The FAU framework has the largest void volume and the molecules enclosed within it are able to spread out and therefore have fewer interactions with the zeolite framework.

The simulated isotherms for faujasite show good agreement with experimental results obtained by Clausse and co-workers [24]. The simulated isotherms are able to model the domains obtained in the experimental isotherm, although simulations at lower pressures would make them more obvious.

## References

(1)     Kayser, H. *Wied. Ann.* **1881**, *14*, 450.

(2)     Bosch, E.; Huber, S.; Weitkamp, J.; Knözinger, H. *Phys. Chem. Chem. Phys.* **1999**, *1*, 579

(3)     Halasz, I.; Kim, S.; Marcus, B. *Molecular Physics* **2002**, *100*, 3123

(4)     van Koningsveld, H.; Tuinstra, F.; van Bekkum, H.; Jansen, J. C. *Acta. Cryst.* **1989**, *B45*, 423.

(5)     Garrot, B.; Couderc, G.; Simonet-Grange, M. H.; Stoeckli, F. *Micropor. Mesopor. Mater* **2002**, *52*, 199.

(6)     Bates, S.; Dwyer, J. *J. Phys. Chem* **1993**, *97*, 5897.

(7)     Freeman, C. M.; Catlow, C. R. A.; Thomas, J. M. *Chem. Phys. Letters* **1991**, *186*, 137.

(8)     Fuchs, A. H. *J. Phys. Chem B* **2001**, *105*, 7375

(9)     Shah, R.; Payne, M. C.; Gale, J. D. *Int. J. of Quantum Chem.* **1997**, *61*, 393.

(10)    Smit, B.; Krishna, R. *Curr. Opin. Solid State and Mat. Sci.* **2001**, *5*, 455.

(11)    Lacher, J. R. *Proc. Camb. Phil. Soc* **1937**, *33*, 518.

(12)    Fowler, R. H.; Guggenheim, E. A. *Statistical Thermodynamics*; Cambridge University Press, 1939.

(13)    Thomas, J. M.; Thomas, W. J. *Principles and practice of heterogeneous catalysis*; VCH: New York, 1997.

(14)    Rees, L. V. C.; Shen, D. Adsorption of gases in zeolite molecular sieves. In *Studies in Surface Science and Catalysis*; Bekkum, H. v., Flanigen, E. M., Jacobs, P. A., Jansen, J. C., Eds., 2001; Vol. 137.

(15)    Brunauer, S. *J. Am. Chem. Soc* **1940**, *62*, 1723.

(16)    Nicholson, D.; Parsonage, N. G. *Computer Simulation and the Statistical Mechanics of Adsorption*; Academic Press, 1982.

(17)    Eder, F.; Lercher, J. A. *Zeolites* **1997**, *18*, 75.

(18)    Mellot, C. F.; Cheetham, A. K. *J. Phys. Chem B* **1999**, *103*, 3864

(19)    Hagler, A. T.; Lifson, S.; Daube, J. *J. Am. Chem. Soc* **1979**, *101*, 5122.

(20) Kramer, G. J.; Farragher, N. P.; Beest, B. W. H. v.; Santen, R. A. v. **1991**, *43*, 5068.

(21) Ghermani, N. E.; Lecomte, C.; Dusausoy, Y. **1996**, *53*.

(22) Auerbach, S. M.; Jaramillo, E. *J. Phys. Chem* **1999**, *103*, 9589.

(23) Accelrys Inc *Sorption Manual, Release 4.5* San Diego, June 2000.

(24) Clausse, B.; Garrot, B.; Cornier, C.; Paulin, C.; Simonot-Grange, M. H.; Boutros, F. *Micropor. Mesopor. Mater.* **1998**, *25*, 169.

(25) Farrell, J. *Micropor. Mesopor. Mater* **2003**, *59*, 205.

(26) Bouvier, F.; Weber, G. *J. Thermal Anal* **1998**, *54*, 881.

(27) Anderson, M. A. *Environ. Sci. Technol.* **2000**, *34*, 725.

(28) Biosym/MSI *Solids Docking Manual* San Diego, October 1995.

(29) Smit, B.; Maesen, J. L. M. *Nature* **1995**, *374*, 42.

(30) Giaya, A.; Thompson, R. W.; Denkewicz, R. *Micropor. Mesopor. Mater* **2000**, *40*, 205.

# Chapter Six: Molecular Dynamics Simulation of DCM, DCE and TCE in FAU

## 6.1 Introduction

The previous chapters have focussed on the various static simulation techniques that can be employed to investigate the adsorption of DCM, DCE and TCE in FAU, MOR and MFI framework structures. This chapter differs from those by investigating the motion of the adsorbate molecules within the zeolite micropores.

## 6.1.1 Diffusion

Diffusion in gases and solids has been extensively studied for more than a century. The discovery of Brownian motion, which is closely related to diffusion, contributed to the understanding of the atomic view of matter and led to the kinetic theory of gases and liquids. Diffusion is caused by the thermal motion and subsequent collision of molecules.

There are two types of diffusion that can take place within zeolite pores; transport diffusion, which occurs as a result of a concentration gradient, and self-diffusion, which occurs within a single-component system at equilibrium. Diffusion within zeolitic pores differs to bulk diffusion in a number of ways, primarily because the molecules have to move through channels with molecular dimensions. The diffusing molecules therefore experience a constant interaction with the zeolite framework atoms. The diffusion of the molecules is also strongly influenced by the size and shape of the channels as well as other factors such as temperature and adsorbent concentration. Another class of diffusion specific to zeolites is single-file diffusion, which occurs in one-dimensional zeolites such as MOR and results from the fact that the channels are not wide enough to allow more than one molecule to pass through at a time. Thus the molecules have to diffuse through the channels in a single file, which significantly reduces the mobility of adsorbates in these systems.

The diffusion of molecules within zeolites can be separated into different regimes depending on the size of the pores, which is illustrated in figure 6.1 [1]. For large pore

diameters, i.e. those greater than 1μm, also referred to as macropores, collisions between molecules are far more prevalent than those between the molecules and the zeolite wall. Thus molecular diffusion is the dominant mechanism and diffusion co-efficients are of the order of $10^{-5} m^2 s^{-1}$. With decreasing pore size the number of collisions between the diffusing molecules and the zeolite framework atoms increases until it becomes smaller than the mean free path i.e. the average distance travelled between two molecules between two collision. At this point the Knudsen diffusion regime comes into operation and diffusion becomes dependent on the pore diameters. At smaller pore diameters, i.e. those that are around 20Å or less the pore diameter becomes comparable to that of the molecule. Thus the diffusing molecule will experience a constant interaction with the zeolite wall and configurational diffusion starts to occur. Diffusion in zeolites usually takes place in this regime and is strongly dependent on the pore size and shape, the connectivity of the zeolite channels, the shape of the diffusing molecule and the interaction between the molecules and the zeolite wall. Configurational diffusion is an activated process with the energy of activation arising largely from steric hindrance. Due to the small distances between the molecules and the zeolite wall the diffusion in this regime is comparable to the diffusion of molecules that are weakly bonded to a surface [2].
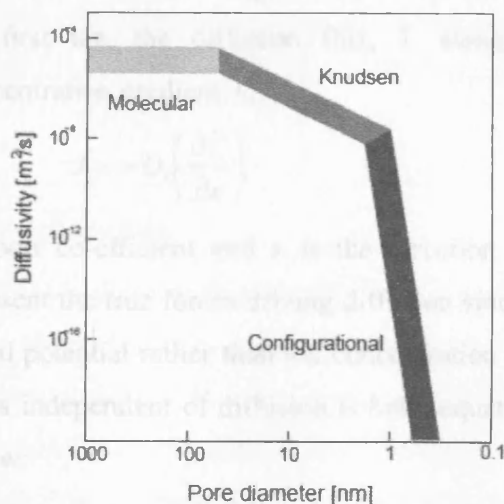


**Figure 6.1**: The different diffusion regimes in zeolites.

Studying diffusion in zeolites is important industrially, for instance to describe and predict the mass transfer through fixed-bed reactors in separation and catalytic processes. From a theoretical perspective studying diffusion allows a detailed study of the interactions between the molecules and the zeolitic framework particularly since differences in zeolite topology can change diffusive behaviour markedly. Indeed theoretical methods are receiving increased interest as they enable diffusion to be studied in a relatively inexpensive and time-effective manner [3,2]. A number of factors that affect the motion of molecules within the zeolite, such as temperature effects and adsorbent concentration can be studied relatively easily. Further, the results obtained through simulations can focus and enhance understanding of experimental results.

## 6.1.2 Transport diffusion and Self-Diffusion

There are two types of diffusion that can take place; transport diffusion, which occurs as a result of a concentration gradient and self-diffusion, which occurs within a single-component system at equilibrium.

## 6.1.3 Transport diffusion - Fickian Diffusion

The theory of diffusion was studied in great detail by Fick in the $19^{th}$ century [4]. According to Fick's first law the diffusion flux, J, along a particular direction is proportional to the concentration gradient, C:

$$J = -D_t \left( \frac{\partial C}{\partial x} \right)$$

6.1

where $D_t$ is the transport co-efficient and x is the direction of the flux. However this equation does not represent the true forces driving diffusion since diffusion is driven by the gradient of the chemical potential rather than the concentration gradient. If the assumption that the concentration is independent of diffusion is held, equation 6.1 can be transformed to give Fick's second law:

$$\frac{\partial C}{\partial t} = -D_t \left( \frac{\partial^2 C}{\partial x^2} \right)$$

6.2

This equation gives the change of concentration with time. Work conducted by Barrer and Jost assumed the diffusivity to be isotropic throughout the crystal, as $D_t$ is independent of the direction in which the particles diffuse [5].

## 6.1.4 Self-Diffusion

As opposed to transport diffusion, which requires a concentration gradient, self-diffusion occurs at equilibrium. Under equilibrium conditions, self-diffusivity can be related to a microscopic quantity called the Mean Squared Displacement (MSD) by the Einstein relation, which was determined during Einstein's study of Brownian motion [6,7]. The MSD is defined as:

$$< r^2(t) > \ = \ <| \vec{r}(t) - \vec{r}(0) |^2 > \ = \frac{1}{N} \sum_{i=1}^{N} (\vec{r}_i(t) - \vec{r}_i(0))^2 \qquad 6.3$$

where N is the number of particles in the system and $\vec{r}_i$(t) is the position of the particle $i$ at time t. This can be related to the self-diffusivity by:

$$D_s = \frac{1}{6} t \left[ <| \vec{r}(t) - \vec{r}(0) |^2 > \right] \qquad 6.4$$

## 6.1.5 Factors affecting diffusivity

Several factors can affect the diffusion of the adsorbate molecules within the zeolite channels. These include adsorbent concentration and temperature, which will now be discussed.

## 6.1.6 Adsorbent concentration

The concentration of the adsorbent molecules can strongly affect the diffusivity. As the molecules diffuse in the channels where it may not be possible for molecules to pass each other, intermolecular interactions will have an affect on their collective diffusivity. Studies by Barrer relate the concentration dependence and diffusivity in zeolites using a simple jump model [5]. According to this model it is assumed that the movement of a molecule from one site to another has an elementary diffusion rate $D_s^0$. The diffusivity will then be proportional to the likelihood of the neighbouring site being empty:

$$D_s(\theta) = D_s^0 \cdot (1-\theta) \qquad 6.5$$

where $\theta$ is the coverage. However it has been shown by a number of authors that the actual situation is somewhat more complicated and that correlation effects also strongly influence the diffusivity [8,9].

According to PFG (Pulse Field Gradient)-NMR measurements by Karger and Pfeifer [10], there are five different types of concentration dependence on the diffusion, analogous to the IUPAC designations for adsorption isotherms and is illustrated in figure 6.2. These different dependences can be attributed to differences in the interaction between the adsorbate and the framework atoms. The type IV profile is most commonly associated with molecular diffusion in zeolites. In this case, the rate of diffusion increases until a critical point is reached where the rate of diffusion remains constant and further increases cause the rate of diffusion to decrease.
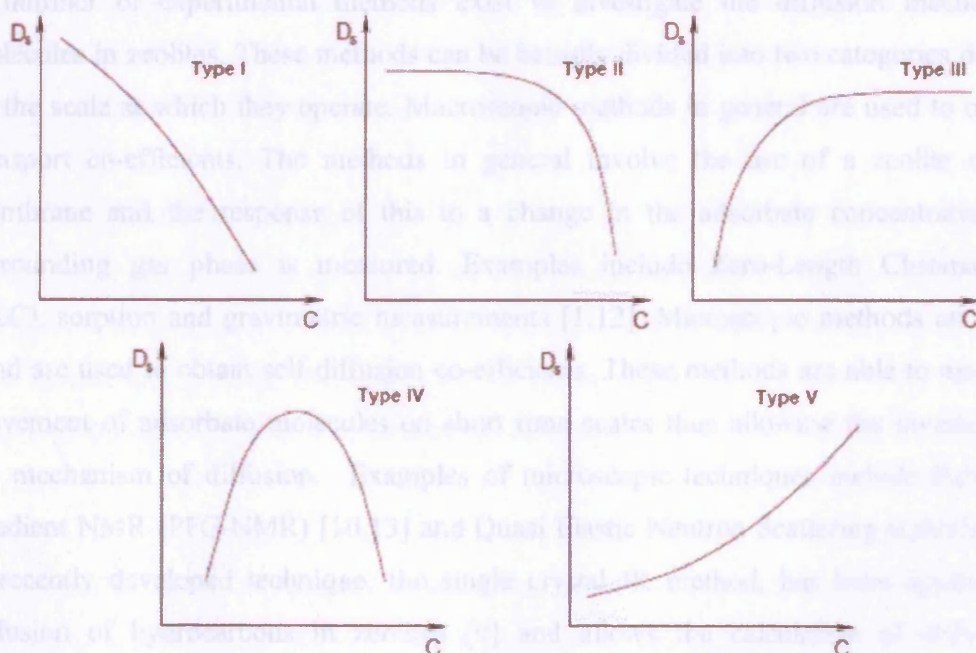


**Figure 6.2:** Five types of concentration dependence on diffusivity.

## 6.1.7 Temperature dependence

Diffusion in zeolites in most cases is an activated process, since it increases with temperature, and the manner in which diffusion takes place is referred to as Jump

Diffusion. In this case a molecule, which closely match the pore size tends to occupy a particular site in the host structure, vibrating until its energy is high enough to surmount the energy barrier needed to jump to a different site. It is generally expected for the self-diffusivities to exhibit Arrhenius temperature dependence [11]:

$$D(T) = D_0 \cdot \exp\left[-\frac{E_{act}}{RT}\right]$$

6.6

where $D_0$ represents the diffusivity at an infinite temperature and relates to the rate of diffusion at which particles attempt to jump to an adjacent adsorption site. $E_{act}$ represents the energy barrier that the adsorbate must overcome in order to move to a neighbouring site. R is the Boltzmann factor and T the temperature. Thus the above expression assumes that diffusion occurs via a series of activated hops.

## 6.1.8 Experimental Methods of studying diffusion

A number of experimental methods exist to investigate the diffusion mechanism of molecules in zeolites. These methods can be broadly divided into two categories depending on the scale at which they operate. Macroscopic methods in general are used to obtain the transport co-efficients. The methods in general involve the use of a zeolite crystal or membrane and the response of this to a change in the adsorbate concentration in the surrounding gas phase is measured. Examples include Zero-Length Chromatography (ZLC), sorption and gravimetric measurements [1,12]. Microscopic methods on the other hand are used to obtain self-diffusion co-efficients. These methods are able to measure the movement of adsorbate molecules on short time scales thus allowing the investigation of the mechanism of diffusion. Examples of microscopic techniques include Pulsed Field Gradient NMR (PFG-NMR) [10,13] and Quasi Elastic Neutron Scattering (QENS)[14,15]. A recently developed technique, the single crystal IR method, has been applied to the diffusion of hydrocarbons in zeolites [9] and allows the calculation of diffusion co-efficients in different directions. These techniques vary in terms of the time and length scales at which they operate as well as their different assumptions made when collecting and analysing data. These differences make it harder for results obtained by different techniques to be compared and as such large discrepancies exist between the data collected by different techniques.

## 6.1.9 The Levitation Effect

A systematic investigation of the diffusion co-efficients, rates of intercage diffusion, and cage passings of monatomic spherical adsorbates in NaY was conducted using molecular simulation methods by Yashonath and co-workers [16]. The study included both rigid and flexible framework structures. They observed a peak in the diffusion co-efficients when the diameter of the adsorbate approached the pore diameter. This peak however was less pronounced in the flexible framework model. This effect may explain the fact that at times very high mean square displacements are obtained for molecules diffusing at low temperatures.

The levitation effect, also referred to the "ring effect" or "superdiffusivity effect", may be explained by the fact that the radial force acting on the adsorbate molecule is almost zero when the size of the adsorbate is comparable to that of the pore it is passing through. In effect the sorbate is "floating" through the pore or channel.

## 6.2 Molecular Dynamics

Molecular Dynamics methods can be used to investigate the microscopic mechanism of diffusion of adsorbates in zeolitic systems. During a given reaction the adsorbed molecules must diffuse to the active site, react, and the products then diffuse out of the pores. Thus studying diffusion processes is crucial in enhancing our understanding of the reaction scheme.

The molecular dynamics approach was first introduced to zeolite modelling some 25 years ago. Initial work focused on the diffusion of simple atoms such as argon and xenon and the zeolite lattices were treated as rigid [2]. Subsequent work involved modelling more complicated molecules such as benzene, cyclohexane, other hydrocarbons and water [17,18,19]. Recent increases in computer technology have allowed the modelling of flexible framework structures. Inclusion of framework vibrations has been shown to make a marked difference to the diffusion of molecules that closely match the pore diameter of the

framework it is diffusing in. Indeed the diffusivities for a flexible framework have been shown to be 30 – 50% greater than in the rigid framework [3].

Advances in computer technology have also resulted in molecular dynamics studies becoming widespread. The molecular dynamics method involves generating successive configurations of a system by solving Newton's laws of motion to obtain a trajectory that specifies how the positions and velocities of the particles in the system vary with time. The time step chosen must be smaller than any important dynamical process such as atomic vibration. This is typically in the order of a few femtoseconds for purely siliceous framework structures. Incorporation of aluminium and charge-balancing cations into the framework however results in the dynamics simulations becoming prohibitively slow. In order to perform a dynamics calculation a description of the interparticle interactions is needed. This is typically done by introducing a forcefield and the quality of the results obtained will depend on the quality of the forcefield parameters. The method has been successfully applied to modelling both single and more recently, multi-component diffusion.

## 6.2.1 The technique – background

Molecular Dynamics (MD) methods are used to investigate the changes in a system over a period of time [2][20]. The MD method works by simulating the motion of a system of particles with respect to the forces present. The change in the system can be described by solving Newton's second law of motion:

$$F_i = m_i a_i \qquad\qquad 6.7$$

Where F is the force acting on the $i^{th}$ particle, m is its mass and a is its acceleration. This equation can be rearranged so that the acceleration can be written as the second derivative of displacement (s) with respect to time, to give a more useful version of Newton's second law:

$$\frac{\delta^2 s}{\delta t^2} = \frac{F_i}{m_i} \qquad\qquad 6.8$$

This differential must be solved for every particle in the system in order to obtain information about the time evolution of the system. Integrating this with respect to time gives the following expression:

$$\frac{\delta s_i}{\delta t} = \left(\frac{F_i}{m_i}\right)t + c_1 \qquad\qquad 6.9$$

Initially, at time t=0 the first term disappears and the velocity is given by the term $c_1$. Using this we can obtain an expression for the velocity at any time:

$$\frac{\delta s_i}{\delta t} = a_i t + u_i \qquad\qquad 6.10$$

Integrating further with respect to time gives:

$$s_i = u_i t + \frac{1}{2}a_i t^2 + c_2 \qquad\qquad 6.11$$

where the constant c represents the current position. Using these equations the initial displacement can be calculated from an initial velocity $u_i$ as well as the acceleration which

can be derived from $a_i = \dfrac{F_i}{m_i}$.

Various algorithms exist to solve these equations, the most common being the Verlet method used in this study [21]. If the average velocity over the time step $\Delta t$ is given by v, then the new position R is given by:

$$R(t + \Delta t) = R(t) + v\Delta t \qquad\qquad 6.12$$

By assuming that $v$ is equal to the velocity at the midpoint of the time interval and the average acceleration between the time periods $t - \Delta t$ and $t + \Delta t$:

$$v(t + \frac{\Delta t}{2}) = v\left(t - \frac{\Delta t}{2}\right) + a\Delta t \qquad\qquad 6.13$$

where a, the acceleration can be calculated from $m^{-1}F(x,t)$. By substitution of this equation into 24 the new position may be obtained:

$$R(t + \Delta t) = R(t) + v(t - \frac{\Delta t}{2}) + m^{-1}F(x,t)\Delta t \qquad\qquad 6.14$$

The first step in conducting a molecular dynamics simulation is to build a model of the system using one of the several visualisers available. Once the program has specified a starting point, an energy minimisation is conducted to obtain a stable starting structure. An energy minimisation is needed due to the fact that there may be strains on the system as a result of inaccurate representation of the geometry. These strains could potentially affect

the results of the simulation by producing unusually large forces for some of the atoms. At the end of a minimisation run the conformation is one that is likely to be assumed at zero Kelvin. Having minimised the system the next stage is the molecular dynamics run. This consists of two parts. First an equilibration, at the end of which the system reaches a configuration consistent with the target temperature, and a production run where data on the behaviour of the system is collected. At the end of a dynamics simulation a trajectory is generated which specifies how the positions and velocities of the molecules vary with time.

Periodic Boundary Conditions (PBC) are usually applied whereby the unit cell is replicated in three dimensions thus allowing simulation of the bulk system and minimising surface effects. The statistical mechanical ensemble generated by the molecular dynamics run is usually the microcanonical, NVE, ensemble where the number of particles, volumes, and total energy are kept constant. The atoms are initially given random velocities depending on the temperature the system is at, using a random number generator and according to the Maxwell-Boltzmann distribution. During the production run Newton's Laws of Motion are solved in an iterative manner. In each time-step the velocities of the atoms in the cell are updated. The process is repeated several thousands of times to allow a picture to be built of the time evolution of the system.

Periodic Boundary Conditions (PBC) are usually applied in molecular dynamics simulations whereby the unit cell is replicated in three dimensions thus allowing simulation of the bulk system and minimising surface effects. The statistical mechanical ensemble generated by the molecular dynamics run is usually the microcanonical, NVE, ensemble where the number of particles, volumes, and total energy are kept constant. The atoms are initially given random velocities depending on the temperature the system is at, using a random number generator and according to the Maxwell-Boltzmann distribution. During the production run Newton's Laws of Motion are solved in an iterative manner. In each time- step the velocities of the atoms in the cell are updated. The length of the time-step must be smaller than any important dynamical process such as atomic vibration. The process is repeated several thousands of times to allow a picture to be built of the time evolution of the system.

## 6.3 Overview of Study

The aim of a molecular dynamics simulation is to investigate the effect of temperature and loading on self-diffusion of DCM, DCE and TCE in the siliceous FAU framework and also to elucidate the microscopic diffusion mechanism of these adsorbate molecules within the structure. The trajectory files generated at the end of a molecular dynamics run are used to obtain the mean squared displacements and diffusion co-efficients. The motion of the molecules are also analysed and discussed.

## 6.4 Methodology

Molecular Dynamics calculations were performed on DCM, DCE and TCE in the FAU framework structure. The initial starting configurations were generated using the Monte Carlo docked structures obtained and analysed in chapter 4. For details of the docking calculations the reader is referred to section 5.4. The structures were then minimised using GULP [22] prior to the Molecular Dynamics simulation. The details of the potential used for the minimisation have been given in section 5.3. The static modeling of the adsorbate-zeolite system enabled the validity of the potentials to be tested.

All molecular dynamics simulations were conducted using the DL_POLY [23] software suite. The Velocity Verlet algorithm was used to integrate Newton's equations of motion. All the calculations were performed within the isokinetic NVT ensemble with a Nosé-Hoover thermostat. A time-step of 0.001ps was used and a cut-off was set to 9.5Å. The zeolite framework was assumed to be fully flexible but the cell parameters remained fixed.

The system was allowed to equilibriate for 80000 time steps to ensure a stable starting configuration with constant system energy. The subsequent dynamics run was conducted for 500000 time steps. The trajectory was recorded every 200 steps whilst the radial distribution function was recorded every 1000 steps.

## 6.5 Results

The results for each of the adsorbates in the FAU framework are now presented. In particular details of the MSD, obtained from the trajectory files generated at the end of the simulation are given. This in turn enables the diffusivity to be calculated. All calculations were conducted at temperatures between 300K and 700K in increments of 50K and at different loadings. The diffusivities at each temperature, for a particular loading, can also be plotted to yield Arhennius plots.

## 6.5.1 DCM in FAU

The mean squared displacements (MSD), a measure of how far the molecule has moved during the simulation, are presented for DCM in FAU in figure 6.3. These are followed by the diffusion co-efficients, which are tabulated for the various loadings and temperatures. These MSD plots are subsequently analysed to give Arrhenius plots, which allow the extrapolation of activation energies.

Figure 6.3a-c show the MSD plots for diffusion of DCM in FAU at low loadings as a function of temperature (2, 4 and 8 molecules per unit cell). The plots show that at these low loadings the MSD increases with temperature. The plots are relatively linear over the timescale of the simulation, which indicates unrestricted three-dimensional diffusion within the zeolite system with MSD values of up to 3500Å at higher temperatures. The slight fluctuations in the MSDs at low loadings (2 molecules per unit cell) are due to unreliable statistics at the end of the simulations.
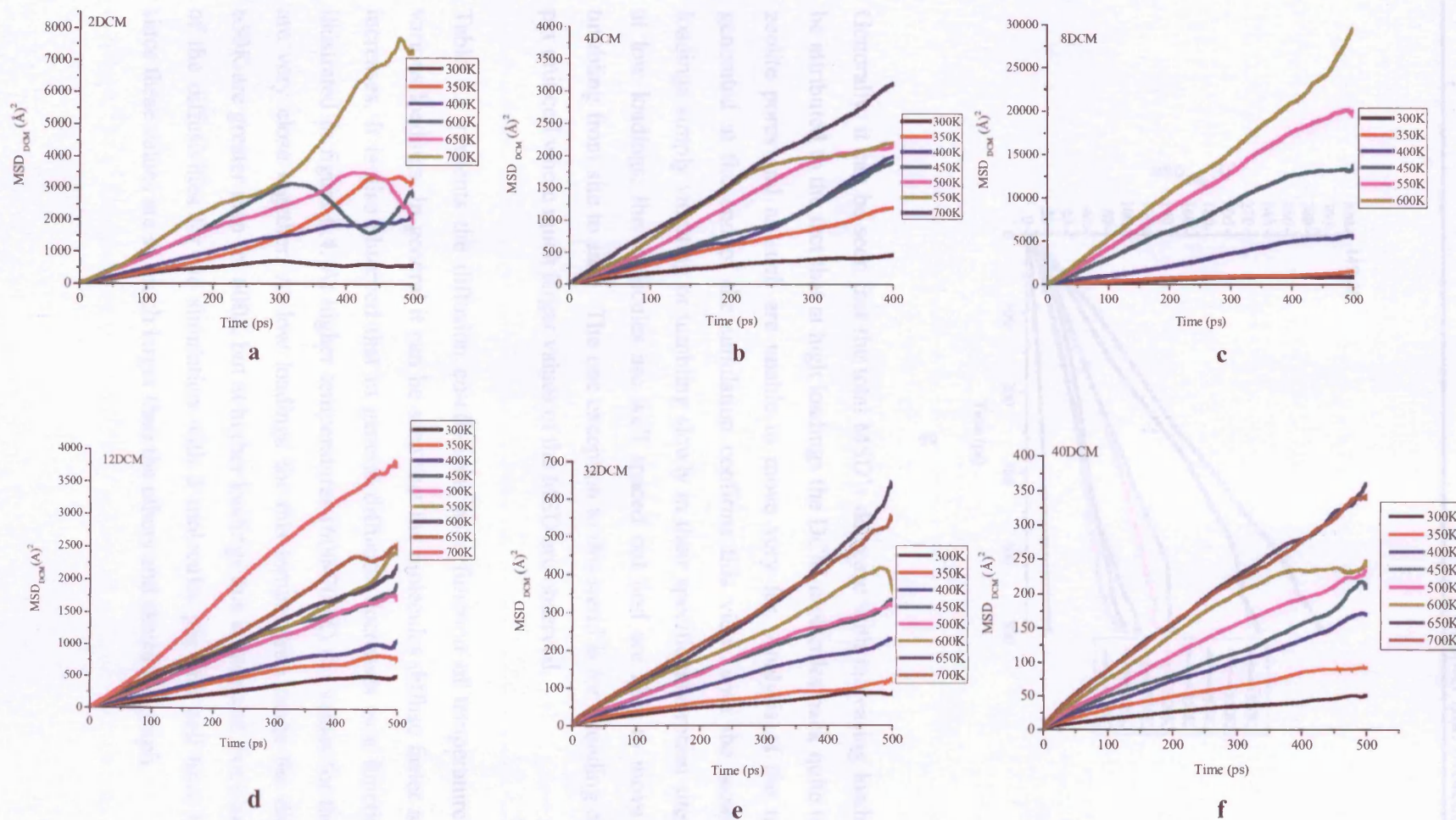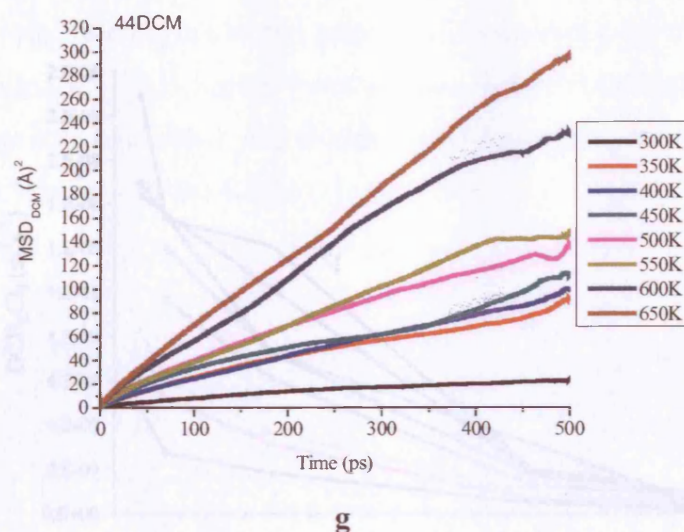
**Figure 6.3:** MSD plots for DCM in FAU at low loadings (a –c), intermediate loading (d) and high loading (e-g (overleaf)).

g

Generally, it can be seen that the total MSD's decrease with increasing loading. This may be attributed to the fact that at high loadings the DCM molecules pack quite tightly into the zeolite pores and as such are unable to move very far. Analysis of the trajectory files generated at the end of the simulation confirms this view, with the molecules at high loadings simply vibrating or tumbling slowly in their specific adsorption sites. In contrast, at low loadings, the molecules are well spaced out and are able to move freely, again tumbling from site to site. The one exception to this trend is for a loading of 8 molecules per unit cell where much larger values of the MSD are observed.

Table 6.1 presents the diffusion co-efficients as a function of temperature for DCM at various loadings. In general it can be seen that the molecules diffuse faster as temperature increases. It is also observed that in general diffusion decreases as a function of loading illustrated in figure 6.4. At higher temperatures (600-700K) the values for the diffusivities are very close together. At low loadings for this temperature range the diffusivities for 650K are greater than for 600K but at higher loadings this is reversed. For clarity the values of the diffusivities for the simulation with 8 molecules per unit cell have been omitted, since these values are so much larger than the others and skews the graph.

**Figure 6.4:** Diffusivity for DCM in FAU as a function of loading.

| Temperature | 2DCM | 4DCM | 8DCM | 12DCM | 32DCM | 40DCM | 44DCM |
|---|---|---|---|---|---|---|---|
| 300K | $4.77 \times 10^{-9}$ | $2.72 \times 10^{-9}$ | $3.85 \times 10^{-9}$ | $1.82 \times 10^{-9}$ | $4.68 \times 10^{-10}$ | $2.54 \times 10^{-10}$ | $1.34 \times 10^{-10}$ |
| 350K | $6.32 \times 10^{-9}$ | $5.18 \times 10^{-9}$ | $6.16 \times 10^{-9}$ | $3.17 \times 10^{-9}$ | $6.12 \times 10^{-10}$ | $4.84 \times 10^{-10}$ | $4.12 \times 10^{-10}$ |
| 400K | $8.29 \times 10^{-9}$ | $6.01 \times 10^{-9}$ | $1.74 \times 10^{-8}$ | $3.70 \times 10^{-9}$ | $9.41 \times 10^{-10}$ | $6.57 \times 10^{-10}$ | $4.02 \times 10^{-10}$ |
| 450K | | $6.78 \times 10^{-9}$ | $5.10 \times 10^{-8}$ | $6.15 \times 10^{-9}$ | $1.26 \times 10^{-9}$ | $7.86 \times 10^{-10}$ | $5.16 \times 10^{-10}$ |
| 500K | | $9.63 \times 10^{-9}$ | | $6.2 \times 10^{-9}$ | $1.25 \times 10^{-9}$ | $9.75 \times 10^{-10}$ | $6.45 \times 10^{-10}$ |
| 550K | | $1.20 \times 10^{-8}$ | $7.10 \times 10^{-8}$ | $7.26 \times 10^{-9}$ | | | $6.29 \times 10^{-10}$ |
| 600K | $1.50 \times 10^{-8}$ | | $8.79 \times 10^{-8}$ | $7.28 \times 10^{-9}$ | $1.67 \times 10^{-9}$ | $1.24 \times 10^{-9}$ | $9.39 \times 10^{-10}$ |
| 650K | $1.44 \times 10^{-8}$ | | | $8.40 \times 10^{-9}$ | $1.83 \times 10^{-9}$ | $1.46 \times 10^{-9}$ | $1.13 \times 10^{-9}$ |
| 700K | $1.90 \times 10^{-8}$ | $1.33 \times 10^{-8}$ | | $1.21 \times 10^{-8}$ | $1.96 \times 10^{-9}$ | $1.44 \times 10^{-9}$ | |

**Table 6.1:** Diffusivities for DCM in FAU at various loadings.

As far as we know there is no data in the literature for diffusivities of DCM in FAU. The values of the diffusivities can however be compared to molecules that are similar in size such as chloroform and methanol. The diffusivities obtained for DCM are found to be two orders of magnitude lower than to those obtained for chloroform diffusion in NaY also by simulation ($2.55 \times 10^{-12}$ $m^2s^{-1}$ for a loading of 40 molecules of chloroform compared to $2.54 \times 10^{-10}$ $m^2s^{-1}$ for DCM) [24] but of the same order of magnitude for methanol in NaY ($1.54 \times 10^{-10} m^2s^{-1}$ for a loading of 32 methanol molecules per unit cell compared to $4.68 \times 10^{-6} m^2s^{-1}$ for DCM). [25]

## 6.5.2 Molecular Graphics

This section presents some molecular graphics to describe the orientation of the adsorbate molecules within the FAU zeolite framework at different loadings. At all loadings the molecules appear to form either very loosely bound dimers (figure 6.5a) or small clusters of 3-4 molecules (figure 6.5b and 6.5c).
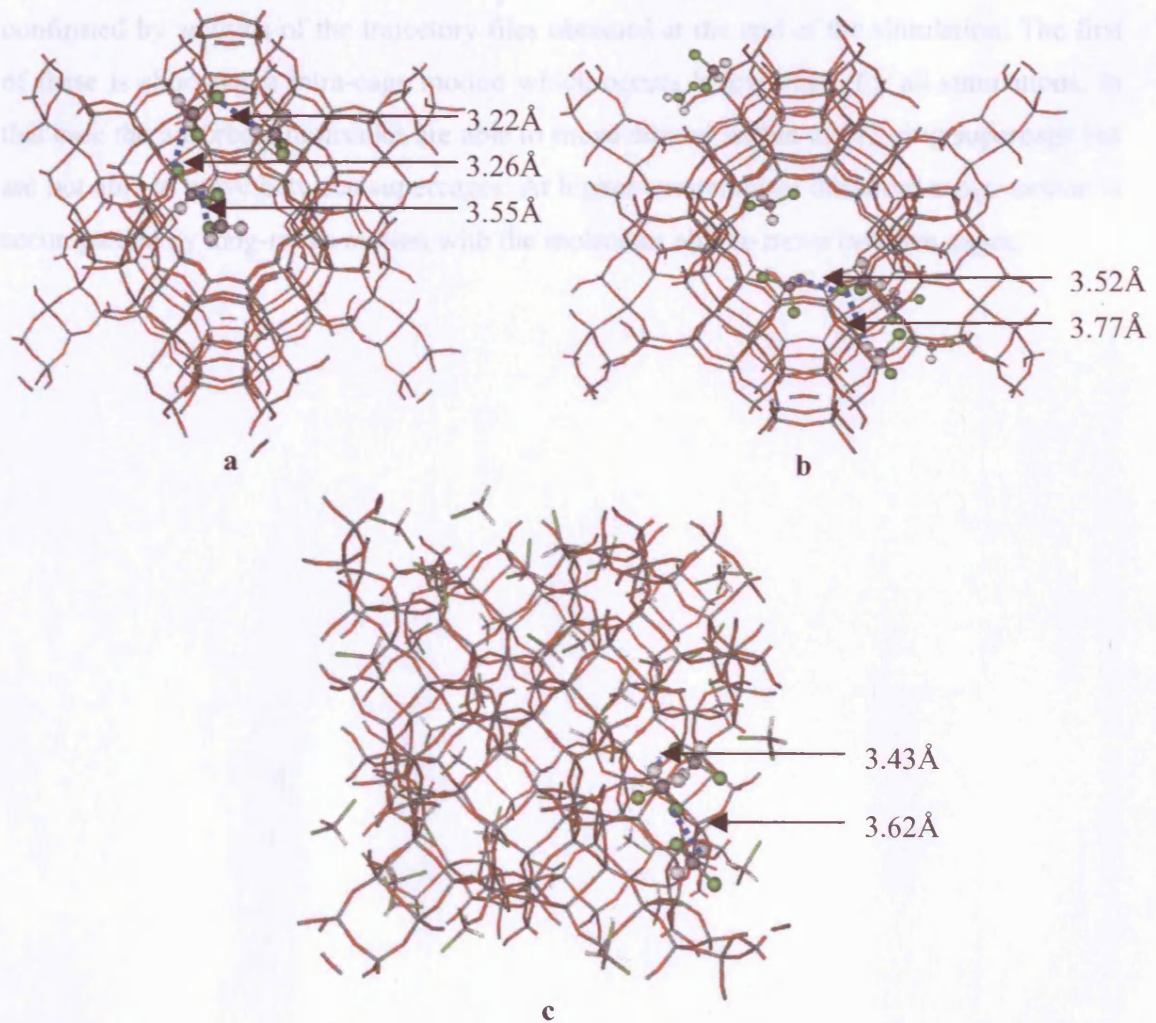


**Figure 6.5:** Molecular graphics showing DCM in FAU at various loadings;

a) 4DCM  b) 8DCM and c) 40DCM.

### 6.5.3 –Arrhenius Plots and activation energies

Arrhenius plots describing how diffusion varies as a function of temperature are shown in figure 6.6 below. Analysis of the gradients of these plots allows activation energies to be obtained. The activation energies for DCM range between 0.7eV and 2.04eV. These plots also allow us to distinguish between two different types of motion occurring, given by a change in the gradient of the plots. In general, two types of motion are observed, which are confirmed by analysis of the trajectory files obtained at the end of the simulation. The first of these is short-range intra-cage motion which occurs below 450K for all simulations. In this case the adsorbate molecules are able to move around within the 12-ring supercage but are not able to move between supercages. At higher temperatures this short-range motion is accompanied by long-range motion with the molecules able to move between cages.
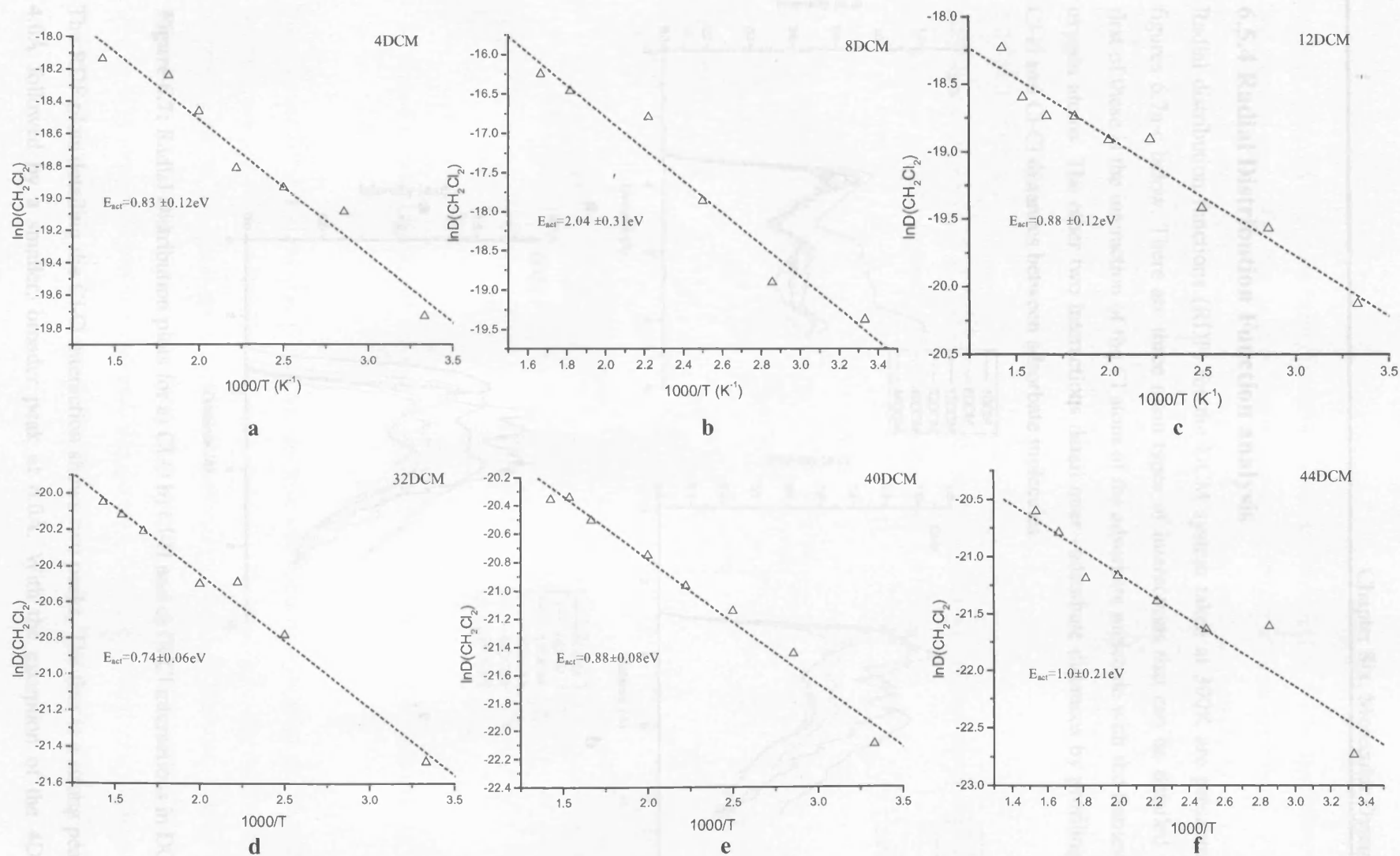
**Figure 6.6:** Arrhenius plots for DCM in FAU at low loadings (a-b), intermediate loadings (c) and high loadings (d-f).

## 6.5.4 Radial Distribution Function analysis

Radial distribution functions (RDF) for the DCM system taken at 300K are presented in figures 6.7a-c below. There are three main types of interactions that can be detailed. The first of these is the interaction of the Cl atom of the adsorbate molecule with the framework oxygen atoms. The other two interactions detail inter –adsorbate distances by profiling the Cl-H and Cl-Cl distances between adsorbate molecules.
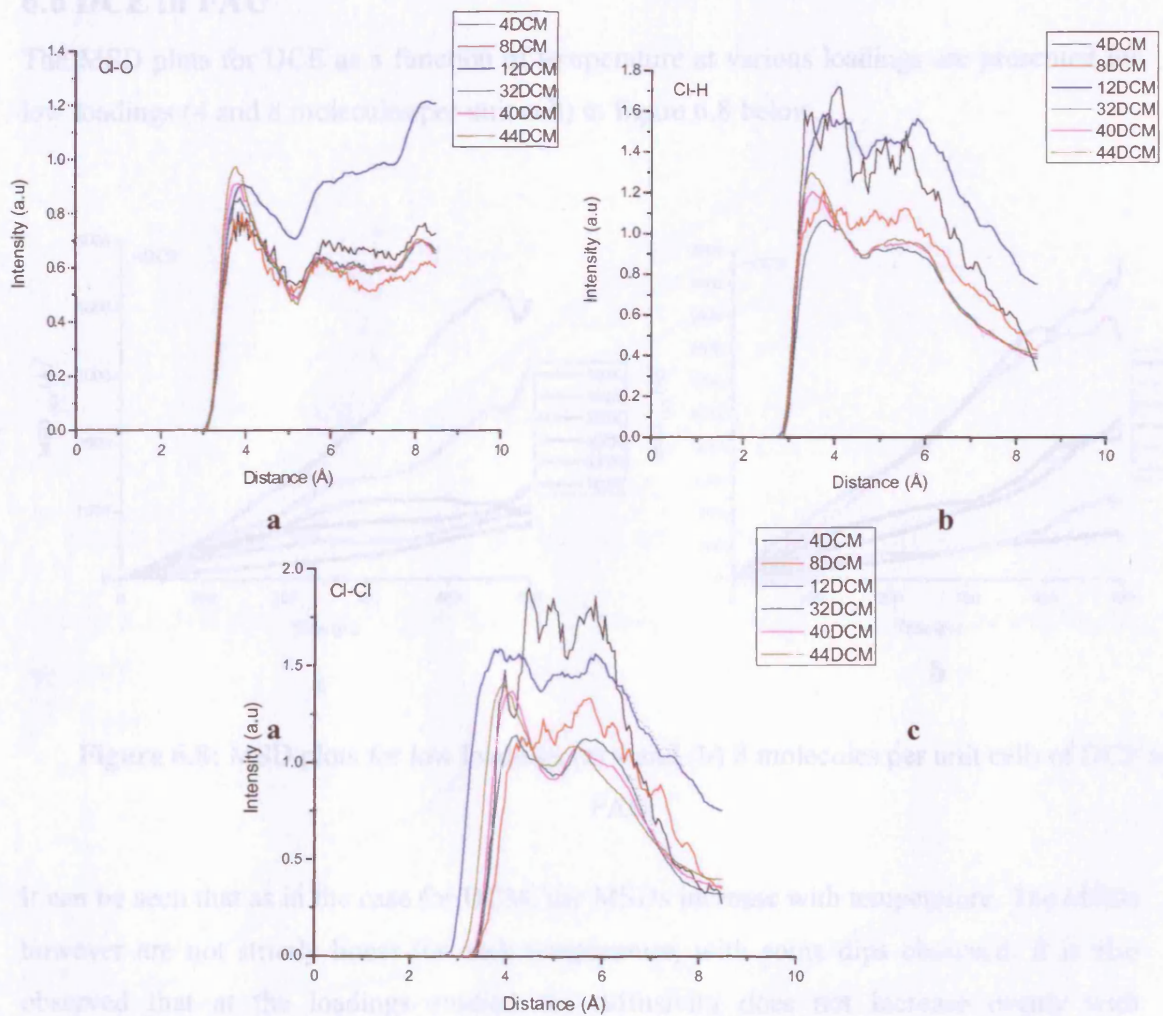


**Figure 6.7:** Radial Distribution plots for a) Cl-O b) Cl-H and c) Cl-Cl interactions in DCM.

The RDF plots detailing the Cl-O interaction shows two peaks. The first is a strong peak at 4.0Å followed by a smaller, broader peak at 6.0Å. With the exception of the 4DCM

loading, the peaks increase with loading. The RDF showing the Cl-H interaction also displays two peaks. The first peak is slightly stronger and sharper than the second one and appears at approximately 3.8Å. The second peak is very broad and appears between 5.0Å and 6.2Å. The Cl-Cl RDF once again displays two peaks. The first peak is very sharp and appears at 4.0Å. The second is higher in intensity, broader than the first and appears between 5.8Å and 6.2Å. All the interactions appear to be van der Waals in nature.

## 6.6 DCE in FAU

The MSD plots for DCE as a function of temperature at various loadings are presented for low loadings (4 and 8 molecules per unit cell) in figure 6.8 below.
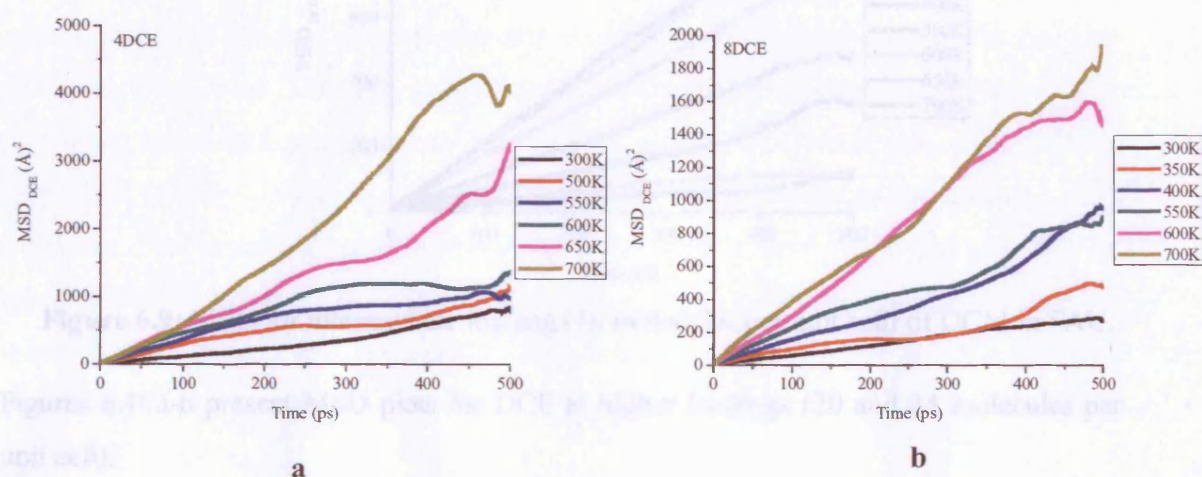


**Figure 6.8:** MSD plots for low loadings (a) 4 and (b) 8 molecules per unit cell) of DCE in FAU.

It can be seen that as in the case for DCM, the MSDs increase with temperature. The MSDs however are not strictly linear for each temperature, with some dips observed. It is also observed that at the loadings studied the diffusivity does not increase evenly with temperature, evidenced for example by the large gap observed between 650K and 700K at a loading of 4 molecules per unit cell and also between 550K and 600K at a loading of 8 molecules per unit cell. A decrease in the total MSD value is observed as the loadings

increase with values of 4000Å for a loading of 4 molecules and half that for 8 molecules per unit cell.

Figure 6.9 shows the MSD plot for DCE molecules at an intermediate loading (16 molecules per unit cell). The diffusivity again increases with temperature and the plots appear to be more linear than at lower loadings. The total MSD decreases to 1200Å compared to 2000Å at 8 molecules per unit cell.
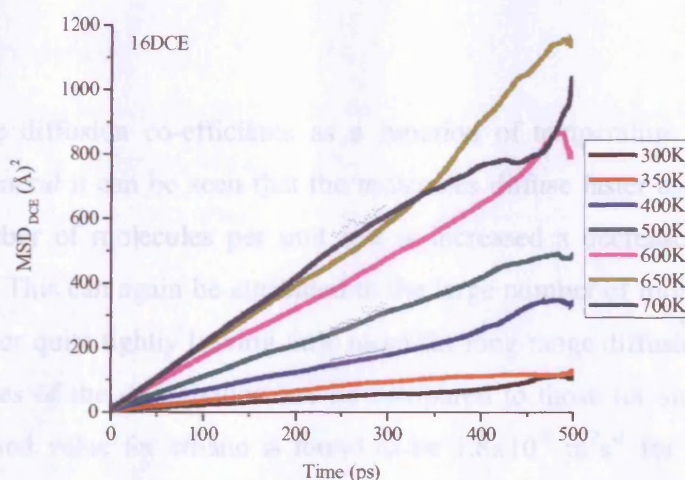


**Figure 6.9:** MSD for intermediate loading (16 molecules per unit cell) of DCM in FAU.

Figures 6.10a-b present MSD plots for DCE at higher loadings (20 and 24 molecules per unit cell).
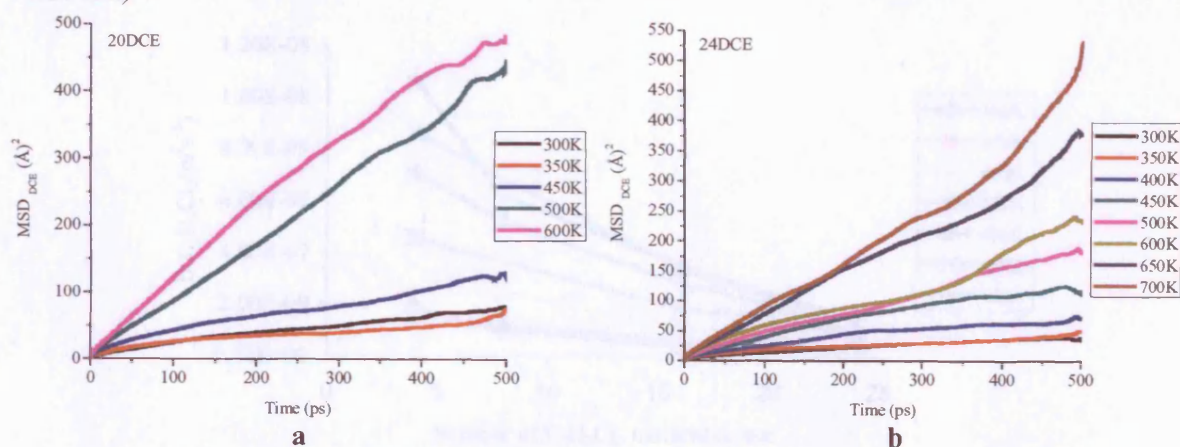


**Figure 6.10:** MSD plot for higher loadings (20 and 24 molecules per unit cell) of DCE in FAU.

The MSD increases with increasing temperature. However the increase in temperature does not appear to occur consistently, observed by the large gaps observed in the plots between 450K and 500K for a loading of 20 molecules per unit cell and between 600K and 650K for a loading of 24 molecules per unit cell. The total MSDs appear to decrease compared to the lower loadings with MSD values of 500 and 370Å for 20 and 24 molecules per unit cell respectively. The overall decrease in total diffusivity as loading increases can be attributed to the fact that the molecules present pack quite closely together and therefore there is little room for long-range diffusion. Instead the molecules are observed to tumble around their initial adsorption sites.

Table 6.2 presents the diffusion co-efficients as a function of temperature for DCE at various loadings. In general it can be seen that the molecules diffuse faster as temperature increases. As the number of molecules per unit cell is increased a decrease in the total diffusivity is observed. This can again be attributed to the large number of molecules in the cell, which pack together quite tightly leaving little room for long-range diffusion. As in the case of DCM the values of the diffusivities can be compared to those for similarly sized molecules. The simulated value for ethane is found to be $1.8 \times 10^{-8}$ $m^2 s^{-1}$ for a loading of approximately 4 molecules per unit cell [26]. This is an order of magnitude lower than the value obtained at the same loading for DCE. Figure 6.11 also shows that the diffusion decreases as loading increases.
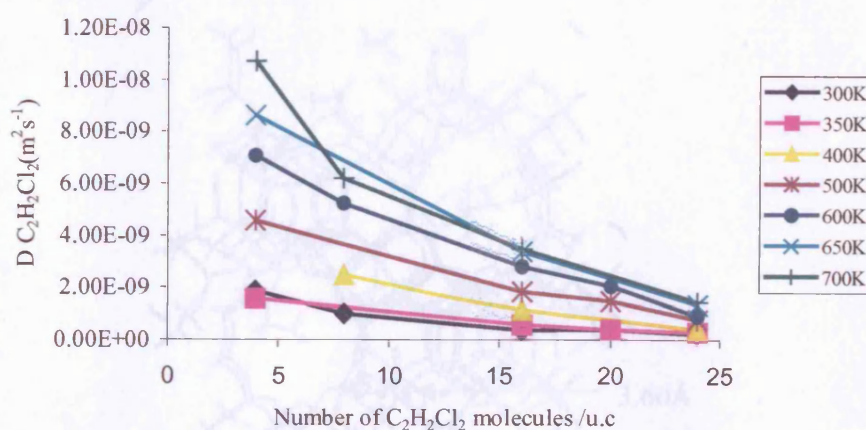


**Figure 6.11:** Diffusivity for DCE in FAU as a function of loading.

| Temperature | 4DCE | 8DCE | 16DCE | 20DCE | 24DCE |
|---|---|---|---|---|---|
| 300K | $1.87 \times 10^{-9}$ | $1.01 \times 10^{-9}$ | $3.75 \times 10^{-10}$ | $3.96 \times 10^{-10}$ | $2.24 \times 10^{-10}$ |
| 350K | | $1.57 \times 10^{-9}$ | $5.90 \times 10^{-10}$ | $3.95 \times 10^{-10}$ | $2.82 \times 10^{-10}$ |
| 400K | | $2.47 \times 10^{-9}$ | $1.14 \times 10^{-9}$ | | $4.08 \times 10^{-10}$ |
| 450K | | | | $6.77 \times 10^{-10}$ | $6.53 \times 10^{-10}$ |
| 500K | $4.56 \times 10^{-9}$ | | $1.84 \times 10^{-9}$ | $1.47 \times 10^{-9}$ | $7.63 \times 10^{-10}$ |
| 550K | $6.02 \times 10^{-9}$ | $3.66 \times 10^{-9}$ | | | |
| 600K | $7.09 \times 10^{-9}$ | $5.23 \times 10^{-9}$ | $2.82 \times 10^{-9}$ | $2.03 \times 10^{-9}$ | $9.10 \times 10^{-10}$ |
| 650K | $8.64 \times 10^{-9}$ | | $3.36 \times 10^{-9}$ | | $1.32 \times 10^{-9}$ |
| 700K | $1.07 \times 10^{-8}$ | $6.22 \times 10^{-9}$ | $3.50 \times 10^{-9}$ | | $1.45 \times 10^{-9}$ |

**Table 6.2:** Diffusion co-efficients for DCE in FAU at various loadings.

## 6.6.1 Molecular Graphics

Molecular graphics to describe the orientation of the DCE adsorbate molecules within the FAU zeolite framework at different loadings are presented in figures 6.12 a-c. At all loadings the molecules appear to form small clusters of 3-4 molecules.
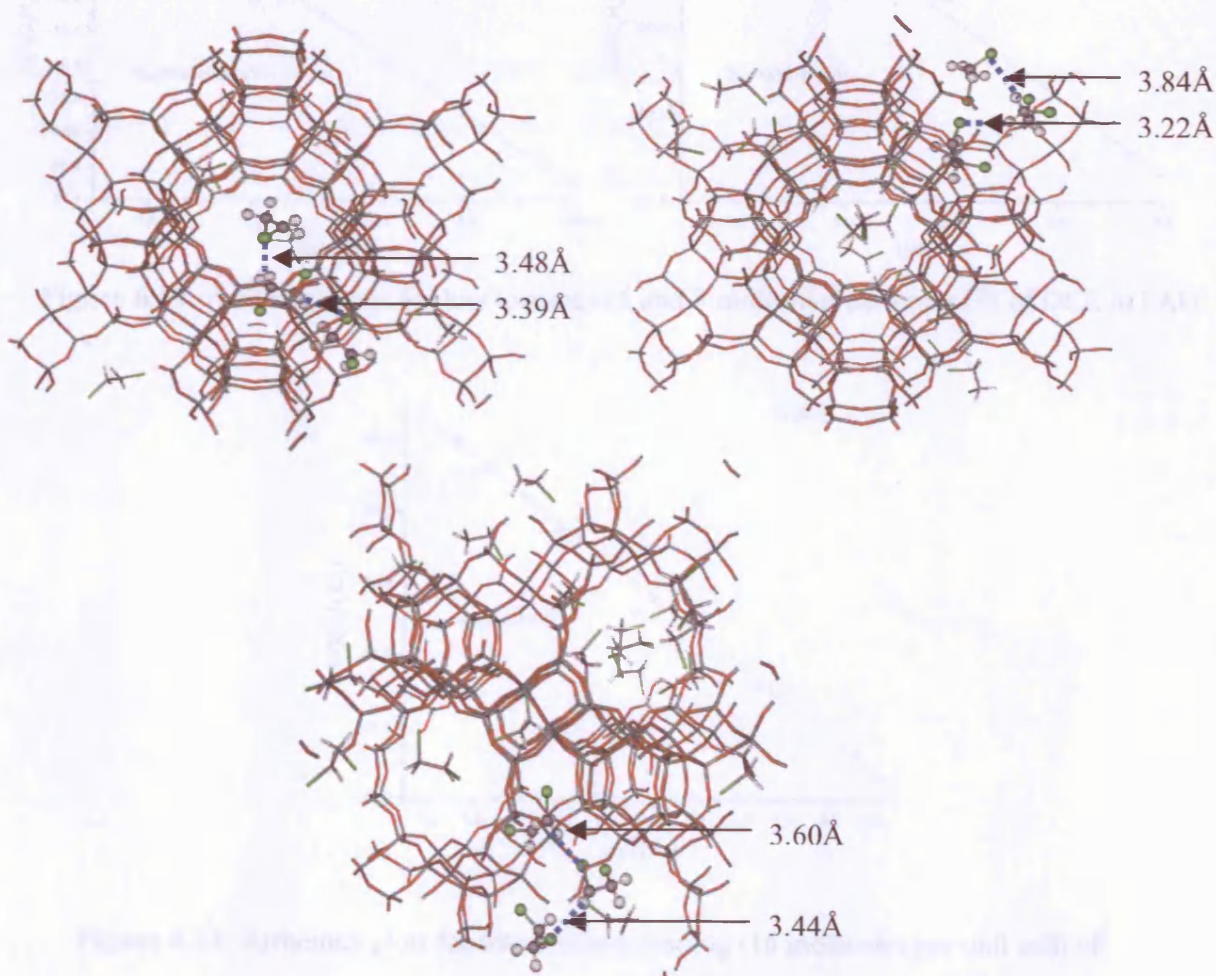


**Figure 6.12:** Molecular graphics showing DCE in FAU at various loadings;

a) 8DCE, b) 16DCE and c) 20DCE molecules per unit cell.

185

## 6.6.2 Arrhenius Plots and Activation Energies

The arrhenius plots and activation energies for DCE in FAU are presented in figures 6.13-6.15 below. As with DCM two types of motion are observed through analysis of the trajectory files, which account for the discontinuities in the plots. Short-range motion is observed at lower temperatures (below 450K) whilst short and long-range motion are observed at higher temperatures. The DCE activation energies vary between 0.86eV and 1.23eV.
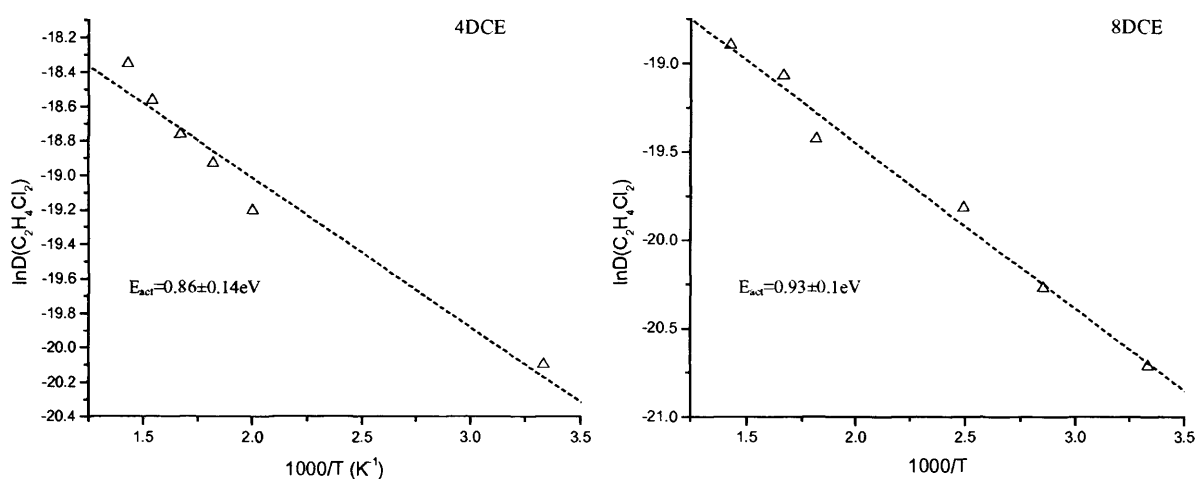


**Figure 6.13:** Arrhenius plots for low loadings (4 and 8 molecules per unit cell) of DCE in FAU
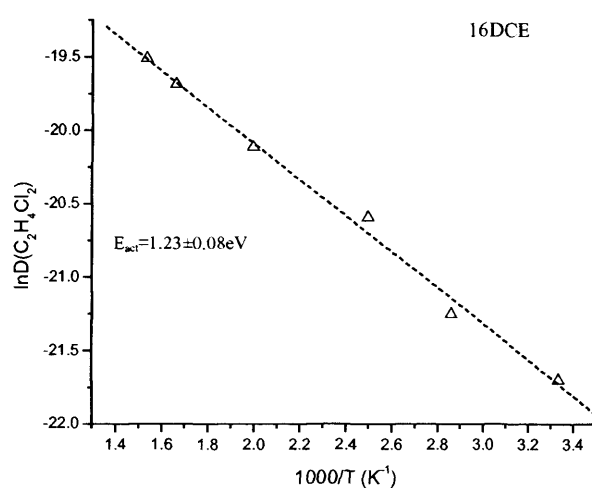


**Figure 6.14:** Arrhenius plots for intermediate loading (16 molecules per unit cell) of DCM in FAU.

186
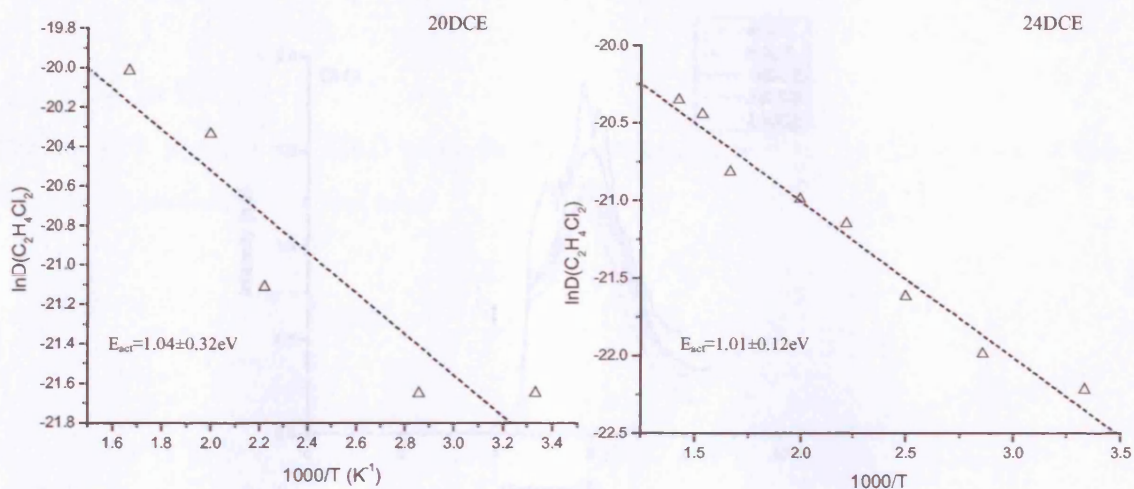
**Figure 6.15:** Arrhenius plots for high loadings (20 and 24 molecules per unit cell) of DCM in FAU.

## 6.6.3 Radial Distribution Function Analysis

Radial distribution functions detailing the three main types of interactions in the DCE system, Cl-framework (O) and intermolecular Cl-H and Cl-Cl taken at 300K are presented in figures 6.16 a-c below.

**c**
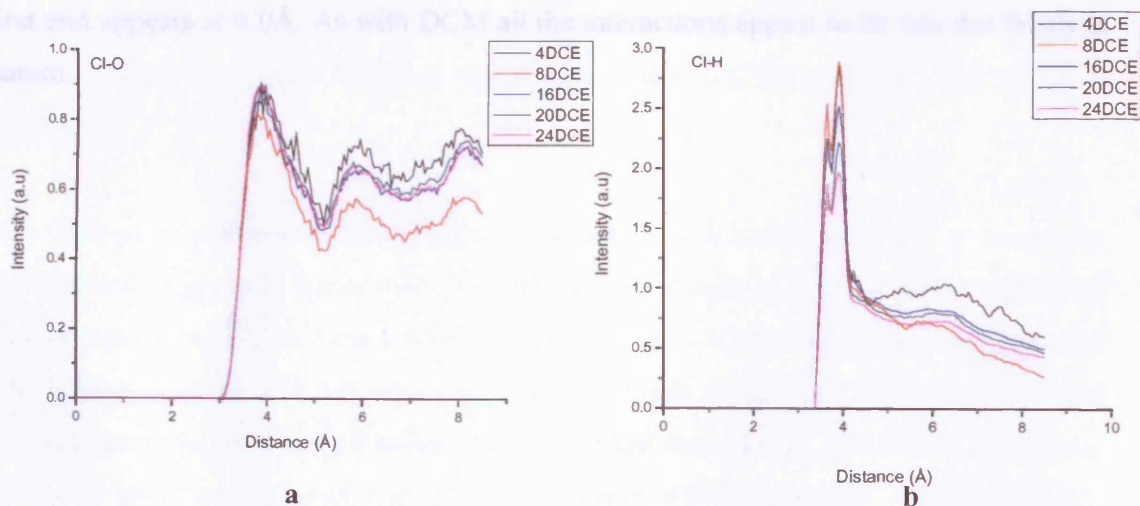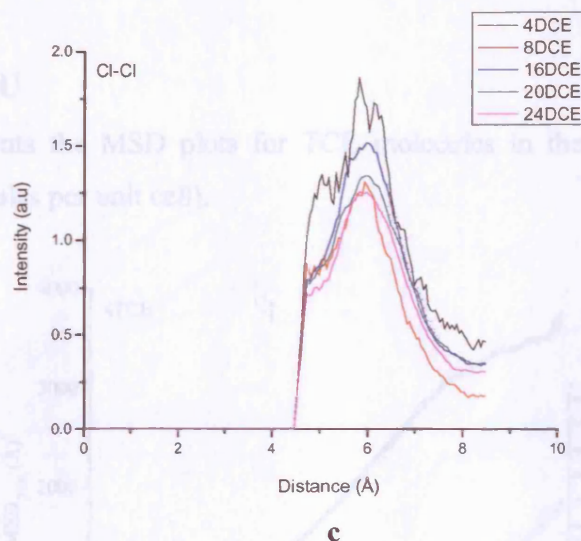
**Figure 6.16:** Radial Distribution plots for a) Cl-O b) Cl-H and c) Cl-Cl interactions in DCE.

The RDF plots detailing the Cl-O interaction shows three peaks. The first is a strong peak at 4.0Å followed by two smaller, broader peaks at 6.0Å and 8.0Å respectively. The RDF showing the Cl-H interaction also displays two very strong peaks (doublet) very close together between 3.8Å and 4.0Å. The Cl-Cl RDF once again displays two peaks. The first peak is very sharp and appears at 4.5Å. The second is higher in intensity, broader than the first and appears at 6.0Å. As with DCM all the interactions appear to be van der Waals in nature.
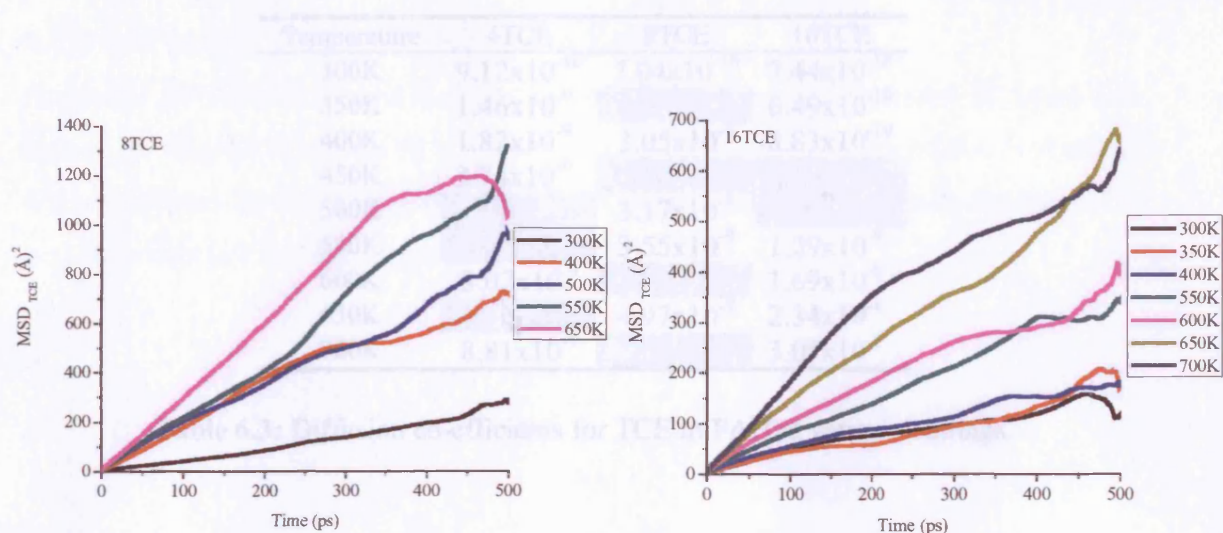
## 6.7 TCE in FAU

Figure 6.17 presents the MSD plots for TCE molecules in the FAU framework at low loadings (4 molecules per unit cell).
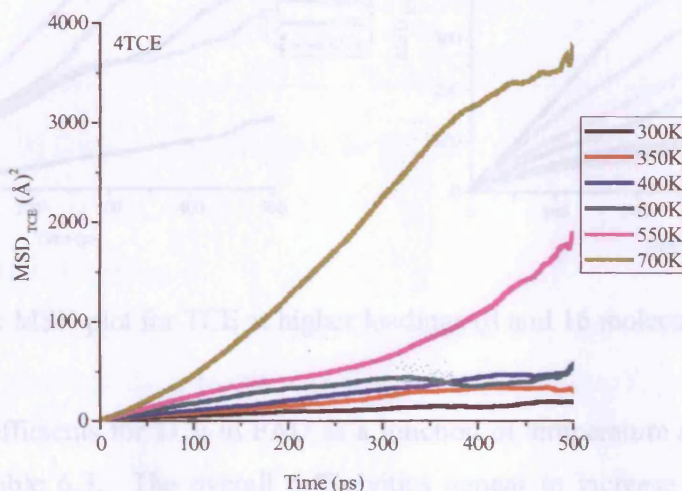


**Figure 6.17:** MSD plot for TCE in FAU at low loading (4 molecules per unit cell).

The plots appear to be fairly linear over the timescale of the simulation and appear to increase with increasing temperature. A large gap is observed between 550K and 700K but this could be due to difficulties in simulations for 600K and 650K, which would be expected to fill this "gap". At higher temperatures the molecules are able to diffuse up to 3500Å.

The MSD plot for intermediate and higher loadings of TCE molecules (8 and 16 molecules per unit cell) is given in figure 6.18. The diffusivities appear to increase with temperature and are more evenly spaced out with no "large gaps" as is observed for lower loadings. The total MSD appears to decrease, with the molecules able to diffuse up to 1200Å and 700Å at high temperatures for 8 and 16 molecules per unit cell respectively. The overall decrease in diffusivity observed can be attributed to the molecules at higher loadings being more tightly packed and unable to diffuse freely through the unit cell. This view is confirmed by analysis of the trajectory files obtained at the end of the simulation.

**Figure 6.18:** MSD plot for TCE at higher loadings (8 and 16 molecules per unit cell).

The diffusion coefficients for TCE in FAU as a function of temperature at various loadings is presented in table 6.3. The overall diffusivities appear to increase with temperature. Diffusion appears to slow down at higher loadings as is illustrated by figure 6.19.
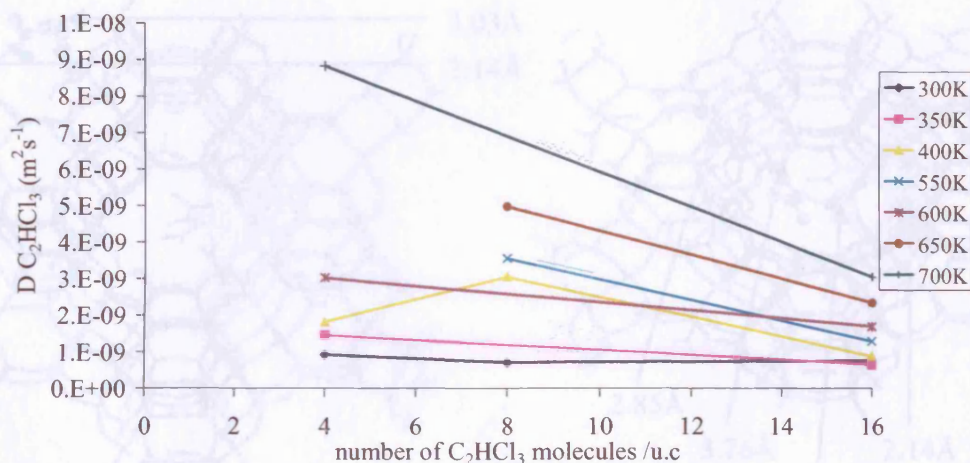


**Figure 6.19:** Diffusivity for TCE in FAU as a function of loading.

| Temperature | 4TCE | 8TCE | 16TCE |
|---|---|---|---|
| 300K | $9.12 \times 10^{-10}$ | $7.04 \times 10^{-10}$ | $7.44 \times 10^{-10}$ |
| 350K | $1.46 \times 10^{-9}$ | | $6.49 \times 10^{-10}$ |
| 400K | $1.82 \times 10^{-9}$ | $3.05 \times 10^{-9}$ | $8.83 \times 10^{-10}$ |
| 450K | $3.74 \times 10^{-9}$ | | |
| 500K | | $3.17 \times 10^{-9}$ | |
| 550K | | $3.55 \times 10^{-9}$ | $1.29 \times 10^{-9}$ |
| 600K | $3.02 \times 10^{-9}$ | | $1.69 \times 10^{-9}$ |
| 650K | | $4.97 \times 10^{-9}$ | $2.34 \times 10^{-9}$ |
| 700K | $8.81 \times 10^{-9}$ | | $3.05 \times 10^{-9}$ |

**Table 6.3:** Diffusion co-efficients for TCE in FAU at various loadings.

## 6.7.2 Molecular Graphics

Figure 6.20 show molecular graphics representing the positions and orientations of the TCE molecules in the zeolite pores at various loadings. At all loadings the molecules appear to form either dimers (figure 6.20a) or small clusters of 3-4 molecules (figure 6.20b and 6.20c).



**Figure 6.20:** Molecular graphics showing TCE in FAU at various loadings;

a) 4TCE, b) 8TCE and c) 16TCE molecules per unit cell.

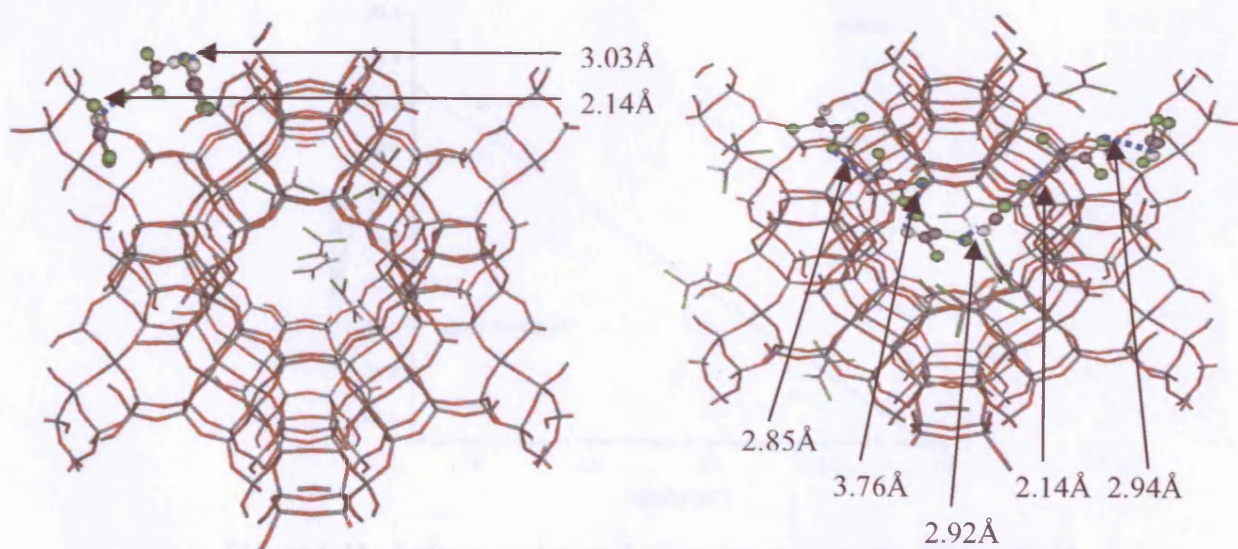### 6.7.3 Arrhenius Plots and Activation Energies

Arrhenius plots and activation energies for the TCE system are presented in figure 6.21 below. As with DCM and DCE, at lower temperatures only inter-cage motion is observed whilst at higher temperatures (over 500K) long-range intra-cage motion is observed. The activation energies for TCE range from 0.73eV to 1.03eV.
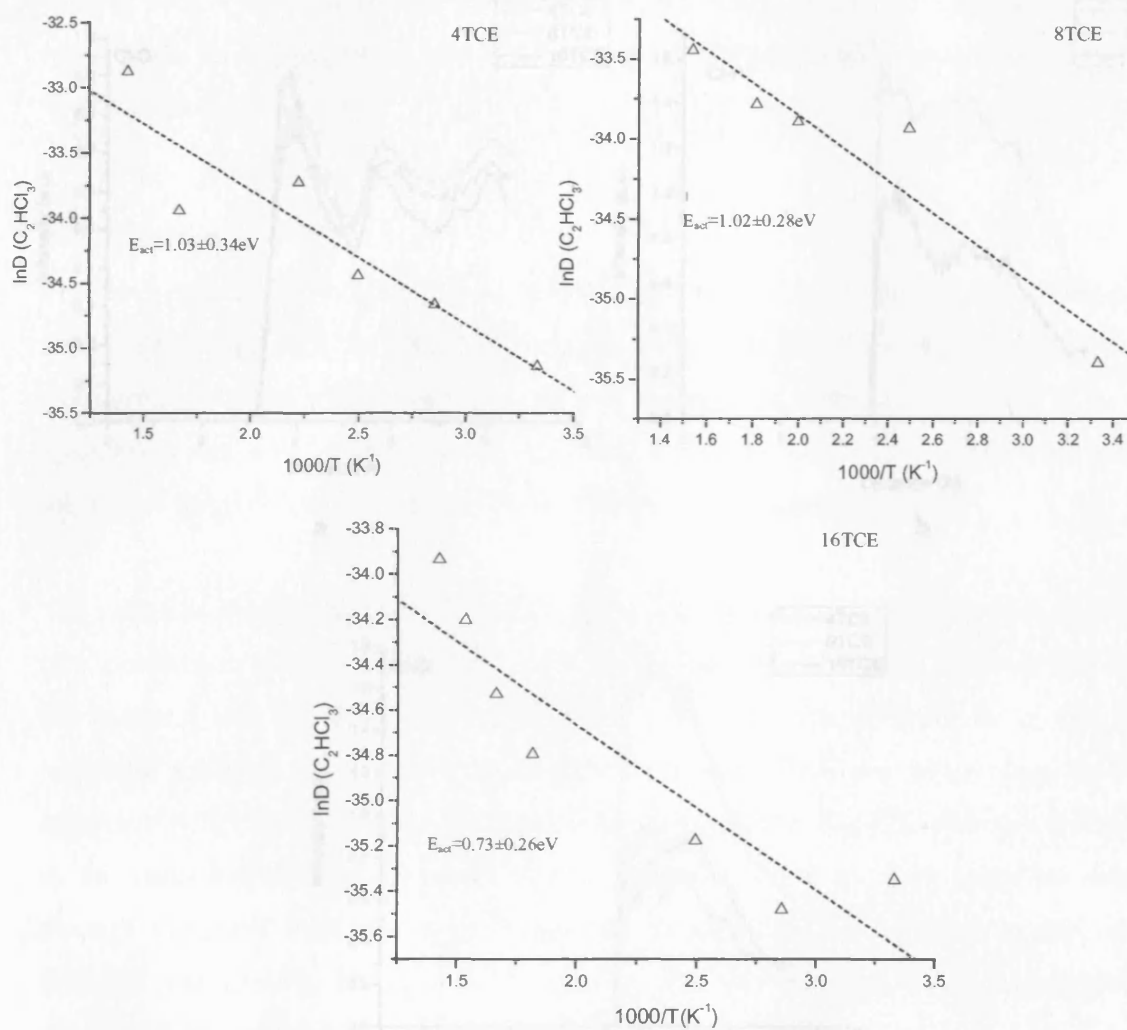


**Figure 6.21:** Arrhenius plots and activation energies for TCE in FAU.

### 6.7.4 Radial Distribution Function Analysis

Radial distribution functions detailing the three main types of interactions in the DCE system, Cl-framework and intermolecular Cl-H and Cl-Cl taken at 300K are presented in figures 6.22 below.



a



b



c
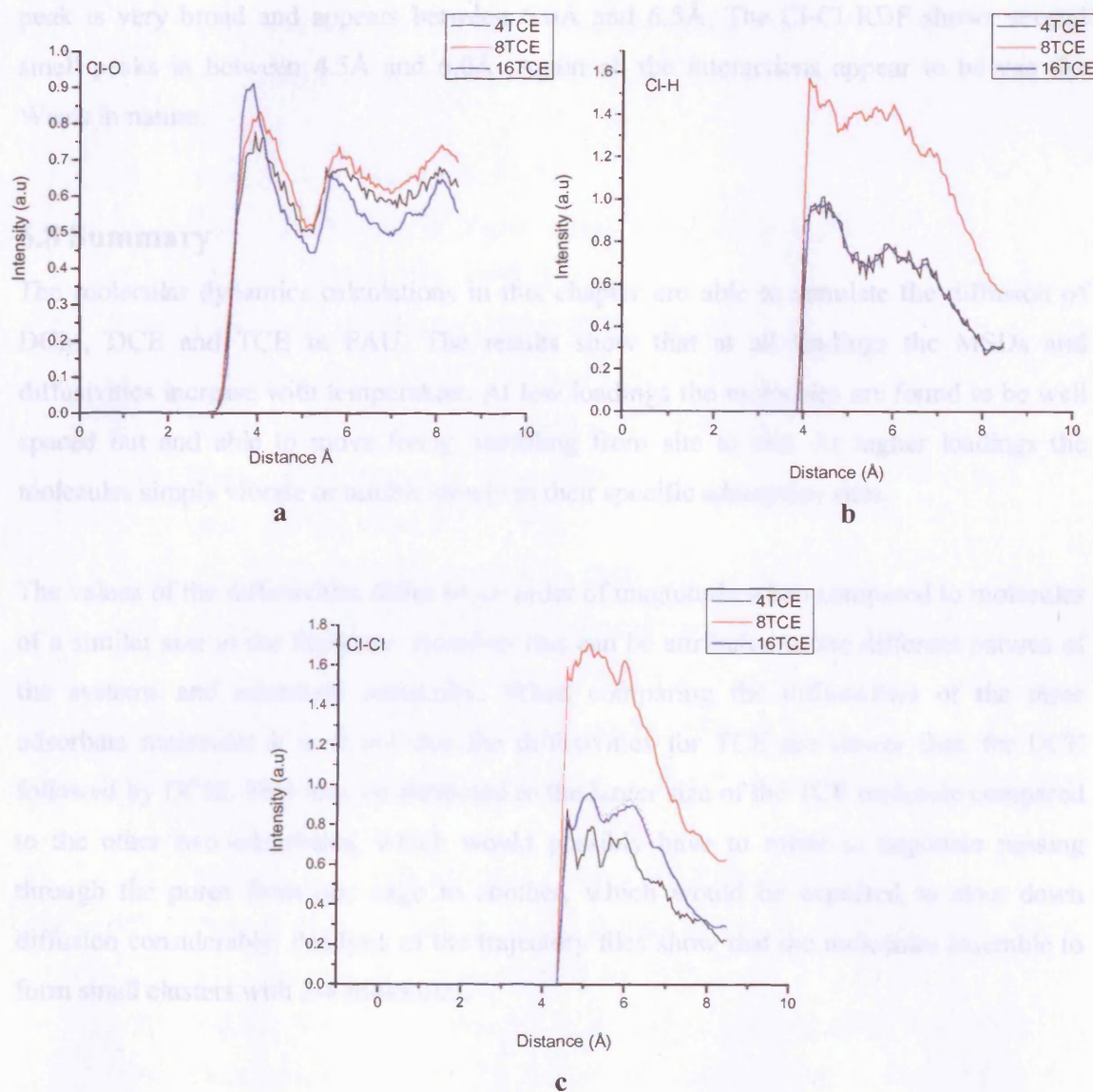
**Figure 6.22:** Radial Distribution plots for a) Cl-O b) Cl-H and c) Cl-Cl interactions.

193

The RDF plots detailing the Cl-O interaction shows three peaks. The first is a strong peak at 4.0Å followed by two smaller, broader peaks at 6.0Å and 8.0Å. The first peak increases with loading whilst in the second peak the peak for 16TCE loading is out of place. The RDF showing the Cl-H interaction also displays two peaks. The first peak is slightly stronger and sharper than the second one and appears at approximately 4.0Å. The second peak is very broad and appears between 6.0Å and 6.5Å. The Cl-Cl RDF shows several small peaks in between 4.5Å and 6.0Å. Again all the interactions appear to be van der Waals in nature.

## 6.8 Summary

The molecular dynamics calculations in this chapter are able to simulate the diffusion of DCM, DCE and TCE in FAU. The results show that at all loadings the MSDs and diffusivities increase with temperature. At low loadings the molecules are found to be well spaced out and able to move freely, tumbling from site to site. At higher loadings the molecules simply vibrate or tumble slowly in their specific adsorption sites.

The values of the diffusivities differ by an order of magnitude when compared to molecules of a similar size in the literature. However this can be attributed to the different natures of the systems and adsorbate molecules. When comparing the diffusivities of the three adsorbate molecules it is found that the diffusivities for TCE are slower than for DCE followed by DCM. This may be attributed to the larger size of the TCE molecule compared to the other two adsorbates, which would possibly have to rotate to negotiate passing through the pores from one cage to another, which would be expected to slow down diffusion considerably. Analysis of the trajectory files show that the molecules assemble to form small clusters with 2-4 molecules.

# References

(1) Post, M. F. M. Diffusion in zeolite molecular sieves. In *Introduction to zeolite science and practice*; Bekkum, H. van., Flanigen, E. M., Jansen, J. C., Eds.; Elsevier: Amsterdam, 1991; pp 391.

(2) Keil, F. J. *Rev. Chem. Eng.* **2000**, *16*, 71.

(3) Auerbach, S. M.; Jousse, F.; Vercauteren, D. P. Dynamics of sorbed molecules in zeolites. In *Computer modelling of microporous and mesoporous materials*; Catlow, C. R. A., Santen, R. A. v., Smit, B., Eds.; pp 1.

(4) Fick, A. *Ann. Phys* **1855**, *94*, 59.

(5) Barrer, R. M.; Jost, W. *Trans. Faraday Soc.* **1949**, *45*, 928.

(6) Einstein, A. *Ann. Phys* **1905**, 549.

(7) Haberlandt, R. *Thin Solid Films* **1998**, *330*, 34.

(8) Theodorou, D. N.; Wei, J. *J. Catal* **1983**, *83*, 205.

(9) Tsikoyiannis, J.; Wei, J. *Chem. Eng. Sci* **1991**, *46*, 233.

(10) Karger, J.; Pfeifer, H. *Zeolites* **1987**, *7*, 90.

(11) Xiao, J.; Wei, J. **1992**, *47*, 1123.

(12) Eic, M.; Ruthven, D. M. *Zeolites* **1988**, *8*, 40.

(13) Pfeifer, H. NMR of molecules adsorbed on solids. In *NMR-Basic principles and processes*; Springer: Berlin, 1972; Vol. 7; pp 53.

(14) Jobic, H.; Bee, M.; Kearley, G. J. *Zeolites* **1989**, *9*, 312.

(15) Lara, E. C. d.; Kahn, R.; Mezei, F. *J. Chem. Soc - Faraday Transactions* **1983**, *79*, 1911.

(16) Rajappa, C.; Yashonath, S. *J. Chem. Phys* **1999**, *110*, 5960.

(17) Henson, N. J.; Cheetham, A. K.; Stockenhuber, M.; Lercher, J. A. *J. Chem. Soc - Faraday Transactions* **1998**, *94*, 3759.

(18) Raj, N.; Sastre, G.; Catlow, C. R. A. *J. Phys. Chem. B* **1999**, *103*, 11007.

(19) Domokos, L.; Lefferts, L.; Seshan, K.; Lercher, J. A. *J. Catal* **2001**, *203*, 351.

(20) Tuckerman, M. E.; Martyna, G. J. *J. Phys. Chem* **2000**, *104*, 159.

(21) Accelrys Inc *Forcefields based simulations Manual.*

(22)    Gale, J. D. *J. Chem. Soc - Faraday Transactions* **1997**, *93*, 629.

(23)    Smith, W.; Forester, T. R. *J. Molecular Graphics* **1996**, *14*, 136.

(24)    Ramsahaye, N.A.; Bell, R.G. *J. Phys. Chem B* **2005**, *109*, 4738

(25)    Bell, R.G; Plant, D.F. Maurin, G *Unpublished Results*

(26)    Chempath, S.; Rajamani K,; Snurr R.Q.; *J. Phys Chem B* **2004**, 108, 13481

# Chapter Seven: Conclusions and Future Work

## 7.1 Summary of Results

A summary of the main points of each of the results chapter is presented below:

The cluster approach adopted in chapter 3 has detailed the alignment and positions of the adsorbate molecules within the zeolite framework. The study shows that in the siliceous clusters the molecules arrange in such a way that they experience optimal interaction within the zeolite framework. In the case of the aluminosilicate clusters the Cl-H interaction is found to contribute a large part to the adsorption energy; however the rest of the molecule attempts to orientate in such a way that it experiences optimal interaction with the framework atoms. The adsorption energy obtained using the cluster approach is significantly lower than the experimental values reported in the literature. This was attributed in part to the nature of the cluster approach, in particular the neglect of the long-range electrostatic effects of the zeolite crystal. A further limitation of this approach is the use of the DFT method. The PW91 functional employed is a pure density functional and as such does not account for dispersive interactions, which in polar adsorbates such as those being modelled, would be expected to contribute a sizable amount to the adsorption energy.

A range of techniques have been used in chapter 4 to attempt to overcome some of the limitations of the cluster approach highlighted above. These included repeating the cluster calculations using a hybrid functional, adopting a periodic DFT approach and utilising the QMPot embedded cluster technique. The hybrid functional results show that the molecule adopts a different location and orientation within the cluster compared to the PW91 functional with the adsorbate molecule being further from the framework in each case. This may explain why the adsorption energy obtained is lower than with the PW91 functional. The periodic DFT calculations were conducted using a unit cell of mordenite and in each case the adsorption energy was found to be underestimated compared to the free-cluster approach. The QMPot embedded approach however produces results that are consistently higher than the cluster approach and are closer to

the experimental heats of adsorption. This improvement over the cluster approach can be attributed to the inclusion of the long-range effects. The interaction energy obtained using the QMPot approach however is still approximately 30kJ/Mol weaker than the experimental value.

Chapter 5 details the results using a Grand Canonical Monte Carlo method. The isotherms and isosteric heat plots obtained are in good agreement with experimental studies. The simulated isotherms are able to model the domains obtained in the experimental isotherm, although simulations at lower pressures would make them more obvious. Our results also show that overall adsorption is strongest in the MFI framework, followed by MOR and then FAU. This trend follows that of the pore sizes. The molecules in the smaller pore cannot spread themselves out and therefore have maximum interaction with the zeolite framework. The FAU framework has the largest void volume and the molecules enclosed within it are able to spread out and therefore have fewer interactions with the zeolite framework.

Chapter 6 presents preliminary results of a molecular dynamics study. The results show that the potential used is able to simulate the diffusion of the adsorbate molecules. The results show that at all loadings the MSDs and diffusivities increase with temperature. At low loadings the molecules are found to be well spaced out and able to move freely, tumbling from site to site. At higher loadings the molecules simply vibrate or tumble slowly in their specific adsorption sites.

The values of the diffusivities differ by an order of magnitude when compared to molecules of a similar size in the literature. However this can be attributed to the different natures of the systems and adsorbate molecules. When comparing the diffusivities of the three adsorbate molecules it is found that the diffusivities for TCE are slower than for DCE followed by DCM. This may be attributed to the larger size of the TCE molecule compared to the other two adsorbates, which would possibly have to rotate to negotiate passing through the pores from one cage to another, which would be expected to slow down diffusion considerably. Analysis of the trajectory files show that the molecules assemble to form small clusters with 2-4 molecules.

## 7.2 Future Work

There is scope for further work in several of the results chapters.

It would be useful to repeat at least some of the free and embedded cluster calculations using a post Hartree-Fock method such as MP2 theory. This would allow the inclusion of electron-correlation effects. Attempts were made to do this for at least one cluster; however these proved to be too computationally expensive to run. The MP2 approach however would still not be able to model dispersive interactions accurately. There would need to be some development in theory, for example development of a functional that will allow dispersive interactions to be modelled. There are groups that are attempting to develop such a functional and it may be useful to repeat the calculations once the functional is available.

The adsorption isotherms obtained in chapter 5 could be repeated at different temperatures to ascertain the effect temperature has on adsorption. In order to compare the isotherms more effectively with experimental data it would be useful to carry out the simulations at lower pressures. However this would mean using a different program since we have already simulated at the lowest pressure possible in Sorption. It would also be useful to perform the calculations under more realistic conditions, for example to look at the effects of water on the adsorption isotherms or to simulate the adsorption isotherms of mixtures of adsorbates.

The molecular dynamics simulations could also be extended to include the other framework structures to test the transferability of the potential between framework structures. As for the sorption calculations it would be interesting to investigate the effects of water on the dynamics of the system and also the effects of a mixture of adsorbates on the diffusion process. It may also possible to model the transport diffusion of the adsorbate molecules in the framework.

**Appendix 1**: Saul-Catlow Potential

### Buckingham Potential

| | | A(eV) | $\rho$ (Å) | C (eV Å$^6$) |
|---|---|---|---|---|
| Al$^{3+}$core | O$^{2-}$shell | 1460.3000 | 0.299120 | |
| O1 core | Al core | 1142.6775 | 0.299120 | |
| O shell | O shell | 22764.000 | 0.149000 | 27.88 |
| Si core | O shell | 1283.9070 | 0.320520 | 10.662 |
| O1 core | Si core | 983.55660 | 0.320520 | 10.662 |
| O1 core | O shell | 22764.000 | 0.149000 | 27.88 |
| H core | O shell | 311.97000 | 0.250000 | |

### Morse Potential

| | | A(eV) | $\rho$ (Å) | C (eV Å$^6$) |
|---|---|---|---|---|
| H core | O1 core | 7.0525000 | 2.1986 | 0.94850 |

### Three Body

| | k (eV rad$^{-1}$) | $\theta_0^\circ$ (deg) |
|---|---|---|
| O-T-O | 2.0972 | 109.47 |

### Charges

| | $q_a$ |
|---|---|
| Si$^{4+}$ | 4.000000 |
| Al$^{3+}$ | 3.000000 |
| O$^{2-}$ core | 0.869020 |
| O$^{2-}$ shell | -2.869020 |
| O1 core | -1.426000 |
| H core | 0.426000 |